MINISTRY OF SCIENCE AND HIGHER EDUCATION
OF THE RUSSIAN FEDERATION
Federal State Budgetary Educational Institution of Higher Education
«Ivanovo State Polytechnic University»

Manuscript rights

陈成豫.

Chen Chengyu

SIMULATION MODELLING OF DIGITAL TWINSOF WOMEN’S PLEATED DRESSES

Dissertation
submitted for the degree of Candidate of Sciences
2.6.16 – Technology of Light Industry Products
(specialization: Design of Garments)

Research Supervisor — Prof., Dr.Sc.,V.E.Kuzmichev

Ivanovo – 2026

Содержание

FULL INTRODUCTION

Relevance of the Research Topic. The relevance of the research topic. The modern garment industry is facing increasing demands for the production of new clothing models. Under the accelerated development of the Industry 4.0 concept, the creation of intelligent systems for the digital prediction of the results of artistic and engineering design of light industry products (LIPs) has become a key task.

The creation of digital twins (DTs) of women's dresses with pleated forms is a significant scientific problem. Its solution depends on the accuracy of mathematical and geometric modelling based on a set of individual indicators of the physical and mechanical properties of fabrics, including drapeability, bending stiffness, tensile anisotropy, and other parameters. To measure these properties, specialized measurement systems, such as fabric kits in CLO3D and Style3D, as well as individual instruments and methods, including the Cusick method, the cantilever method according to ASTM D1388, and others, are used. Fabric drapeability is a determining factor in the form generation of women's garments. Traditional methods for evaluating drapeability have significant limitations: they do not take into account the three-dimensional nature of garment draping on the human figure in the presence of sewn seams.

Existing methods, while providing a sufficient degree of adequacy for digital twins, are labor-intensive, require specialized measuring equipment, and, most importantly, are not integrated into end-to-end digital processes for designing garments with complex pleated forms. Such forms are obtained by applying structural pattern modelling techniques while taking into account the property indicators of textile materials. This creates a gap between physical garment prototypes and their digital twins. Modern garment CAD systems, such as CLO3D and Style3D, make it possible to simulate fabric behavior; however, this requires a set of parameters measured on flat samples, whose shape is far removed from the deformable areas of a pleated garment form.

The development of artificial intelligence (AI) technologies opens up new possibilities for using their potential as measurement tools capable of "reading" the mechanical properties of fabrics directly from their visual images. However, the absence of standardized protocols for such "reading" and the lack of a metrological framework for evaluating the accuracy of digital twins of light industry products constrain the development of this direction. Therefore, the development of methods and protocols for the rapid and accurate generation of digital twins of light industry products and their application in simulation modelling (SM) is a relevant scientific and technical task.

The relevance of this research is determined by the need to develop new methods and tools for evaluating drapeability, integrated with AI, computer vision, and 3D modelling technologies, in order to create systems for predicting the pleated form of dresses at the stage of design preparation for production during pattern development.

State of Research on the Topic. Quantitative studies of low-stress mechanics and the spatial form generation of fabrics are based on the classical works of F. T. Peirce and C. C. Chu, as well as on J. C. Cusick’s concept of the drape coefficient, which has become a long-standing reference point in this field. In the area of objective evaluation of material properties, the development of the KES system by S. Kawabata, M. Niwa, and R. Postle, as well as the creation of the engineering testing system FAST/SiroFAST by CSIRO, contributed to the establishment of an interpretable relationship in the chain “fabric parameters — garment appearance”.

The evolution of simulation modelling methods and digital evaluation of fabric properties has relied to a considerable extent on advances in computer graphics in the field of physically based simulation of deformable fabrics, developed within the concepts of D. Terzopoulos, D. Baraff and A. Witkin, and D. Breen. The systematization of key virtual garment technologies by P. Volino and N. Magnenat-Thalmann provided an important theoretical basis for subsequent modelling in garment CAD systems, thereby creating an applied engineering foundation for the implementation of digital twins of garments. The patent analysis conducted in this study revealed a growing trend in patent activity in the field of 3D modelling of light industry products: from 2010 to 2024, the share of patents related to 3D modelling increased from 4.2% to 42.8% among all patents associated with information technologies in the textile industry. The main directions include 3D virtual fitting of garments, simulation of fabric behavior, interactive garment design, and automated recognition of fabric parameters from images.

Neural networks and computer vision for the direct extraction, or inversion, of mechanical parameters of fabrics from their images have been used in the works of K. Bhat, K. Bouman, and C. Rodriguez-Pardo. These studies made it possible to form a promising concept of “AI as a measurement component governed by a strict protocol” for the purpose of creating digital twins of products. Owing to the studies of X. Zeng at GEMTEX/ENSAIT and C. Wong at AiDLab/PolyU, an interdisciplinary research ecosystem for the application of AI in textiles and garments has been formed. The greatest development potential is associated with methods that combine computer vision with language models.

In the Russian Federation, scientific research in the field of simulation modelling is carried out at Ivanovo State Polytechnic University and the Kosygin Russian State University.

Relation to Scientific Programs. The work was carried out with the support of the Russian Science Foundation, grant No. 25-11-00022, “Technology of Virtual Testing of Textile Materials for 3D Garment Modelling” (https://rscf.ru/project/25-11-00022/).

The aim of the dissertation research is to reduce the duration of the simulation modelling process for women’s dresses with pleated forms.

To achieve this aim, the following **tasks were solved:**

1. To conduct a critical analysis of modern methods for determining drapeability and other indicators of the physical and mechanical properties of fabrics in real and virtual environments.

2. To develop a new method for evaluating the anthropomorphic drapeability of textile materials, reproducing the conditions of fixing a fabric sample on the shoulder girdle of the human

figure, and to implement a device based on this method that functions consistently in both physical and virtual environments.

3. To evaluate the effectiveness of using the anthropomorphic drape coefficient in comparison with existing methods.

4. To develop an algorithm for applying the anthropomorphic drape coefficient, measured on short and long samples, to predict external form indicators and to study the influence of pattern parameters on the form generation of women's dresses in the simulation modelling of their digital twins.

5. To create tools for simulation modelling of fabric digital twins based on neural networks for measuring tensile forces at small elongations, bending stiffness, surface density, and thickness, and for generating fabric digital twins in 3D software. To develop a library of photographic 2D and 3D fabric images that is necessary and sufficient for the generation of fabric digital twins.

6.To develop the structure of a women's dress for studying the surface pleating formed under the influence of pleats of different depths and directions.

7. To develop a method for evaluating the surface pleating of a women's dress based on computer vision, as well as an algorithm for its application in selecting the conditions for structural pattern modelling and ensuring the visual similarity of draped dresses made from different fabrics.

8. To conduct a comprehensive validation of the developed methods for evaluating drapeability, parameterizing the pleated surface, and generating fabric digital twins by comparing digital twins with real dresses.

Object of the Research – fabrics, women's dresses, and the process of their simulation modelling.

Subject of the Research – the regularities governing the form generation of the pleated surface of women's dresses.

Research Methods and Tools. The following research methods and tools were used in this work: computer vision methods using ImageJ; methods for physical and mechanical testing of fabrics, including tensile testing under low loads using a Metroteks MT110-G tensile testing machine, bending stiffness testing by a modified cantilever method, and determination of the drape coefficient by the Cusick method; 3D modelling and simulation methods using Style3D and Rhino 7; correlation and regression analysis methods using SPSS and GraphPad; statistical data processing methods, including calculation of MAPE, confidence intervals, and analysis of variance (ANOVA); neural-network-based machine learning methods using GPT-5.1, Gemini 3 Pro, Grok 4.1, and Qwen3-Max; as well as virtual and physical experiments. Photopolymer printing technology was used for 3D printing the device designed to calculate the anthropomorphic drape coefficient.

Scientific Novelty lies in the development of a methodology for simulation modelling of digital twins of the pleated surfaces of dresses.

The following scientific results were obtained for the first time:

1. A method for evaluating fabric drapeability was developed. The method models the

interaction between a garment and an anthropomorphic-like surface, makes it possible to take into account the influence of structural parameters of shoulder garment patterns, including cut configuration and overall dimensions, and was implemented in a physical device.

2. The concept of creating digital twins of fabrics using a neural network as a simulation modelling tool was substantiated. This concept is based on the formalization of input data and the formalization of the measurement process for indicators of extensibility, stiffness, thickness, surface density, and drapeability under real conditions, with the use of reference photographs of fabrics in flat and pleated states.

3. A regression model was obtained that relates the morphology of the pleated surface of a women's dress, quantitatively expressed through the percentage of bright area in frontal images, and fabric drapeability to the pleating coefficient introduced at the stage of structural pattern modelling.

The work corresponds to the following provisions of the passport of the scientific specialty:

7. **Digital prediction**, mathematical methods and information technologies for modelling technological processes of primary raw material processing, production organization, and the manufacture of fibers, yarns, materials, and light industry products.

8.Technologies for simulation modelling of **digital twins** of fibers, yarns, **materials**, light industry products, and human figures.

26. Methods for the systems analysis of form and material properties in designed light industry products.

Theoretical Significance of the study lies in the development of the theoretical foundations for controlling the pleating of morphologically similar surfaces of single-layer garments using fabric digital twins generated on the basis of the anthropomorphic drape coefficient.

Personal Contribution of the Author. At all stages of the work, the author, under the supervision of the research supervisor, personally participated in setting the aim and formulating the main research tasks, planning and conducting experiments, discussing the obtained results, formulating conclusions and testing hypotheses, and preparing publication materials together with co-authors. The applicant's contribution to the published works ranges from 63% to 80%.

Key Provisions, Submitted for Defense: (1) a method for evaluating drapeability, distinguished by its anthropomorphic character and its ability to reproduce the conditions of garment design and manufacturing; (2) a technology for generating fabric digital twins based on contactless, non-instrumental measurement of five groups of indicators; (3) a simulation model of the pleated dress form and pattern correction based on the criterion of morphological similarity.

The practical significance of the work lies in the creation of tools for obtaining digital twins of fabrics and women's dresses that are accessible to light industry enterprises without the need to purchase expensive equipment.

The proposed algorithm for the quantitative transformation of the pleated surface and material drapeability into parameters for structural pattern modelling makes it possible to significantly reduce the costs of producing physical samples and contributes to the development of parametric design in the fashion industry.

The results of the work can be used at garment manufacturing enterprises, in design studios, in the educational process of universities for training specialists in the field of digital garment design, as well as for the development of new modules for the automatic digitization of materials.

The degree of reliability of the results is confirmed by the use of calibrated laboratory equipment and standardized methods for obtaining reference values; a large volume of experimental data, including three types of fabrics with different properties and multiple sample variations; the application of modern statistical processing methods, including ANOVA and confidence intervals; a high level of correlation and low relative error values when comparing virtual and physical samples; as well as positive approbation of the work at international conferences.

Approbation of the work. The main results of the dissertation were presented and discussed at the following conferences: national youth scientific and technical conferences with international participation, POISK, Ivanovo, 2024, 2025, and 2026; the international Smart World Congress, Calgary, Canada, 2025; and the international IFFTI Conference, London College of Fashion, University of the Arts London, 2025.

Publications. Three printed works have been published on the topic of the dissertation, including two articles in a peer-reviewed scientific journal included in the list of the Higher Attestation Commission, Izvestiya Vysshikh Uchebnykh Zavedenii. Technology of the Textile Industry, one article in a journal indexed in the Web of Science database, and four conference papers.

Structure and scope of the dissertation. The dissertation consists of an introduction, five chapters, a conclusion, a bibliography of 175 titles, and appendices. The total length of the work is 189 typewritten pages, with 3 pages of appendices, including 36 figures and 25 tables. The originality of the dissertation text is 99.91%.

BRIEF INTRODUCTION

Modern 3D garment design systems make it possible to create virtual fabrics and virtual garments; however, a virtual model itself is not a digital twin. A digital twin must demonstrate verifiable consistency with the real object at the levels of parameters, form, and response. Traditional fabric testing methods provide standardized results, but the sample geometry and support conditions used in such tests differ from the conditions under which garments are formed on the human figure. Therefore, it is necessary to develop a method for evaluating drapeability that takes into account boundary conditions closer to those of garment construction.

In this dissertation, digital twins of fabrics and garments are considered as the result of a process that includes simulation modelling, simulation, and validation. In this process, fabric parameters cannot be isolated from the conditions under which they are obtained, the way they are introduced into the software environment, and the subsequent response of the virtual garment. Therefore, the study is aimed not only at obtaining individual indicators of physical and mechanical properties, but also at verifying whether these indicators can ensure reproducible garment form generation in a virtual environment.

Fabric drapeability is of particular importance in this work, since it links the low-stress mechanical behaviour of the material with the three-dimensional silhouette form of the garment. To bring the test conditions closer to those of garment formation, an anthropomorphic method for evaluating drapeability was developed based on a shoulder-like support surface. This approach makes it possible to move from the standard evaluation of sample drapeability to a new anthropomorphic parameter that can be used to predict the dress form and adjust construction decisions.

In addition, this work examines the possibility of obtaining fabric parameters using neural networks based on standardized photographic evidence and a prompt protocol. This approach reduces dependence on labour-intensive laboratory procedures, but it requires metrological verification of the accuracy, stability, and applicability of the obtained parameters. Therefore, the structure of the study integrates three interrelated directions into a new methodology of simulation modelling: the development of an anthropomorphic method for evaluating drapeability, the generation of digital twins of fabrics, and the prediction of the pleated dress form with subsequent validation of the results.

CHAPTER1. CURRENT STATE OF RESEARCH ON DIGITAL TWINS OF TEXTILE MATERIALS AND GARMENTS

The digitalization of the garment design process has required a qualitative revision of the descriptive structure of all its elements, including human figures, textile materials, garments, and design and manufacturing technologies. Digital twins have become the equivalents of material processes and objects [161]. Their emergence was preceded by many years of testing, and the generation of digital twins of textile materials provides one of the most convincing examples of the synthesis of several directions at once: testing methodology, the development of the instrumental base, and process modelling.

Research on the properties of textile materials and the measurement of drapeability has evolved from experience-based assessments of fabric handle and appearance to the objective characterization of low-stress mechanical behavior. The physical basis for interpreting fabric deformation includes thickness, surface density, bending, shear, tensile, and compression properties, while drapeability is used to describe the spatial form that arises under the action of gravity and boundary constraints in garments. Therefore, the measurement of fabric property indicators for garments and the evaluation of their drapeability form an interconnected research system, in which the first group of indicators explains the material basis of deformation, while drapeability characterizes its visible form-generating result.

With the development of testing instruments, computer-based image processing methods, and three-dimensional virtual modelling technologies, methods for measuring property indicators have been continuously improved, shifting from subjective empirical evaluation toward objective quantitative analysis. On the one hand, traditional tests of physical and mechanical property indicators under low-stress conditions have created a basis for understanding the draping behavior of fabrics and garments. On the other hand, direct methods for measuring the drape coefficient, the projected contour of a sample, and the number of folds make it possible to express drapeability more explicitly. Digital technologies have made it possible to conduct such tests at the stage of virtual modelling, where the results are used for the virtual reconstruction of the material, the formation of its digital twin, and the three-dimensional simulation of garments. A unified digital space for fabrics and garments creates unique conditions for identifying objective regularities between the property indicators of textile materials and the modelling of digital twins.

However, existing studies still demonstrate insufficient integration between the measurement of property indicators, particularly the evaluation of drapeability, and virtual modelling at the garment level. Traditional material testing and drapeability measurements provide standardized and reproducible results, but the sample shapes and modelling conditions do not correspond to the design and use conditions of real garments. Therefore, an integrated research pathway is required, linking material measurement, drapeability characterization, virtual modelling, and garment-oriented application.

Accordingly, this chapter examines the main achievements in the measurement of textile material property indicators, the evaluation of drapeability, and research on digital twins of textiles and garments. Special attention is given to traditional testing systems, physical and virtual devices for measuring drapeability, the development of digital twins of textile materials, virtual garment simulation, and validation methods. The chapter identifies the main limitations of existing studies in terms of testing realism and the applicability of parameters at the stages of garment modelling and construction. These provisions form the theoretical basis and problem-oriented direction of the subsequent chapters.

1.1 Current State of Research on the Evaluation and Application of Draping Properties of Textile Materials

1.1.1 Methods for Characterizing and Evaluating Drapeability

Fabric drapeability refers to the ability of a textile material to form a three-dimensional hanging shape under its own weight and boundary constraints. It links low-stress mechanical behavior with the visible appearance of garments, including softness, silhouette stability, fold waviness, local expansion, and overall form generation [1,11,13]. Early evaluations of drapeability mainly relied on visual impressions, such as softness, stiffness, fluidity, and fullness; however, such experiential assessments depended substantially on the observer and the observation conditions. Therefore, the development of drapeability evaluation can be understood as a transition from subjective visual judgment to mechanical and geometric quantitative description.

In traditional studies, drapeability is evaluated according to the projected area of the sample, the number of folds, and the contour curve under specified support conditions. This means that traditional drapeability studies mainly characterize the morphology of drape at the sample level, rather than the complete garment appearance formed under real wearing conditions on the human figure [4–7,19,20]. Draping behavior is determined by several low-stress physical and mechanical properties rather than by a single factor. Bending affects the ability of the material to hang and form folds; shear influences contour expansion and the adaptation of the sample to the support surface; surface density and thickness are associated with gravity and overall stability. Early studies established the theoretical and experimental basis for describing drapeability through bending energy, gravity, and objective indicators of physical and mechanical properties, thereby forming the traditional logic of “material sample testing — interpretation of draping behavior — evaluation of the test result” [11–17].

Traditional drapeability evaluation developed in two main directions. The first direction indirectly assesses the tendency of a material to drape through bending, while the second directly measures the result for a standard sample under specified support conditions. Figure 1.1 shows early instruments used in the transition from bending-based evaluation to the direct evaluation of fabric drapeability.

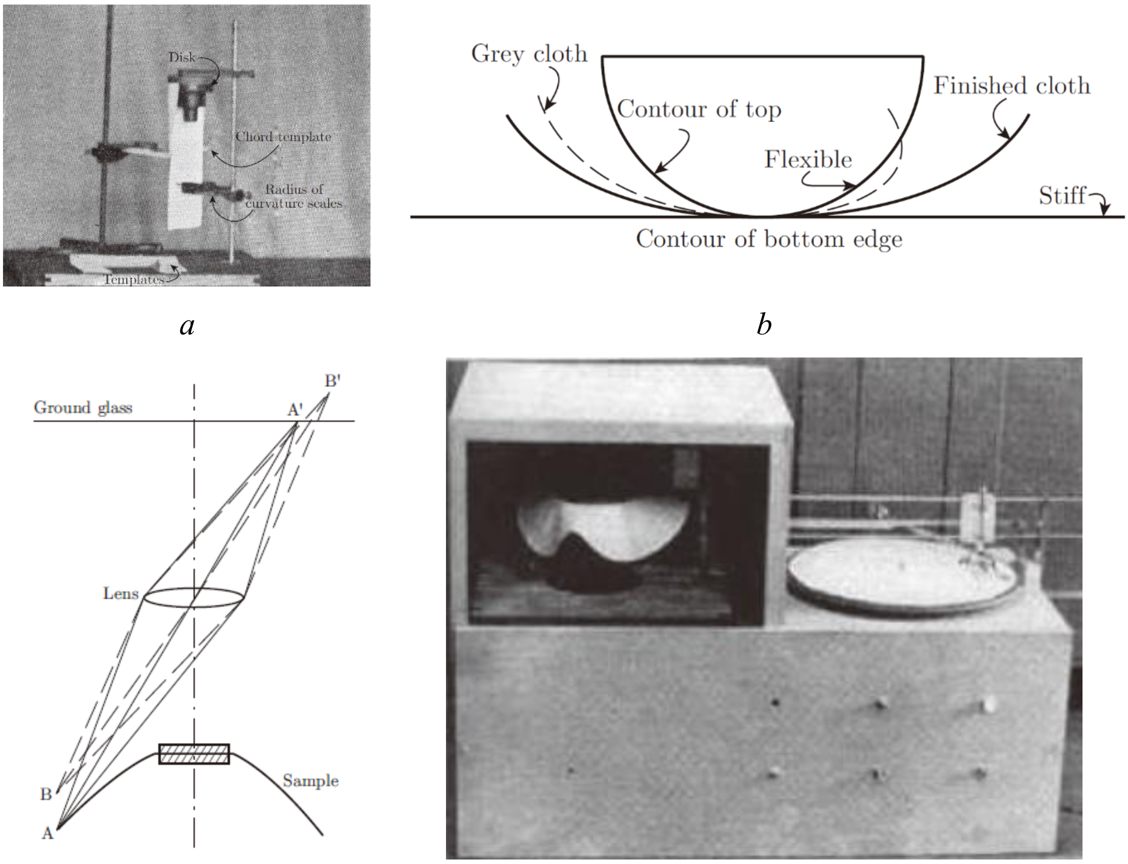

a *b*

c *d*

Figure 1.1 — Early instruments for evaluating fabric drapeability: *a* — Bellinson drapemeter; *b* — comparison of contours from the top view; *c* — F.R.L. optical drapemeter; *d* — improved F.R.L. drapemeter [4, 158, 159].

As shown in Figure 1.1, early drapeability evaluation developed from observation of the edge contour to optical projection and area measurement. Figure 1.1a shows the Bellinson drapemeter, in which a disk, a chord template, and curvature-radius scales were used to compare the edge deflection of a suspended fabric sample. Figure 1.1b shows that flexible and stiff fabrics could be distinguished by the contours of the lower edge, although the result still mainly reflected two-dimensional deformation. Figure 1.1c shows the F.R.L. optical drapemeter, in which points A and B on the edge of the sample were projected as A′ and B′ onto ground glass. Figure 1.1d shows the improved F.R.L. drapemeter with automatic contour recording and area measurement. This sequence demonstrates that drapeability evaluation gradually shifted from qualitative contour comparison to direct geometric quantitative measurement.

Before direct measurement of drapeability became widely accepted, the evaluation of bending ability provided an important mechanical pathway for interpreting the tendency of fabric to drape. In the cantilever method proposed by Peirce, fabric is regarded as a thin plate bending under its own weight. By measuring the projected length at which the free end of the sample reaches a specified angle, the bending length and bending stiffness can be calculated, thereby transforming perceptual assessments such as "softness" and "stiffness" into measurable mechanical quantities [1]. Booth systematically described the structure and testing principle of the Shirley Stiffness Tester, making the cantilever method more understandable and standardized [2]. By comparing several methods for testing fabric stiffness, Abbott showed that Peirce's cantilever method agreed well with subjective stiffness assessment and confirmed the role of bending measurement in the transition from sensory experience to objective quantitative evaluation [3]. However, this method essentially describes the two-dimensional bending response of a strip-shaped sample. Therefore, it can only indirectly characterize the tendency of fabric to drape and remains insufficient for describing the complex three-dimensional contour of drape.

Direct measurement of drapeability was developed on the basis of circular sample support and projected-contour analysis. The F.R.L. drapemeter introduced optical projection of the sample, and Cusick further standardized the instrument design, the calculation of the drape coefficient, the area method, and the cut-and-weigh method. These developments shifted drapeability evaluation from stiffness-based inference to direct quantitative description of morphology [4–10].

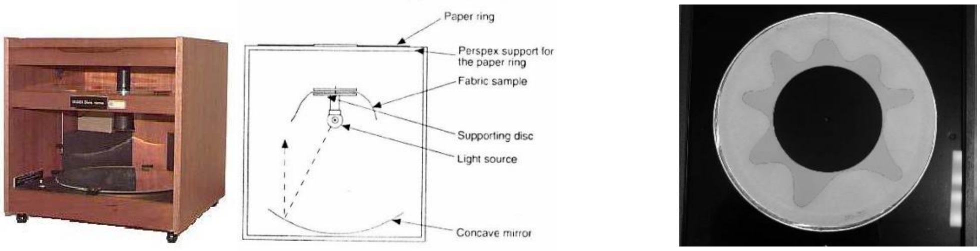

a *b*

Figure 1.2 — Measurement of drapeability according to Cusick: *a* — instrument; *b* — contour [4].

As shown in Figure 1.2, the Cusick method measures fabric drapeability by projecting the contour of a circular sample supported at the center. Figure 1.2a shows the standardized measuring instrument, while Figure 1.2b shows a typical projected contour of the unsupported annular area. Based on this projected contour, fabric drapeability came to be evaluated as an area ratio, which made the method suitable for comparative testing and standardization. However, as research developed, scholars gradually concluded that a single area-ratio indicator was insufficient to fully describe the differences between the complex contours of a draped sample. Therefore, on the basis of the Cusick system, traditional drapeability evaluation was gradually expanded by introducing parameters such as the number of folds, fold intensity, circularity, and the distance coefficient relative to the support boundary. Vangheluwe and Kiekens examined the time dependence of the drape coefficient, showing that a single static reading cannot fully represent draping behavior [18]. Robson and Long introduced the number of folds, fold intensity, and circularity using an image analysis system, thereby strengthening the characterization of contour details [19]. The drape distance coefficient proposed by Jeong supplemented the limitations of area-based indicators from the perspective of the average distance to the boundary [20]. Yang and Matsudaira further extended measurement to oscillatory motion and proposed the dynamic drape coefficient, advancing traditional drapeability research from a static single-value characteristic to multiparameter and dynamic image-based analysis [21]. Table 1.1 presents representative traditional methods for evaluating stiffness and drapeability, together with their main calculated parameters.

Table 1.1 — Representative traditional methods for evaluating fabric stiffness and drapeability

Method / Author	Main Descriptor	Typical Calculation Method	Typical Instrument
Peirce (1930) [1]	Bending length C; bending stiffness G	C is calculated from the cantilever length and bending angle, while G is further recalculated taking into account the fabric mass	Shirley Stiffness Tester
Chu et al. (1950) [4]	DC	Projected covered area of the annular region / total area of the annular region	F.R.L. optical drapemeter
Cusick (1968), area method [5–7]	DC	$(A_p - A_s) / (A_o - A_s) \times 100\%$	Cusick drapemeter + area meter
Cusick (1968), cut-and-weigh method [7]	DC	$(W_p - W_s) / (W_o - W_s) \times 100\%$	Cusick drapemeter + paper ring
Jeong (1998) [20]	DDR	Ratio based on the mean distance to the boundary and the radius of the support	Image analysis system
Robson and Long (2000) [19]	Roundness; number of nodes; node severity	Based on contour area, perimeter, and node identification	Automated image analysis system
Yang et al. (2001) [21]	Dynamic drape coefficient	Dynamic parameters are determined from changes in projected area in sequential frames	Dynamic drapemeter + image acquisition system

As shown in Table 1.1, traditional methods for evaluating stiffness and drapeability generally developed from bending-based evaluation to the measurement of projected morphology, from single-factor assessment to multiparameter characterization, and from static measurement to dynamic image analysis. These methods laid the foundation for the standardization, quantitative description, and comparability of drapeability studies. However, their results are formed under specific sample shapes, support modes, and measurement procedures. Therefore, drapeability evaluation depends on the testing devices and experimental conditions.

1.1.2 Evolution of Devices for Drapeability Testing

According to the existing literature, the evolution of devices for drapeability testing has mainly followed three directions. The first direction is associated with changes in the support structure, that is, the transition from regular geometric supports to support forms with a more pronounced guiding effect on shape formation. The second direction is associated with changes in the observation mode, namely the transition from single projected observation to image acquisition, contour extraction, and three-dimensional reconstruction. The third direction is associated with changes in the test object, namely the expansion from standard flat samples to skirt samples, garment samples, and garment objects related to body-support conditions [19–23]. These changes show that drapeability testing devices have developed not only as measuring equipment, but also as experimental systems responding to garment-oriented research questions. Table 1.2 presents the evolution of support form, data acquisition mode, test objects, and technical characteristics of drapeability testing devices.

Table 1.2 — Evolution of Methods for Evaluating Drapeability

Method	Representative Device or System	Support Form	Data Acquisition Mode	Test Object
Mechanical bending tests	Peirce cantilever / Shirley device [1,2]	Linear edge support	Manual reading	Strip sample
Static drapeability	F.R.L. drapemeter [4]	Central support with a circular disk	Optical projection	Circular flat sample
Standardized DC measurement	Cusick drapemeter [5–7]	Central support with a circular disk	Area measurement, tracing, or cut-and-weigh method	Circular flat sample
Image analysis	Image acquisition system with disk support [19,20]	Central support with a circular disk	Image segmentation and contour extraction	Circular flat sample
Dynamic drapeability	Dynamic drapemeter [21]	Oscillating or rotating support disk	Continuous image acquisition	Circular flat sample

Three-dimensional measurement	3D drapemeter / 3D scanning system [22]	Modified or automated support	3D scanning and reconstruction	Fabric sample or draped sample
Garment-oriented testing	3D body scanner / mannequin-based modelling [23]	Support by a mannequin or human body	Extraction of point cloud, mesh, and 3D parameters	Skirt sample or garment object

As shown in Table 1.2, the evolution of drapeability testing devices involved changes in three key variables: support form, data acquisition mode, and sample form. The Peirce cantilever and the Shirley device transformed strip bending into measurable mechanical quantities, but the response was limited to the two-dimensional deformation of a strip sample. The F.R.L. and Cusick drapemeters established a standardized material-level testing system based on support by a circular disk and measurement of projected area. This system improved comparability; however, the test object remained a circular sample, and the support boundary was highly simplified. Image analysis, dynamic recording, and 3D scanning increased the amount and dimensionality of information on drapeability, but most testing systems still retained simplified sample forms. Therefore, the key limitation revealed by this evolution lies not in the absence of measurement technology, but in the persistent gap between standardized support conditions and garment-related boundary conditions. Figure 1.3 shows a comparison between the contours of horizontal dress sections and the projections of samples made from the same fabrics.

a

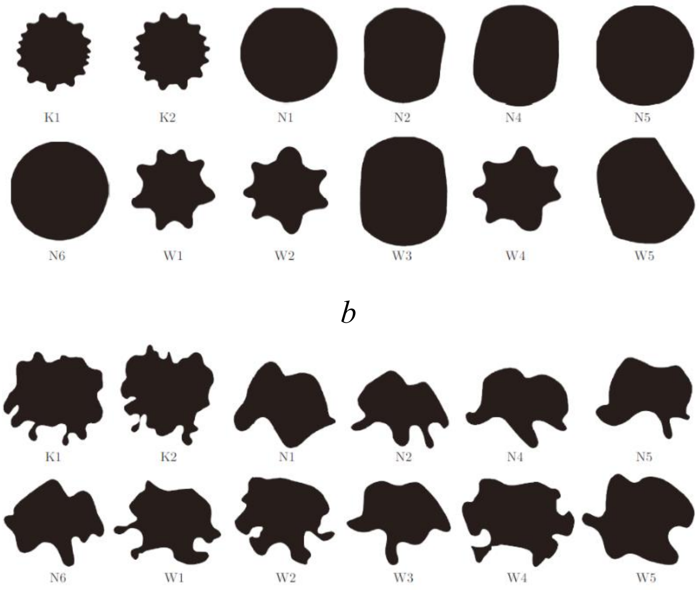

b

c

Figure 1.3 — Drapeability of fabric samples and garments: *a* — dresses on a mannequin; *b* — images of draped fabric samples (projections); *c* — horizontal sections (projections) of dresses at the hem level [160].

As shown in Figure 1.3, the morphological responses of the sample and the garment do not coincide. This comparison shows that fabric sample drape and garment drape are not equivalent objects, even for comparative purposes. Therefore, garment-oriented drapeability studies require a refinement of the support conditions so that they reflect the boundary constraints of real garments.

The further development of drapeability testing devices can be understood as a process of parallel development between standardized material comparison and garment morphology. On the one hand, disk support has advantages in terms of reproducibility and comparability of results and therefore remains the basic form for traditional DC measurement. This is also due to the extensive experimental base accumulated in online reports, articles, and monographs. This base can be used at any time with the help of artificial intelligence. On the other hand, image analysis, dynamic testing, and 3D scanning have expanded the composition of information to include projected area, contour features, temporal changes, and spatial geometry [19–23]. This trend shows that the testing system has gradually transformed from a simple support platform into an integrated system of “support — data acquisition — analysis”.

1.1.3 Development of Virtual Drapeability Testing

The need for virtual drapeability testing emerged as a result of the development of digital garment design technologies. In such tests, fabric behavior is reconstructed in virtual space by defining material parameters, geometric parameters of the support, gravity settings, contact area, and boundary conditions; the resulting sample morphology is then evaluated using indices measured in two-dimensional or three-dimensional space. The development of these methods takes place in a multidisciplinary field and is closely related to physical fabric simulation, garment CAD, human body shape modelling, and virtual garment simulation systems [24,25,31–34]. Unlike conventional testing, virtual drapeability testing takes into account the physical response under specified material, support, and boundary conditions. A digital twin requires additional verification of the correspondence between virtual and real objects. Therefore, although virtual drapeability testing provides a technical basis for drapeability research, it is not automatically equivalent to the results of physical testing [25,27,39,40].

Research on virtual drapeability has expanded from the simulation of a single fabric sample to an integrated research framework involving the system “fabric — support environment — garment” [31–34]. As research has developed, its main content has gradually expanded into four interrelated stages: construction of the material model, digital reconstruction of support scenarios, formation of drape morphology based on simulation, and extraction, comparison, and validation of simulation results [27,29,30,35–40]. Compared with traditional physical testing, this research pathway is no longer focused only on a single index. Instead, it places greater emphasis on the consistency among material parameters, geometric structure, support boundaries, and simulation results. Its purpose is to bring virtual results as close as possible to physical results and to use them for prediction and design applications.

Existing studies have shown that virtual drapeability testing usually includes parameter acquisition, model construction, simulation analysis, and result validation. First, fabric parameters suitable for constructing a virtual fabric model must be obtained. Then, in the digital environment, models of fabric samples, garments, the human body, or support objects must be created, while gravity, contact, friction, and boundary constraints must also be specified. After that, drape morphology is generated in the virtual environment, and measurable outputs are extracted from it, such as contour, area, number of folds, fold distribution, hem shape, and silhouette. Finally, the virtual results are compared with the results of real tests or real garment samples to determine their correspondence in morphology and response characteristics [27,29,33–40]. Figure 1.4 shows the general scheme of virtual drapeability testing.

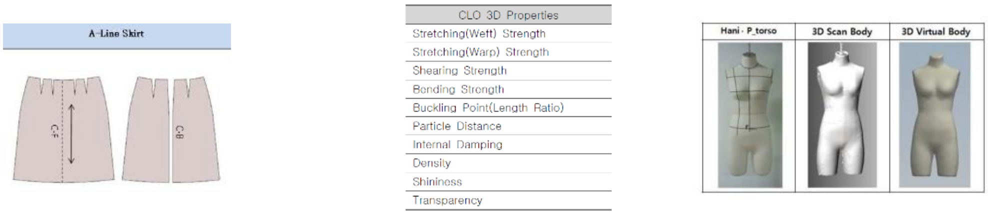

CLO 3D Properties
Stretching(Weft) Strength
Stretching(Warp) Strength
Shearing Strength
Bending Strength
Buckling Point(Length Ratio)
Particle Distance
Internal Damping
Density
Shininess
Transparency

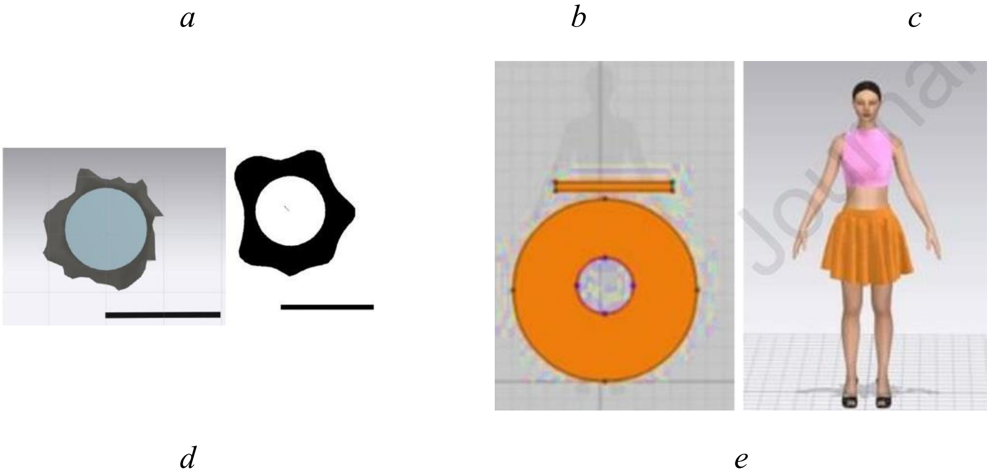

Figure 1.4 — Workflow of virtual drapeability testing: *a* — pattern design; *b* — material parameters; *c* — avatar creation; *d* — contour extraction; *e* — simulation and visualization [151, 98].

As shown in Figure 1.4, virtual drapeability testing should be understood as a workflow rather than as a single software operation. Figure 1.4a–c shows that simulation begins with pattern construction, input of material parameters, and avatar creation; these stages define the geometric, material, and support basis of the virtual test. Figure 1.4d–e shows that the final visual result must be transformed into measurable contours or morphology-related output data. Therefore, the effectiveness of virtual drapeability testing depends not only on visualization quality, but also on whether a consistent technical chain can be established between parameter input, support conditions, simulation results, and result evaluation.

Table 1.3 — Structure and Content of the Developed Processes for Virtual Drapeability Testing

Category	Support Environment	Object of Study	Research Function	Evaluation Output
Platform foundation [31,32]	Early garment CAD environment	2D patterns and virtual garments	Implementation of garment dressing and draping functions	3D visualization of garments
Platform foundation [32]	3D garment design environment	Virtual garment	Construction of a 3D garment design environment	Design workflow and appearance
Real–virtual comparison [35,37]	Virtual skirt environment	Skirt	Comparison of virtual and real skirt forms	Comparison of contour and hem shape
Real–virtual comparison of garments [37]	Virtual body / skirt system	Flared skirt	Evaluation of drape in 3D garment simulation	Comparison of contour, appearance, and drape form
Parametrically oriented study of virtual drape [38]	Body model + OptiTex	Virtual garment	Influence of mechanical properties on virtual	Analysis of contour, folds, and drape

			garment drape	response
Parametrically oriented real–virtual comparison [39]	Real–virtual correspondence environment	Fabric sample	Comparison of real and virtual drape results	Comparison of area, nodes, and fold shape
Parameter input and silhouette validation [40]	Virtual avatar + CLO 3D	Virtual garment	Influence of material input on the accuracy of the virtual contour	Comparison of silhouette and drapeability
Accuracy validation [29]	3D scanning + simulation comparison	Garment / drape morphology	Simulation accuracy and geometric consistency	Real–virtual comparison based on 3D scanning

As shown in Table 1.3, virtual drapeability testing has developed along several methodological routes. Platform-oriented studies established a basic environment for constructing virtual garments, fitting them on avatars, and simulating dressing processes [31–34]. Real–virtual comparison studies shifted attention from visual generation to the consistency of contour, hem shape, and drape morphology [35–37]. Parametrically oriented studies further examined how the mechanical properties of materials and software input parameters affect virtual drape and silhouette accuracy [38–40]. Accuracy-oriented studies introduced 3D scanning and geometric comparison to evaluate the consistency between simulated and real drape morphology [29]. This sequence shows that virtual drapeability testing has gradually shifted from software-based visualization to parametrically controlled and validation-oriented research. Figure 1.5 presents representative validation methods used to assess the consistency between real and virtual drape results.

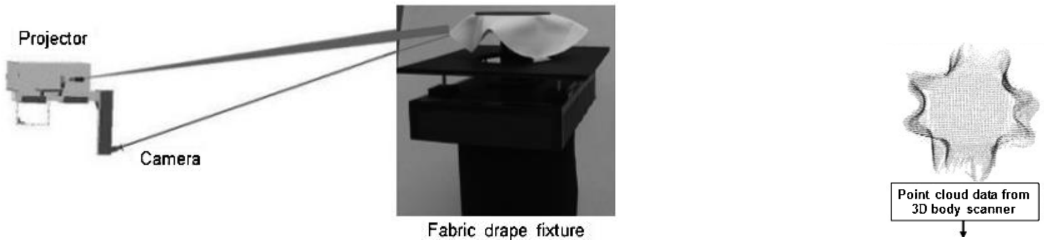

a

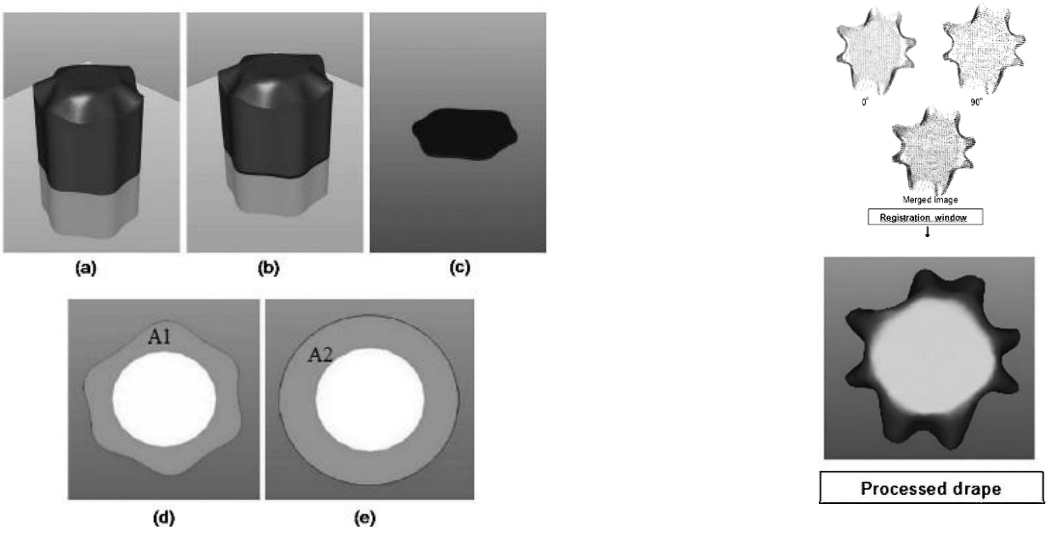

c *б*

Figure 1.5 — 3D validation of virtual drape morphology: *a* — fixture for scanning a draped sample; *b* — point cloud processing; *c* — extraction of the drape coefficient [29].

As shown in Figure 1.5, validation based on 3D scanning provides a geometric reference for assessing whether virtual drape results are consistent with real drape morphology. Figure 1.5a shows that physical data acquisition is no longer limited to a projected shadow or a top-view contour; instead, a projector, camera, and draping fixture are combined to record the real three-dimensional shape of a circular draped sample. Figure 1.5b shows that the obtained data must be registered, merged, and processed before they can become a usable geometric model. This means that validation depends not only on image acquisition, but also on the quality of point cloud model reconstruction. Figure 1.5c shows that the reconstructed draped surface can then be projected and converted into measurable areas for extracting the drape coefficient (DC). Therefore, 3D scanning-based validation forms a complete chain from physical drape acquisition, point cloud reconstruction, and geometric processing to quantitative parameter extraction.

This validation logic shows that virtual drapeability testing should be evaluated using real geometric references and measurable indices, rather than visual similarity alone. However, Figure 1.5 still represents a circular sample on a standardized support. Although 3D scanning improves the accuracy of real–virtual geometric comparison, it does not fully solve issues related to garment-level support, contact with the body, seam constraints, or complex pattern structures. Therefore, virtual drapeability testing should move from the validation of fabric samples toward the validation of garment-oriented drape morphology.

Although existing virtual drapeability studies have expanded to garment-level objects, representative cases are still mainly limited to simple skirts, especially circular and flared skirts. Systematic studies of garments with more complex structures and boundary relationships, such as dresses, remain insufficient [35–37].

Thus, virtual drapeability testing is developing from the generation of three-dimensional appearance to verifiable simulation of physical response, from virtual testing of fabric samples to the analysis of garment-level morphology, and from single geometric comparison to multi-index consistency evaluation. Existing studies have shown that the input of mechanical parameters affects the contour of virtual garments, fold formation, and silhouette accuracy, while 3D scanning and geometric comparison provide a more reliable basis for real–virtual validation [26,28,29,35–40]. However, validation objects are still often limited to standard samples or simple skirt structures, and the quantitative index system for complex garment-level morphology remains insufficient.

Material parameter acquisition is a critical prerequisite for virtual drapeability testing, since both fabric sample simulations and garment-level simulations depend on reliable physical input data. Existing studies usually use KES, FAST, or software-supported tools to obtain material parameters, and different acquisition routes may affect the final virtual contour and drape result [27,38,40]. Therefore, parameter acquisition should be regarded as part of the virtual drapeability testing system, which should include AI-based measurement of fabric parameters and the construction of digital twins of textile materials.

1.2 Current State of AI-Based Measurement of Fabric Parameters

1.2.1 Visual Representation of Fabric Properties

Visual representation is the initial basis through which AI enters research on fabric parameters. Before fabric properties can be evaluated, interpreted, or transformed, the visual features of fabrics must be represented in a computable form. Surface texture, surface waviness, fold state, and drape contour are observable features for judging fabric characteristics. With the development of computer vision and image analysis, the results of such observation are gradually transformed into computable image features and patterns, creating a basis for intelligent recognition based on visual representation.

The visual representation of fabric properties refers to the process of describing, identifying, and inferring the surface state, structural organization, morphological response, and related properties of fabrics through images, videos, or multi-view visual evidence. It should be understood as an intermediate layer of evidence connecting image information with material property indicators, rather than as the final result of parameter measurement in the strict metrological sense.

From the perspective of research objects, the visual representation of fabric properties can be divided into three levels. The first level concerns directly visible structural and surface features, including color, pattern, texture, weave, yarn direction, surface roughness, and gloss. The second level concerns integral properties, in which visual features are combined with tactile, draping, or other descriptive indices to form higher-level classification and grouping results. The third level concerns indirect features related to physical and mechanical characteristics, such as perceived thickness, softness or density, stiffness, elasticity, rigidity, and tendency to drape. These three levels reflect the fact that the visibility of fabric properties is not uniform. Features such as weave and surface texture can be recognized from direct visual signals, whereas bending stiffness, handle, and draping tendency often require inference based on morphological response, dynamic deformation, or model-based reasoning. These distinctions define the boundary of visual representation: it can provide evidence for property perception, but its validity depends on the type of visual evidence and the inference mechanism used.

Existing studies show that visual representation has become an important basis for intelligent recognition and perception of fabric properties. Research methods have advanced from the analysis of features in a single image to the integration of multichannel evidence, interpretation of dynamic response, and AI-based inference of properties. The material recognition database developed by Bell et al., as well as the work of Schwartz and Nishino on local visual attributes of materials, show that material properties can be recognized by visual systems because images contain stable and learnable surface features [41,42]. In the textile field, this research logic has been specified in tasks such as weave recognition, geometric reconstruction, dynamic property evaluation, defect detection, and handle-related prediction [43–55].

Vision-language models can connect image evidence with natural-language instructions and support zero-shot reasoning about structural features, relative differences, and visible attributes. However, in the absence of controlled data acquisition, calibration, and validation, these capabilities still represent visual interpretation rather than strict parameter measurement [56–60]. An example of this approach is shown in Figure 1.6.

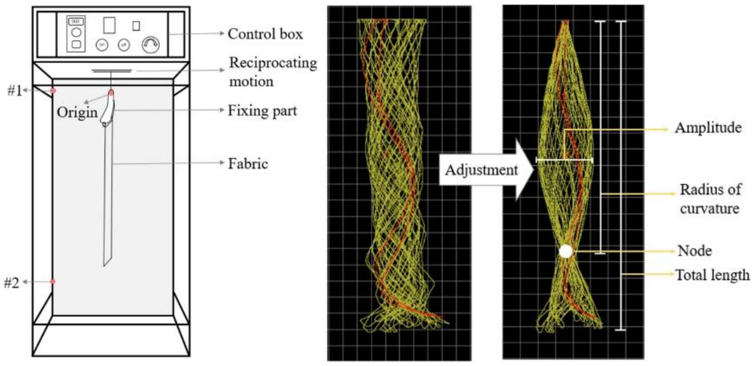

a

б

Figure 1.6 — Dynamic visual evidence and AI-based inference: *a* — dynamic measurement of drapeability; *b* — AI prediction framework for fabric handle [154, 54].

As shown in Figure 1.6, the visual representation of fabric properties has expanded from the recognition of static texture to dynamic morphological response and AI-based inference of properties. Figure 1.6a shows that drape-related properties can be represented through contour changes, response to motion, and morphological stability during dynamic testing, rather than only through the final static contour. This type of evidence is particularly important for properties such as drapeability, flexibility, and stability during motion. Figure 1.6b shows that AI-based inference attempts to connect visual evidence with tactile perception, mechanical behavior, draping characteristics, and simulation-related applications. Therefore, dynamic visual evidence expands the representation of fabric properties from visible surface features to reaction-based property interpretation. However, this type of inference still depends on the selection of evidence, model structure, calibration, and validation, and should not in itself be regarded as strict parameter measurement.

The first type of visual evidence - microscopic and structural evidence. In fabric images, repetitive textural patterns, yarn orientation, weave geometry, interlacing rules, and local surface undulation can provide direct indicators for recognizing fabric structure. Research by Wang et al. has shown that fabric images can be used to identify the weave pattern and estimate yarn linear density, the weave repeat, and surface roughness. Yu et al. further demonstrated that even a single microscopic image can support the reconstruction of geometry at the yarn level [46, 47]. These studies indicate that the scope of visual representation is expanding from the identification of flat textures to structural interpretation.

Second type of visual representation - integrated modelling of the attribute space. Compared to weave recognition, this type of research combines multiple descriptors related to appearance, drape, tactile perception, and physical response. In this research approach, fabric properties are represented not merely by texture or weave, but by the interrelationship of several attributes.

The third type of visual evidence - morphological and dynamic evidence of the response. Certain fabric properties are difficult to discern directly from a single static image. For example, stiffness, areal density, softness, and drape characteristics are typically revealed by how the fabric deforms, moves, wrinkles, or stabilizes under external conditions. Research by Bowman et al., which assessed stiffness and areal density from fabric video, alongside work by Mamun et al. on recognizing fabric weaves from video, demonstrates that the source of visual evidence has expanded from static images to dynamic spatiotemporal information [48, 49]. In this context, the image is no longer merely a record of surface texture but serves as evidence of the fabric's response to movement or boundary constraints (Table 1.4).

Table 1.4 – Content of research areas and results obtained

Type of Direction	Form of Input Data	Main Task	Typical Output
General studies of visual material recognition	Natural images; local image patches	Material recognition; identification of local material attributes	Material category; local visual attributes [41,42]
Traditional image analysis	Microscopic images; surface images	Weave recognition; yarn counting; roughness analysis	Weave repeat; number of yarns; roughness [43,47]
Deep visual recognition	Standardized fabric images	Weave classification; defect detection; recognition of handwoven fabrics; real-time inspection and authentication	Weave class; defect class; fabric identity [44,45,50–52,55]
Reconstruction of structural geometry and perception of dynamic properties	Microscopic images; fabric videos	Reconstruction of structural geometry; evaluation of dynamic properties; video-based pattern recognition	Yarn-level geometry; stiffness; surface density; pattern class [46,48,49]
Reviews and trend summaries	Synthesis of literature and datasets	Review of studies on fabric property and handle prediction	Research objects, method types, and limitations [54]

As shown in Table 1.4, the visual representation of fabric properties has developed from recognition of surface appearance to reconstruction of structural geometry, perception of dynamic properties, defect detection, handle-related prediction, and open cross-modal perception. This development shows that visual evidence can support not only the recognition of fabric categories, but also provide indirect information about structural organization, deformation behavior, and perceived material properties. However, the visibility of different properties is not uniform. Features such as color, texture, weave, and local defects can usually be represented directly through visual information, whereas thickness, softness, bending stiffness, and tendency to drape often require inference from indirect or dynamic visual evidence. Therefore, visual representation can provide fundamental support for fabric property recognition and parameter perception, but it cannot directly replace the parameter acquisition process required for simulation-oriented applications.

Overall, existing studies demonstrate the important role of visual representation in the recognition and perception of fabric properties. However, their results still mainly serve the tasks of recognition, classification, and indirect inference. When the research objective shifts toward parameter acquisition and data input for simulation, it becomes necessary to consider the potential of AI for structured measurement of fabric parameters. This issue leads to the discussion of the paradigm shift in AI-based fabric measurement.

1.2.2 Paradigm Shift in AI-Based Fabric Measurement

Based on studies of visual representation, AI is widely used for fabric property recognition, classification, and parameter prediction. However, with the development of digital twin research and simulation-oriented garment studies, the role of AI in obtaining fabric properties has begun to change. Visual recognition mainly answers the questions of what the fabric is or how it looks, whereas parameter acquisition must answer which parameters can be measured and whether these parameters can support subsequent simulation, validation, and garment-related analysis. Therefore, when the research objective shifts from recognition to parameter acquisition, the role of AI also changes: it is no longer merely a tool for visual classification or regression-based prediction, but increasingly needs to support parameter interpretation, structured output, and result verification.

Early applications of AI in textile material research were mainly focused on classification, recognition, and parameter prediction. Typical tasks included fabric type recognition, weave structure classification, surface defect detection, handle grade evaluation, and regression-based estimation of certain mechanical parameters or performance indicators [44,45,48,50,53–55]. For example, Bouman et al. estimated bending stiffness and surface density from fabric videos [48], while Domínguez-Elvira et al. estimated fabric mechanics from manufacturer metadata in order to reduce the cost of parameter acquisition for digital garment modelling [53]. The systematic review by Tu et al. also shows that AI can form a clear research trajectory in fabric property and handle prediction through input–output mapping based on existing samples and labeled data [54]. Therefore, this route is more accurately understood as a classification-oriented data-driven approach or a regression-based proxy approach, rather than as a measurement process in the strict sense. Figure 1.7 shows data-driven regression routes for estimating fabric properties.

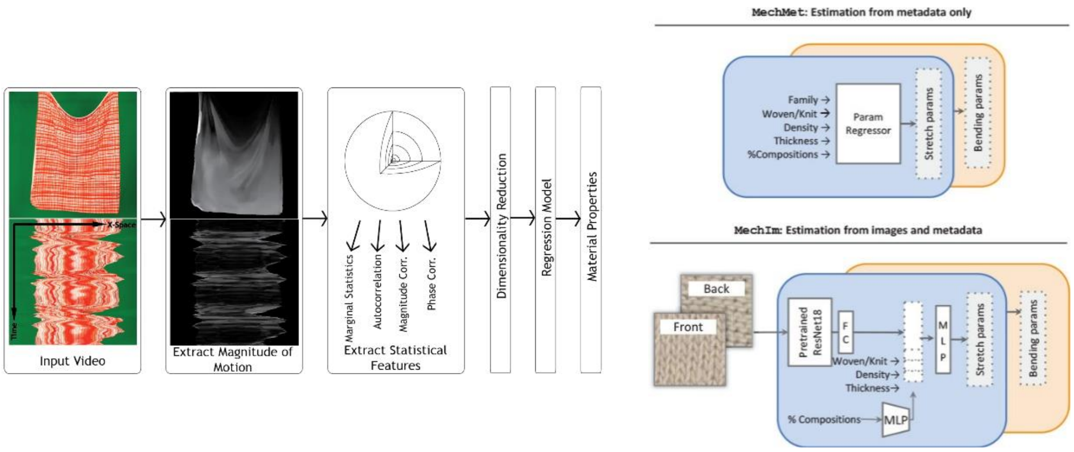

a *б*

Figure 1.7 — Regression-based estimation of fabric properties: *a* — video-based regression; *b* — metadata-based inference [48, 53].

As shown in Figure 1.7, AI-based acquisition of fabric properties mainly follows a data-driven regression route. Figure 1.7a shows that fabric properties such as stiffness and surface density can be estimated from video evidence by learning the relationship between the observed motion of the fabric and previously measured physical values. Figure 1.7b shows that metadata and descriptive information can be used to infer fabric mechanics. In both cases, AI is applied after an experimental reference system has been established [44,45,48,53–55].

When the research objective shifts toward data input for simulation and digital twin construction, the limitations of the prediction-oriented paradigm become more evident. First, the outputs of such methods usually depend on the distribution of the training data and are essentially the results of statistical matching rather than readings based on explicit measurement logic. Second, their reliability is usually evaluated through training error, test error, or prediction accuracy, rather than through controlled input conditions, process constraints, and output consistency. Third, the stability of the outputs may vary across AI models, datasets, and application scenarios, which makes it difficult for such methods to directly satisfy the requirements for parameter consistency and verifiability in virtual drapeability testing, digital twin construction, and garment form prediction [53,54]. Therefore, prediction-oriented methods are useful estimation tools, but they are not yet fully equivalent to measurement-oriented methods for parameter acquisition.

This shift is not limited to the textile field. Multimodal vision-language models such as BLIP-2, LLaVA, InstructBLIP, GPT-4V, and GPT4Vis have demonstrated the ability to perform more open-ended judgments and explanations of structural features, relative differences, and attribute manifestations in images under natural-language task constraints [56–60]. In the broader field of materials science, large language models are also used for property prediction, hypothesis generation, and reasoning about structure–property relationships [61–65]. These studies show that the role of AI is expanding from the prediction of fixed labels to the interpretation of and reasoning about attributes under specified task conditions (Figure 1.8).

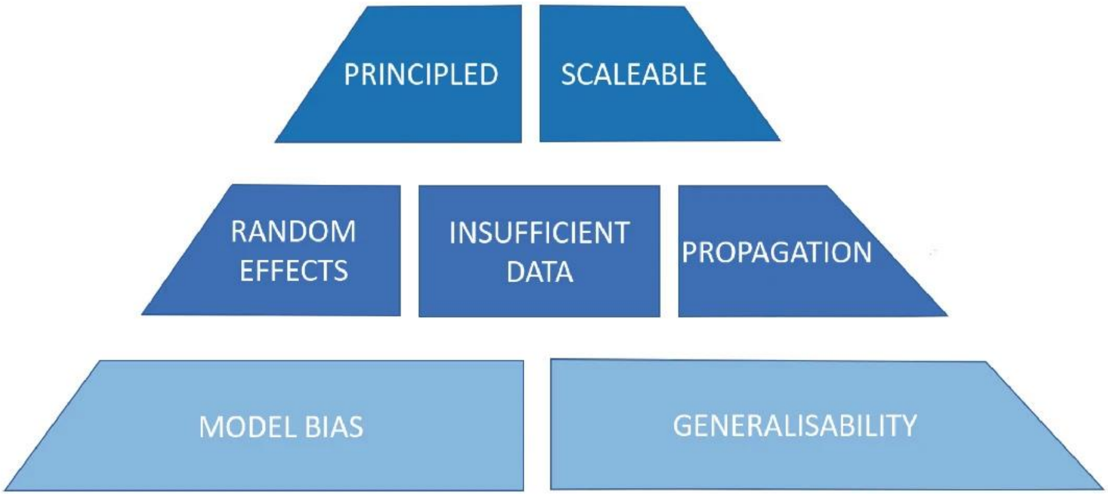

Figure 1.8 — Requirements for protocol-based AI measurement [80].

As shown in Figure 1.8, when AI is positioned as a measurement-oriented system, the central issue is not limited to prediction accuracy alone. It also requires controlled input conditions, consideration of AI model bias, sufficient and adequate data, generalizability across samples and scenarios, as well as the assessment of uncertainty and error propagation. These requirements show that AI-based measurement should be regarded as a controlled process rather than as an isolated model output. For the acquisition of fabric parameters, this means that standardized visual evidence, a fixed task protocol, structured parameter fields, comparison with physical tests, and verifiable outputs are necessary conditions. Therefore, promising protocol-based AI measurement differs from earlier regression-based prediction not in the use of a different image source, but in the integration of AI into a controlled and verifiable workflow for parameter acquisition.

Taken together, Figures 1.7 and 1.8 show that the difference between the routes of AI-based acquisition of fabric properties lies in the position that AI occupies within the parameter acquisition workflow. The first regression-surrogate route mainly estimates parameters after an experimental reference system has been established; the multimodal reasoning route enhances the ability of AI to interpret visual evidence under task constraints. The second, protocol-based route additionally requires controlled input, a fixed output structure, comparison with a physical reference, and evaluation with consideration of uncertainty. Therefore, the paradigm shift in AI-based fabric measurement is essentially a transition from post hoc statistical estimation to protocol-constrained and metrologically informed parameter acquisition. Table 1.5 shows the differences between regression-based estimation and protocol-based AI measurement.

Table 1.5 — Main Differences Between Regression-Based Estimation and AI-Based Measurement

Aspect	Data-driven Regression-Based	Protocol-Based AI Measurement

	Estimation	
Position of AI in the workflow	Final part of the experiment	Within the parameter acquisition workflow
Main input	Numerical features, historical databases, labeled samples	Controlled images, metadata, fixed task protocol
Main aim	To improve approximation efficiency and prediction accuracy	To obtain repeatable, comparable, and verifiable parametric outputs
Output form	Single-number prediction or class label	Structured parameters, anomaly identification, and verification cues
Requirement for input control	Relatively low	High; requires a unified shooting and annotation protocol
Main focus of evaluation	Approximation error; classification accuracy	Stable output under controlled conditions and the possibility of subsequent calibration
Application scenario	Post hoc analysis; trend prediction; process optimization	Digital measurement; parameter reading; data input for digital twins

As shown in Table 1.5, regression-based estimation and protocol-based AI measurement differ in their position within the workflow, requirements for input data control, output form, and evaluation logic. Regression-based estimation mainly learns input–output relationships from existing data and is therefore suitable for post hoc analysis, trend prediction, and process optimization. Protocol-based AI measurement places AI within the parameter acquisition workflow and requires controlled visual evidence, fixed task definitions, structured output fields, and verifiable results. This shift does not mean that traditional prediction methods have lost their value. On the contrary, it shows that when the research task enters the field of digital twin construction, simulation-oriented design, and garment form prediction, AI must shift from general estimation to controlled parameter acquisition.

Therefore, the role of AI in fabric parameter acquisition is no longer limited to general prediction. Under a controlled protocol, structured output, and comparison with a physical reference, it begins to approach the functional logic of a measurement-oriented system. Once this role is established, metrological issues of accuracy, stability, traceability, and uncertainty must be considered further.

1.2.3 Metrological Foundations of AI-Based Measurement

When AI is used to infer parameters, it begins to function as a measurement-oriented parametric tool. Therefore, AI-based fabric measurement must be considered within a stricter framework for evaluating reliability. According to the basic logic of metrology, a measurement result must be associated with a clearly defined measurand, a controlled measurement process, and an interpretable expression of the result. This means that the evaluation of an AI system cannot remain only at the level of prediction accuracy, loss functions, or overall model performance. It is also necessary to consider whether the output values possess accuracy, stability, traceability, and an expression of uncertainty.

For a measurement system, the key issues usually include accuracy, repeatability, reproducibility or stability, traceability, and uncertainty. When these functions are transferred to AI, their basic meaning is preserved, but the sources and forms of their manifestation change. In traditional instruments, errors may mainly arise from sensors, loading settings, calibration conditions, and operator procedures. In AI-based fabric measurement, errors may simultaneously arise from input images, the state of the sample, lighting, shooting distance, the prompt protocol, the AI model version, the output integration strategy, and the interpretation mechanism. Therefore, although AI-based measurement does not appear as a conventional hardware instrument and **is instead a contactless non-instrumental tool**, it should still be evaluated according to measurement-related reliability requirements. Figure 1.9 shows the main dimensions for verifying the reliability of AI-based fabric measurement.

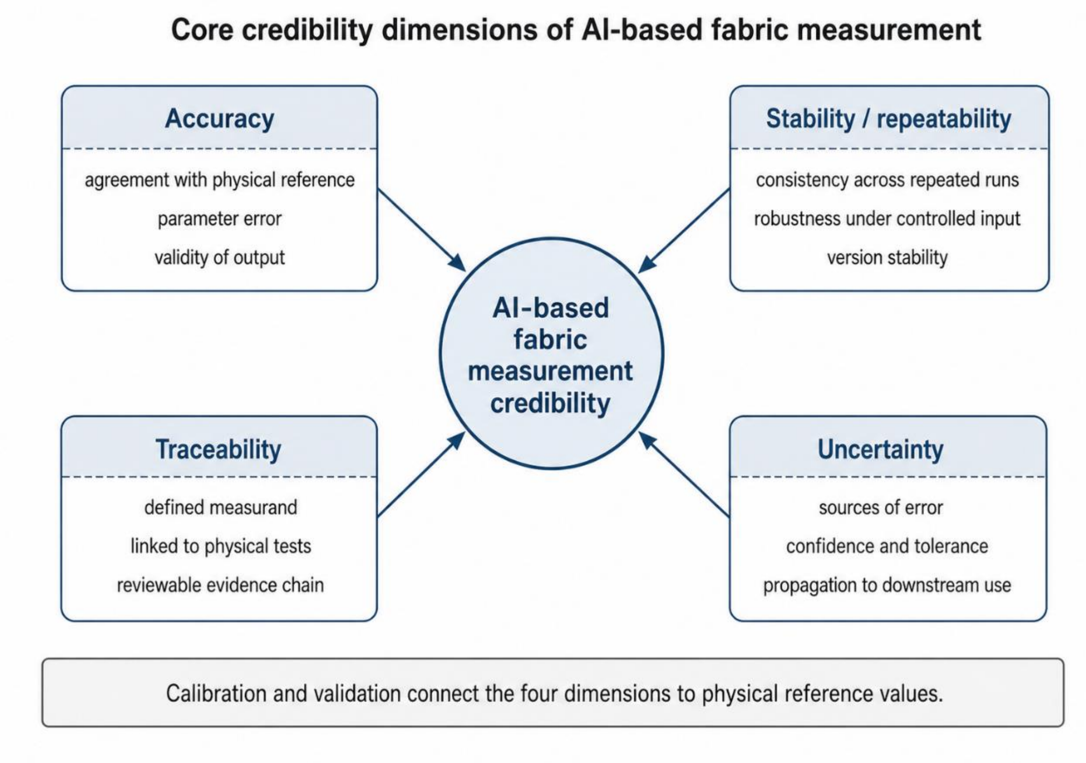

Figure 1.9 — Evaluation of the Reliability of AI-Based Fabric Measurement

As shown in Figure 1.9, the reliability of AI-based fabric measurement depends on four interrelated dimensions:

1) accuracy determines how close AI outputs are to physical reference values;

2) stability determines whether the system can produce consistent results under repeated runs, controlled input conditions, or changes in the model version;

3) traceability determines whether the output can be linked to defined measurands, physical tests, input evidence, model versions, and verifiable records;

4) uncertainty determines whether the sources, ranges, and subsequent propagation of errors can be identified. These dimensions must be evaluated jointly, because a numerically accurate output may still be unstable, non-traceable, or unsuitable for simulation and garment form prediction.

Accuracy and stability constitute the first two requirements for AI-based fabric measurement. Accuracy evaluates the deviation between AI outputs and physical reference values using indices such as absolute error, relative error, RMSE, MAE, or MAPE. However, accuracy should not be interpreted only as one-time numerical closeness, since systematic bias and subsequent effects in simulation must also be considered. Stability evaluates whether the outputs remain consistent under repeated iterations, controlled image combinations, different sample batches, and changes in the AI model version. Therefore, AI-based measurement cannot be evaluated only on the basis of a single accurate result.

Traceability and uncertainty further determine whether AI outputs can enter a reliable measurement process. Traceability requires that the result be linked to input evidence, parameter definitions, physical reference tests, model versions, and protocol records. Uncertainty concerns error sources associated with image acquisition, sample condition, reference-value error, prompt sensitivity, model-version drift, and post-processing. These factors show that AI-based measurement must be evaluated as a controlled system rather than as an isolated model response.

Calibration and validation are the mechanisms that connect reliability dimensions with physical reference values. Calibration reduces systematic deviation between AI outputs and actually measured values, establishes correction relationships between parameter groups, and improves the applicability of AI outputs for simulation or digital twin construction. Validation determines whether calibrated or uncalibrated outputs can support subsequent modelling tasks, such as virtual fabric construction, drapeability simulation, garment contour generation, and garment form prediction. This means that AI-based measurement should be evaluated not only at the parameter level, but also at the level of simulation results and applied outcomes.

Table 1.6 — Metrological Elements of AI-Based Textile Measurement

Element	Main Content	Typical Manifestation in Textile Scenarios
Evaluation of the measurand	Clear specification of the measurement object and output form	Bending stiffness range, anisotropy level, drape trend parameters
Controlled input	Standardization of the sample, lighting, background, view, and	Standardized fabric photographs, unified ROI, fixed shooting protocol

	distance	
Calibration chain	Correspondence between the AI output and the physical reference	Alignment with KES, FAST, Cusick, thickness gauge, and GSM data
Traceability	Traceability of data, model, and workflow	Complete records of original images, protocol templates, model versions, and post-processing scripts
Uncertainty evaluation	Identification and quantitative evaluation of error sources	Fluctuations in repeated inference, inter-batch drift, out-of-distribution risk
Validation metrics	Accuracy, stability, and consistency	MAPE, MAE, RMSE, correlation analysis, consistency comparison
Verification mechanism	Human–AI collaboration and logic for refusing output	Low-confidence outputs are transferred to manual retesting
Limits of applicability	Application conditions and refusal conditions	Limited application for highly reflective, transparent, or severely wrinkled fabrics

As shown in Table 1.6, AI-based textile measurement requires an accurate result of contactless non-instrumental evaluation, a defined output form, controlled input, a calibration chain, traceable records, uncertainty evaluation, validation metrics, a verification mechanism, and limits of applicability. These elements determine what conclusions an AI system is permitted to draw regarding the comparability of input evidence, its relationship with physical reference values, and the conditions of validity. Without these elements, the results of AI-based measurement would be closer to empirical predictions than to rigorous measurement results.

Taken together, Figure 1.9 and Table 1.6 describe the basic metrological logic of AI-based fabric measurement. Figure 1.9 defines the reliability dimensions that AI-based measurement must satisfy. Table 1.6 organizes the necessary elements into a measurement-oriented structure of a controlled digital measurement process, including evidence acquisition, protocol definition, output structuring, calibration, traceability, uncertainty evaluation, and validation.

Therefore, AI-based measurement should be understood as a systematic method, and the metrological foundation of AI-based fabric measurement lies in transforming the unrestricted capabilities of the model into controlled parameter acquisition.

1.3 Current State of Research on Digital Twins of Textiles and Garments Based on 3D Modelling

1.3.1 Construction of a Digital Twin of a Textile Material

The essence of a digital twin lies in transforming the real behavior of fabric under low-stress mechanical conditions into a parameterized virtual material system that can be invoked, calculated, and verified in a three-dimensional environment [85–89]. Unlike conventional three-dimensional surface modeling, a digital twin represents a deformable material body whose morphology changes under the action of gravity, boundary constraints, contact, and imposed restrictions. The evaluation of a fabric digital twin, in addition to the visual realism of the rendered fabric itself, must include the assessment of behavioral responses comparable to those of real fabric under corresponding physical and boundary conditions [90–98].

Existing studies show that the virtual construction of a fabric twin depends on a physically meaningful set of parameters. Thickness and surface density define geometric scale and weight; tensile parameters describe directional elongation; bending and shear parameters influence folds, contour softness, and surface adaptation; compression and friction affect contact, fold stability, and garment fit on the body. Without these inputs, a virtual garment may appear visually plausible, but it will be weak in terms of engineering reliability and transferability [85–98]. Figure 1.10 shows the role of fabric mechanical parameters and the problems of their implementation in 3D garment simulation.

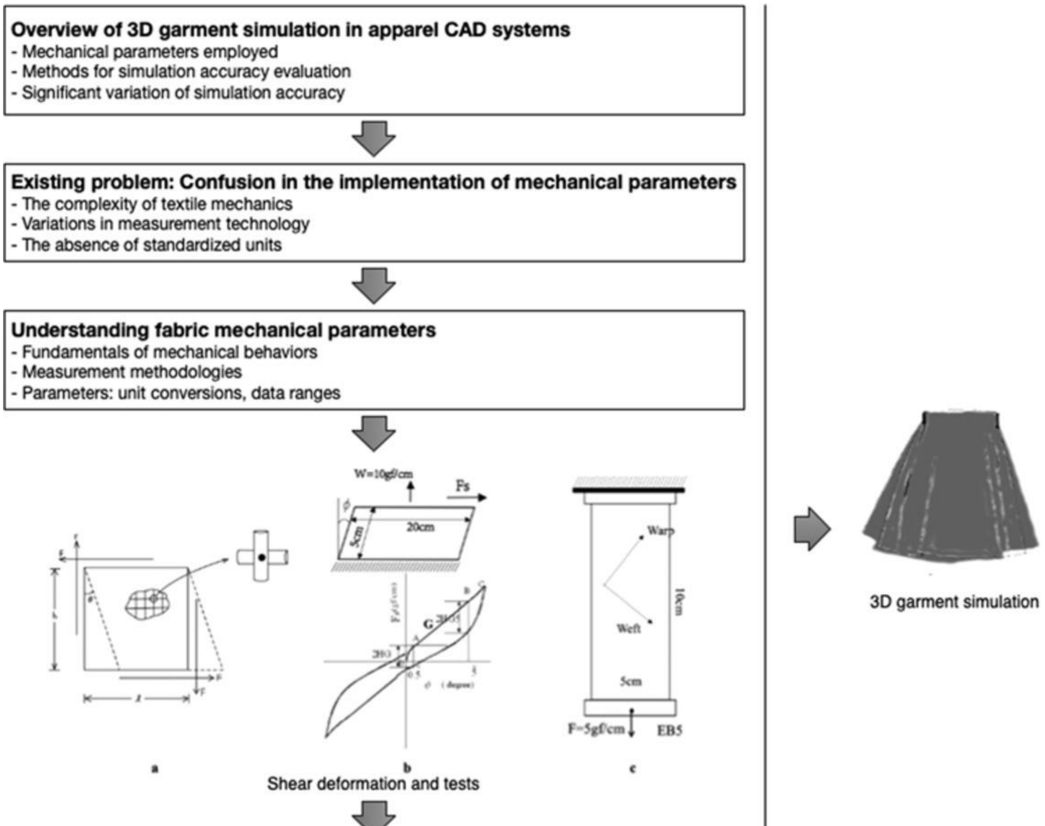

Figure 1.10 — Fabric Parameters in 3D Garment Simulation [97]

As shown in Figure 1.10, fabric mechanical parameters form the basis of 3D garment simulation. Simulation accuracy is influenced by fabric type, mechanical complexity, the measurement technology used, and the availability of unified units or conversion rules. The lower part of Figure 1.10 further shows that each parameter must be interpreted through its behavioral meaning, measurement method, unit conversion, and applicable data range before it can be entered into a fabric digital twin model. Therefore, the construction of a digital twin is a parametrically mediated process that includes measurement, standardization, conversion, virtual assignment, and validation [97]. Table 1.7 presents the main categories of parameters, acquisition methods, and modeling roles in the construction of digital twins.

Table 1.7 — Application of Fabric Property Indicators in Virtual Modeling

Parameter Category	Typical Acquisition Method	Main Role in Virtual Modeling
Thickness; surface density	Thickness gauge; GSM test	Determine self-weight, volumetric impression, and basic inertial characteristics
Tensile indicators	KES, FAST, uniaxial / biaxial tensile tests	Determine extensibility in the warp, weft, and bias directions, local deformation, and tendency to conform to the body
Bending indicators	KES, bending length test, cantilever method	Determine fold stiffness, hem softness, and tendency to drape
Shear indicators	KES, FAST	Determine angular deformation and torsional adaptation on complex curvilinear surfaces
Compression and surface friction indicators	KES, friction test	Influence interlayer contact, folding state, and stability during wear
Drapeability	Disk or cylindrical drape test, image analysis, 3D scanning	Link material parameters with appearance results, such as external contour, number of nodes, and projected area

As shown in Table 1.7, the input data for a fabric digital twin constitute a multilevel system of parameters. These parameters do not have identical functions in modeling and cannot be regarded as interchangeable indicators. Therefore, the construction of a digital twin requires verification of whether these parameters can be expressed in a form that is compatible with software and physically interpretable [85,90–98]. This also explains why the same fabric may produce different simulation results on different three-dimensional platforms: differences may arise from the method of parameter definition, input scale, unit conversion, and interpretation of the material model, and not only from the geometry of the product [91–97].

The first step from real fabric to a digital twin is the standardized acquisition of physical parameters. Fabric measurement systems represented by KES-Kawabata provide a relatively complete route for measuring bending, shear, tensile, surface, and compression properties and are therefore widely used in studies of virtual garments and the construction of material databases [85,90–92,97]. FAST systems, commercial measurement systems, single-factor bending and drapeability tests, as well as image-based measurement methods, are also used to obtain parameters for virtual simulation [93–98]. However, existing studies show that different testing systems are not directly interchangeable. They differ in the way the measurand is defined, sample size, loading state, output unit, and data format. Consequently, obtaining a numerical parameter does not necessarily mean that it can be directly entered into a three-dimensional platform, nor does it guarantee that the resulting virtual material will have realistic draping behavior [91–97].

The second key issue is the correspondence between experimental parameters and virtual material parameters. Physical testing can produce load–elongation curves, shear force–angle curves, or direct values such as thickness and surface density. By contrast, simulation platforms require specific numerical values such as bending stiffness, shear stiffness, tensile resistance, density, friction, and damping. These two groups of data representation are not inherently equivalent; therefore, approximation, conversion, normalization, range adjustment, or empirical calibration is often required. This problem is especially important for fabrics because anisotropy in the warp, weft, and bias directions affects the results. For this reason, existing studies focus on more complete material characterization and on parameters specific to platform interfaces [86–98].

In addition to parameter correspondence, the construction of a digital twin also involves solving the problems of scaling and result representation. In tests of real and virtual samples, they may be compared using the drape coefficient, projected area, number of folds, external contour, or three-dimensional geometry. In a finished garment, material behavior is further mediated by pattern construction, seam connections, body support, and boundary conditions [90,96–98]. This distinction means that a digital twin can be considered both at the independent fabric level and as the material basis of a garment digital twin: the former focuses on parameter acquisition, correspondence, and representation in a virtual environment, whereas the latter requires consideration of the interaction of these parameters with patterns, seams, the body figure, and wearing scenarios in order to form the appearance of the finished garment.

Overall, digital twin research has formed a relatively clear methodological chain: physical testing defines material parameters; parameter correspondence and virtual assignment transform measured data into a computable material model; numerical simulation generates draping and appearance responses; and real–virtual comparison evaluates whether the virtual material corresponds to the real textile [85–98]. However, this research direction still has three limitations. First, the mechanisms for parameter correspondence between different testing systems and software platforms remain insufficiently unified [91–97]. Second, existing studies often emphasize the relationship between parameter input and visual output, whereas the transparency and interpretability of the intermediate material model are not discussed sufficiently [86,87,95]. Third, a digital twin at the fabric sample level does not automatically form a digital twin at the garment level. Therefore, the constructional basis of fabric digital twins must be further linked with three-dimensional virtual simulation technology in garment engineering and with methods for validating garment digital twins.

1.3.2 Three-Dimensional Virtual Garment Simulation

Traditional two-dimensional garment CAD systems are effective for pattern construction, grading, and marker layout, but the final fit, silhouette, distribution of allowances, and appearance state of a garment must be evaluated in three-dimensional space. Therefore, as the focus of garment engineering shifted from the correctness of pattern construction to the behavior of the garment on the body, the necessary components of garment digitalization emerged: three-dimensional body modeling, garment generation, virtual stitching, and material simulation [81–84,99–107].

In garment engineering, a 3D virtual simulation platform usually performs several key functions. First, it creates a digital object of the human body as a measurable and parameterizable spatial support for garment loading and fit evaluation. Second, it supports the transformation of two-dimensional pattern pieces into a three-dimensional garment through pattern placement, virtual stitching, dressing simulation, and dynamic solving. Third, it links material parameters with gravity, so that the garment becomes not a static geometric shell, but a deformable object with a physical response. Fourth, it allows simulation results to be extracted, compared, and used for structural correction or pattern optimization. Figure 1.11 shows the transformation of two-dimensional pattern pieces into a three-dimensional garment during virtual prototyping.

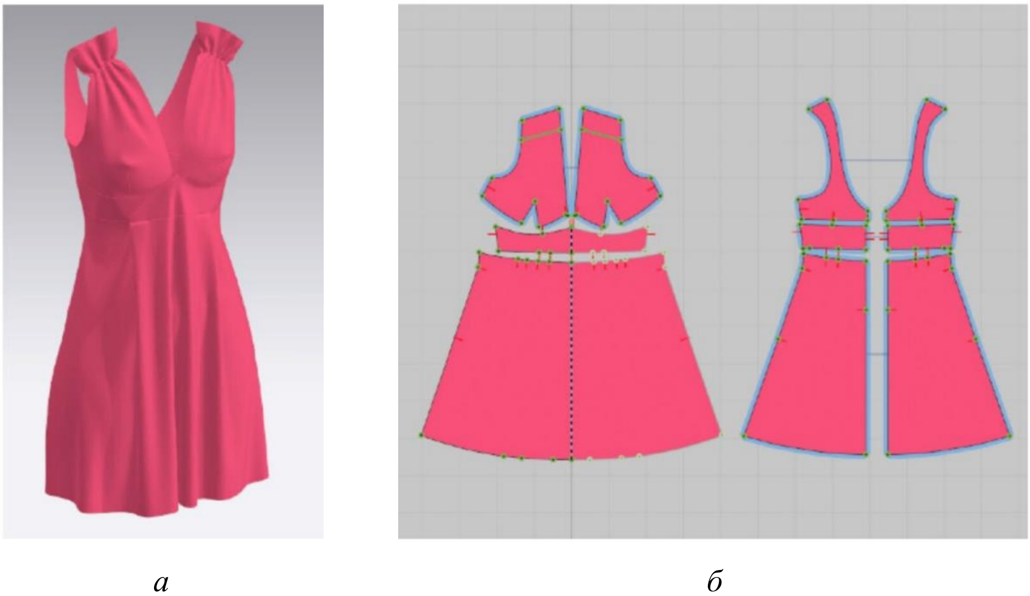

а *б*

Figure 1.11 — Transformation of garments from 2D to 3D: *a* — 3D virtual garment; *b* — view of 2D pattern pieces [106].

As shown in Figure 1.11, a three-dimensional garment is formed through the organization of two-dimensional pattern pieces, virtual stitching, avatar placement, material assignment, and dynamic simulation. This relationship explains why 3D virtual garment simulation is fundamentally different from conventional rendering: the simulated garment must preserve its structural connection with its pattern pieces. If this connection is absent, the virtual garment may appear visually plausible, but it cannot support pattern correction, engineering feedback, or digital twin validation.

After the garment is created, the reliability of its virtual form depends on the accuracy of material simulation. Existing studies usually classify methods of virtual drapeability and garment animation into geometric, physically based, and hybrid methods [83,84]. Geometric methods emphasize visual output and computational efficiency; physically based methods treat the garment as a deformable body with mass, elasticity, bending, shear, and contact responses; hybrid methods attempt to balance computational speed and physical plausibility [85–89]. The growing attention to these mechanisms shows that the reliability of a virtual garment is determined not by visual realism alone, but by whether it reproduces reasonable form-generation effects under specified material parameters, gravity, contact, and boundary conditions.

In recent studies, material simulation has also been linked with pattern optimization, because garment simulation must support reverse analysis of garment form, generation of two-dimensional pattern pieces from three-dimensional geometry, and pattern correction according to fabric-related parameters. This development changes the function of 3D garment simulation from visual prototyping to engineering feedback. Figure 1.12 shows the development from 3D garment simulation to surface unfolding and feedback for pattern optimization.

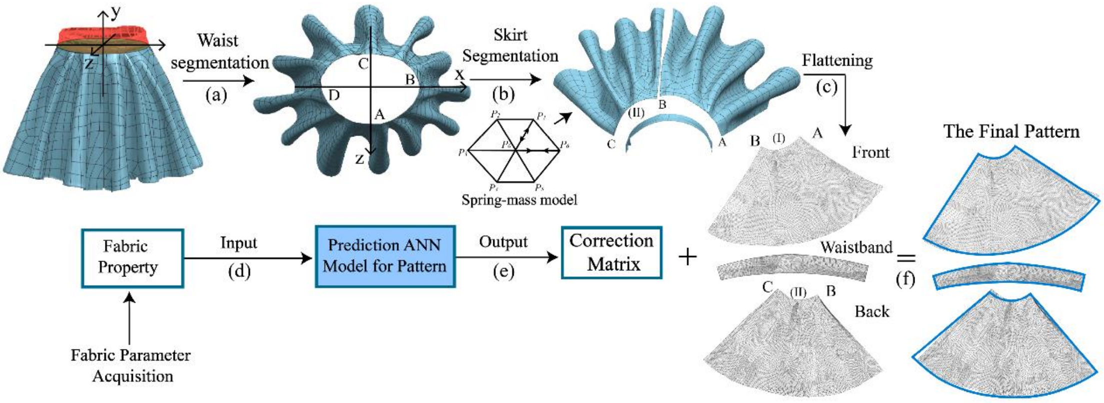

Figure 1.12 — Surface Unfolding and Pattern Optimization [157]

As shown in Figure 1.12, 3D garment simulation can be further linked with the modification of the original patterns through surface segmentation, surface unfolding onto a plane, fabric parameter input, and corrective modeling. Figure 1.12a–c shows that the simulated three-dimensional surface of the garment can be transformed into a form related to the two-dimensional pattern, providing a pathway from spatial morphology back to flat construction. Figure 1.12d–f shows that fabric parameters can be introduced into prediction and correction procedures to obtain an optimized final pattern. The scheme shows that 3D garment simulation can support reverse engineering from simulated garment geometry to pattern correction, which is important for garment digital twins because this process links material properties, virtual garment morphology, and correction of pattern parameters within a single technical chain.

Overall, 3D virtual simulation technology provides the platform basis for garment digital twins. It makes it possible to integrate the human body, pattern pieces, textile materials, virtual stitching, gravity, contact, and simulation outputs into a unified digital environment. Effective use of a 3D simulation platform requires parameter consistency, structural traceability, validity of material response, and real–virtual verification. Establishing the status of a digital twin further depends on the completeness of parameter input, structural correspondence, simulation response, and the validation framework.

1.3.3 Validation of Digital Twins of Textiles and Garments

The key issue in generating a digital twin is whether it can ensure verifiable correspondence with the real object in terms of parameters, morphology, and response. Without validation, a three-dimensional model can be regarded only as a digital representation or a simulation result, rather than as a digital twin in the strict sense. Therefore, validation and evaluation are necessary conditions for determining the research validity of a virtual object [111–113].

For textile and garment research, the consistency between real and virtual objects includes at least three levels:

1) the first level involves verification of parametric consistency, that is, whether the virtual material parameters, dimensional parameters, and structural parameters correspond to the real object;

2) the second level involves verification of morphological consistency, that is, whether the contour, area, number of nodes, folds, local regions, and overall silhouette demonstrate comparable geometric similarity;

3) the third level involves verification of response consistency, that is, whether real and virtual objects exhibit similar trends and response patterns when the material, pattern, or support conditions are changed.

Therefore, digital twin validation is a multilevel evaluation process involving input parameters, visible morphology, and behavioral response [114–120]. Table 1.8 presents the main validation levels and indices for digital twins of textiles and garments.

Table 1.8 — Main Validation Levels and Indices for Digital Twins of Textiles and Garments

Validation Level	Typical Object of Comparison	Common Evaluation Approach or Index
Parametric consistency	Material parameters, dimensional parameters, structural parameters, assembly relationships	Parameter error, deviation, correlation, calibration comparison
Morphological consistency	Contour, area, number of nodes, folds, silhouette, ROI	IoU, Dice, boundary deviation, area difference, node difference, SSIM, heat-map overlay
Response consistency	Result trends caused by changes in material, structure, and support conditions	Trend consistency, comparison of response curves, evaluation of equivalent response, prediction error of form parameters

As shown in Table 1.8, different validation levels require different objects of comparison and indices. Parametric consistency is evaluated through error, deviation, correlation, and calibration comparison. Morphological consistency is evaluated using indices based on contour, area, folds, silhouette, and ROI. Response consistency is evaluated through trend comparison, comparison of response curves, assessment of equivalent response, and prediction error.

1.4 Research Gaps and Problem Statement

1.4.1 Limitations of Traditional Drapeability Testing Methods

Traditional drapeability testing methods define standardized sample forms, support conditions, and calculation rules for comparing fabric stiffness, drape coefficient (DC), number of folds, contour characteristics, and low-stress responses. Their value lies in reproducibility and comparability at the material level; however, when the research object shifts from fabric-level evaluation to the analysis of garment-level form generation, their applicability becomes limited [123–127].

The first limitation lies in the mismatch between standard samples and real garment structures. Traditional tests usually use strip, circular, or other regular flat samples, whereas garment form depends on seams, joining methods, yarn direction, cutting orientation, and local structural constraints. Hu, Chung, and Lo showed that seam parameters can change the draping behavior of fabric, and Demir and Balcı Kılıç further demonstrated the influence of stitch type and seam direction under dynamic draping conditions [121,130]. Orzada, Moore, and Collier established that off-grain cutting affects both fabric drape and garment drape, while Sun's cruciform sample method was proposed to reflect warp–weft differences that cannot be captured by testing samples cut in a single direction [122,127]. These studies show that the drapeability results of a fabric sample cannot be directly transferred to multi-piece garments when structural factors are excluded.

The second limitation is related to support conditions. Classical drapeability tests mainly use regular supports, such as a cantilever or a disk. These supports are suitable for standardized comparison, but they simplify the body-related boundaries that determine garment form generation. In real garments, garment morphology depends on the shoulders, bust, waist, hips, their interrelationships, seam positions, and local contact with the body. Issa et al. used 3D-printed mannequins to measure the static and dynamic drapeability of fabrics and garments, showing that body- or mannequin-based support conditions can produce draping responses different from those obtained using regular support devices [128]. Therefore, the standardized boundary of traditional drapeability testing is simultaneously its main limitation when garment-related morphology is considered.

The third limitation concerns the dimensionality of evaluation indices. Traditional characterization of drapeability is usually based on length, DC, projected area, number of folds, distance to the boundary, or two-dimensional contour parameters. These indices are effective for ranking materials and comparing fabric samples, but they compress complex three-dimensional morphology into simplified scalar or planar descriptors. Chen and Govindaraj emphasized that drapeability is essentially a three-dimensional shell problem, while Park et al. and Kwon et al. showed that fold position, contour curvature, and boundary waviness reveal morphological differences beyond a single DC value [123–126]. Hussain et al. further introduced three-dimensional point-cloud parameters because two-dimensional indices are insufficient for describing the spatial morphology of drape [129]. This shows that traditional indices are limited when it is necessary to analyze fold depth, local spatial deformation, and contour response at the garment level.

Table 1.9 presents the main limitations of traditional drapeability testing methods and their consequences for garment engineering.

Table 1.9 — Limitations of Traditional Testing Methods

Type of Limitation	Specific Manifestation	Influence on Garment Engineering
Exclusion of garment structure	Standard samples usually exclude seams, stitch types, joining methods, and cutting orientation	Difficult to represent the draping behavior of assembled garments [121,122,127,130]
Simplified support conditions	Test supports are mainly linear edges, circular disks, or regular boundaries	Weak correspondence with garment states supported by the shoulders, body, or mannequin [128]
Compression of	Results are often expressed through	Insufficient representation of fold

spatial information	DC, projected area, number of nodes, or two-dimensional contour parameters	depth, spatial contour, and three-dimensional morphology [123–126,129]
Limited transferability to the garment level	Material-level results cannot directly explain garment form generation under structural and boundary constraints	Difficult to support garment form prediction and pattern correction [121–130]

As shown in Table 1.9, the limitation of traditional drapeability testing methods lies in the mismatch between the standardized logic of testing and the conditions of form generation at the garment level. Traditional methods can effectively compare fabric drapeability under controlled sample conditions. However, they remain insufficient for representing the influence of seams, combinations of yarn directions, body-related boundaries, and the three-dimensional morphology of garments. Therefore, garment-oriented drapeability research requires testing methods that preserve experimental comparability while introducing support conditions and structural constraints closer to the real states of garments.

1.4.2 Key Problems in the Generation of Digital Twins

With the development of three-dimensional modeling, virtual fitting, and garment simulation technologies, textile and garment research has gradually shifted from geometric visualization to the construction of digital twins. However, generating a digital twin is not equivalent to creating a three-dimensional object. A reliable digital twin requires correspondence between physical parameters, virtual material models, support scenarios, and simulation responses. Therefore, the main problem in modern digital twin generation is no longer whether a virtual fabric or garment can be displayed, but whether the generated object can maintain verifiable consistency with the real object in terms of parameter input, scenario reconstruction, and behavioral response [135–140].

The first problem lies in the complexity of fabric parameter acquisition. Existing workflows for generating fabric digital twins still depend to a considerable extent on physical testing chains involving multiple standards, instruments, and operations. Standards such as ASTM D1388, ASTM D1777, ASTM D5034, and ASTM D4032 are respectively associated with measurements of bending, thickness, tensile properties, or circular bending stiffness and strength [131–134]. These tests provide important physical data, but they do not form a unified integrated route for parameter acquisition. In the practical construction of digital fabrics, samples in the warp, weft, and bias directions often have to be prepared separately; different instruments are used for different properties; and the obtained values require additional processing before being entered into simulation software. Thus, parameter acquisition is the main bottleneck determining the cost, efficiency, and reliability of digital twin generation.

The second problem is related to the gap between physical test results and software input parameters. Commercial garment simulation systems usually generate virtual fabrics through fabric libraries, Fabric Kits, fabric simulators, or material cards [135–140]. These tools make the generation of fabric digital twins operationally feasible, but they also introduce platform dependence. The outputs of physical tests do not always have a direct one-to-one correspondence with the internal parameters required by the software. Differences in units of measurement, data ranges, input fields, solver mechanisms, and material models may lead to different simulation results for the same fabric. Consequently, the key difficulty lies not only in how to measure fabric properties, but also in how to transform measured data into software-compatible and physically interpretable virtual material parameters.

The third problem is the consistency of the scenario and the form of the test rigs. Digital twin generation requires the reconstruction not only of material properties, but also of support objects, boundary conditions, contact states, and simulation scenarios. In studies related to fabric drapeability, support by a disk, mannequin, human body, or garment structure may produce different morphological responses. If the virtual scenario does not correspond to the real testing scenario, accurate material parameters alone cannot guarantee a reliable simulation result. This problem transfers the limitation of traditional drapeability testing from the physical testing stage to the digital construction stage.

The fourth problem is the insufficient stability of platforms. Different software systems use different models, parameter interfaces, collision rules, and numerical solvers. Therefore, a fabric digital twin created on one platform may not reproduce the same drapeability or garment morphology on another platform. This shows that digital twin generation is determined by the interaction between measured data, virtual material representation, and software-specific simulation mechanisms. Without a stable correspondence relationship between these components, the generated virtual object remains closer to a platform-dependent simulation result than to a transferable digital twin.

Table 1.10 presents the main bottlenecks in the traditional workflow for generating textile digital twins.

Table 1.10 — Bottlenecks in the Generation of Fabric Digital Twins

Workflow Stage	Main Operation	Main Bottleneck
Sample preparation	Cutting samples in the warp, weft, and bias directions	Labor-intensive preprocessing; sensitivity to operational consistency [131,137]
Measurement of	Conducting ASTM D1388,	Multiple methods and instruments are

bending and thickness	ASTM D1777, ASTM D4032, or related tests	required [131,132,134]
Measurement of tensile properties or strength	Conducting grab tests or software-related tensile measurements	Test outputs are not always directly equivalent to software parameters [133,137]
Input into software	Entering measured values into fabric simulators or material cards	Manual input increases the risk of errors and depends on platform-specific fields [136,138]
Generation based on fabric libraries or scanning	Using fabric libraries, Fabric Kits, or digital fabric scanning modules	Strong platform dependence; limited transferability between software programs [135,139,140]
Validation and simulation adjustment	Observing drape, stretch, texture, or garment response and adjusting parameters	Adjustment depends on experience; the validation workflow is often fragmented [135,140]

Overall, the key problem in digital twin generation is construction reliability. A virtual fabric or garment can be created using existing software tools, but its status as a digital twin depends on how consistently physical parameters, virtual material models, support scenarios, and simulation responses are linked. If this relationship remains unstable, the resulting virtual object cannot reliably support garment form prediction, pattern correction, or real–virtual validation.

1.4.3 Inadequacy of methods for predicting garment shape and adjusting pattern parameters based on drape

Modern digital apparel development still relies primarily on an iterative process of sample generation, evaluation, and correction. Digital pattern-making systems, virtual prototyping, and 3D fitting technologies can accelerate this process [141–150]. Consequently, a key limitation is the absence of a direct predictive mechanism capable of forecasting garment shape parameters based on fabric drape characteristics under conditions that closely simulate actual garment behavior.

The first gap lies in the lack of a quantitative link between fabric drape and garment shape. Research into digital pattern-making, personalized patterns, optimized grading, parametric design, and automated pattern generation has improved the efficiency of pattern development and size adaptation [141–144, 150]. However, these studies primarily address how patterns can be generated, modified, or graded more efficiently. They do not establish a direct quantitative mechanism by which fabric drape parameters can help predict garment morphology. While existing research generally confirms that fabric properties influence garment appearance, this influence is typically discussed as an observed trend rather than through the efficacy of an operational model for predicting garment shape parameters.

The second gap concerns the adjustment of pattern parameters. In apparel engineering, the value of shape analysis lies in the ability to translate identified discrepancies into structural adjustment rules. Existing research on fit, size chart optimization, and the relationships between body measurements and patterns reveals persistent inconsistencies across construction systems [143, 149]. The problem becomes more complex when fabric drape and garment morphology are factored into this relationship. Currently, there is a lack of methods capable of proceeding from drape measurements to the determination of specific pattern adjustment values. This issue also highlights a limitation of virtual prototyping. Methods such as assessing the similarity between virtual and real garments, geometrically comparing virtual and physical products, and utilizing virtual e-bespoke systems have improved the ability to identify appearance or fit issues prior to physical production [145–148]. However, these methods primarily support *post hoc* comparison, validation, and optimization. While they help designers identify discrepancies between virtual and physical products, they do not determine how pattern parameters should be adjusted in advance to account for fabric draping behavior. Consequently, although virtual prototyping reduces some trial-and-error costs, it has not yet established a robust feed-forward design mechanism. Table 1.11 outlines the key limitations regarding the prediction of garment shape and the adjustment of pattern parameters based on drape characteristics.

Table 1.11 – Limitations in predicting garment shape

Research Direction	Current Progress	Main Limitation
Development of Digital Patterns	Improves the efficiency of personalized pattern generation.	Mainly solves pattern generation, but lacks a fabric-to-shape matching mechanism [141,150].
Size and Grading Optimization	Improves fit for specific user groups or sizing systems.	Focuses on the adaptation of body sizes rather than fabric-driven shape prediction [142,143].
Parametric and Automatic Pattern Drafting	Reduces a portion of manual labor in pattern drafting.	Limited in expressing fabric response and physical constraints [144,150].
Virtual Prototyping and Similarity Evaluation	Allows earlier identification of discrepancies in appearance and fit.	Mainly used for *post-hoc* comparison; lacks feed-forward predictive ability [145–148].
Study of Body-Pattern Relationships	Identifies inconsistencies in transformation rules from body to pattern.	Difficult to establish stable correction rules when introducing fabric drape [149].

Overall, the main limitation of current research lies in the gap between material evaluation, garment shape-forming response, and pattern correction.

1.5 The purpose and direction of this research

Based on the research gaps identified above, the central problem of this dissertation is to establish a continuous methodological pathway linking textile material measurement and digital twin construction with garment-oriented drape testing, clothing shape prediction, and pattern parameter correction.

The aim of this dissertation is to develop an integrated methodological framework for the design of digital twins of textile materials and garments based on 3D technology.

The specific objectives of this dissertation are as follows:

1. To form a unified methodological framework including textile and garment samples, software platforms, testing procedures, imaging conditions, and validation indices.
2. To develop methods for constructing a fabric digital twin based on physical testing and protocol-guided AI measurements, and to evaluate their applicability in 3D simulation.
3. To develop and validate a garment-oriented anthropomorphic drape testing method and apparatus with physical-virtual implementation in garment design.
4. To develop methods for predicting women's dress shape and correcting pattern parameters.
5. To integrate the proposed methods into a complete workflow for designing digital twins of textile materials and garments.

Figure 1.13 shows the general research framework of this dissertation.

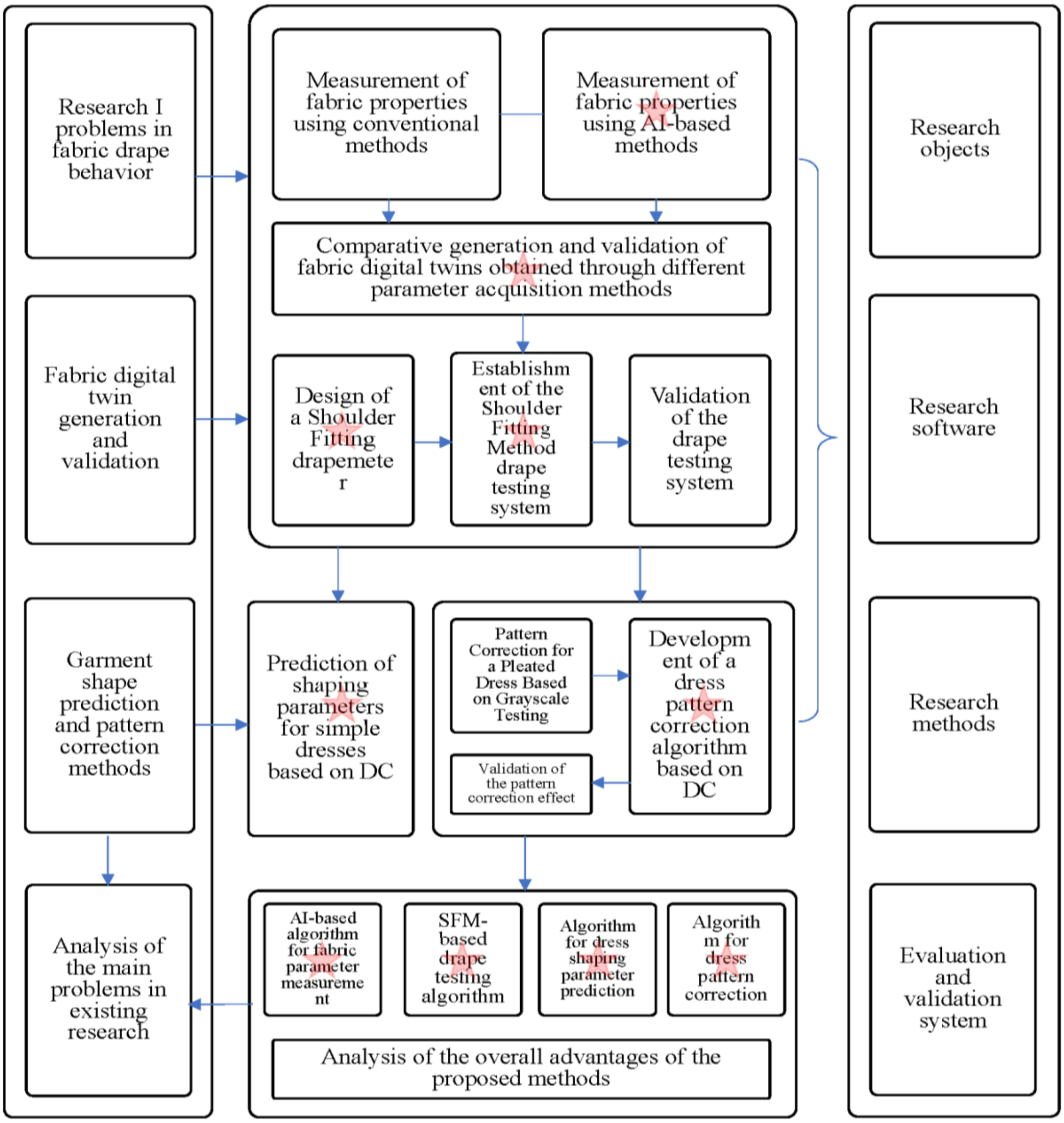

Figure 1.13 - General research framework

As shown in Fig. 1.13, this dissertation follows a sequential research route from the methodological framework to textile material digital twin construction, garment-oriented drape testing, clothing shape prediction, pattern parameter correction, and integrated workflow development.

CHAPTER 2. OBJECTS AND METHODS OF RESEARCH

2.1 Objects of Research

2.1.1 Fabrics

Fabrics were studied as material and virtual objects. Real fabrics were used to determine indicators of physical and mechanical properties, to present appearance, to evaluate the same indicators using artificial intelligence (AI), to generate fabric digital twins, to test drape, and to validate the three-dimensional silhouette shape of women's dresses. Virtual fabrics were applied in virtual experiments to test a new drape assessment method, including the selection of anthropomorphic stand parameters, justification of sample sizes, and analysis of differences in drape. Consequently, real and virtual fabrics were used at different experimental levels.

Five types of clothing fabrics, designated as F1–F5, were used as real objects. Fabrics F1–F3 represented the main group of materials for the complete characterization of all developed measurement methods, digital twin construction, and dress shape parameter prediction. Fabrics F4 and F5 formed a group to verify the applicability of the obtained results in garment design. Table 2.1 shows the basic information about the real fabrics.

Table 2.1 – Basic information about real fabrics

Code	Name	Weave Structure	Composition, %
F1	Denim fabric	Twill weave 3/1	97% cotton, 3% spandex
F2	Acetate imitation fabric	Satin weave	97% polyester, 3% spandex
F3	Tencel-poplin	Plain weave	100% cotton
F4	Greige fabric	Plain weave	100% cotton
F5	Validation fabric	Twill weave 3/1	100% cotton

The choice of such materials provided a diversity of fiber composition and weave structures. Fig. 2.1 shows the appearance of the fabrics.

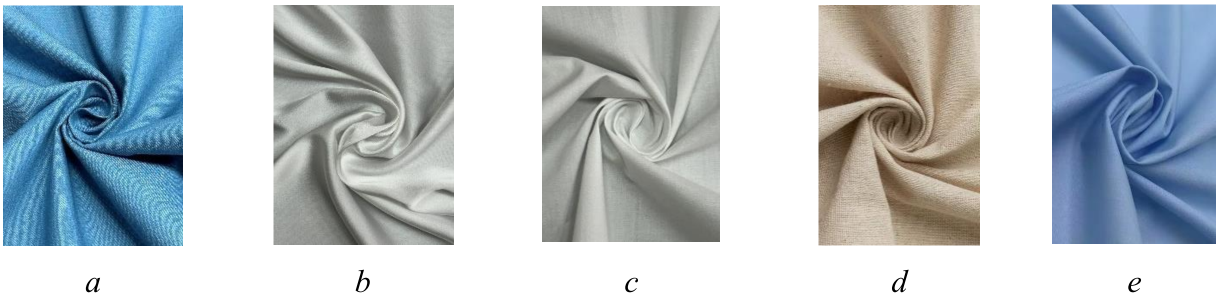

a *b* *c* *d* *e*

Figure 2.1 – Appearance of fabrics: *a* – F1, *b* – F2, *c* – F3, *d* – F4, *e* – F5

As shown in Fig. 2.1, real fabrics differ in surface texture, smoothness, and appearance. Their images complement the structural and compositional information in Table 2.1 and contain visual information for subsequent image-based measurement procedures and validation of finished products.

Virtual fabrics were selected from the Style3D fabric library and designated as VF1–VF5, C1-C3. They were used to develop the drape testing method, rather than as digital twins of the real fabrics F1–F5. Table 2.2 shows the parameters of the virtual fabrics defined in the software.

Table 2.2 – Virtual fabrics from the Style3D fabric library used to develop the drape testing method

Code	Virtual Fabric	Image	Surface Density (GSM), g/m²	Thickness, mm	Bending Stiffness, cN·mm^2·s^{-2}·rad^{-1}		
					Warp	Weft	Bias
VF1	Lycra fabric		130	0.47	100	50	60
VF2	Cotton-linen plain-type fabric		123	0.21	250	100	200
VF3	Polyester Paracord Crepe		102	0.29	350	250	300
VF4	Silk crepe-satin		52	0.13	650	100	200
VF5	Heavy plain-type fabric		90	0.43	850	800	850
C1	Polyester-cotton twill fabric		115	0.26	590	300	460
C2	Polyester corduroy		103	0.19	290	110	116

C3	Pure cotton plain fabric		56	0.17	250	100	150

As shown in Table 2.2, VF1–VF5 and C1–C3 have characteristics defined by the software from the Style3D library and are not interpreted as laboratory-measured indicators.

2.1.2 Dress patterns and models

The research objects included a basic dress (BD) and a pleated dress (PLD). The BD was used to establish the relationship between the fabric drape coefficient, measured using the new Shoulder Fitting Method (SFM), and the form parameters of the garment. In this work, the fabric drape coefficient calculated by the SFM method was denoted as DC_{SFM} and used as an input indicator for predicting dress form parameters. The PLD was used to establish the relationship between the number of pleats, fabric DC_{SFM}, and the formation of pleats. Both types of dresses had a sleeveless construction in order to reduce the influence of sleeves and the armhole line on dress morphology and to directly investigate the effect of fabric drapeability. Figure 2.2 shows the measurement scheme for the form parameters of the BD.

а *б*

Figure 2.2 — Pattern scheme of the basic dress BD and parameters of its volumetric-silhouette form:
a — pattern scheme; *b* — measurement scheme for parameters P_{d1}, P_{d2}, P_{d3}, and P_{d4}.

Figure 2.2b shows the measurement schemes for four parameters:

P_{d1} — vertical length from the side neck base point to the hem;

P_{d2} — frontal projected width of the dress at the hem;

P_{d3} — inclination angle of the side contour from the lower point of the armhole to the hem;

P_{d4} — drapeability indicator of the basic dress (BD), characterizing the degree of change in the dress form after it is placed on the mannequin.

These four parameters were used to describe the forms of the basic dress BD with different lengths. Table 2.3 shows the pattern parameters of basic dresses of different lengths, from the minimum form BD1 to the maximum form BD5.

Table 2.3 — Parameters of BD Patterns

Symbol	L_{BD}, cm	W_{BD}, cm
BD1	45	27
BD2	65	31
BD3	85	35
BD4	105	39
BD5	125	43

As shown in Table 2.3, the different dress forms BD1–BD5 were obtained through the coordinated increase of the pattern length LBD and the pattern width W_{BD}.

The pleated dress (PLD) was created by structural pattern modeling of the basic dress BD. The pleats were arranged from the shoulder to the bust along the seam joining the upper and lower parts. Different pleating levels were generated while keeping the pleat positions unchanged; only the pleat depths were varied. This setup excluded the influence of variations in pleat position on the nature of the surface pleating, making it possible to analyze the relationship between the pleating of the pattern piece, the fabric DC_{SFM}, and pleat morphology. In order to exclude the influence of changes in pleat position (P) on the morphology of the pleated surface of the PLD, the five variants of the pleated dress patterns (PLDP1–PLDP5) retained identical pleat positions, while only the amount of pleat spread in the pattern was changed. Figure 2.3 shows the pattern of the basic dress BD, the pattern-spreading process for the PLD, the fixed pleat positions, and the superposition of the five PLD pattern variants.

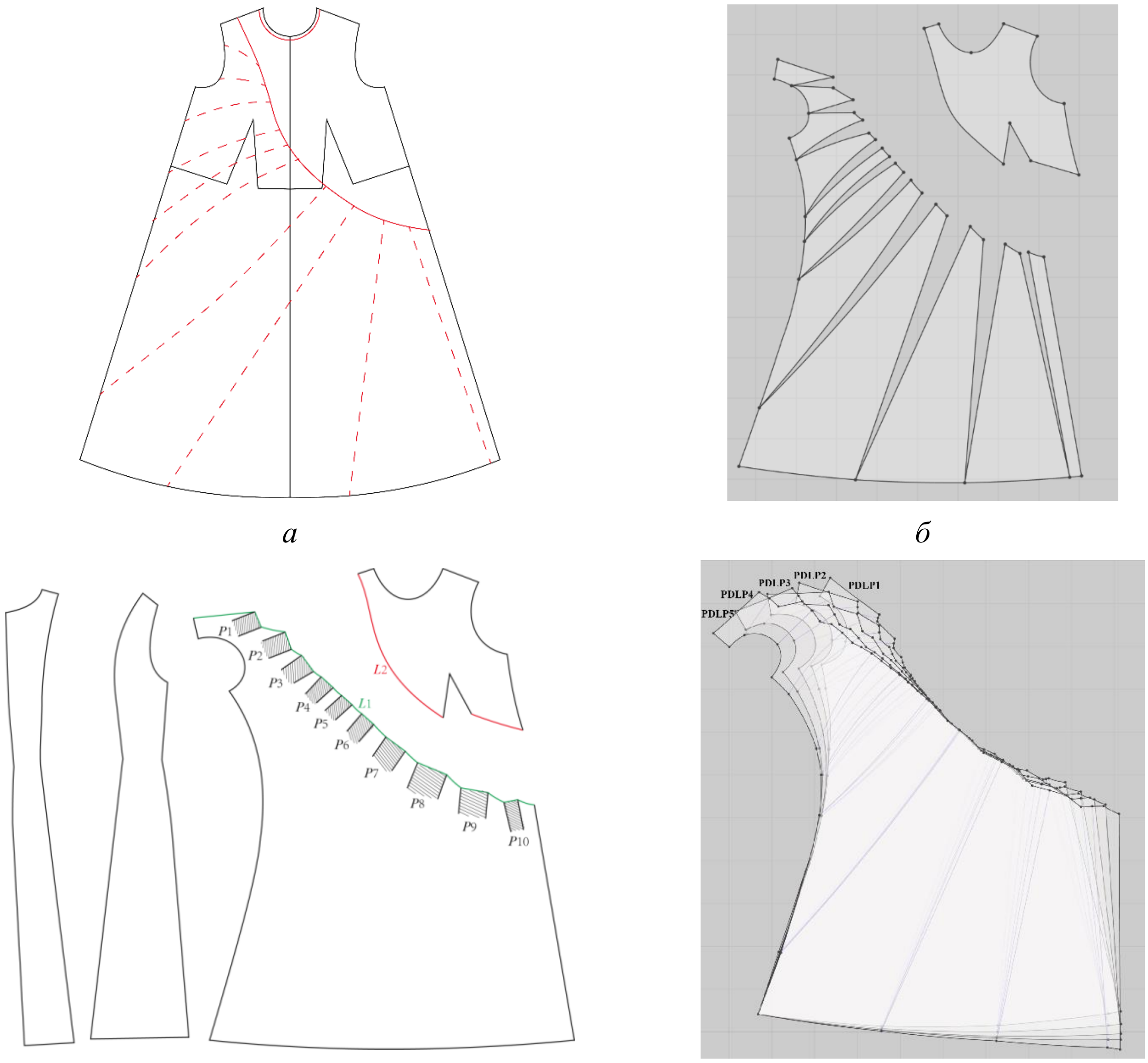

а *б*

в *г*

Figure 2.3 — Scheme for constructing the pleated dress pattern PLD and defining pleating levels:

a — pattern of the basic dress BD and slash lines;

b — PLD pattern after spreading along the slash lines;

c — fixed pleat positions and determination of L_1 and L_2 on the three-dimensional form of the PLD;

d — superposition of the five variants of the pleated dress patterns PLDP1–PLDP5.

Figure 2.3*a* shows the pattern of the basic dress BD, which was used to define the initial contour, structural division, and pleat-spreading zone before transformation into the PLD. The red dashed lines on the pattern indicate the slash lines and show the direction of pleat opening from the upper structural zone toward the lower part of the skirt. This pattern defines the initial structure and the direction of the cuts before spreading the PLD pattern.

Figure 2.3*b* shows the result of spreading the PLD pattern. After the BD pattern was cut along the red dashed lines shown in Figure 2.3*a*, the pattern was spread to obtain the additional area required for pleat formation. This process transforms the basic non-pleated BD pattern into a PLD pattern with a pleated structure and serves as the basis for constructing the five pleating levels.

Figure 2.3*c* shows the pleat positions and length parameters on the three-dimensional form of the PLD. The three-dimensional form of the PLD contains ten fixed pleat positions (P), designated as P_1–P_{10}. The positions P_1–P_{10} remained the same in all five variants of the PLD patterns so that the differences between them were determined primarily by the amount of pleat spreading rather than by changes in pleat position. L_1 denotes the initial length of the corresponding section before pattern spreading, while L_2 denotes the length of the same section after spreading. The increase of L_2 relative to L_1 characterizes the amount of pleat spreading at that position.

Рис. 2.3,*г* показывает наложение пяти вариантов чертежей PLD. Пять вариантов чертежей с разными уровнями складчатости обозначены как PLDP1–PLDP5. Наложение чертежей позволяет сравнить влияние увеличения складчатости на внешний контур чертежа PLD, конструктивные линии соединения и степень раскрытия нижней части платья. КоэффициентскладчатостиΔ рассчитывали следующим образом:

$$\Delta = \frac{L_2 - L_1}{L_1} \tag{2.1}$$

where Δ is the pleating coefficient, L_1 is the length of the cut before conical spreading, and L_2 is the length after conical spreading.

Table 2.4 shows the graded number of pleats and pleating coefficients for the five variants of the PLD patterns.

Table 2.4 — Pleat Parameters *P1–P10* for the Five Variants of the PLD Patterns

PLDP	Pleating coefficient Δ	Pleat dimensions, cm									
		1	2	3	4	5	6	7	8	9	10
1	0.48	1.66	2.19	2.59	1.69	1.21	1.67	3.45	5.35	4.30	1.30
2	0.67	2.66	3.19	3.59	2.69	2.21	2.67	4.45	6.35	5.30	2.30
3	0.86	3.66	4.19	4.59	3.69	3.21	3.67	5.45	7.35	6.30	3.30
4	1.05	4.66	5.19	5.59	4.69	4.21	4.67	6.45	8.35	7.30	4.30
5	1.24	5.66	6.19	6.59	5.69	5.21	5.67	7.45	9.35	8.30	5.30

As shown in Table 2.4, the PLDP1 structure has the initial level of pleat amount. From PLDP2 to PLDP5, the pleat amount at each position was increased by 1 cm compared with the previous level. Overall, the pleating coefficient Δ increased from 0.48 to 1.24. Using this grading method, five levels of pleat intensity were obtained while maintaining the same structure of pleat positions.

BD and PLD performed different functions as research objects. For describing the volumetric-spatial form of the BD, the parameters L_{BD}, W_{BD}, and P_{d1}–P_{d4} were used as key indicators for predicting the overall dress form. For describing the surface state of the PLD, the fixed pleat positions P_1–P_{10}, the levels PLDP1–PLDP5, and the pleating coefficient were used.

2.2 Software

2.2.1 Software for Three-Dimensional Modelling and Simulation

The software for three-dimensional modeling and simulation included Style3D Studio V9.2.880 and Rhinoceros 7. Style3D Studio V9.2.880 is software for three-dimensional garment design and simulation developed by Style3D. Rhinoceros 7 is three-dimensional geometric modeling software developed by Robert McNeel & Associates. These two software packages were used, respectively, for virtual garment simulation and for modeling and measuring geometric objects.

Style3D Studio V9.2.880 was used for fabric editing, virtual fabric selection, pattern construction, stitching of pattern pieces, dynamic garment simulation, and output of standard-view images. Style3D was selected as the main platform for conducting simulations because it made it possible to generate fabric digital twins, simulate the drapeability of samples on the new test rig (Chapter 3), and simulate the basic and pleated dresses within a single software environment. This platform reduced the influence of differences in fabric interpretation, solver behavior, export of fabric digital twins, and garment form generation.

Rhinoceros 7 was used for modeling the new anthropomorphic SFM drapemeter and for measuring curves, contours, distances, and local geometric parameters.

2.2.2 Artificial intelligence models

AI models were used to obtain indicators of the geometrical and physico-mechanical properties of fabrics required for constructing a fabric digital twin by a contactless non-instrumental method based on standardized photographs. In each test, input data were used in the format “image + text prompt”: the image was a photograph of the fabric obtained according to a fixed shooting scheme, while the text component corresponded to a specific version of the prompt protocol. The model output was a structured set of parameters, including thickness, surface density, tensile forces at small elongations, bending parameters, and the drape coefficient (*DC*). In this work, AI models were considered not as text generation tools, but as contactless means of obtaining parameters based on visual data and textual constraints.

To ensure the comparability of the results, the AI models were accessed in their official online environments without fine-tuning, additional training, local deployment, modification of model weights, or external measurement plugins. For each group of tests, the same combination of input images, prompt version, and output format was maintained. Since the platforms used belong to closed or semi-closed online systems, the model weights, full reasoning process, sampler, and low-level decoding process were not accessible. The seed, temperature, and top-p parameters were not fixed or adjusted as experimental variables. Repeated tests were performed through independent runs, and each output result was regarded as a separate measurement result.

Four multimodal artificial intelligence models were selected as parameter acquisition tools under the following technical conditions.

1) GPT-5.1 Thinking (OpenAI).
GPT-5.1 Thinking was accessed through ChatGPT Plus or the official OpenAI environment. The model supports joint text and image input, and produces results in textual form as a structured table of parameters. The model has long-context processing capability: according to the official technical description, the context window is 400,000 tokens, and the maximum output length is 128,000 tokens; different levels of reasoning effort are also supported. In the experiment, the model's visual understanding and reasoning capability was used to read morphological, textural, and draping features in fabric photographs and subsequently output numerical parameters in accordance with the prompt protocol.

2) Gemini 3 Pro (Google DeepMind).
Gemini 3 Pro was accessed through the official Gemini environment or Google AI Studio. The model supports multimodal input, including text, images, video, audio, and PDF, and generates output data in textual form. According to the official technical description, Gemini Pro series models have an input context window of 1,048,576 tokens and a maximum output length of 65,536 tokens, and also support Thinking and structured output. In the experiment, only images and a text prompt were used to obtain fabric parameters according to a unified protocol.

3) Grok 4.1 (xAI).
Grok 4.1 was accessed through the official xAI environment. The model supports text and image input, and generates output data in textual form. Grok 4.x series models have long-context processing capability and support reasoning modes. In the experiment, Grok 4.1 was used to recognize the macro-contour, fold form, local texture, and signs of gravitational deformation in standardized fabric photographs, followed by the output of a parameter vector according to the fixed prompt protocol. When accessed through the web environment, low-level reasoning settings and sampling parameters were not used as adjustable experimental variables.

4) Qwen3-Max (Alibaba Cloud).
Qwen3-Max was accessed through the official Tongyi Qianwen environment. In the experimental record, the model's name was fixed in accordance with the interface displayed during testing. The model was used to process fabric images and the text prompt, followed by the output of fabric

parameters. Models associated with Qwen3-Max have long-context processing capability: according to the official description, the context window is 262,144 tokens, and the maximum output length can reach 65,536 tokens.

The function of the specified models in this work was limited to the parameter acquisition stage. The model extracted visual information from standardized images that was suitable for parametric inference; the prompt protocol defined the parameter names, units of measurement, admissible physical ranges, constraints, and output format; and the error evaluation method was used to compare the model output values with experimental reference values. With this organization, the comparison concerned not the open algorithmic structures of the models, but the parametric results obtained under the same visual data and the same textual constraints. Differences between model outputs mainly reflected their visual understanding capability, numerical stability, and physical consistency.

2.2.3 Image analysis software

Image preprocessing and extraction of grayscale-response indicators were performed using Adobe Photoshop and ImageJ. Adobe Photoshop was used for standardized preprocessing of the original images, including background removal, cropping, boundary cleaning, segmentation of garment panels, and selection of local structural regions. Adobe Photoshop was not used for quantitative measurements. Its function was to transform the original images into standardized input images with clear boundaries, a uniform background, and recognizable regions for subsequent analysis in ImageJ.

ImageJ was used for quantitative image analysis. After the processed images were imported into ImageJ, the following operations were performed sequentially: calibration of the analysis regions, conversion to an 8-bit grayscale image, threshold segmentation, threshold scanning, and extraction of grayscale-response indicators. The PLD analysis was not based on the external contour of the entire garment. Instead, the objects of analysis were structural regions selected on the frontal image, where the pleats were concentrated. These regions included the overall pleated region and two regions of interest (ROI): ROI-1 and ROI-2. For PLD images, the main grayscale-response indicators under changes in the pleating coefficient were as follows:

1) the percentage of bright area in the overall pleated region, $A_{overall}$. The overall pleated region was used to characterize the general response of the dress to pleating adjustment in the main pleated zone of the PLD on the frontal image.

2) the percentage of bright area in region of interest ROI-1, A_{ROI1}. ROI-1 was used to characterize the local grayscale response of the upper zone of pleat concentration along the seam joining the upper and lower parts.

3) the percentage of bright area in the selected ROI-2, A_{ROI2}. ROI-2 was used to characterize the local grayscale response of the zone where the pleats spread diagonally toward the hem and laterally.

4) the mean gray value in the corresponding bright-response region. The mean gray value was obtained from the statistical results in ImageJ and was used for auxiliary evaluation of the stability of the gray level in the bright-response region.

The same rules of image preprocessing, threshold scanning, and indicator extraction were applied to the three regions, ensuring the comparability of results between different fabrics, pattern levels, and analysis regions. Figure 2.4 shows the image used to define the object of PLD grayscale-response analysis, the overall pleated region, and the positions of the local ROIs.

a *b* *c* *d*

e *f* *g*

Figure 2.4 — Objects and analysis regions for characterizing the grayscale

response of the PLD:
a — pleats near the seam joining the upper and lower parts of the dress as ROI-1;
b — pleats in the zone of diagonal spreading toward the hem and laterally as ROI-2;
c — overall pleated region of the target PLD, combining the ROI-1 and ROI-2 zones;
d — original image of the target PLD before cropping;
e — PLD made from fabric F1;
f — PLD made from fabric F2;
g — PLD made from fabric F3.

As shown in Figure 2.4, ROI-1, ROI-2, and the overall pleated region were selected on the same frontal image of the PLD. ROI-1 is located in the upper zone of pleat concentration and reflects the local grayscale response formed by short pleats and dense pleat edges in the shoulder-to-bust region. ROI-2 is located in the zone of diagonal pleat spreading and reflects the grayscale response associated with longer diagonal pleats, changes in local curvature, and fabric deformation during draping. The overall pleated region covers the main structural zone of the frontal PLD image affected by pleat formation and is used to extract the overall grayscale response.

The selection of these pleat-form variants was determined by the need to verify the applicability of the newly developed drapeability evaluation method (Chapter 3) for predicting the ability of fabrics to form pleats on dress surfaces under different conditions:

1) under the action of gravity (Figure 2.2b);

2) under the action of a stitched seam (Figure 2.4a);

3) under conditions of free spreading within a limited area (Figure 2.4b).

The frontal PLD image was first processed in Adobe Photoshop to remove the background, clean the boundaries, and segment the structural regions. It was then imported into ImageJ and converted into an 8-bit grayscale image. The grayscale range was 0–255, where 0 corresponds to black and 255 to white. During threshold segmentation, pixels with a gray value equal to or higher than the specified threshold were assigned to the bright-response region, while pixels with a gray value below the specified threshold were assigned to the region without bright response. The bright-response region mainly corresponded to pleat ridges, fold lines, and continuously illuminated surfaces. Compared with dark regions, the bright region was less dependent on shadow depth, fabric light transmittance, and the influence of the black mannequin. Therefore, the grayscale response of the PLD pleat form was characterized primarily through the percentage of bright-area share.

After the grayscale threshold was set, ImageJ automatically calculated the percentage of the bright area based on the threshold segmentation result. The percentage of bright area in the overall pleated region was denoted as $A_{overall}$; this indicator characterizes the share of the bright-response area in the overall pleated region. The percentage of bright area in ROI-1 was denoted as A_{ROI1}; this indicator characterizes the share of the bright-response area within ROI-1. The percentage of bright area in ROI-2 was denoted as A_{ROI2}; this indicator characterizes the share of the bright-response area within ROI-2. All three indicators were expressed as percentages and used to describe the grayscale response of the PLD pleat form at the overall and local levels.

Because the fabrics differed in color depth, surface reflectance, texture brightness, and shadow distribution within the pleats, a single fixed threshold could not be directly applied to all PLD images. Therefore, threshold scanning was used in ImageJ to obtain a continuous relationship between the percentage of bright area and the threshold value. The normalized threshold-scanning curve was used to determine the main response interval and to exclude plateau sections at both ends of the curve. The Otsu threshold was used as an objective reference threshold based on the grayscale histogram; its algorithmic principle is given in source [165]. However, the Otsu threshold was not used as a single fixed threshold for all fabrics and all analysis regions. The final threshold was determined by considering the effective response interval of the scanning curve, the Otsu reference threshold, and the stability of the bright-response region.

In accordance with the stated rules for image preprocessing, region separation, threshold scanning, and indicator extraction, the PLD images formed a grayscale-response data structure that included fabric type, pattern level, analysis region, and threshold.

2.2.4 Software for statistics and data analysis

Experimental data processing, statistical analysis, and presentation of results were performed using IBM SPSS Statistics and Microsoft Excel. Excel was used for data entry, variable coding, basic statistical processing, and table formatting, while SPSS was used for statistical testing, model construction, and evaluation of statistical significance.

IBM SPSS Statistics was used for statistical data analysis, correlation analysis, regression modeling, and significance testing of the results of SFM drapeability tests, prediction of BD form parameters, evaluation of AI measurements, and correction of PLD patterns. Depending on the type of data and the aim of the analysis, Pearson correlation analysis, linear regression analysis, the t-test for comparing mean values, the Wilcoxon signed-rank test, and analysis of variance (ANOVA) were used. Pearson correlation analysis was used to evaluate linear relationships between DC_{SFM}, BD form parameters, PLD grayscale-response indicators, and pattern parameters. Linear regression analysis was applied to construct predictive models between input variables and output parameters. The t-test and Wilcoxon test were used to compare error distributions under different testing conditions or at different time points. ANOVA was applied to evaluate the influence of fabric type, the scheme of visual evidence, and model configuration on the error level.

Microsoft Excel was used for organizing raw data, grouping data, performing basic calculations, summarizing results, and preparing graphs. Microsoft Excel was used to organize experimental data and conduct basic calculations. Fabric codes, sample numbers, pattern levels, DC_{SFM}, BD form parameters, PLD grayscale-response indicators, AI measurement results, and laboratory reference values were entered, grouped, and checked in Excel. Excel was also used to calculate the mean value, standard deviation, coefficient of variation (CV), relative error, absolute percentage error (APE), mean absolute percentage error (MAPE), and selected summary statistics, as well as to generate the data tables required for statistical analysis and graph construction.

The stability of repeated measurements was characterized by the mean value, standard deviation, and CV. The mean value reflected the central tendency of repeated measurements within one group; the standard deviation characterized the absolute fluctuation of measured values relative to the mean; and CV indicated the relative variability of the standard deviation in relation to the mean value. Laboratory measurements and repeated test results were presented in the form "mean value ± standard deviation." When comparing parameters with different units of measurement or different orders of magnitude, CV was used to evaluate relative variability between data groups. For data with a mean value close to zero, CV may be overestimated; therefore, this indicator was applied mainly to repeated measurements with a stable positive mean value.

The error of an individual parameter measured by AI was evaluated using APE. APE was used to assess the relative deviation of an individual value obtained by AI from the laboratory reference value:

$$APE_i = \left| \frac{X_{AI,i} - X_{Lab,i}}{X_{Lab,i}} \right| \times 100\% \tag{2.2}$$

where APE_i is the absolute percentage error of the i-th parameter; $X_{AI,i}$ is the value of the i-th parameter measured by AI; and $X_{Lab,i}$ is the corresponding laboratory reference value. APE does not preserve the direction of the error and characterizes only the magnitude of deviation. The index i corresponds to the codes of the physico-mechanical fabric parameters ①–㉔ in Table 2.5.

The overall error of the set of parameters measured by AI was evaluated using MAPE. MAPE was calculated as the mean value of APE for all parameters evaluated under the same testing condition:

$$MAPE = \frac{1}{n} \sum_{i=1}^{n} APE_i \tag{2.3}$$

where $MAPE$ is the mean absolute percentage error of the set of parameters measured by AI; n is the number of parameters included in the evaluation; and APE_i is the absolute percentage error of the i-th parameter. For the complete vector of physico-mechanical fabric parameters, $n = 24$, corresponding to parameter codes ①–㉔. When an individual parameter group was evaluated, n corresponded to the actual number of parameters in that group.

MAPE was used to evaluate the overall measurement accuracy for different AI models, prompt versions, and visual-evidence schemes. Inter-fabric stability was characterized by the standard deviation of MAPE for different fabrics and the 95% confidence interval of the mean MAPE. The standard deviation of MAPE reflected fluctuations in the error of one testing scheme across different fabrics. The 95% confidence interval characterized the uncertainty of the mean MAPE with a limited number of fabrics studied. These statistical indicators were calculated in Excel or SPSS based on the MAPE data for the corresponding groups.

APE and MAPE were applied to evaluate the accuracy of AI measurement according to the codes of the physico-mechanical fabric parameters ①–㉔. Prediction of BD form parameters, modeling of the PLD grayscale response, and verification of pattern correction were evaluated using relative error, correlation coefficient, coefficient of determination, statistical significance level, and image similarity indicators, respectively.

2.3 Research Methods

2.3.1 Testing of the Physico-Mechanical Properties of Fabrics

Fabric testing was carried out to measure reference parameters. The test parameters included the following indicators.

1) Thickness. The thickness test was conducted in accordance with ASTM D1777-96 (2019) [161]. Fabric thickness was measured under a specified pressure at five locations on the same sample in order to obtain the mean value. The output parameter was fabric thickness T_f, expressed in mm.

2) Surface density (GSM). The GSM test was conducted in accordance with ASTM D3776 [160]. A fabric sample with a known area was weighed on an electronic balance, and the measured mass was converted into mass per unit area. Five samples were tested for each fabric, and the mean value was used as the reference value. The output parameter was mass per unit area G, expressed in g/m^2.

3) Tensile forces at small elongations in the warp, weft, and 45° bias directions. The tensile-force test at small elongations was conducted in accordance with ASTM D5034 [162]. A Metroteks MT 110-G tensile testing machine was used to record the load–elongation curves of the samples. Five repeated samples were tested in each direction. Tensile loads corresponding to elongations of 1, 2, 3, 4, and 5 mm were extracted from the automatically recorded curve. If the target elongation did not coincide with an original measurement point, the load value was determined by linear interpolation between two adjacent data points. The output parameters were

tensile forces at small deformations in the warp, weft, and bias directions, expressed in kgf (cN).

4) Bending parameters in the warp, weft, and 45° bias directions. The bending-related test was conducted using a modified cantilever method adapted from ASTM D1388 [163]. The device consisted of a horizontal platform, an inclined support surface, and two rulers for recording bending-related distance parameters. Samples were cut in the warp, weft, and bias directions and allowed to bend under the action of gravity. The contact distance was recorded as the horizontal distance from the edge of the platform to the first point of contact between the sample and the lower support. The travel distance was recorded as the horizontal distance required for the end of the sample to reach the inclined reference line. In this dissertation, the contact distance and the travel distance were treated as bending-related distance parameters.

5) Drape coefficient (*DC*). The circular drapeability test was conducted in accordance with ISO 9073-9:2008 [164]. A circular sample was placed on a Cusick drapemeter to form a natural drape profile under the action of gravity. The projected image of the sample was photographed from above and imported into ImageJ for scale calibration and projected-area measurement. The output parameter was the drape coefficient (*DC*), which characterizes fabric behavior on a traditional circular support.

Thickness, GSM, tensile forces at small elongations, and bending parameters were used as the input parameter set for constructing the fabric digital twin. DC was used as a traditional drapeability indicator for evaluating AI measurements and validating the new drapeability test [158–164].

All fabric samples were conditioned in a standard textile atmosphere before testing. The ambient temperature was 20 ± 2 °C, the relative humidity was 65 ± 4%, and the conditioning time was not less than 24 h [159]. The warp and weft directions were identified and marked before cutting the samples in order to ensure directional consistency during tensile, bending, and drapeability testing, as well as during photography. Samples were cut from different areas of each fabric to reduce the influence of edge effects, local defects, and local structural variations on the measurement results [158,159].

Figure 2.5 shows the sample schemes for the different tests.

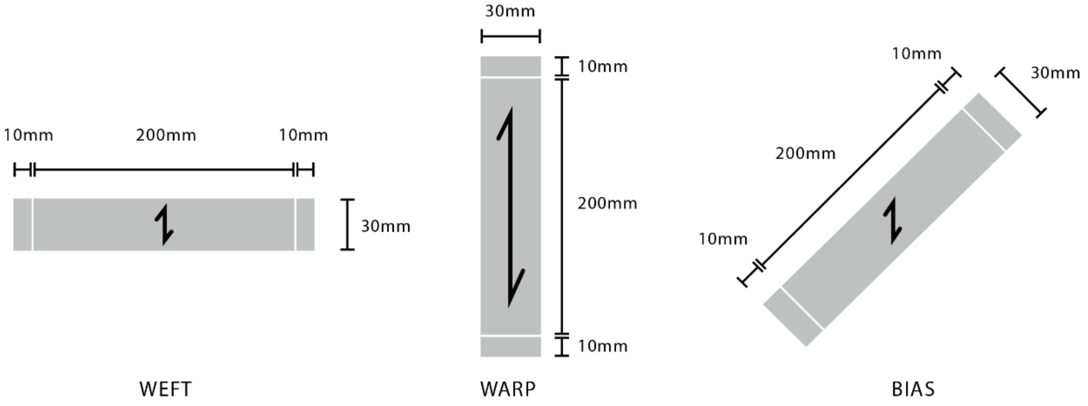

Figure 2.5 — Dimensions of physical samples prepared for GSM, thickness,

tensile, and bending tests

As shown in Figure 2.5, different physical property tests required different sample geometries and effective testing areas. Flat samples were used for the GSM and thickness tests. Samples for tensile and bending tests were cut in the warp, weft, and bias directions. A circular sample was used for the drapeability test, and the traditional circular drape coefficient (*DC*) was calculated from its projected area. Figure 2.6 shows the instruments and measurement principles used in the tests.

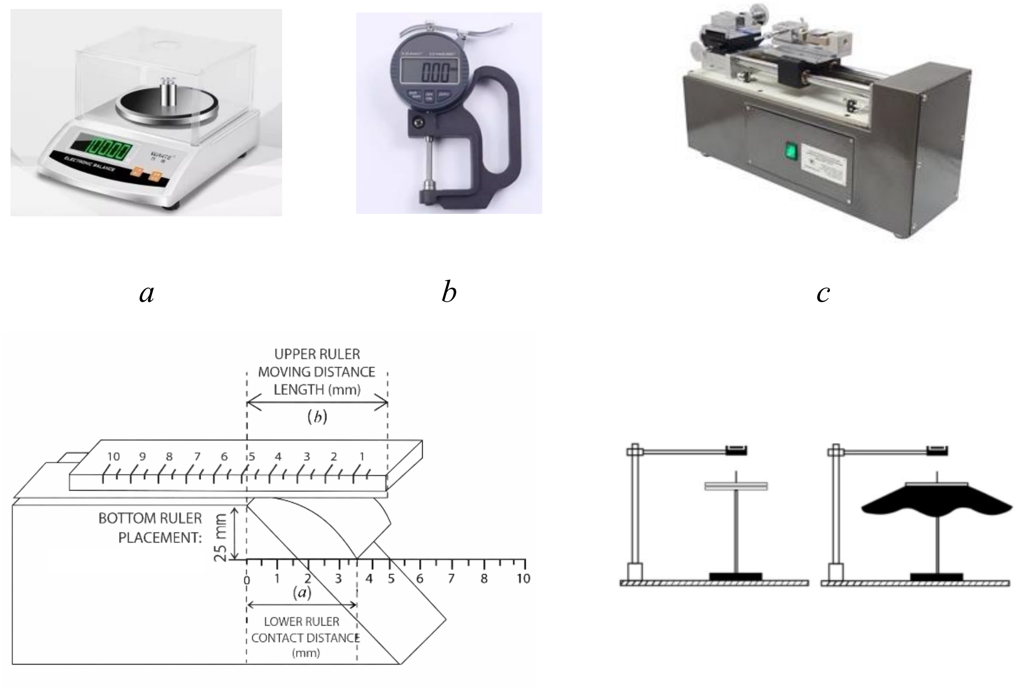

a *b* *c*

d *e*

Figure 2.6 — Instruments and measurement principles used in the tests:
a — GSM measurement;
b — thickness measurement;
c — tensile test;
d — bending test;
e — circular drapeability test.

Equation (2.4) shows the calculation of the circular drape coefficient *DC*:

$$DC = \frac{A_s - A_d}{A_D - A_d} \qquad (2.4)$$

where *DC* is the drape coefficient, A_s is the projected shadow area of the draped sample, A_d is the area of the support disk, and A_D is the total area of the original flat undraped circular sample.

The *DC* obtained using Equation (2.4) is a dimensionless parameter used to characterize fabric drapeability under the traditional circular support condition.

Table 2.5 shows the parameter coding system used to align physical reference values with AI measurement results.

Table 2.5 — Output Parameters Obtained During Physical Property Testing

Property	Measured Parameter	Measurement Direction	Unit	Parameter Code
Thickness	T_f	–	mm	①
GSM	*G*	–	g/m²	②
Tensile load at small deformations of 1–5 mm	1 mm	Warp	kgf (cN)	③
	2 mm			④
	3 mm			⑤
	4 mm			⑥
	5 mm			⑦
	1 mm	Weft		⑧
	2 mm			⑨
	3 mm			⑩
	4 mm			⑪
	5 mm			⑫
	1 mm	Bias 45°		⑬
	2 mm			⑭
	3 mm			⑮
	4 mm			⑯
	5 mm			⑰
Bending	Contact distance	Warp	mm	⑱
	Moving distance			⑲
	Contact distance	Weft		⑳
	Moving distance			㉑
	Contact distance	Bias 45°		㉒
	Moving distance			㉓
Drape coefficient	*DC*	–	–	㉔

This coding system prevents confusion between parameters with different units, directions, and physical meanings, and makes it possible to calculate MAPE through direct correspondence between each AI result and its corresponding physical reference. The symbol *DC* distinguishes the result of the traditional drapeability test from DC_{SFM}, obtained using the SFM method described in

Chapter 3.

2.3.2 Method for Predicting Basic Dress Form Parameters

The method for predicting basic dress form-generation parameters was used to establish a quantitative relationship between DC_{SFM} and the form parameters of the basic dress (BD). DC_{SFM} served as the input variable, while the basic dress parameters P_{d1}, P_{d2}, P_{d3}, and P_{d4} served as response variables. P_{d1}, P_{d2}, and P_{d3} characterized changes in the BD form in terms of length, frontal projected width, and inclination angle of the side contour, respectively, while P_{d4} characterized the drapeability coefficient at the hem level of the garment. This method made it possible to predict BD form parameters based on DC_{SFM} and to reduce the amount of work associated with the direct production or modelling of full garment samples.

The modelling data were grouped by fabric type and BD level. BD1–BD5 corresponded to five dress-length levels. Within each fabric group, the mean values of repeated DC_{SFM} measurements at one level were used as input values, while the mean values of P_{d1}, P_{d2}, P_{d3}, and P_{d4} for the corresponding BD level were used as form response values. This correspondence ensured consistency between the input DC_{SFM} values and the BD form levels and prevented data from different levels from being combined into a single overall mean value.

DC_{SFM} for medium-length samples was used for auxiliary evaluation of the transitional relationship between the draping response at the sample level and the draping response at the BD level, but it was not included in the prediction equations for P_{d1}–P_{d4} as an input variable. In the final prediction model, DC_{SFM} was used as the input variable, and P_{d1}, P_{d2}, P_{d3}, and P_{d4} were used as output parameters.

Correlation analysis was used to verify the presence of a statistical relationship between DC_{SFM} and the BD form parameters made from fabrics F1, F2, and F3. The objects of analysis were the relationships between DC_{SFM} and the parameters P_{d1}, P_{d2}, P_{d3}, and P_{d4}. Since each fabric included only five BD levels, the results of the correlation analysis were interpreted together with the quality of regression approximation and validation error. Based on the correlation analysis, linear regression models of the following form were obtained for each fabric F1, F2, and F3:

$$Pd = a \cdot DCSFM + b \tag{2.5}$$

where P_d is one of the form parameters P_{d1}, P_{d2}, P_{d3}, or P_{d4}; DC_{SFM} is the drape coefficient measured by the SFM method; and a and b are regression coefficients.

At the validation stage, DC_{SFM} was used as the input variable. After substituting DC_{SFM} into the corresponding regression equation for the given fabric, predicted values of P_{d1}, P_{d2}, P_{d3}, and P_{d4} were obtained. The predicted values were compared with the measured form parameters of the validation basic dress (VD) to verify the adequacy of the equations.

2.4 Evaluation and Validation Methods

2.4.1 Method for Evaluating Parameter Prediction Consistency and Statistical Testing

The method for evaluating parameter prediction consistency and statistical testing was used to assess the consistency between predicted and measured values, as well as to determine statistical differences between parameters or error distributions under different experimental conditions. The prediction results for BD form parameters were evaluated using relative error (RE). The linear relationship between DC_{SFM} and BD form parameters was evaluated using Pearson correlation analysis. The degree of approximation of the regression model was characterized by the coefficient of determination R^2. Differences between the results of virtual and physical tests were evaluated using the independent-samples t-test. AI measurement errors obtained at different time points or with different model versions were compared using the Wilcoxon signed-rank test. The influence of the type of visual evidence, fabric type, and their interaction on AI measurement error was evaluated using analysis of variance.

The prediction consistency of the BD form parameters P_{d1}, P_{d2}, P_{d3}, and P_{d4} was expressed through RE. The calculation was performed as follows:

$$RE = \frac{P_{\mathrm{pre}} - P_{\mathrm{mea}}}{P_{\mathrm{mea}}} \times 100\% \tag{2.6}$$

where RE is the relative error; P_{pre} is the predicted value of the BD form parameter; and P_{mea} is the corresponding measured value. When $RE > 0$, the predicted value is higher than the measured value; when $RE < 0$, the predicted value is lower than the measured value.

Pearson correlation analysis was used to evaluate the strength of the linear relationship between DC_{SFM} and the parameters P_{d1}, P_{d2}, P_{d3}, and P_{d4}. The correlation coefficient reflected the degree of linear association between variables, while the significance level was used to determine the statistical significance of this relationship within the studied sample. Since each fabric included only five BD levels, the correlation coefficient and p-value were interpreted together with the distribution of points, the degree of regression approximation, and the validation error.

Linear regression analysis was used to establish the predictive relationship between DC_{SFM} and BD form parameters. The degree of approximation of the regression model was evaluated using R^2.

Mean differences between the results of virtual and physical tests were evaluated using the independent-samples t-test. When the assumption of homogeneity of variances was satisfied, the independent-samples t-test with equal variances was used. When the assumption of homogeneity of variances was violated, interpretation was performed using the Welch correction. The significance level was set at $p < 0.05$.

Error distributions at different time points or for different AI model versions were evaluated using the Wilcoxon signed-rank test. APE values obtained for the same fabric, the same sample group, and the same parameter position were used as paired data. This test was applied to determine whether a systematic change occurred in the error distribution between two testing conditions. The Wilcoxon signed-rank test does not require a normal distribution of paired differences and is therefore suitable for comparing AI measurement errors between time points or model versions.

The influence of fabric type, visual-evidence type, and their interaction on APE was evaluated using analysis of variance. Parameter category could be used as a grouping or control factor to reduce the influence of differences in parameter dimensionality and baseline error level. The results of analysis of variance were interpreted according to the p-value and effect size. If the assumptions of homogeneity of variances or residual distribution were not sufficiently satisfied, the results of analysis of variance were considered as characteristics of factor-effect tendencies and were interpreted together with descriptive statistics or nonparametric tests.

Thus, the specified statistical methods were applied to different evaluation objects:

1) RE for evaluating the prediction error of BD form parameters,

2) Pearson correlation analysis and R^2 for evaluating the linear relationship and degree of approximation between DC_{SFM} and BD form parameters,

3) the t-test for comparing the results of virtual and physical SFM tests,

4) the Wilcoxon signed-rank test and analysis of variance for comparing AI measurement error distributions and analyzing factor effects.

2.4.2 Method for Verifying Geometric Consistency of the Contour and Local Regions

The method for verifying geometric consistency of the contour and local regions was used to evaluate the geometric correspondence between the reference object and the validation object on a two-dimensional projection plane. Binary foreground masks were used as the objects of comparison. The method was applied to evaluate the degree of overlap and boundary deviation of the overall dress silhouette, the contour of the waist–hip region, the local shoulder region, and the control region of the upper part. This geometric ROI was a binary region and was not used to evaluate gray values, texture structure, or bright response.

The reference image and the validation image were converted into binary foreground masks under the same view and scale. The binary mask of the reference object was denoted as M_{ref}, and the binary mask of the validation object was denoted as M_{val}. When evaluating the overall silhouette, M_{ref} and M_{val} represented the complete foreground region of the dress. When evaluating local regions, they represented the corresponding binary ROI regions. Before mask comparison, spatial alignment was performed by translation, without additional scaling, stretching, or correction of non-rigid deformations.

The degree of regional overlap between the reference and validation masks was evaluated using the intersection over union (IoU). IoU corresponds to the definition of the Jaccard index and is used to evaluate the ratio of the intersection area of two binary regions to their union area; the closer the value is to 1, the higher the degree of overlap between the two regions [167]. In this work, IoU was used to evaluate the degree of correspondence between the two-dimensional projection of the reference object and the validation object in the overall contour or local ROI.

The Dice coefficient was used as an additional overlap indicator to clarify the degree of correspondence between two binary regions. Like IoU, the Dice coefficient belongs to regional overlap metrics and is suitable for evaluating spatial consistency between binary segmentation results [167]. In contour verification, the Dice coefficient was used together with IoU to evaluate the degree of overlap between the reference and validation masks.

Expansion or shrinkage of the validation mask relative to the reference mask was evaluated using the relative area difference. This indicator belongs to region-size difference metrics and is used to determine whether the validation object has a larger or smaller area than the reference object [167,168]. A positive value of the relative area difference indicates that the area of the validation region is larger than that of the reference region, while a negative value indicates a decrease in the area of the validation region relative to the reference. This indicator preserves the direction of area change and is suitable for evaluating the general tendency of expansion or shrinkage of the validation contour relative to the reference contour.

Boundary deviation was used to describe the spatial difference between the reference and validation boundaries. The boundary deviation results were expressed as the mean boundary deviation, the 95th percentile boundary deviation, and the maximum boundary deviation. The mean boundary deviation reflected the overall level of boundary displacement, the 95th percentile characterized the upper range of deviations for most boundary points, and the maximum deviation was used to identify the most pronounced local boundary inconsistency.

The ROI for geometric consistency and ROI-1 and ROI-2 for PLD grayscale-response analysis had different meanings. The ROI for geometric consistency was based on binary contours or local binary regions and was used to calculate IoU, the Dice coefficient, relative area difference, and boundary deviation. ROI-1 and ROI-2 were based on grayscale image regions and were used for threshold scanning, extraction of the bright-area percentage, and evaluation of structural similarity. Therefore, verification of geometric consistency of the contour and local regions reflected only the spatial correspondence of the two-dimensional projection contour or local binary region and did not replace the evaluation of grayscale response or textural structural similarity.

2.4.3 Method for Verifying Equivalent Response and Structural Similarity

The method for verifying equivalent response and structural similarity was used to evaluate the consistency of grayscale response and local structural similarity between the target PLD and the validation PLD in key pleated regions. The overall pleated region, ROI-1, and ROI-2 were used as analysis regions. The overall pleated region was applied to evaluate the closeness of the general grayscale response in the main pleated zone, while ROI-1 and ROI-2 were used to evaluate the consistency of grayscale response and structural texture at different local structural positions.

Frontal images of the target PLD and validation PLD were converted into 8-bit grayscale images according to the image-processing procedure defined in Section 2.2.3. The overall pleated region, ROI-1, and ROI-2 were then selected according to the same rules. The percentage of bright area in the target PLD within a specified analysis region was denoted as A_{tar}, while the percentage of bright area in the validation PLD within the corresponding region was denoted as A_{val}. If the analysis region was the overall pleated region, this indicator corresponded to $A_{overall}$. If the analysis region was ROI-1 or ROI-2, the indicator corresponded to A_{ROI1} or A_{ROI2}.

The grayscale response of the target PLD and validation PLD was compared based on the principle of equivalent thresholds. Equivalent thresholds do not require the same fixed threshold to be used for both images. Instead, within the corresponding admissible threshold ranges, threshold combinations were selected that produced close values of the bright-area percentage. This approach accounted for gray-level differences caused by fabric color, gloss, and shadow distribution, while requiring similarity in the segmented bright-response area of the pleats. At the same time, the threshold-shift range was recorded to avoid artificially reducing response differences through arbitrary threshold selection. The difference in grayscale response between the target PLD and validation PLD in the same analysis region was calculated as follows:

$$D_{\mathrm{resp}} = | A_{\mathrm{val}} - A_{\mathrm{tar}} | \qquad (2.7)$$

where D_{resp} is the grayscale-response difference, expressed in percentage points; A_{tar} is the percentage of bright area in the target PLD within the corresponding analysis region; and A_{val} is the percentage of bright area in the validation PLD within the same analysis region. The smaller Dresp is, the closer the bright grayscale response of the target PLD and validation PLD in that region. The larger D_{resp} is, the more pronounced the difference in grayscale response. This indicator was used to evaluate response consistency based on the bright-area share and was not applied to evaluate the MAPE of AI-measured parameters or the geometric overlap of the overall garment contour.

In addition to the grayscale-response difference, threshold shift and response tendency were used as auxiliary indicators for evaluating the validity of the equivalent response. Threshold shift reflected the difference between the thresholds required for the target and validation images to obtain a close area-based response. Response tendency was used to determine whether the direction of change in the bright-area percentage was consistent between the target PLD and validation PLD under different pattern levels or different correction schemes. If the directions of change between adjacent levels were consistent, the tendency of the grayscale response in the corresponding region was considered consistent. If the directions of change were inconsistent, this indicated a local response difference in that region.

Local structural similarity was evaluated using the structural similarity index measure (SSIM). SSIM was calculated according to the standard method proposed by Wang et al. [166] and was used to compare the local structure of grayscale images between the target PLD and validation PLD in ROI-1 and ROI-2. SSIM considers luminance, contrast, and structure. A value close to 1 indicates higher overall similarity between two local grayscale images. The object evaluated by SSIM was the two-dimensional grayscale ROI image; this indicator did not directly evaluate the three-dimensional form of the garment, the stress state of the fabric, or the magnitude of pattern correction.

The luminance, contrast, and structure components of SSIM were used to explain the sources of changes in local similarity. The luminance component reflected the closeness of the mean gray level of the two ROIs. The contrast component reflected the closeness of the amplitude of light–dark variation. The structure component reflected the consistency of local pleat texture, gray-level distribution, and the direction of structural response. These three components were used as auxiliary indicators for interpreting SSIM results and were not applied separately as criteria for complete consistency of the PLD form.

Equivalent response and SSIM corresponded to two different validation levels. Equivalent response was used to determine whether the target PLD and validation PLD formed a close bright-area response in the overall pleated region, ROI-1, and ROI-2. SSIM was used to determine the similarity of the local grayscale structure in ROI-1 and ROI-2. The first level emphasized consistency in the magnitude of grayscale response, while the second emphasized consistency in the local image structure. The combined use of these indicators made it possible to evaluate the consistency of the visual response between the target object and the validation object after PLD pattern correction.

CHAPTER 3. DESIGN AND IMPLEMENTATION OF A NEW DEVICE FOR DRAPEABILITY TESTING

3.1 Justification and Modelling of a Virtual Anthropomorphic Drapemeter

3.1.1 Justification of the Need for a New Device

Traditional virtual drapeability tests usually use simplified geometric supports, such as spherical, cylindrical, and conical stands. Under these conditions, a fabric sample deforms under the action of gravity, and the drape coefficient (*DC*) is calculated from the projected area after draping. Such stands provide stable and reproducible support boundaries for basic drape simulation. However, they are idealized geometric surfaces. The support line, contact curvature, and method of sample fixation differ substantially from the conditions associated with the shoulder-girdle region, where clothing is formed on the human body. Therefore, the *DC* obtained on such geometric stands mainly reflects the drapeability state of a flat sample under simplified support conditions, rather than the behavior of fabric in garments under body-oriented boundary constraints [172].

Figure 3.1 shows the virtual geometric stands used for preliminary comparison.

a *b* *c*

Figure 3.1 — Virtual geometric supports used for preliminary comparison of drapeability: *a* — spherical support in CLO 3D; *b* — cylindrical support in Style3D; *c* — conical support in Style3D

As shown in Figure 3.1, the three virtual supports represent typical simplified three-dimensional supports. The spherical support provides a continuous curved surface, the cylindrical support provides a curved support of a linear type, and the conical support provides an inclined support. Although these supports can form visible drape contours, their boundary conditions are defined by regular geometric primitives rather than by body morphology. Therefore, they are more suitable for basic comparison of drape states.

To verify whether geometric supports make it possible to distinguish the influence of fabric structure, three types of samples differing in yarn direction and joining seam type were tested using the same virtual draping procedure. DC was calculated from the projected area after draping. Table 3.1 shows the DC and CV values obtained for two-piece samples joined by seams on spherical, conical, and cylindrical supports.

Table 3.1 — DC and CV Values of Samples on Virtual Geometric Supports

Sample Structure	Drape Coefficient *DC*		
	Sphere	Cone	Cylinder
Warp–Warp + flat seam	0.44	0.48	0.43
Warp–Weft + overlaid seam	0.43	0.47	0.42
Warp–Weft + flat-fell seam	0.41	0.49	0.41
Mean	0.43	0.48	0.42
CV,%	0.07	0.04	0.05

As shown in Table 3.1, the spherical support provided the highest CV, equal to 0.07, whereas the CV values for the conical and cylindrical supports were 0.04 and 0.05. However, the DC range within each support remained narrow. This means that regular geometric supports are capable of forming a measurable drape contour, but they do not provide sufficient differentiation in the indicators and do not reflect the influence of sample cutting direction and seam structure.

The limitation revealed by the comparison of geometric supports lies not in the absence of drape deformation in the virtual environment, but in the mismatch between simplified support contact surfaces and the real conditions of garment draping. In real garments, fabric drape is constrained by the shoulder line, shoulder slope, local contact with the upper body, stiffness of the shoulder seam, and the relative orientation of the front and back sample pieces. These factors influence the initial position of sample form generation, the path of force transmission, and the expansion of the lower edge. Therefore, a drapemeter intended for evaluating fabric under conditions that simulate garment behavior must not only allow the fabric to hang naturally under gravity, but also reproduce a shoulder-like support surface of the human figure.

Based on this requirement, the contact surface between the garment and the human shoulder was selected as the main morphological basis of the new virtual drapemeter. Compared with spherical, conical, and cylindrical supports, the shoulder support boundary is more suitable for the new SFM testing system because it introduces garment-related structural constraints, including the position of the shoulder seam, the relationship between the front and back sample pieces, the arrangement of yarn direction, and the expansion of the lower edge. Accordingly, the new virtual drapemeter was modeled not on the basis of a regular geometric primitive, but on the basis of a standardized shoulder-support surface.

3.1.2 Modeling of the Virtual Drapemeter and Determination of Geometric Parameters

After the shoulder support boundary had been defined as the basis for modeling the new drapemeter, the virtual drapemeter was constructed using data from the Chinese sizing system for women’s clothing, with size 160/84A [169] used as the reference body size. The support form did not copy the shoulder region of a specific body figure, but synthesized the characteristics of the shoulder regions of 10 female virtual bodies (160/76Y–160/100C). Through local extraction, measurement of sectional parameters, and averaging, a standardized shoulder-support surface was obtained. This procedure preserved the basic curvature characteristics of the support boundary of the human shoulder while reducing the influence of individual body morphology on the testing boundary. Figure 3.2 shows the process of generating the shoulder region and determining the geometric parameters of the virtual shoulder-support surface.

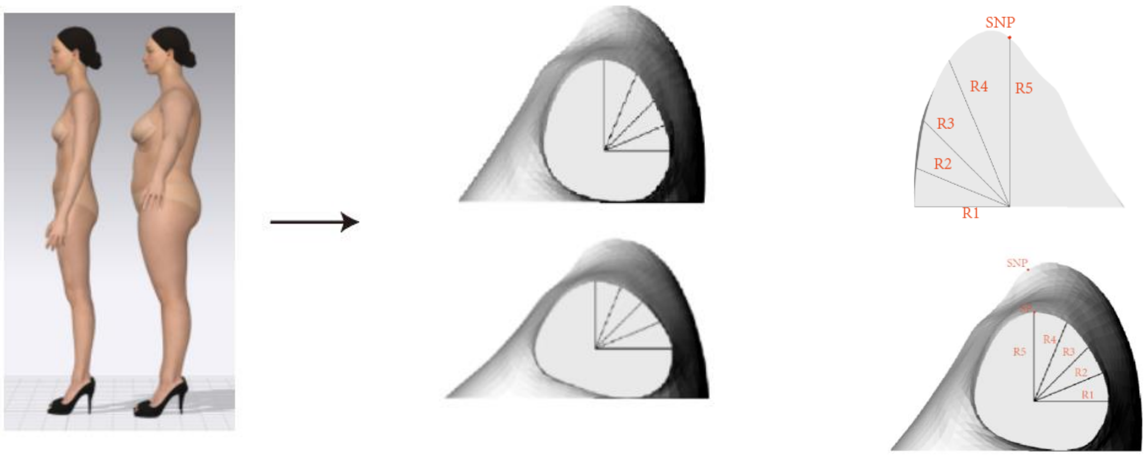

a *b*

Figure 3.2 — Extraction and parametric definition of the virtual shoulder-support surface:
a — virtual figures of different size grades and the selected shoulder region;
b — definition of the geometric parameters of the support surface

As shown in Figure 3.2, the modeling process included four sequential stages.

First, female virtual figures covering different size variants according to the Chinese women's clothing sizing system were created in CLO 3D.

Second, the models in OBJ format were imported into Rhinoceros 7, where the human body mesh was segmented and converted into a NURBS surface (non-uniform rational B-spline) for subsequent geometric extraction and surface reconstruction.

Third, the shoulder and neck support region was selected according to key anthropometric points. The width of the support structure was determined by the distance from the side neck point (SNP) to the shoulder point (SP), while the height was determined by the distance from the SNP to the lower boundary of the armhole.

Finally, the selected shoulder surfaces were measured and averaged within a unified system of sectional parameters, which made it possible to reconstruct the virtual shoulder-support surface. Figure 3.2*a* shows examples of female virtual figures of different sizes, while Figure 3.2*b* shows vertical sections through the SP and SNP and the measurements R1–R5 used for geometric standardization.

To define a stable geometric boundary of the virtual support, vertical sections through the SP and SNP were selected as the main control sections. Five radius parameters, R1–R5, were defined on each section. The angular interval between adjacent radii was set at 22.5° to describe the change in curvature from the lower boundary of the support surface to the upper region. The shoulder line was described by two parameters: surface length and linear distance, making it possible to distinguish the curvilinear measurement length along the shoulder surface from the spatial straight-line distance between two control points. Table 3.2 shows the averaged values of these parameters.

Table 3.2 — Averaged Geometric Parameters of the Virtual Shoulder-Support Surface

Radius of Cross-Section at SP, mm					Radius of Cross-Section at SNP, mm					Shoulder Line, mm	
R1	R2	R3	R4	R5	R1	R2	R3	R4	R5	Surface distance	Linear distance
68.3	66.4	68	75	78.7	105.6	111.9	130.7	162.2	165.8	128.54	124.32

As shown in Table 3.2, compared with the section through the SP, the R1–R5 values in the SNP section were generally larger, which corresponds to the morphology of female figures. The surface length of the shoulder line was 128.54 mm, while the linear distance was 124.32 mm. The difference of 4.22 mm shows that the shoulder line was not a simple straight connection, but represented a spatial trajectory with a certain degree of curvature along the shoulder–neck surface. Together, these parameters defined the width, height, and curvature of the virtual shoulder-support surface for the virtual drapeability test.

Based on the geometric parameters presented in Table 3.2, the virtual shoulder-support surface was reconstructed in Rhinoceros 7 and imported into Style3D in OBJ format. The reconstructed model was used as a virtual drapemeter for subsequent SFM tests. Figure 3.3 shows the final form of the virtual shoulder support in Style3D.


a *b* *c* *d*

Figure 3.3 — New virtual shoulder support generated in Style3D: *a* — front view; *b* — left view; *c* — back view; *d* — right view

The virtual drapemeter provides a unified geometric boundary for sample design, sample placement, and DC_{SFM} measurement. Compared with regular geometric supports (Figure 3.1), the new support introduces garment-related boundary conditions into the virtual environment, including the shoulder line, shoulder slope, side neck point, shoulder point, and lower armhole boundary.

These conditions allow the sample to form a draping morphology closer to the natural state of fabric on the support surface of a body figure. The new method was named the Shoulder Fitting Method (SFM).

3.2 Design and Implementation of the Physical Prototype of the Drapemeter Based on the New Method

After the virtual shoulder-support surface had been modelled and its geometric parameters determined, the virtual drapemeter was further fabricated as a physical prototype using 3D printing. The physical drapemeter was designed to preserve the characteristics of the support surface during sample draping. Figure 3.4 shows the front view, side view, and auxiliary laser device.

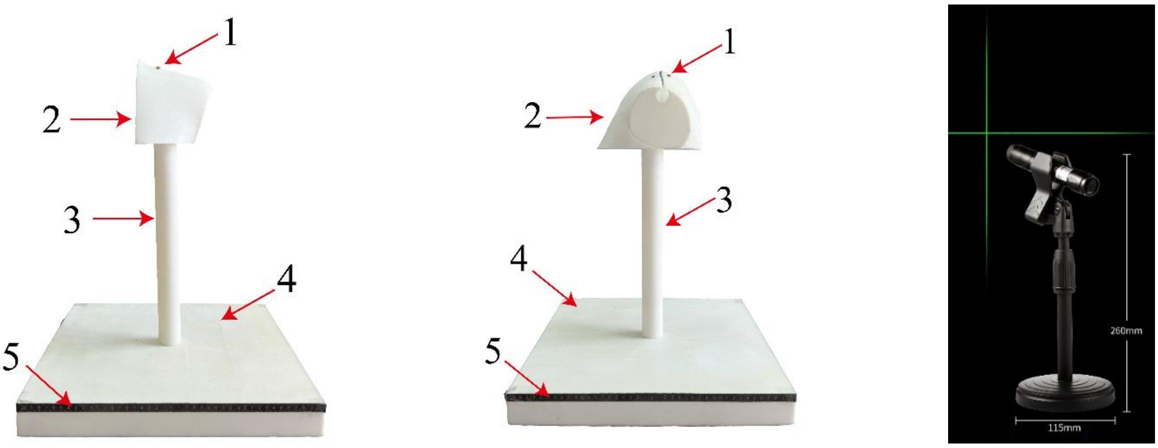

a *b* *c*

Figure 3.4 — Physical prototype of the drapemeter and auxiliary measuring device: *a* — front view; *b* — side view; *c* — auxiliary laser reference device

As shown in Figure 3.4, the physical drapemeter consists of five main parts, while the auxiliary laser reference device is used as a separate auxiliary measuring tool. Label 1 corresponds to the magnet, 2 to the support, 3 to the threaded modular support column, 4 to the base, and 5 to the ruler along the front edge. The magnet is located in the upper part of the support and serves to stabilize the initial position of the sample during placement and to reduce local displacement before the sample is released. The support is the main testing interface, which directly provides a shoulder-like boundary support for the sample. The support length is 124.04 mm, the width is 197.04 mm, and the height is 142.44 mm. These dimensions correspond to the geometric logic of the virtual body surface, so that the support boundary used in the physical test remains consistent with the boundary used in the virtual test. The threaded modular support column connects the support and the base. Each column section is 35 cm long, and four sections are provided so that the support height can be adjusted according to the required sample length and the available hanging space. The base measures 40 cm × 40 cm × 5 cm, providing a stable horizontal foundation for the drapemeter and reducing the influence of device displacement during sample draping. The ruler along the front edge is placed along the front edge of the base and serves as a linear reference for recording the hem width.

As shown in Figure 3.4c, the auxiliary laser reference device has a height of 260 mm and a base width of 115 mm, and provides two intersecting laser beams: one horizontal and one vertical. The vertical laser beam can be used to evaluate deviation of the sample centerline or side contour, while the horizontal beam is used to determine the height of the hem line and the position of local reference points. The use of the auxiliary laser reference device improves the consistency of sample alignment and geometric measurements during physical testing.

During the test, the sample is first placed on the support so that its upper support region contacts the shoulder-like curved surface. The magnet stabilizes the initial state of the sample at the moment of contact and prevents noticeable displacement before the sample is released. After release, the sample drapes naturally under the action of gravity. The ruler along the front edge is used to measure the width at the lower edge, while the laser device is used to measure horizontal and vertical dimensions.

3.3. Test Specimens

The samples for evaluating drapeability included the standard Cusick circular sample and new samples for the developed Shoulder Fitting Method (SFM) test rig. The standard Cusick circular sample was a flat circular sample, and the circular drape coefficient (*DC*) was obtained on the basis of this test. This sample served as the traditional reference for evaluating fabric drapeability.

The SFM samples included a short sample (SS), a long sample (LS), and a one-piece dress-shaped sample. The short sample SS was formed by joining two pieces in the shoulder region and was used to model the influence of garment shoulder seams, stiffness, and the direction of fabric draping. Three shoulder seam structures were designed for the SS: s_1 — plain seam, s_2 — lapped seam with enclosed edges, and s_3 — flat-felled seam. The long sample LS was created on the basis of the SS by increasing its length and width in order to form an intermediate form between the SS and the dress. The one-piece sample had three lower-edge treatment variants, h_1, h_2, and h_3, to compare the influence of hem construction on the drape contour in the absence of a shoulder seam. Figure 3.5 shows the structural forms and design variables of the samples.

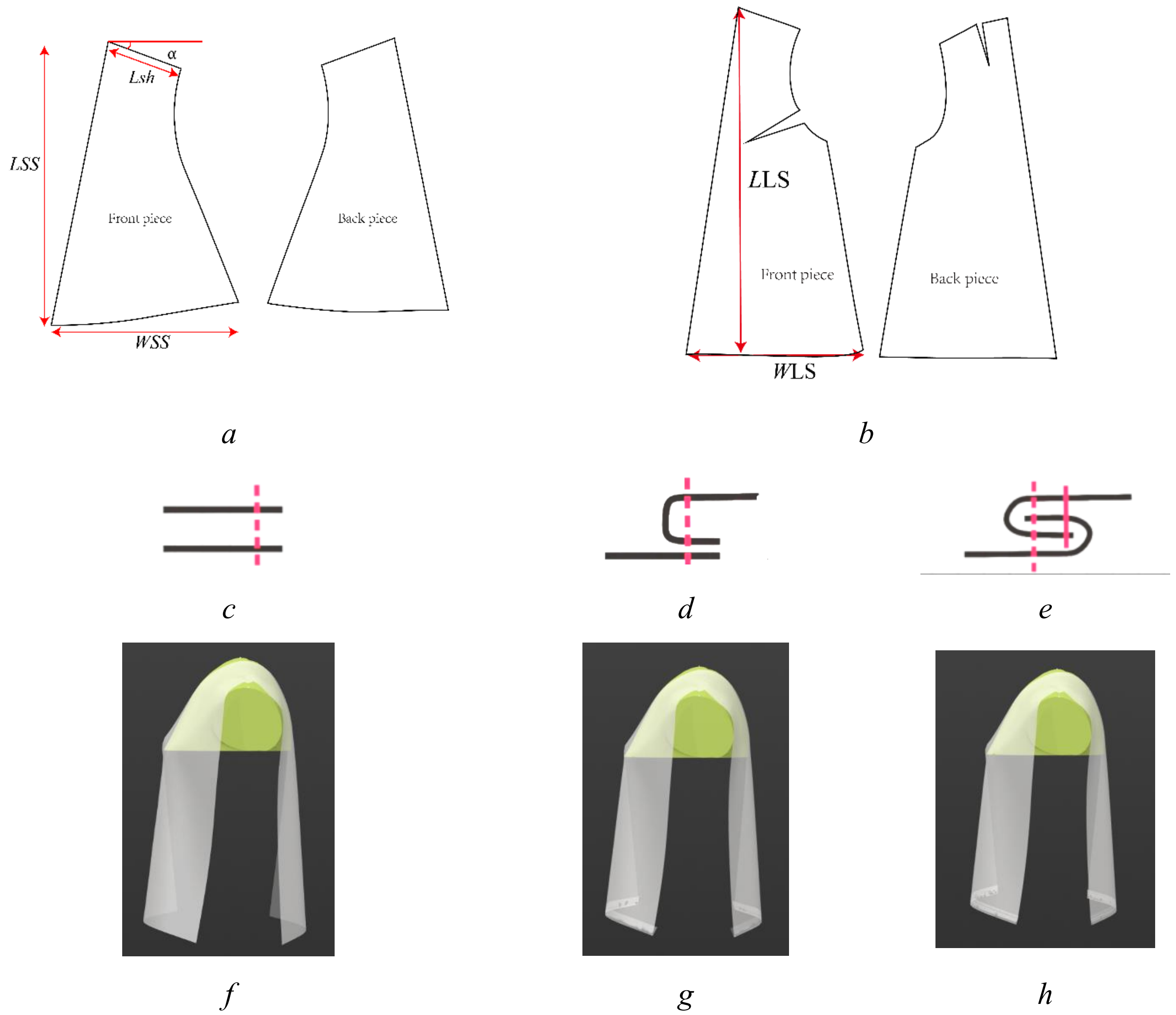

Figure 3.5 — Geometric forms and local design variables of the samples: *a* — SS; *b* — LS; *c* — s_1 plain seam; *d* — s_2 lapped seam with enclosed edges; *e* — s_3 flat-felled seam; *f* — h_1 lower edge without hemming; *g* — h_2 lower edge with folded edge; *h* — h_3 lower edge with a hemmed seam

As shown in Figure 3.5, the SS and LS performed different testing functions. The SS was used as the basic sample structure for testing drapeability by the SFM method, with a focus on the influence of shoulder slope angle, sample width, shoulder seam structure, and cutting direction. The LS extended the SS in length and width, allowing the test object to transition toward a more hanging form closer to a garment. The seam structures s_1, s_2, and s_3 introduced different local stiffness conditions along the shoulder seam. The lower-edge treatments h_1, h_2, and h_3 were used only for the one-piece sample so that the effect of hem treatment could be observed without the influence of a shoulder seam.

After determining the structural forms of the samples, their parameters, variation levels, and experimental functions had to be fixed. Table 3.3 shows the sample types and corresponding design variables.

Table 3.3 — Functions of Samples

Sample Type	Parameter	Symbol	Value or Type	Parameter Status
Circular sample	Diameter	-	30 cm	Fixed
SS	Sum of the front and back shoulder slope angles	α	20°, 25°, 30°, 35°, 40°	Variable
	Shoulder cut length	L_{sh}	12 cm	Fixed
	SS length	L_{SS}	45 cm	Fixed
	SS width	W_{SS}	21, 25.2, 29.4, 33.6, 37.8, 42 cm	Variable
	Shoulder seam structure	s	s_1 — plain seam; s_2 — lapped seam with enclosed edges; s_3 — flat-felled seam	Variable
	Cutting direction	o	o_1 — warp direction; o_2 — weft direction; o_3 — bias direction	Variable
One-piece sample	Lower-edge treatment	h	h_1 — lower edge without hemming; h_2 — folded lower edge; h_3 — hemmed seam	Variable
LS	LS length	L_{LS}	45, 55, 65, 75, 85 cm	Variable
	LS width	W_{LS}	25, 29, 32, 35, 38 cm	Variable

As shown in Table 3.3, the circular sample, SS, one-piece sample, and LS corresponded to different testing purposes. The circular sample was used to obtain the traditional *DC* reference. The range of shoulder-seam slope angles for the SS was set within 20–40°, derived from the range of front and back shoulder angles in basic pattern drafts. An interval of 5° was used to form a controlled gradient of shoulder slope. The shoulder length L_{sh} was set at 12 cm according to the average length of the human shoulder. The SS length L_{SS} was set at 45 cm to correspond to the shoulder-to-waist distance and to provide sufficient space for natural draping. The width W_{SS} was derived from the range of bust proportions, and the lower-width values from 21 cm to 42 cm represented variation from narrow to wider forms.

The shoulder seam structure was used to compare differences in local stiffness caused by different seam constructions. The cutting direction o was selected as warp, weft, and bias directions to study the influence of fabric anisotropy. The one-piece sample did not contain a shoulder seam and had different lower-edge treatments. Therefore, h_1, h_2, and h_3 were not used as variables for predicting garment form, but served as structural control parameters under conditions without a shoulder seam. The LS length and width were organized as paired size levels rather than as full factorial combinations in order to form a transitional scale from the SS drape state to dress drape.

According to Table 3.3, the SS sample group consisted of three fabric types, five levels of shoulder slope angle, six width levels, three shoulder seam structures, and three cutting directions, forming 3 × 5 × 6 × 3 × 3 = 810 combinations. The one-piece sample included three structural variants according to the three lower-edge treatments. The LS group consisted of three fabric types and five paired levels of length and width, forming 3 × 5 = 15 combinations. The circular sample was cut from each tested fabric and was used only to obtain the traditional *DC* reference.

3.4 Formation of the Drapeability Testing Algorithm Based on the New Method

3.4.1 Formation of the Algorithm in the Virtual Environment

The key task was to determine how the sample should be positioned, how a stable draped state should be achieved, and which geometric parameters should be measured to calculate DC_{SFM}. Unlike the traditional drapeability method based on a circular disk, the SFM support is neither a horizontal disk nor a regular geometric support, but a curved support surface that imitates the shoulder region of the human body. Therefore, the measurement system could not simply follow the *DC* calculation algorithm based on projected area. For this reason, the measurement schemes for the SS and LS samples had to be defined according to their spatial characteristics.

To ensure consistency of the initial state of the SS in the virtual test, the position of the virtual sample on the SFM support was controlled using the Arrange Point function in Style3D. Arrange Point is not a measurement point for DC_{SFM} and does not participate in the subsequent calculation of parameters; it is used only to define the initial spatial position of the sample before it is released under the action of gravity. In the virtual test, ArrangePoint1 and ArrangePoint2 were defined to control the initial positions of the front and back parts of the SS on the two sides of the SFM support, respectively.

The positions of the placement points were determined according to the geometry of the shoulder-support zone and the arrangement of the front and back parts of the SS relative to this zone. The distance between ArrangePoint1 and ArrangePoint2 was 24 cm, which ensured a constant spatial interval between the two parts in the shoulder-support zone. Each placement point was set at the center of the corresponding placement plane, and the distance from the point to this plane was 5 cm. This clearance prevented the sample from intersecting with the support or the placement plane in the initial state and reduced the influence of accidental contact before the start of simulation.

This setup reduced random displacement, rotation, and local pre-stretching of the virtual sample, ensuring comparable initial boundary conditions for different SS samples. After the sample was released, the placement points did not restrict the free draping of its lower part; therefore, the stabilized form was determined by the fabric parameters, sample structure, and the SFM shoulder-support boundary. Figure 3.6 shows the initial placement of the SS on the SFM support and its stabilized draped state.

a *b*

Figure 3.6 — Fixed placement position and stabilized draped state of the SS: *a* — initial placement of the SS in the fixed position; *b* — stabilized draped state of the SS

As shown in Figure 3.6, ArrangePoint1 and ArrangePoint2 define the initial spatial correspondence between the SS and the SFM support. In Figure 3.6a, the front and back parts of the SS are located on the two sides of the shoulder-support zone, and the shoulder-joining region of the sample maintains stable correspondence with the support. This placement forms the same initial position for the samples before the simulation is started.

Figure 3.6b shows the state of the SS after it has reached a stable draped form under the action of gravity. At this stage, the placement points are no longer objects of result interpretation; instead, the sample morphology characterizes natural hanging, expansion in the front–back direction, changes in lower-edge width, and bending of the edge contour under the specified shoulder-support boundary. Therefore, Figure 3.6 is used to explain the logic of the virtual test: initial placement, release of the sample for draping, and subsequent measurement after stabilization.

After the SS reached a stable draped state, the measurement task was transformed into the extraction of geometric parameters. In preliminary virtual tests, three candidate measurement methods were compared:

Method I was based on the ratio between the support area and the projected area of the sample;

Method II was based on the ratio between the original area of the flat sample and the projected area;

Method III combined the change in the maximum front–back distance with the change in the mean lower-edge width.

The numerical range, mean value, and CV for the three methods were used to determine the best measurement method for the SS. Table 3.4 compares the candidate measurement methods for the SS.

Table 3.4 — Candidate Measurement Methods for the SS

Test Method		Equation	No.	Result			
				Min.	Max.	Mean	CV, %
I	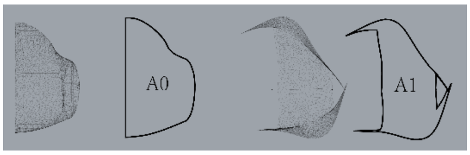	$DC_{SFM-I} = \frac{A_0}{A_1}$	(3.1)	0.54	0.78	0.62	0.38
II	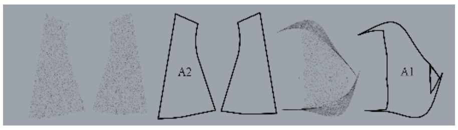	$DC_{SFM-II} = \frac{A_2}{A_1}$	(3.2)	0.16	0.23	0.19	0.36
III	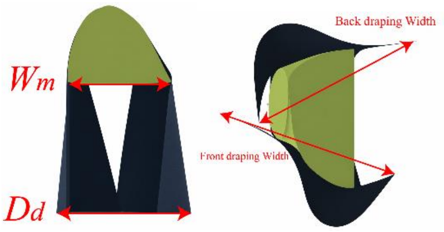	$DC_{SFM} = \frac{\Delta_2}{\Delta_1}$	(3.3)	0.24	0.86	0.66	0.93

As shown in Table 3.4, A_0, A_1, and A_2 denote the areas used only for comparing the candidate SS measurement methods. In Method I, A_0 denotes the fixed area of the shoulder-support region before draping, while A_1 denotes the projected area of the sample after draping under the same observation condition. In Method II, A_2 denotes the original flat area of the sample before draping, while A_1 is also used as the projected area of the sample after draping. Therefore, Methods I and II are area-ratio-based methods, but they differ in the choice of the initial area used for calculation.

The calculation of DC_{SFM} in Method III is shown in Equation (3.3), where DC_{SFM} is the drape coefficient measured by the SFM method; Δ_1 is the normalized expansion parameter in the front–back direction; and Δ_2 is the normalized parameter of mean-width change. Δ_1 denotes the expansion response of the draped sample in the front–back direction relative to the effective width of the SFM drapemeter, and its calculation is shown in Equation (3.4).

$$\Delta_1 = \frac{D_d}{W_m} \tag{3.4}$$

where D_d is the maximum front–back distance of the sample after draping, and W_m is the effective width of the SFM drapemeter.

Δ_2 denotes the relative change in the mean width of the sample before and after draping, and its calculation is shown in Equation (3.5).

$$\Delta_2 = \frac{W_0 - W_d}{W_0} \tag{3.5}$$

where W_0 is the mean width of the sample before draping, and W_d is the mean width of the sample after draping.

The comparison showed that methods based only on area ratios did not provide sufficient differentiation of structural differences for the SS. Method I gave a mean value of 0.62 and a CV of 0.38, indicating its ability to reflect the overall projected contour, but with limited sensitivity to differences in sample structure. Method II gave a narrower numerical interval from 0.16 to 0.23, with a CV of 0.36. This means that replacing the fixed shoulder-support area with the original flat sample area did not substantially enhance the response to structural changes. Method III gave the widest numerical interval, from 0.24 to 0.86, and the highest CV, equal to 0.93. Therefore, the inclusion of the front–back parameter and mean-width change better reflects the asymmetric deformation of the SS on the shoulder support. Based on these results, Method III was selected as the formal method for calculating DC_{SFM} for the SS.

After the measurement method had been determined, the SS sample parameters still required standardization, because sample width and shoulder-slope angle jointly affect front–back expansion, changes in lower-edge width, and bending of the hem contour under the shoulder-support boundary condition. Under the fixed virtual fabric condition VF3, DC_{SFM} values were calculated for different combinations of SS sample width and shoulder angle according to Method III. Table 3.5 shows the DC_{SFM} values for VF3 at different SS sample widths and shoulder angles.

Table 3.5 — DC_{SFM} Values for the SS Sample Made from Virtual Fabric VF3

Sample Size, cm	Shoulder slope angle, °				
	20	25	30	35	40
21	0,65	0,57	0,44	0,33	0,27
25,2	0,68	0,64	0,61	0,51	0,46
29,4	0,87	0,78	0,66	0,50	0,44
33,6	0,82	0,79	0,74	0,66	0,54
37,8	0,90	0,85	0,77	0,64	0,60
42	0,86	0,84	0,79	0,75	0,73
Mean	0,797	0,745	0,668	0,565	0,507
CV, %	12,8	15,0	18,9	27,1	32,1

As shown in Table 3.5, when the shoulder angle increased from 20° to 40°, the mean DC_{SFM} value decreased from 0.797 to 0.507. This indicates that a larger shoulder angle restricted sample expansion. At the same time, the CV showed that the 40° shoulder angle provided stronger differentiation between different sample-width conditions. Under the condition of 40° and a width of 21 cm, the sample had a DC_{SFM} value of 0.27, which was used for Method III in the subsequent comparison of five virtual fabrics. Therefore, a shoulder angle of 40° and a sample width of 21 cm were selected as the standard comparison conditions for comparing Method III with traditional *DC* coefficients based on projected area. This condition was used only to compare the differentiating ability of different *DC* calculation methods, whereas the full gradient of shoulder-line angles and widths was retained in the subsequent factorial analysis for the SS sample.

To evaluate the ability of Method III to differentially assess input factors, it was further compared with three widely used *DC* definitions based on projected area. The selected three methods calculate *DC* based on the projected area of the sample or the support region; however, their numerical directionality and sensitivity to drape differences are not identical [170]. The traditional projected-area method calculates *DC* as the ratio of the projected area after draping to the area of the undeformed flat sample, as shown in Equation (3.6).

$$DC_1 = \frac{A_p}{A_0} \tag{3.6}$$

where DC_1 is the drape coefficient obtained by the traditional projected-area method; A_p is the projected area of the sample after draping; and A_0 is the area of the sample in the undeformed flat state. In this definition, a fabric with better drapeability usually forms a smaller projected area; therefore, DC_1 is inversely related to drapeability.

The modified method subtracts the support area from the projected-area calculation in order to reduce the influence of the support region on the effective draped area, as shown in Equation (3.7).

$$DC_2 = \frac{A_p - A_{st}}{A_0 - A_{st}} \tag{3.7}$$

where DC_2 is the drape coefficient obtained by the modified projected-area method, and A_{st} is the projected area of the support. This method calculates only the effective draped region outside the support area and is therefore closer to the effective draping region used in traditional cut-and-weigh methods and image-analysis methods.

The complementary projected-area method calculates DC_3 as the ratio between the uncovered projected area and the effective area outside the support region, as shown in Equation (3.8).

$$DC_3 = \frac{A_0 - A_p}{A_0 - A_{st}} \tag{3.8}$$

where DC_3 is the drape coefficient obtained by the complementary projected-area method. Unlike DC_1 and DC_2, DC_3 increases as drapeability increases; therefore, its numerical directionality is closer to the content of Method III.

The four methods were compared within the same virtual modeling and measurement process. In Method III, the SS sample with a shoulder-slope angle of 40° and a width of 21 cm was used. The SS sample construction included warp and bias yarn directions and the plain seam s_1. In the three projected-area-based methods, circular samples placed on a spherical support were used (Figure 3.1a). Five virtual fabrics from the Style3D fabric library, designated VF1–VF5, were tested (Chapter 2). After drape simulation in Style3D, the samples were imported into Rhino 7 in OBJ format to extract projected contours and area parameters. Figure 3.7 shows the testing process for the SFM method and the traditional projected-area-based methods in Style3D and Rhino 7.

a *b* *c* *d*

Figure 3.7 — Testing process for the SFM method and traditional projected-area-based methods in Style3D and Rhino 7: *a* — simulation of the SS sample on the SFM support; *b* — simulation of the circular sample on the spherical support; *c* — projected contour of the SS sample; *d* — projected contour of the circular sample

As shown in Figure 3.7, the main differences between Method III and the three projected-area-based methods lie in the support boundary, sample form, and measured response. In Figure 3.7a, the SS sample forms an asymmetric draped state along the shoulder-support surface of the SFM support, and the measured responses are expansion in the front–back direction and change in lower-edge width. In Figure 3.7b, the circular sample forms a more regular radial draped state on the spherical support, and the measured response is mainly the projected area. Figures 3.7c and 3.7d show the projected contours extracted in Rhino 7 for the two sample types. The SFM sample contour contains clear parameter differences, whereas the circular sample contour mainly reflects the radial projection boundary. Therefore, the comparison of the four methods is not only a comparison of formulas, but also a comparison of the ability of the shoulder-support boundary and the traditional geometric support boundary to reflect the draping response of samples.

For the same group of virtual fabrics, *DC* values were calculated using Method III, the traditional projected-area method, the modified projected-area method, and the complementary projected-area method. The mean value and CV were used to characterize each method's ability to show differences between the selected fabrics VF1–VF5. Table 3.6 shows the *DC* comparison between Method III and the three traditional projected-area-based methods.

Table 3.6 — Comparison of *DC* Values for Different Calculation Methods

Fabric	*DC* Value			
	Method III	Traditional Projected-Area Method	Modified Projected-Area Method	Complementary Projected-Area Method
VF1	0,34	0,23	0,06	0,95
VF2	0,30	0,26	0,10	0,92
VF3	0,27	0,26	0,11	0,92
VF4	0,22	0,27	0,12	0,91
VF5	0,13	0,28	0,14	0,89

Mean	0,25	0,26	0,11	0,92
CV, %	32,8	7,4	28,8	2,4

As shown in Table 3.6, the four methods showed clear differences in their ability to respond to differences between virtual fabrics. The advantage of Method III lies not simply in changing the numerical directionality of *DC*, but in simultaneously including front–back expansion and the change in mean lower-edge width in the calculation. This geometric response reflects the combined influence of shoulder-line slope angle, sample width, seam type, cutting direction, and material differences. Compared with methods based on a single projected-area indicator, Method III is more suitable for describing the asymmetric deformation of a sample under the SFM shoulder-support boundary condition. Therefore, Method III was defined as the formal DC_{SFM} measurement method for the SS level and was used as the basic calculation method for subsequent SS factorial analysis, virtual–physical consistency verification, and dress form-generation prediction.

After determining the implementation conditions for the SS sample measurement method, it was necessary to further clarify unified placement rules for virtual SS, virtual LS, and physical SS samples in the SFM test in order to ensure consistency between different testing environments. Figure 3.8 shows the placement of SS, LS, and physical SS samples in the SFM test.

a *b* *c*

Figure 3.8 — Placement of samples for the SFM drape test: *a* — placement of the SS in the virtual test; *b* — placement of the LS in the virtual test; *c* — placement of the physical SS sample

As shown in Figure 3.8a and Figure 3.8b, after the SS and LS samples were placed in the virtual environment, both samples were aligned along the shoulder-support line and used the same shoulder boundary as the initial constraint. Figure 3.8c shows the placement of the physical SS sample on the SFM drapemeter; the sample is also aligned with the marked shoulder line and fixed on the shoulder-support boundary. Therefore, the differences between the virtual SS, virtual LS, and physical SS are not related to changes in the placement rule, but mainly to sample scale, structural parameters, and geometric response after draping. This figure provides a unified operational basis for the subsequent selection of the LS measurement scheme and for comparing the virtual and physical tests.

Figure 3.9 shows the measurement scheme for the corresponding DC_{SFM} parameters.

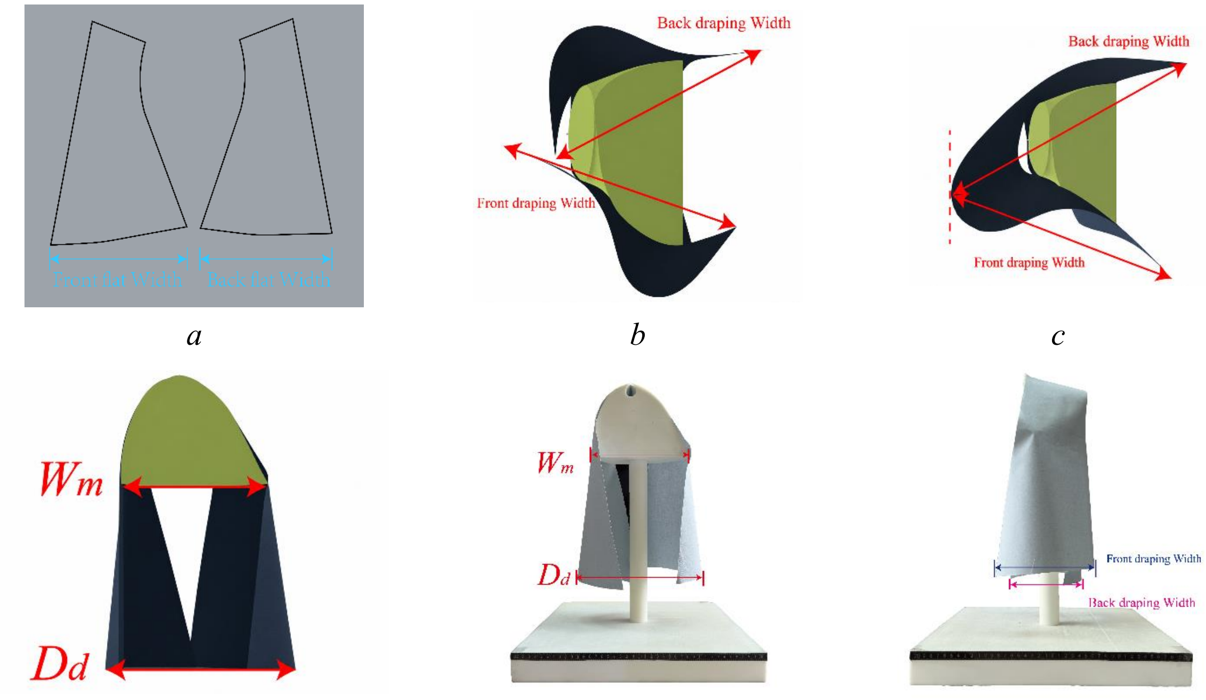

a *b* *c*

d *e* *f*

Figure 3.9 — Measurement scheme of parameters for calculating DC_{SFM}: *a* — measurement of the flat width of the SS before draping; *b* — measurement of the SS width after draping; *c* — measurement of the LS width after draping; *d* — virtual measurement of Dd and Wm for the SS; *e* — physical measurement of Dd and Wm for the SS; *f* — physical measurement of the SS width after draping

As shown in Figure 3.9, DC_{SFM} integrates the measurement of front–back expansion and mean width. Figure 3.9a shows the flat SS before draping, where the front and back flat widths were used to calculate W_0. Figure 3.9b shows the virtual SS after draping, where the front and back draped widths were used to calculate Wd. Figure 3.9c shows the width measurement of the LS after draping. Unlike the SS sample, the LS sample has a larger width after draping; therefore, the measurement of Δ_2 is based on the corresponding front and back widths of the draped sample rather than on direct copying of the widths of the short sample. Figures 3.9d and 3.9e show the virtual and physical measurements of D_d and W_m, respectively. In both cases, D_d is taken as the maximum front–back width of the draped sample, while W_m is taken as the effective width of the SFM drapemeter. Figure 3.9f shows the physical measurement of the front and back draped widths of the SS, corresponding to the physical measurement of W_d. These figures show that the same DC_{SFM}

calculation structure was used for the short SS and medium-length LS samples; however, the measurement points for Δ2 were adjusted according to the sample contour.

For the LS level, the measurement scheme was developed by taking into account the expanded draped contour compared with the SS. Four candidate measurement schemes were investigated in Rhino 7, as shown in Figure 3.10.

a *b* *c* *d*

Figure 3.10 — Candidate DC_{SFM} measurement schemes for the medium LS sample in Rhinoceros 7: *a* — Scheme 1; *b* — Scheme 2; *c* — Scheme 3; *d* — Scheme 4

As shown in Figure 3.10, the differences between the four LS schemes mainly lie in the choice of the horizontal front–back distance:

— the distance between the front and back points, reflecting overall expansion and sensitive to changes in the coordinates of the contour endpoint (Figure 3.10a);

— the distance from the front point to the side-seam point, making the measurement trajectory closer to the actual direction of LS expansion along the side structure (Figure 3.10b);

— the distance from the front point to the side-seam point, preserving the side-seam feature but weakening the expression of the spatial curvilinear trajectory (Figure 3.10c);

— the distance from the front point to the back side-seam point, providing a longer spatial measurement trajectory but potentially overemphasizing local variations of the side seam (Figure 3.10d).

These comparisons show that the LS requires a measurement scheme adapted to its elongated contour and parametrization of side expansion, rather than a direct contour measurement as in the case of the SS.

The distribution of DC_{SFM}, mean value, and CV obtained using the four LS measurement schemes for three fabrics and five measurement levels were used to evaluate the sensitivity of each scheme to sample-length variation and inter-fabric differences. Table 3.7 presents the DC_{SFM} distribution for the medium LS sample under the four candidate schemes.

Table 3.7 — DC_{SFM} Values for the LS Under Four Candidate Measurement Schemes

Sample	DC_{SFM}											
	Scheme 1			Scheme 2			Scheme 3			Scheme 4		
	F1	F2	F3	F1	F2	F3	F1	F2	F3	F1	F2	F3

LS1	0.128	0.197	0.123	0.039	0.132	0.045	0.152	0.330	0.145	0.063	0.249	0.062
LS2	0.095	0.176	0.100	0.044	0.131	0.051	0.109	0.296	0.115	0.058	0.235	0.065
LS3	0.093	0.189	0.111	0.058	0.148	0.074	0.096	0.288	0.131	0.060	0.233	0.092
LS4	0.102	0.201	0.119	0.073	0.161	0.096	0.102	0.290	0.178	0.073	0.235	0.150
LS5	0.124	0.211	0.151	0.099	0.171	0.129	0.125	0.328	0.247	0.102	0.235	0.214
Mean	0.108	0.195	0.121	0.063	0.149	0.079	0.117	0.307	0.163	0.071	0.238	0.117
CV, %	13.6	6.1	14.1	38.9	11.6	41.2	32.3	24.5	13.1	19.7	0.3	55.8

As shown in Table 3.7, the four schemes demonstrated different responses to different measurement levels depending on fabric type. Scheme 1 produced a relatively smooth change in DC_{SFM}, with CV values for all three fabrics remaining below 15%, indicating insufficient sensitivity of Scheme 1. Although this scheme records the distance between the front and back contour points, the use of the horizontal distance between endpoints does not reflect the influence of vertical draping and side expansion. By comparison, Scheme 2 shows more pronounced size sensitivity for fabrics F1 and F3. For fabric F2, DC_{SFM} values demonstrated a relatively stable increasing trend across the LS size levels. From a geometric point of view, Scheme 2 uses the direct shortest measurement from the front point to the side-seam point, which records LS expansion in the front–back direction and reflects the influence of the side seam on the draped contour. Therefore, Scheme 2 provides the best balance between geometric meaning, size sensitivity, and stability, and was selected as the formal measurement scheme for the LS sample in the SFM system.

To ensure a consistent operational basis for SFM, the virtual and physical tests must correspond to each other in terms of support geometry, sample placement, drape stabilization, and extraction of geometric variables. Table 3.8 shows the correspondence of operations and measured results between the virtual and physical SFM tests.

Table 3.8 — Correspondence of SFM Operations in Virtual and Physical Tests

Step	Virtual SFM Test	Physical SFM Test	Controlled Output
1	Construct or import the SFM drapemeter in Style3D	Use the physical SFM drapemeter obtained from the same support geometry	Shoulder-imitating support surface
2	Place the SS or LS along the shoulder line of the virtual drapemeter	Align the sewn sample with the marked shoulder line of the physical drapemeter	Sample alignment boundary
3	Run gravity simulation until a	Release the sample and allow it to reach a stable	Stable draped geometry

	stable draped form is reached	draped state under the action of gravity	
4	Obtain W_0 from the flat sample geometry and measure D_d and Wd from the draped geometry	Obtain W_0 from the flat physical sample and measure D_d and W_d from the calibrated draped image or recorded contour	Geometric variables for Δ_1 and Δ_2
5	Calculate DC_{SFM} using Equations (3.3)–(3.5)	Calculate DC_{SFM} using the same equations	Comparable SFM drape coefficient DC_{SFM}

As shown in Table 3.8, the virtual and physical tests on the new SFM rig are coordinated through support geometry, sample alignment, drape stabilization, extraction of geometric variables, and calculation of the drape coefficient. This operational correspondence ensures that W_0, W_d, D_d, W_m, Δ_1 and Δ_2 are defined consistently for the virtual and physical SFM tests.

Thus, the SFM measurement system was formed for two samples: the short SS and the medium LS. For the SS sample, Method III was adopted, in which the combination of the change in maximum front–back distance and the change in mean lower width was used as the main geometric response. This level supports the construction of a basic database of drape response and the analysis of structural factors, such as shoulder-slope angle, sample width, seam type, and cutting direction. For the LS sample, Scheme 2 was adopted, in which the shortest distance from the front point to the side-seam point and the maximum width were used as the basic measurements.

3.4.2 Drape coefficient results for short specimens and key influencing factors

The structural factors influencing DC_{SFM} of the short sample were analyzed. The variables included seam type, cutting direction, shoulder-slope angle, and lower width of the sample [174].

The first analysis focused on the selection of seam type and cutting direction. CV was used to evaluate whether these factors could enhance differences in DC_{SFM} between fabrics and sample configurations. Table 3.9 shows the CV values for DC_{SFM} of the short sample under different seam types and cutting directions, where s_1, s_2, and s_3 denote seam types.

Table 3.9 — CV for DC_{SFM} of the Short Sample Under Different Cutting Directions and Seam Types

Cutting Direction	DC_{SFM} Values								
	F1			F2			F3		
	s_1	s_2	s_3	s_1	s_2	s_3	s_1	s_2	s_3
Warp	0.73	0.67	0.65	0.50	0.54	0.69	0.33	0.64	0.83

Weft	0.80	0.69	0.68	0.56	0.52	0.72	0.51	0.59	0.79
Bias	0.76	0.68	0.67	0.58	0.53	0.58	0.59	0.60	0.80

As shown in Table 3.9, the three seam types produced different levels of DC_{SFM} dispersion. Samples with the plain seam s_1 showed a clear response to changes in cutting direction and fabric type, indicating the suitability of the plain seam for observation. For seam s_1, the CV values of the SS sample were compared for the warp, weft, and bias cutting directions. Figure 3.11 shows the CV for different cutting directions.

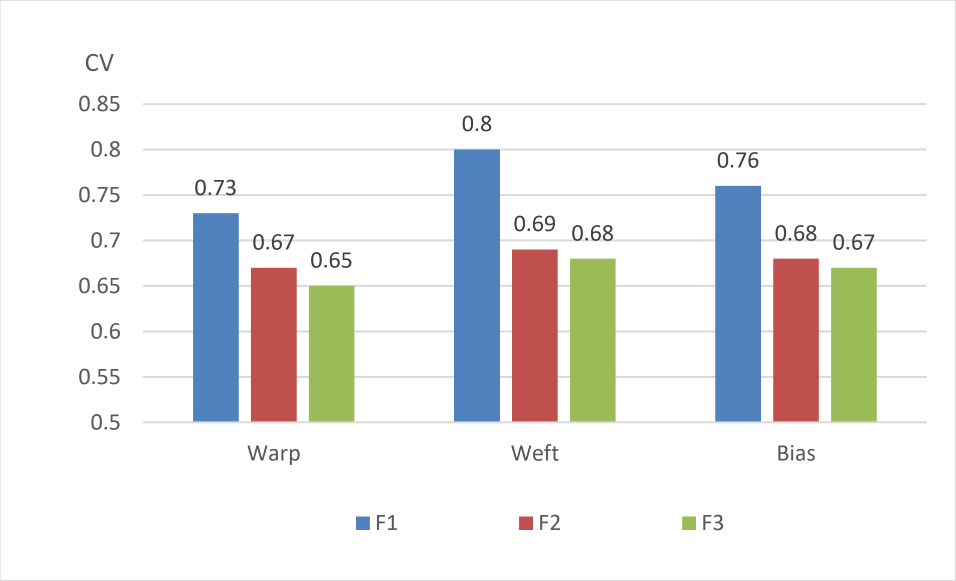

Figure 3.11 — CV for DC_{SFM} of the Short Sample Under Different Cutting Directions and the Plain Seam

As shown in Figure 3.11, samples cut in the weft direction show the greatest difference between the three fabrics; therefore, the weft cutting direction was used in the subsequent SS analysis.

The shoulder-slope angle and lower width of the sample were analyzed as the main geometric variables. The DC_{SFM} values obtained under the condition of seam s_1 and weft-direction cutting are presented in Table 3.10.

Table 3.10 — DC_{SFM} of the Short Sample at Different Shoulder-Slope Angles and Lower Sample Widths

SS Width, cm	DC_{SFM} for different angles and different fabrics														
	20°			25°			30°			35°			40°		
	F1	F2	F3	F1	F2	F3	F1	F2	F3	F1	F2	F3	F1	F2	F3
21	0.09	0.15	0.17	0.04	0.10	0.13	0.02	0.07	0.09	0.02	0.06	0.08	0.01	0.03	0.06

25.2	0.18	0.24	0.35	0.15	0.19	0.19	0.10	0.17	0.18	0.10	0.11	0.12	0.07	0.10	0.12
29.4	0.31	0.40	0.41	0.29	0.35	0.31	0.22	0.28	0.29	0.19	0.24	0.20	0.15	0.19	0.20
33.6	0.50	0.56	0.65	0.47	0.52	0.60	0.34	0.43	0.46	0.31	0.34	0.34	0.23	0.28	0.27
37.8	0.78	0.81	0.87	0.66	0.80	0.82	0.56	0.62	0.68	0.50	0.53	0.49	0.38	0.47	0.46
42	0.98	0.96	0.95	0.86	0.91	0.99	0.78	0.77	0.86	0.73	0.74	0.70	0.61	0.67	0.64
Mean	0.47	0.52	0.57	0.41	0.48	0.51	0.34	0.39	0.43	0.31	0.34	0.32	0.24	0.29	0.29

As shown in Table 3.10, when the sample width increased from 21 cm to 42 cm, the DC_{SFM} values clearly increased for all three fabrics at all angles. This means that a larger width allows the sample to form more pronounced form generation. At a shoulder-slope angle of 20°, the sample demonstrates the maximum drapeability potential.

To further study the influence of the shoulder seam and lower-edge treatment, samples with shoulder seams were compared with one-piece samples without shoulder seams. Figure 3.12 shows the influence of the presence and absence of the shoulder seam, as well as the lower-edge treatment of the one-piece sample, on DC_{SFM} of the short sample, where h_1, h_2, and h_3 denote the three lower-edge treatment variants of the one-piece sample: unfinished edge, folded edge, and hemmed seam, respectively.

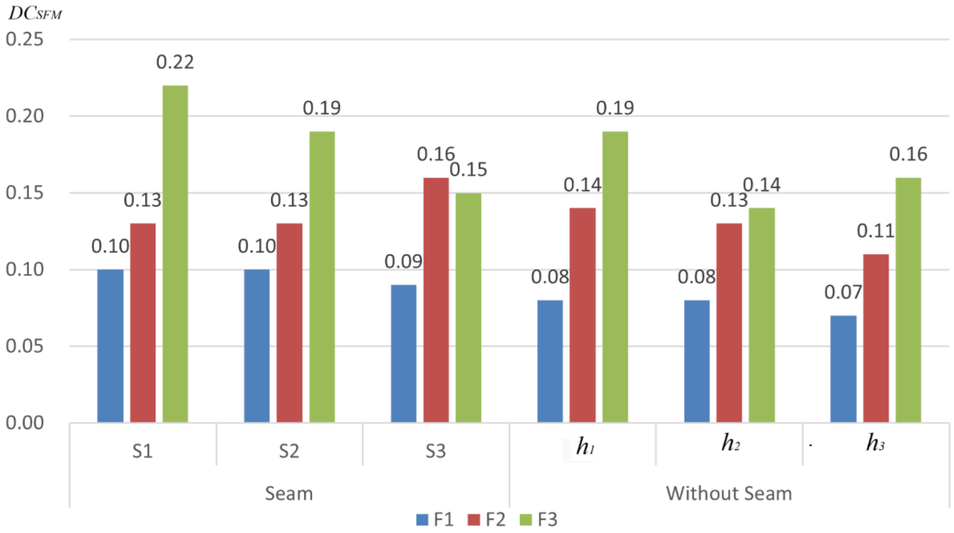

Figure 3.12 — Influence of Shoulder Seam Construction and Lower-Edge

Treatment of the One-Piece Sample on DC_{SFM}

As shown in Figure 3.12, seam s_1 produced the highest DC_{SFM} response for fabric F3 and remained comparable with the other seams for fabrics F1 and F2. The shoulder seam structure affects local stiffness and the initial formation of folds from the shoulder slope. In the one-piece sample groups, the influence of h_1, h_2, and h_3 was limited. This shows that, in the virtual environment, the influence of lower-edge treatment on DC_{SFM} is not pronounced. Therefore, lower-edge treatment was excluded as a main variable in subsequent SS tests, while the plain shoulder seam s_1 was retained as the main seam structure.

To compare the relative contributions of fabric physico-mechanical property indicators and sample parameters, correlation analysis was performed. X_1 denotes tensile force, X_2 denotes bending stiffness, X_3 denotes tensile elongation, X_4 denotes the shoulder-slope angle, and X_5 denotes the lower width of the sample. The correlation coefficients between these variables and DC_{SFM} of the short sample are given in Table 3.11.

Table 3.11 — Correlation Coefficients Between DC_{SFM}, Geometric Parameters of the Short Sample SS, and Indicators of the Physico-Mechanical Properties of Fabrics (n = 270)

	X_1	X_2	X_3	X_4	X_5	DC_{SFM}
X_1	1					
X_2	-0.211^{**}	1				
X_3	-0.045	0	1			
X_4	0	0	0	1		
X_5	0	0	0	0	1	
DC_{SFM}	0.044	-0.049	-0.079	-0.306^{**}	0.920^{**}	1

Note: ** indicates significance at the 0.01 level.

As shown in Table 3.11, DC_{SFM} of the short sample has a strong positive correlation with sample width X_5 and a significant negative correlation with shoulder-slope angle X_4. By contrast, the correlations between DC_{SFM} and X_1, X_2, and X_3 did not show significant relationships. This indicates that, within the current virtual test matrix, sample design parameters exert a stronger influence on DC_{SFM} than the selected fabric physico-mechanical parameters.

To visualize the relationships between the two significant design parameters, angle X_4 and width X_5, and DC_{SFM}, their dependencies are shown in Figure 3.13.

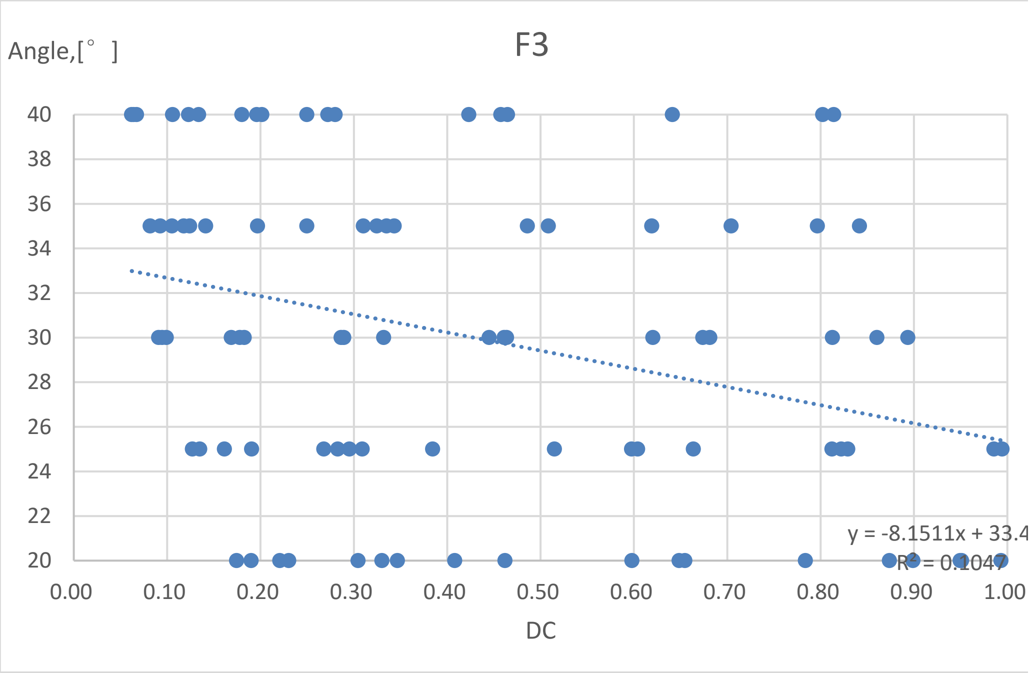

Figure 3.13 — Representative Relationship Between Angle X_4 and DC_{SFM} of the Short Sample for Fabric F3

Figure 3.14 shows the representative relationship between sample width X_5 and DC_{SFM} using F2 as an example.

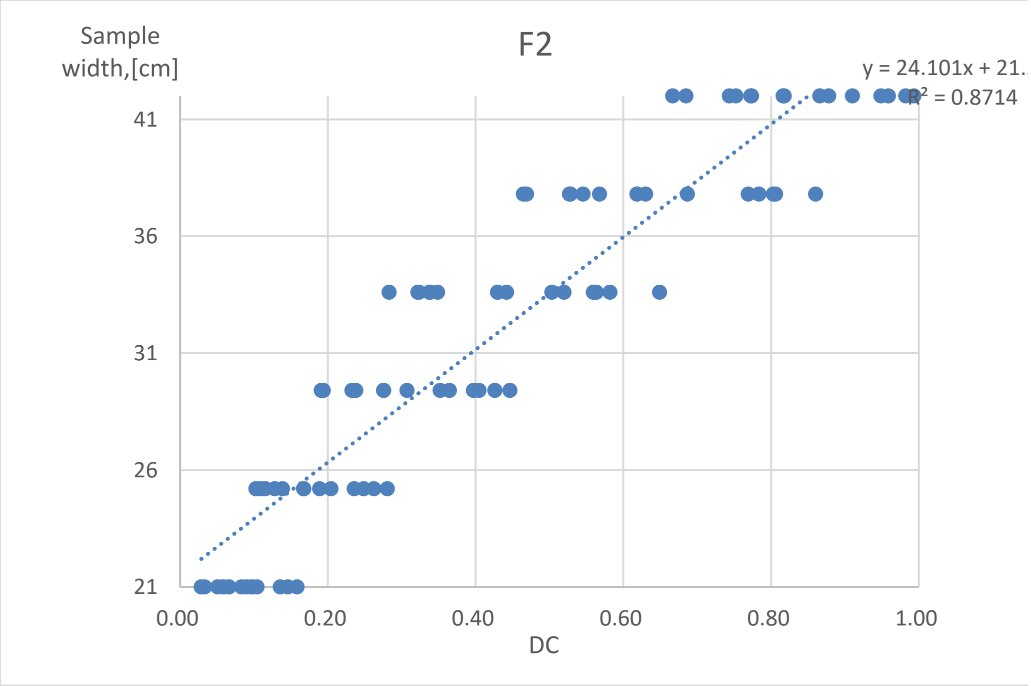

Figure 3.14 — Representative Relationship Between Lower-Edge Width X_5 and DC_{SFM} of the Short Sample for F2

Based on the correlation analysis, a two-factor linear regression model was constructed in which shoulder-slope angle X_4 and lower sample width X_5 were used as predictors of DC_{SFM} of the short sample. The regression equation is given in Equation (3.9).

$$DC_{SFM} = -0.369 - 0.012X_4 + 0.036X_5 \tag{3.9}$$

where DC_{SFM} is the drape coefficient of the short sample SS obtained by the SFM method, X_4 is the shoulder-slope angle, degrees, and X_5 is the lower width of the sample, cm.

To verify whether Equation (3.9) can predict DC_{SFM}, three fabrics from Style3D were used as control fabrics, designated C1, C2, and C3 (Chapter 2). The comparison of measured and predicted DC_{SFM} values for the control fabrics is presented in Table 3.12.

Table 3.12 — Verification of DC_{SFM} Prediction on Control Fabrics

Control Fabric	Material	Shoulder Angle, °	SS Width, cm	DC_{SFM}	
				Measured	Predicted
C1	Twill	20	30	0.50	0.47
C2	Polyester	20	34	0.60	0.61
C3	Cotton	28	34	0.54	0.52

As shown in Table 3.12, Equation (3.9) provides good prediction quality for DC_{SFM}: the absolute differences were 0.01–0.03. Despite the limited size of the validation set of control fabrics, the small absolute differences show that the coefficient can be predicted within the studied range using two variables.

The measured and predicted DC_{SFM} values were further compared using a t-test for comparison of means. Table 3.13 presents the statistical comparison between measured and predicted DC_{SFM} values.

Таблица 3.13 – Парное сравнение измеренных и прогнозируемых значений DC_{SFM}

DC_{SFM}	Mean	SD	t	p
Measured	0.5467	0.0507	0.268	0.799
Predicted	0.5333	0.0701		

As shown in Table 3.13, the p-value was 0.799, which exceeds the significance level of 0.05. Therefore, within this control validation, no significant difference was found between the measured and predicted DC_{SFM} values. This result should be interpreted as preliminary statistical evidence supporting Equation (3.9), rather than as a complete validation of the regression model.

3.5 Validation of the New Method Based on the Physical Prototype

3.5.1. Verification of Consistency Between Virtual and Physical Results

Validation was carried out on samples with a total shoulder-slope angle of 40°, a plain shoulder seam s_1, weft-direction cutting, and six lower-width values of the sample. Six samples were studied for each fabric, and the mean DC_{SFM} value was used as the representative SFM response for virtual–physical comparison. Table 3.14 shows the DC_{SFM} matrix for virtual and physical SS samples.

Table 3.14 — DC_{SFM} Values for Virtual and Physical SS Samples

Width of the sample at the bottom, cm	DC_{SFM} Values					
	F1		F2		F3	
	Virtual	Physical	Virtual	Physical	Virtual	Physical
21	0.76	0.75	0.79	0.73	0.76	0.71
25.2	0.75	0.67	0.73	0.55	0.71	0.74
29.4	0.72	0.72	0.64	0.53	0.67	0.65
33.6	0.60	0.70	0.52	0.47	0.64	0.59
37.8	0.55	0.62	0.45	0.34	0.55	0.52
42	0.48	0.48	0.36	0.30	0.37	0.48
Mean	0.64	0.66	0.58	0.49	0.62	0.62
CV, %	18.15	14.82	28.67	32.06	22.69	16.86

As shown in Table 3.14, the virtual and physical SS groups showed comparable mean DC_{SFM} values. Fabric F3 showed the closest agreement in mean values between virtual and physical tests, followed by F1 and F2. The CV values indicate that F2 had higher dispersion in both virtual and physical tests, with values of 28.67% and 32.06%, respectively. This shows that F2 was more sensitive to changes in lower-edge width, whereas F1 and F3 demonstrated relatively more stable responses at the width level.

To further determine whether the mean differences between the virtual and physical SS samples were statistically significant, independent-samples t-tests were performed using six DC_{SFM} values across the lower-width levels for each fabric. Table 3.15 shows the results of the independent-samples t-test between the virtual and physical SS samples.

Table 3.15 — Results of the Independent-Samples t-Test Between Virtual and Physical SS Samples

Fabric	*t*	*p*	df	Significance at α = 0,05	Mean Difference, V−R
F1	−0,215	0,834	10	Статистическинезначимо	−0,013
F2	1,019	0,332			+0,095
F3	0,023	0,982			+0,002

As shown in Table 3.15, the p-values for F1, F2, and F3 were 0.834, 0.332, and 0.982, respectively, all of which exceeded 0.05. Therefore, at the α = 0.05 level, no significant difference was found between the virtual and physical DC_{SFM} values for the SS samples for any of the three fabrics.

3.5.2. Comparison of disk and new methods

Since these methods differ in sample form, support boundary, and formulas for calculating the drape coefficient, the absolute values of DC and DC_{SFM} are not directly equivalent. Figure 3.15 shows the virtual and physical states of circular samples made from fabrics F1–F3 obtained using the disk method.

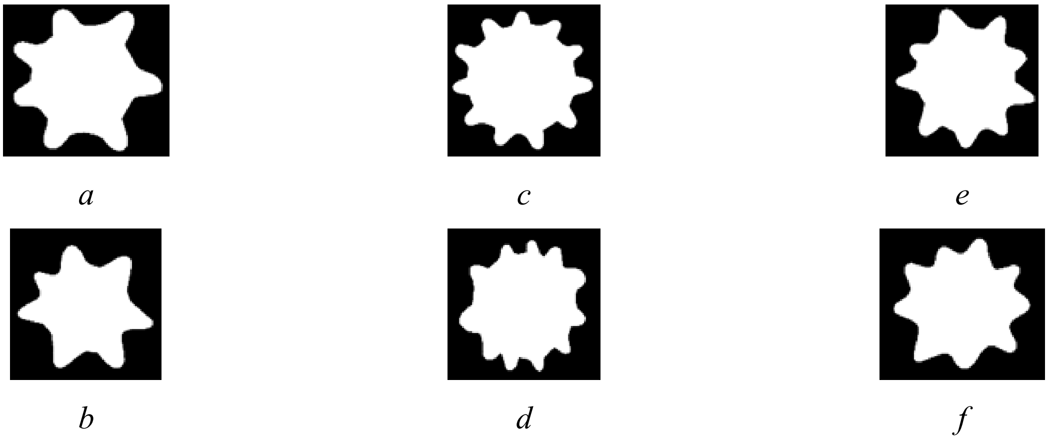

Figure 3.15 — Virtual and physical circular samples made from fabrics F1–F3 obtained using the disk method: *a* — virtual drape of F1; *b* — physical drape of F1; *c* — virtual drape of F2; *d* — physical drape of F2; *e* — virtual drape of F3; *f* — physical drape of F3

As shown in Figure 3.15, the virtual and physical circular samples formed radial drape contours around the central support region.

The relative virtual–physical difference was calculated in the form of Equation (2.6), with the predicted value in the original formula replaced by the virtual value and the measured value replaced by the physical value. A positive difference indicates that the virtual test result was higher than the physical test result, while a negative difference indicates that the virtual test result was lower than the physical result. Table 3.16 shows the DC values obtained using the disk method, the DC_{SFM} values obtained using the new method, the corresponding virtual–physical differences, the inter-fabric CV, and the mean absolute virtual–physical differences.

Table 3.16 — Virtual–Physical Differences and Inter-Fabric CV for the Disk Method and the New Method

Index	Fabric / Statistic	Drape Coefficient	
		DC, Disk Method	DC_{SFM}, New Method
Virtual value	F1	0,37	0,64

	F2	0,34	0,58
	F3	0,39	0,62
	Cross-fabric CV, %	6,86	4,98
Physical value	F1	0,42	0,66
	F2	0,33	0,49
	F3	0,45	0,62
	Cross-fabric CV, %	15,61	15,06
Virtual–physical difference, %	F1	−11,9	−3,0
	F2	+3,0	+18,4
	F3	−13,3	0,0
	Mean absolute virtual–real difference, %	9,42	7,13

As shown in Table 3.16, both methods identify fabric F2 as the fabric with the lowest draping response. The virtual–physical differences further reveal the correspondence between digital twin testing and physical testing under the two support conditions. In the disk method, the virtual DC values for F1 and F3 were lower than the corresponding physical DC values. In the new method, the virtual DC_{SFM} value for F1 was slightly lower than the physical value, with a difference of −3.0%, whereas F3 showed almost no virtual–physical deviation, with a difference of 0.0%. F2 showed the largest deviation in the Shoulder Fitting Method: the virtual value was higher than the physical value by +18.4%. Therefore, the Shoulder Fitting Method provided closer virtual–physical agreement than the disk method for F1 and F3, but produced a more pronounced fabric-specific deviation for F2.

The mean absolute difference describes the overall level of virtual–physical deviation across the three fabrics. The mean absolute difference was 9.42% for the disk method and 7.13% for the new method. This comparison shows that the Shoulder Fitting Method produced a lower overall virtual–physical deviation across F1–F3 than the disk method. However, this reduction was not uniformly distributed across all fabrics. The smaller deviations in the new method for F1 and F3 were the main factors that produced the lower mean absolute difference, whereas fabric F2 clearly shows that its specific characteristics had a strong influence. Therefore, the results obtained using the new method should not be interpreted as a direct numerical replacement for the disk method; rather, the new method represents a different expression of draping response.

The CV comparison showed that, in the virtual tests, the CV was 6.86% for the disk method and 4.98% for the new method, with the new method providing a lower level of dispersion.

Thus, the comparison between the disk method and the new method showed that they correspond to different levels of drapeability evaluation. The disk method remains suitable as a traditional material-level reference for characterizing changes in the projected area of circular samples under a regular support boundary. The new method is closer to the state of fabric draping in the shoulder-surface region. Based on this response characteristic, the new method can be used as a method for obtaining sample-level draping input data for subsequent analysis and prediction of dress form generation.

Выводы по главе 3

1. An algorithm for testing fabric drapeability by the new method was developed, including a virtual and physical drapemeter, two types of samples — short and medium — a scheme for calculating the drape coefficient DC_{SFM}, and a procedure for virtual–physical verification.

2. Based on the parameters of the shoulder region of female figures, a test rig was manufactured, including an anthropomorphic shoulder support with magnetic sample fixation, a modular column, a base, a ruler, and a laser device. The dimensions of samples of different lengths were substantiated, and expressions for calculating drape coefficients were proposed.

3. The comparison of spherical, conical, and cylindrical virtual supports showed that regular geometric boundaries insufficiently reflect the influence of fabric property indicators: the CV values were only 0.05–0.07, and the range of drape coefficient DC values was narrow. The new method provides a coefficient of variation of 0.14–0.32.

4. Analysis of the form-generation characteristics of the samples showed that the drape coefficient depends more strongly on the geometric parameters of the sample than on the indicators of the physico-mechanical properties of fabrics. A regression model for predicting the drape coefficient was constructed. Verification on control fabrics showed the adequacy of the equation and small absolute differences between measured and predicted values.

5. Virtual–physical verification confirmed the comparability of the results obtained when testing samples on the new rig in virtual and physical environments: no statistically significant differences were found between the two groups of results.

6. Comparison with the traditional disk method showed that the new method does not directly replace the traditional method, but characterizes a different level of drapeability associated with the shoulder support and sample structure. The mean virtual–physical difference was 9.42% for the disk method and 7.13% for the new method. The new method can be used as a basis for further analysis of the relationship between sample drapeability and dress form generation.

CHAPTER 4. CONSTRUCTION AND VALIDATION OF FABRIC DIGITAL TWINS BASED ON ARTIFICIAL INTELLIGENCE MEASUREMENTS

4.1. Image Set and Parameter Coding System for Artificial Intelligence Measurements

In this chapter, a standardized visual dataset, a physical-parameter coding system, and the Style3D environment were used to form a contactless non-instrumental measurement method for fabric property indicators using artificial intelligence (AI). The image set provided controlled visual input data, the AI models transformed visual-textual data into physico-mechanical fabric parameters according to the prompt protocol, and the parameter coding system aligned the AI measurement results with laboratory reference values. The obtained parameters were then used to construct fabric digital twins using fabricDT in Style3D.

The visual dataset for AI measurements was used to provide standardized visual input data for multimodal AI models. This image set was not a training dataset, but a source of visual data for inferring physical fabric parameters. The image set included two-dimensional 2D images and three-dimensional 3D images. The 2D images provided information about fabric appearance, scale, weave structure, and surface details, while the 3D deformation images reflected the morphological responses of fabrics under gravity, support boundaries, and low-load deformation. Together, these two types of images formed the input data for measuring thickness, surface density, tensile forces at small deformations, bending stiffness, and the circular drape coefficient DC. Figure 4.1 shows the structure of the image set for AI measurements.

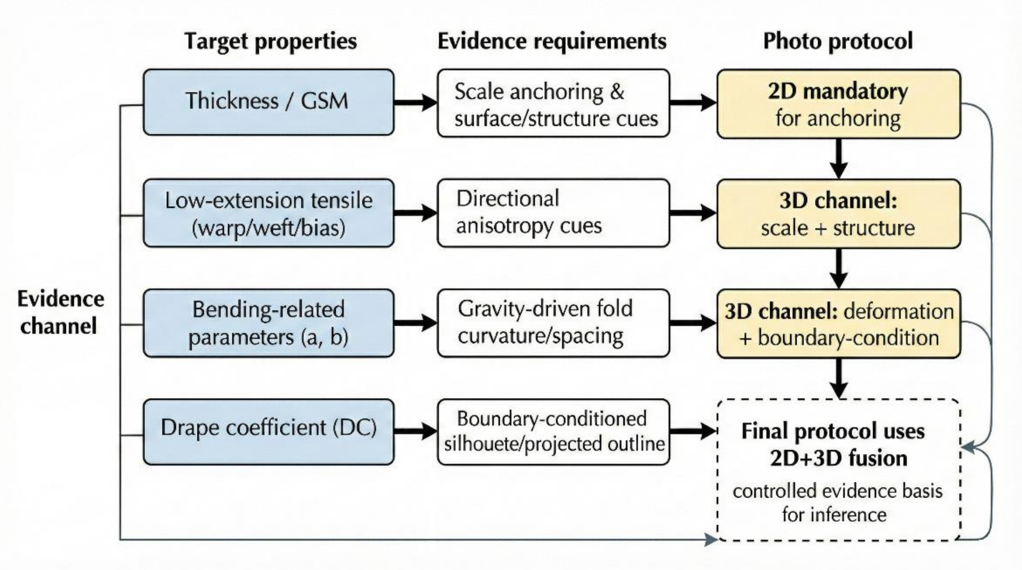

Figure 4.1 — Structure of the image set for AI measurement of fabric property indicators

As shown in Figure 4.1, the visual dataset for AI-based measurements is organized according to the relationship between the target physical properties and visual channels. The two-dimensional image channel provides scale orientation, flat appearance, and information about weave structure, whereas the three-dimensional image channel provides information about the action of gravity, support boundaries, and deformation morphology. Fabric thickness and surface density can be identified from two-dimensional images. Tensile force at small elongations, bending stiffness, and the circular drape coefficient DC require three-dimensional images to account for the number and depth of folds, edge curvature, drape contour, and directional deformation.

The visual dataset for AI measurements included six types of photographs, designated as P1–P6. P1 and P2 are two-dimensional images that record the flat state and surface texture of the fabric, respectively. P3–P6 are three-dimensional deformation images that record Cusick circular drapeability, spiral twistability, drapeability according to the new SFM method, and vertical hanging, respectively. P3 mainly provides visual evidence for the DC coefficient, while P5 mainly provides data on the morphology of the pleated surface according to the SFM method, associated with DC_{SFM}.

All photographs of the three fabrics were taken under identical environmental conditions after conditioning the samples under the standard conditions described in Section 2.3.1. A Canon EOS R7 mirrorless camera with an APS-C CMOS sensor and a Canon RF 35 mm f/1.8 IS STM macro lens was used in the experiment. The camera model, lens model, focal length, distance from the camera to the object, lighting geometry, exposure settings, and image resolution remained constant for all fabrics and photograph types. The camera was mounted on a tripod with a leveling base to maintain the optical axis perpendicular to the object plane and to reduce perspective distortion. Images were captured using a remote trigger to maintain consistent positioning and prevent camera shake. Figure 4.2 shows the image set, where P1–P2 represent flat fabric images, and P3–P6 represent fabrics at the moment of deformation.

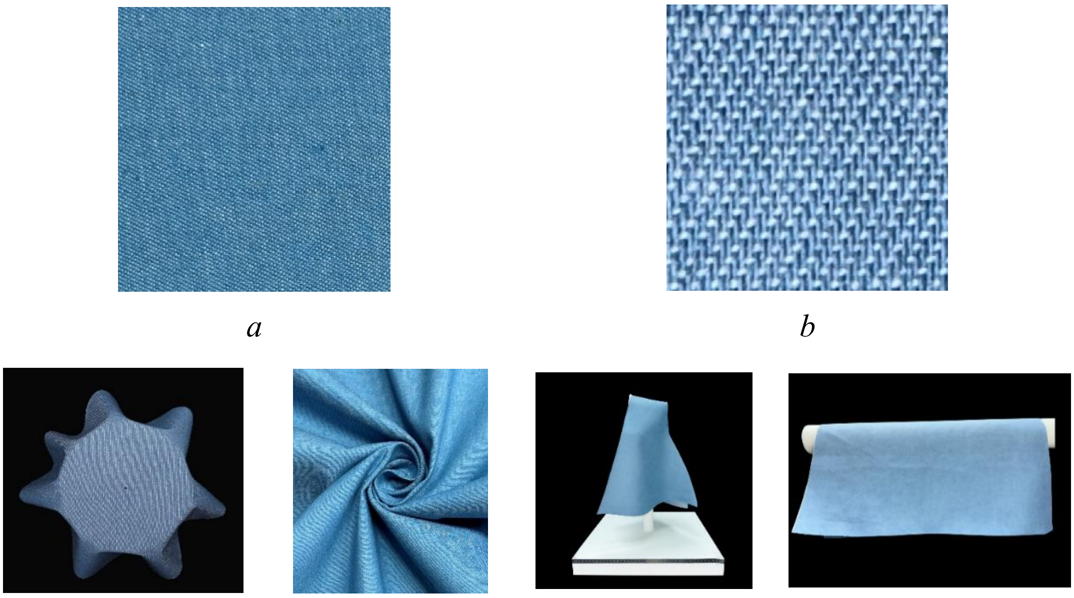

a *b*

c *d* *e* *f*

Figure 4.2 — Types of photographs: *a* — flat image P1; *b* — close-up surface texture P2; *c* — Cusick circular drape P3; *d* — spiral twistability P4; *e* — drapeability according to the new SFM method P5; *f* — vertical hanging P6

P1 records the flat state of the fabric and is used to observe overall flatness, edge curling, and surface macrostructure. P2 records local surface details and is used to observe yarn fineness, weave structure, structural density, and surface hairiness. P3 records the traditional circular drapeability state and is used to observe the projected contour, number of folds, and fold depth, providing the main morphological data for inferring the drape coefficient DC. P4 records the state of spiral twistability and is used to observe the direction of spiral folds, fold density, and differences in deformation. P5 records the drapeability state according to the new SFM method and is used to observe overall morphology, edge curvature, and asymmetric folds on a shoulder-imitating support, providing data for morphological analysis associated with DC_{SFM}. P6 records the hanging state on a column and is used to observe hanging length, spacing between folds, and edge curvature under linear support.

Table 4.1 summarizes how each photograph code is transformed into parameter-related visual data.

Table 4.1 — Visual Signals and Physical Property Groups in the Image Set for AI Measurements

Code	Photograph Type	Main Visual Signals	Physical Properties
P1	Flat layout	Surface macrostructure, edge curling, fold retention, overall flatness	Thickness, GSM
P2	Close-up	Yarn fineness, weave structure, structural density, surface hairiness, and gloss	
P3	Cusick drapeability	Gravity-induced contour and fold features, including projected contour, number of folds, and depth	DC, bending-related response
P4	Spiral twistability	Orientation and distribution of folds under spiral deformation, reflecting directional differences and deformation modes	Tensile response at small deformations, bending-related response
P5	Drapeability according to the new SFM method	Overall drape morphology under a shoulder-imitating support condition, including the development of asymmetric folds, hem curvature, and shoulder-to-hem drape morphology	DC_{SFM}, bending-related response
P6	Hanging on a column	Gravity-induced drape under linear or column support, with emphasis on sagging and spacing between folds along the draping direction	DC-related response, bending-related response, tensile response at small deformations

To compare AI measurement results with laboratory reference values, the output parameters were organized into a unified coding system (Table 2.5).

4.2. Construction and Calibration of the Prompt Protocol for AI Measurements

4.2.1. Library of Prompt Elements

The AI measurement protocol was constructed as a structured prompt designed to obtain physico-mechanical fabric parameters from images P1–P6. Unlike an ordinary text query, this prompt was regarded as a measurement protocol that defined the admissible scope of evidence, the composition of output parameters, units of measurement, physical constraints, and the form of result presentation.

The prompt elements were grouped into two categories: basic elements (B) and variable elements (V). The basic block formed the foundation of the protocol and ensured the same context and main constraints across different versions. The elements supported the metrological context, evidence boundaries, and basic physical constraints shared by the prompt versions, thereby ensuring the comparability of subsequent comparisons.

The variable block recorded structural changes introduced during the iterations, including the organization of measured elements, the method for presenting numerical values, the integration of evidence from multiple photographs, the closed-loop summarization mechanism, and convergence rules. Table 4.2 shows the modular elements used to encode the prompt as a measurable protocol.

Table 4.2 — Library of Prompt Elements

Element ID	Element Name	Block Type	Content	Role
E01	Metrological definition	***B***	A role statement assigning the model as a fabric testing expert for mechanical properties and drape	Fixes the subject area and response formulation
E02	Evidence-boundary rule	***B***	A constraint stating that results must be inferred from photographs and that the prompt must not claim the use of standard instruments	Limits admissible evidence and prevents invalid methodological claims
E03	Consistency constraint with background knowledge	***B***	An instruction requiring all outputs to be consistent with the provided background knowledge	Introduces explicit prior constraints as part of the protocol foundation
E04	Rules of physical admissibility and consistency	***B***	Constraints such as non-negativity, admissible ranges, and internal requirements for directional consistency	Ensures physical plausibility and internal consistency of outputs

E05	Uncertainty-handling rule	***B***	A rule requiring conservative expression when data are insufficient	Prevents overconfidence and stabilizes outputs under limited data
E06	Measurement definition	***V***	A section listing the target properties and mandatory reporting fields	Defines the scope of output data and can be adapted for other purposes
E07	Standardized table template	***B***	A fixed table structure with predefined fields, units, and order	Standardizes reporting for comparison and calculation
E08	Output format	***B***	A requirement to provide results in structured tables and limit non-essential text	Improves machine readability and reduces output deviation
E09	Numerical-value presentation mode	***V***	A rule defining range output, single-value output, or transition from a range to a single value	Controls the interface between uncertainty expression and quantitative evaluation
E10	Visual-signal justification rule	***B***	A requirement to provide observable visual evidence supporting the stated values	Supports auditability and reasoning traceability
E11	Iterative update rule	***V***	An instruction allowing modifications based on results from the previous round	Enables iterative stabilization and improved consistency
E12	Multi-photograph fusion schedule	***V***	A rule defining the order of evidence integration, such as one-step fusion or stepwise fusion	Defines how data from different photographs are combined
E13	Evidence-priority allocation	***V***	A rule assigning which photograph types mainly support which physical properties	Reduces conflicts in multi-photo justification and improves consistency
E14	Closed-loop summarization mechanism	***V***	A requirement to produce intermediate summary reports and a final table	Organizes outputs into a verifiable closed loop
E15	Convergence and stability rule	***V***	A rule ensuring stabilization across rounds,	Limits output fluctuation and

			such as range narrowing or convergence conditions	supports reproducibility

As shown in Table 4.2, after the library of elements and the block structure were defined, the five prompt versions were represented as element configurations, so that the protocol structure of each version could be encoded using the same set of elements. This representation shifts the description of iteration from differences at the wording level to differences at the protocol-structure level. Each prompt version is regarded as a combination of basic and variable elements.

4.2.2 Prompt Engineering Protoco

To ensure auditable structural recording, a unified notation was used. ***B*** indicates that an element is activated as a basic element, while ***V*** indicates that an element is activated as a variable element. For selected variable elements, **V**-number labels were used to distinguish protocol interfaces. In particular, the numerical-value presentation mode uses V1 for range output, V2 for single numerical-value output, and V3 for the two-stage "range-to-single-numerical-value" workflow. The multi-photograph fusion schedule uses V4 for stepwise input and V5 for simultaneous joint input. The stabilization rules use V6 for nested-range limitation and V7 for the progressive range-narrowing process.

Table 4.3 shows the configuration of elements E01–E15 for the five prompt versions.

Table 4.3 — Prompt Structure

Prompt	Element E															Photo
	01	02	03	04	05	06	07	08	09	10	11	12	13	14	15	
1	***B***	***B***	-	***B***	*B*	***V***	***B***	***B***	V_1	***B***	-	-	-	-	-	*P1–P4*
2	***B***	***B***	*B*	***B***	-	***V***	***B***	***B***	V_2	***B***	*V*	V_4	*V*	*V*	-	*P1–P4*
3	***B***	***B***	*B*	***B***	-	***V***	***B***	***B***	V_2	***B***	-	V_5	-	-	-	*P1–P4*
4	***B***	***B***	*B*	***B***	*B*	***V***	***B***	***B***	V_3	***B***	*V*	V_4	*V*	*V*	V_6	*P1–P4*
5	***B***	***B***	*B*	***B***	*B*	***V***	***B***	***B***	V_3	***B***	*V*	V_4	*V*	*V*	V_7	*P1–P4*

As shown in Table 4.3, the five prompt versions have a stable protocol foundation, which includes the basic elements E01, E02, E04, and E06–E08. The main structural differences are concentrated in the variable blocks. In particular, Prompt 1 emphasizes range-based presentation and does not include the background-knowledge constraint, corresponding to a protocol without explicit prior data. Prompts 2 and 3 introduce background knowledge and contain single values, but differ in the way evidence is combined. Prompt 2 uses stepwise input of evidence and summarizes it at the end, whereas Prompt 3 combines four photographs jointly within one measurement cycle.

Prompts 4 and 5 include basic information and constraints with explicit closed-loop and stabilization algorithms: both use the “range-to-single-value” interface and stepwise evidence input with iterative updating to reduce output instability. Prompt 4 applies a restriction to the value range, while Prompt 5 uses progressive narrowing and final consolidation.

The photograph system was formalized using two complementary levels: at the first level, photographs P1–P2 provide 2D evidence, while photographs P3–P6 provide 3D morphological evidence; at the second level, photographs P1, P2, P4, and P6 are defined as standard-type configurations that can be easily reproduced, whereas P3 and P5 are defined as special-type configurations requiring more specific setup. Table 4.4 shows the resulting relationship between target property groups, evidence channels, photograph configurations, and prompt modules.

Table 4.4 — Relationship Between Input and Output Requirements

Target Property Group	Evidence Requirements	Evidence Channel	Photographs Used	Main Prompt Elements
Thickness, GSM	Scale orientation, overall appearance, macro-flatness	2D	P1 + P2	E02, E03, E10, E13
Tensile forces at small elongations	Signals of directional deformation and resistance to formation under controlled manipulation	3D	P4, P6	E02, E03, E04, E10, E12, E13
Cantilever bending-related distances	Curvature / sagging / spacing between folds under the action of gravity	3D	P3, P6	E02, E03, E04, E10, E13
DC and DC_{SFM}	3D silhouette, number / depth of folds, deformation under the action of gravity	3D	P3, P5, P6	E02, E03, E04, E10

The main differences between the prompts are concentrated in three aspects: evidence-fusion strategy, numerical-value presentation mode, and closed-loop mechanism. The evidence-fusion strategy determines whether consistency constraints are applied within a single generation or are gradually strengthened through multiple updates. The numerical-value presentation mode determines whether results are output directly as individual values or first encoded as ranges to reflect uncertainty and then transformed into specific values. The closed-loop mechanism determines whether the results are organized into a verifiable workflow through an intermediate comparison table and a final table with convergence rules applied. Table 4.5 shows the configurable protocol modules.

Table 4.5 — Execution and Output Settings for Prompt Versions

Prompt	Evidence integration and input order	Output mode	Explicit update of previous data	Closed-loop and convergence mechanism	Methodological objective
1	Stepwise application of constraints	Range	No	Implicit	Establishes a conservative structured baseline protocol
2	Integration of P1–P4	Single value	No	Summary table plus final table	Provides directly comparable single values with closed-loop reporting
3	Single-round integration with mandatory use of all photos	Single value	No	Implicit	Provides global consistency constraints in a single pass
4	Stepwise unlocking with iterative updating	Minimum–maximum–mean values	Yes	Nested convergence	Controls drift through verifiable convergence rules
5	Test-based updating and final consolidation	Range → single value	Yes	Progressive narrowing	Standardizes the closed-loop protocol and strengthens verifiability

As shown in Table 4.5, the prompt versions differ mainly in the controlled protocol regulators that govern evidence fusion, value presentation, and organization of output into a verifiable closed-loop workflow.

The prompt structure is provided in Appendix A.

4.3 Calibration and Configuration of the Measurement Protocol

The AI measurement protocol was calibrated and configured using three interrelated procedures. These procedures corresponded to three controlled factors: the prompt protocol, the AI measurement model, and the photographic-evidence protocol. This section describes the methods used to construct the protocol.

1. Calibration of the prompt protocol. The prompt protocol was calibrated using a fixed AI model and fixed photographic-evidence input P1–P4. Five prompt versions were sequentially constructed and compared. The differences between the versions were not described in terms of text length or wording differences, but were recorded according to the activation state of elements, the numerical-output mode, the multi-image fusion mode, and the closed-loop convergence mechanism, as shown in Tables 4.3 and 4.5. Parameters ①–㉔ obtained using each prompt version were compared with the physical reference parameters, and MAPE was used to evaluate the error.

2. Selection of the AI model. GPT-5.1, Gemini 3 Pro, Grok 4.1, and Qwen3-Max received the same photographic evidence P1–P4 and output the complete set of parameters ①–㉔. The results were compared with the corresponding physical reference parameters from Table 4.6, and MAPE was used to evaluate the error. This procedure compared the capabilities of different multimodal AI models for measuring fabric parameters under identical prompts and images.

3.Determination of the photographic-evidence protocol. The photographic-evidence test was divided into three parts. The first part compared P1, P2, and P1 + P2 to determine whether the flat fabric image and close-up texture image provided complementary evidence. The second part compared measurement errors when using P4 at different rotation angles to obtain spiral drape. The third part compared measurement errors when using P6 during hanging of samples cut in the warp, weft, and bias directions. All photographic-evidence protocols were evaluated based on parameters ①–㉔, and MAPE was used to quantitatively assess their errors relative to the physical reference parameters.

These three procedures jointly defined the operating conditions of AI. The first procedure fixed the prompt protocol, the second fixed the AI model, and the third fixed the rules for obtaining photographic evidence. The prompt, model, and image protocol determined through these procedures jointly formed the AI measurement protocol used for subsequent construction of the fabric digital twin (DT). The final AI measurement protocol consisted of the standard prompt component, the selected AI model, the combination of two-dimensional evidence P1 and P2, image P4 with a defined rotation angle, and image P6 with a defined placement direction. P3 and P5 were retained as evidence of drapeability morphology.

4.3.1. Calibration of the Prompt Protocol

Table 4.6 shows the laboratory reference parameters used to calculate APE and MAPE during calibration of the prompt versions.

Table 4.6 — Laboratory Reference Values of the Physico-Mechanical Properties of Fabrics F1–F3

Fabric	Yarn Direction	GSM, g/m^2	Thickness, mm	Tensile force, kgf (cN), after a specified sample elongation, mm					Bending, mm		DC
				1	2	3	4	5	Contact Distance	Moving Distance	
F1	Warp	136.36 ± 3.25	0.33±0.02	0.148±0.01	0.344±0.02	0.555±0.04	0.798±0.07	1.123±0.09	46±1.87	52.8±3.56	0.42±0.01
	Weft			0.030±0.02	0.058±0.04	0.084±0.07	0.111±0.09	0.138±0.11	21.2±0.84	32.6±0.89	
	Bias			0.010±0.01	0.011±0.01	0.016±0.01	0.019±0.01	0.022±0.01	28.8±1.3	37.6±1.14	
F2	Warp	90.91±1.94	0.18±0.01	0.238±0.12	0.647±0.28	1.504±0.55	2.500±0.77	3.654±0.87	13.6±1.82	28.8±0.84	0.33±0.01
	Weft			0.024±0.01	0.047±0.01	0.080±0.02	0.117±0.03	0.158±0.03	9.4±0.67	24.6±0.55	
	Bias			0.010±0.01	0.020±0.01	0.030±0.01	0.040±0.01	0.050±0.01	12.8±0.45	27.2±1.1	
F3	Warp	101.52±2.47	0.15±0.01	0.248±0.11	0.678±0.34	1.190±0.56	1.808±0.82	2.629±1.2	33.3±2.17	42.4±2.88	0.45±0.01
	Weft			0.056±0.01	0.108±0.02	0.161±0.04	0.217±0.04	0.279±0.04	22.6±1.14	33.6±0.89	
	Bias			0.016±0.01	0.034±0.01	0.045±0.01	0.060±0.01	0.072±0.01	24.4±2.3	32.8±3.35	

As shown in Table 4.6, the three fabrics have pronounced differences across all indicators. The combined results show that the fabrics differ from one another, providing a broad basis for the subsequent tests.

The route for obtaining AI parameters was iteratively calibrated through the development of the prompt protocol. Calibration was carried out using a fixed AI model and a stable set of photographic evidence P1–P4. The main part of the prompt described elements E01–E15, the numerical-output mode, the order of integrating photographic evidence, and the convergence mechanism, because these structural differences determined the measurement conditions.

Figure 4.3 shows the MAPE values for the parameters estimated by the GPT-5.1 model using prompt versions 1–5, grouped by property category.

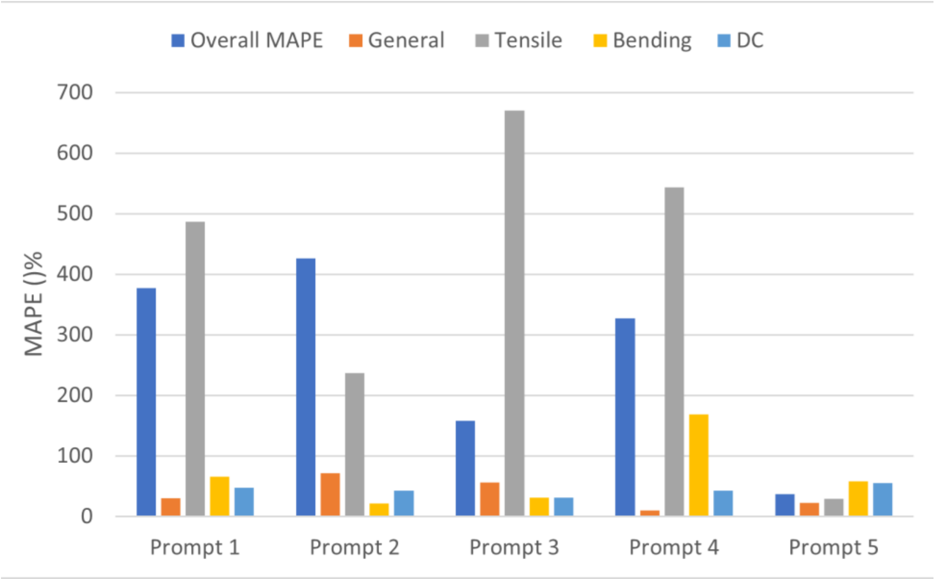

Figure 4.3 — MAPE Values for Indicators Estimated by AI for Prompts 1–5

As shown in Figure 4.3, the errors depend strongly on the prompt structure. Prompts 1 and 2 produce high and unstable errors, while Prompt 3 substantially reduced the overall error level. Prompt 4 confirmed that additional protocol constraints do not automatically improve measurement accuracy. Prompt 5 achieved the lowest overall MAPE value, equal to 37%, and had the most suitable structure among the five versions. The grouped errors also show that tensile parameters are the main source of error, indicating the high variability of this parameter group.

The results of the five prompts were compared with the corresponding laboratory results. Table 4.7 compares the fabric property indicators of F1 obtained through AI estimation with those measured by traditional methods.

Table 4.7 — Property Indicators Estimated Using Prompts 1–5 and the Corresponding Contact Laboratory Measurement Results for F1

Indicator code (Table 2.5)	Indicator assessed by the proposal					Real value obtained using the traditional method
	1	2	3	4	5	
①	0.4	0.55	0.45	0.32	0.36	0.33
②	190	240	240	160	185	136.36
③	0.21	0.09	0.27	0.11	0.2	0.148
④	0.36	0.18	0.716	0.21	0.53	0.344
⑤	0.57	0.32	1.161	0.32	0.86	0.555
⑥	0.87	0.49	1.607	0.42	1.19	0.798
⑦	1.5	0.68	2.052	0.5	1.52	1.123
⑧	0.165	0.07	0.2	0.09	0.03	0.03
⑨	0.27	0.13	0.38	0.18	0.057	0.058

⑩	0.4	0.2	0.56	0.27	0.085	0.084
⑪	0.59	0.27	0.74	0.39	0.111	0.111
⑫	0.78	0.32	0.92	0.5	0.14	0.138
⑬	0.085	0.06	0.14	0.07	0.006	0.01
⑭	0.14	0.08	0.182	0.15	0.008	0.011
⑮	0.185	0.1	0.224	0.23	0.009	0.016
⑯	0.23	0.12	0.266	0.34	0.01	0.019
⑰	0.25	0.13	0.308	0.44	0.012	0.022
⑱	40	34	30	115	34	46
⑲	43	42	27	62.5	81	52.8
⑳	48	30	20	108	29	21
㉑	51	38	45	67.5	72	32.6
㉒	60	24	40	85	30	28
㉓	62	34	30	82.5	76	37.6
㉔	0.62	0.6	0.55	0.6	0.65	0.42
MAPE, %	377	426	158	327	37	-

As shown in Table 4.7, the enrichment of the prompts with additional information led to a reduction in error across all parameters: the overall MAPE value changed from 377% in Prompt 1 to 37% in Prompt 5. These changes show that prompt improvement was not a simple linear process, but was accompanied by a redistribution of errors among the selected indicators. At the level of individual parameters, the advantage of Prompt 5 did not lie in every parameter becoming the closest to the laboratory reference value. For example, parameter ① was closer to the laboratory reference value in Prompt 4, parameter ⑳ in Prompt 3, and parameter ㉒ in Prompt 2. The advantage of Prompt 5 was manifested primarily at the level of the complete parameter set and in the reduction of the overall MAPE value to 37%. Therefore, Prompt 5 was selected as the standard protocol.

To further study the influence of prompt structure on parameter-estimation accuracy, its effect was compared across four sequential transitions: Prompt 1 → Prompt 2, Prompt 2 → Prompt 3, Prompt 3 → Prompt 4, and Prompt 4 → Prompt 5. Table 4.8 shows the protocol changes and the evolution of parameter-level errors between adjacent prompt versions.

Table 4.8 — Protocol Changes and Evolution of Parameter-Level Errors Between Adjacent Prompt Versions

Indicator	Core Prompt Adjustment			
	1→2	2→3	3→4	4→5
Number of Enhanced Parameters	16	3	15	15

Number of degraded parameters	8	21	9	9
Average ΔAPE across 24 encoded parameters, %	+49	−268	+169	−290
Enhanced codes	③, ⑧–⑰, ⑳–㉔	①, ⑳, ㉔	①–⑭, ⑲	⑦–⑱, ⑳, ㉒–㉓
Degraded codes	①–②, ④–⑦, ⑱–⑲	③–⑲, ㉑–㉓	⑮–⑱, ⑳–㉔	①–⑥, ⑲, ㉑, ㉔
Greatest improvement	⑯ Diagonal elongation of 4 mm (−578.9%)	⑳Contact distance during weft-wise bending (−38.1%)	⑬ Diagonal extension, 1 mm (−700%)	⑰ Diagonal tension, 5 mm (−1854.5%)
Greatest Deterioration	①Thickness (+45.5 pp)	⑭Diagonal elongation of 2 mm (+927.3%)	⑰Diagonal elongation, 5 mm (+600%)	⑲Bending displacement (warp direction) (+35%)

Note: ΔAPE denotes the change in APE expressed in percentage points. A negative value indicates a decrease in error, whereas a positive value indicates an increase in error.

As shown in Table 4.8, the generation iteration redistributed errors at the parameter level. The transition from Prompt 2 to Prompt 3 showed the most pronounced imbalance in terms of the number of parameters: only three parameters improved, while 21 parameters worsened. Although the mean ΔAPE across the 24 coded parameters decreased by 268 percentage points, the prompt modification did not provide a uniform improvement in parameter stability, especially for tensile parameters at small elongations and bending parameters. By contrast, the transition from Prompt 4 to Prompt 5 produced the largest reduction in APE, reaching 290 percentage points across the 24 parameters.

Thus, prompt calibration defined the standard protocol version for subsequent AI measurements. Prompt 5 combined evidence boundaries, physical constraints, structured output, iterative updating, closed-loop summarization, and progressive range narrowing. This configuration provided the lowest overall MAPE among the five versions and was used as the fixed protocol for subsequent AI model selection and photographic protocol determination.

4.3.2 Selection of the AI Model

The AI measurement model was selected using a fixed prompt protocol and the same photographic-evidence set P1–P4. GPT-5.1, Qwen3-Max, Gemini 3 Pro, and Grok-4.1 received the same input image set and output the complete set of parameters ①–㉔. The obtained values were compared with the laboratory reference values, and the overall MAPE was used as the main indicator for selecting the AI model. Table 4.9 shows the results used to select the AI model under the calibrated prompt protocol for fabric F1.

Table 4.9 — Results of Estimating Fabric F1 Property Indicators Using Different AI Models

Parameter code	Parameter value estimated by AI				Real value obtained using the traditional method
	GPT-5.1	Qwen3-Max	Gemini 3 Pro	Grok-4.1	
①	0.36	0.20	0.315	0.44	0.33
②	185	130	152.5	220	136.36
③	0.2	0.6	0.39	2.28	0.148
④	0.53	1.59	1.043	3.85	0.344
⑤	0.86	2.58	1.696	5.18	0.555
⑥	1.19	3.57	2.349	6.48	0.798
⑦	1.52	4.56	3	7.65	1.123
⑧	0.03	0.085	0.058	0.34	0.03
⑨	0.057	0.162	0.11	0.48	0.058
⑩	0.085	0.238	0.162	0.6	0.084
⑪	0.111	0.315	0.214	0.72	0.111
⑫	0.14	0.391	0.267	0.85	0.138
⑬	0.006	0.016	0.0105	0.06	0.01
⑭	0.008	0.02	0.0135	0.07	0.011
⑮	0.009	0.025	0.0165	0.09	0.016
⑯	0.01	0.029	0.0195	0.1	0.019
⑰	0.012	0.035	0.023	0.13	0.022
⑱	34	27	46	24.5	46
⑲	81	36	56	35	52.8
⑳	29	23	32	14.5	21

㉑	72	32	42	28	32.6
㉒	30	25	40	19.5	28
㉓	76	35	50	31	37
㉔	0.65	0.55	0.44	0.45	0.42
MAPE, %	37	129	68	446	-

As shown in Table 4.9, GPT-5.1 achieved the lowest MAPE value of 37%. GPT-5.1 showed higher overall consistency across the complete parameter set, especially in the group of tensile parameters and in several bending-related parameters. Gemini 3 Pro produced plausible values for ①, ⑱, and ㉔. Qwen3-Max showed more substantial deviations in tensile parameters at small elongations, while Grok-4.1 produced the highest overall MAPE value because of large errors in most tensile parameters. These results show that model selection was necessary, since the same prompt caused considerable variation across different AI models.

The errors for the parameters were converted into scores as “100 − MAPE”; if MAPE exceeded 100%, the score was set to 0. Therefore, a higher score indicates a lower error in the corresponding parameter category. Figure 4.4 shows the distribution of scores for the parameter groups.

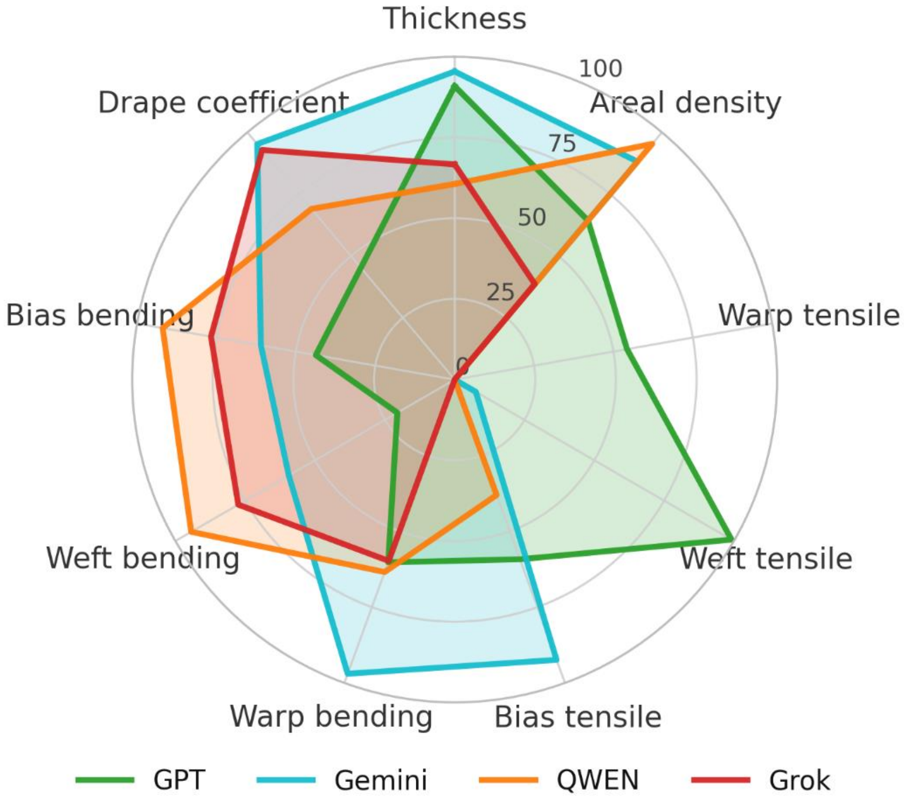

Figure 4.4 — Radar Chart for Different AI Models

As shown in Figure 4.4, the models demonstrate different effectiveness at the parameter level. GPT-5.1 showed the most balanced overall profile, especially for thickness, weft-direction tensile behavior, and DC, whereas its score for parameters related to bending in the bias direction was relatively low. Gemini 3 Pro showed high scores for thickness, DC, parameters related to bending in the warp direction, and tensile behavior in the bias direction; however, its score for warp-direction tensile behavior was close to 0, indicating a serious deviation in this parameter category. Qwen3-Max performed well for GSM and bending-related parameters, but its scores for tensile parameters were generally lower. Grok-4.1 showed acceptable results for DC and bending-related categories; however, its scores for thickness, GSM, and tensile parameters were low. These results confirm that the differences between the models were not limited only to the overall MAPE presented in Table 4.9. Each model has strengths and weaknesses at the parameter-category level, while GPT-5.1 provides the most balanced structure of output values among the four tested AI models.

4.3.3 Determination of the Photographic-Evidence Set

Based on the comprehensive comparison, GPT-5.1 was selected as the main AI model for the subsequent study.

Selection of photographs. To determine the influence of the number of fabric photographs on the accuracy of parameter estimation, three prompts with different photograph sets were compared: P1, P2, and P1 + P2. The MAPE error was decomposed into four groups: basic physical properties, including two parameters, namely thickness and GSM; tensile parameters, including 15 parameters; bending parameters, including six parameters; and DC, including one parameter. Table 4.10 shows the MAPE values for fabric F1.

Table 4.10 — Comparison of MAPE for P1, P2, and P1 + P2 Input Data for F1

Input Photograph	MAPE values, %			Relative Error for DC, %	Overall MAPE, %
	General Properties	Tensile Parameters	Bending Parameters		
P1	63.05	103.21	97.84	11.90	94.71
P2	41.52	221.29	75.21	35.71	162.06
P1+P2	70.38	27.80	108.87	26.19	51.55

As shown in Table 4.10, after the photographic evidence P1 and P2 was combined, the MAPE for tensile parameters decreased to 27.8%, and the overall MAPE decreased to 51.55%. Combining the photographs made it possible to reduce the overall MAPE; therefore, P1 and P2 were retained as mandatory components of the prompt, and their combination provided the lowest overall error and substantially improved the estimation results for the most unstable parameter group.

Image P4 required justification of the rotation angle for obtaining spiral folds, since spiral deformation changes the visible density of folds and the length of their propagation. Three possible controlled rotation angles were selected: 180°, 360°, and 540°. The obtained parameters were evaluated using overall MAPE, MAPE for tensile parameters, MAPE for bending parameters, and APE for DC. Table 4.11 shows the error values at different P4 rotation angles.

Table 4.11 — Influence of the Rotation Angle in Photograph P4 on Measurement Error for Fabric F1

Rotation Angle	MAPE values, %			Relative Error for DC, %
	Tensile	Bending	Overall	
180°	113.62	160.06	113.91	11.9
360°	28.37	135.66	54.85	4.76
540°	282.07	94.96	202.66	0

As shown in Table 4.11, twisting by 360° led to the lowest overall MAPE value, equal to 54.85%. This indicates that the 360° condition provides a more balanced fabric deformation for estimating tensile parameters at small elongations and for estimating DC. Although twisting by 540° provided APE = 0 for DC and a relatively low MAPE for bending parameters, it caused a strong overestimation of tensile parameters: the MAPE for tensile parameters increased to 282.07%, and the overall MAPE increased to 202.66%. Therefore, 360° was selected as the standard P4 rotation angle.

Photograph P6, which records hanging on a column, shows visible sagging and folds that depend on the cutting direction. Therefore, three sample-placement variants were tested: along the warp, along the weft, and along the bias. Table 4.12 shows the grouped MAPE values used to select the P6 placement conditions.

Table 4.12 — Influence of the Sample Cutting Direction in Photograph P6 on Measurement Error for Fabric F1

Cutting direction of the sample in photograph P6	MAPE values, %			Relative Error DC, %
	Tensile	Bending	Overall	
Основа	22.94	33.19	34.10	42.86
Уток	48.85	146.20	127.55	30.95
Диагональ 45°	71.58	40.15	62.44	59.52

As shown in Table 4.12, placing the sample along the warp direction provided the lowest overall MAPE value and the lowest errors in the groups of basic physical properties, tensile parameters, and bending parameters. These results show that the image in photograph P6 of the sample cut in the warp direction provides the most balanced estimation results. Therefore, P6-Warp was selected as the standardized placement for subsequent AI-based parameter acquisition.

Thus, based on the analysis of the results presented in Tables 4.10–4.12, the following photographs were included in the prompt-construction protocol:

- photographs P1 + P2 were used as mandatory evidence for visualizing the 2D state of fabrics;
- photograph P4 was used for visualizing the ability of the fabric to undergo spiral twisting at 360°;
- photograph P6 was used for visualizing the response of the fabric to gravity in the warp direction.

Independent contribution of each photograph. To quantitatively evaluate the independent contribution of each photograph and exclude interaction effects arising from the combination of several photographs, six photograph types were studied as independent inputs for estimating the parameters of three fabrics, F1, F2, and F3. In each test, the prompt remained unchanged, and only the photograph type was varied. Table 4.13 shows whether a single-photograph prompt could support output of the complete parameter set.

Table 4.13 — MAPE for All Parameters When a Single Photograph P1–P6 Was Included in the Prompt

Photograph Type (Single Input)	MAPE, %, for fabrics		
	F1	F2	F3
P1	94.71	6.89	30.19
P2	162.06	19.55	35.93
P3	48.68	48.33	34.23
P4	54.85	67.9	85.18
P5	71.8	10.8	59.4
P6	34.1	139.38	38.74

As shown in Table 4.13, the contribution of each single photograph differs markedly among the three fabrics: the comparison confirms that no photograph type provides a consistently low error for all three fabrics. For example, photograph P6 is the most effective single input for fabric F1, but it produces a high error for fabric F2. These results show that visual data from one photograph are insufficient as a general protocol for outputting the complete parameter set.

To further determine whether a single photograph is sufficient for different fabrics, since using only the lowest MAPE value as a criterion was considered insufficient for generalization, the mean, median, SD, and descriptive 95% confidence interval were calculated for each photograph. This statistical processing is important for separating the mean error level and establishing the spread between fabrics. Table 4.14 presents the statistical data used to evaluate the influence of each photograph.

Table 4.14 — Statistical Processing Results for the Influence of Photographs on the Accuracy of Estimating Indicators for All Fabrics F1–F3

Photograph Type	Statistical estimates of MAPE, %				Inter-Fabric Interpretation
	Mean	Median	Dispersion	Confidence interval	
P1	43,93	30,19	45,49	[0; 156,93]	Competitive mean error level, but fabric-dependen
P2	72,51	35,93	77,98	[0; 266,23]	High instability between fabrics
P3	43,75	48,33	8,24	[23,28; 64,22]	Lowest mean error and lowest dispersion
P4	69,31	67,90	15,21	[31,53; 107,09]	Relatively stable, but with a high mean error
P5	47,33	59,40	32,24	[0; 127,42]	Effective for fabric F2, but less stable between fabrics
P6	70,74	38,74	59,49	[0; 218,53]	Effective for fabrics F1 and F3, but unstable for fabric F2

As shown in Table 4.14, photograph P3 provided the highest inter-fabric stability among the six inputs and all photographs: the mean MAPE was 43.75%, SD was 8.24%, and the 95% confidence interval was [23.28; 64.22].

These results are consistent with the statistically confirmed influence of single photographs in Table 4.13: P3 showed the smallest dispersion for all fabrics F1–F3; however, its mean MAPE remained at 43.75%. The large spread in Table 4.14 shows that the error when using one photograph depends not only on the photograph type, but also on the fabric type. To statistically test this assumption, a two-factor analysis of variance was performed. Photograph type and fabric type were considered fixed factors, while parameter dimension was considered a blocking factor. Table 4.15 shows the statistical indicators used to evaluate the influence of photograph type, fabric type, and their interaction on absolute percentage error, APE.

Table 4.15 — Analysis of Variance for the Influence of Photograph Type, Fabric, and Their Interaction Effects

Source of Variation	Degrees of Freedom, df1; df2	Fisher's F-Test	p-Value	Effect Size ηp^2
Photograph type (P1–P6)	5, 391	6,16	$1,63 \times 10^{-5}$	0,073
Fabric type (F1–F3)	2, 391	17,17	$7,12 \times 10^{-8}$	0,081
Photograph type × fabric type	10, 391	22,46	$3,41 \times 10^{-33}$	0,365

Note: df1 and df2 denote the degrees of freedom of the factor and the residual error, respectively. Fisher’s F-test is used to test the statistical significance of the factor effect. The p-value indicates the level of statistical significance. ηp^2 denotes partial eta squared and is used to evaluate effect size. All indicators in the table are dimensionless.

As shown in Table 4.15, photograph type had a statistically significant effect on the APE of individual parameters: $F = 6.16$, $p = 1.63 \times 10^{-5}$, $\eta p^2 = 0.073$. The small p-value shows that the differences between photographs P1–P6 were statistically stable. However, $\eta p^2 = 0.073$ indicates a small effect size; therefore, photograph type influenced the error, but was not the main source of variation.

Fabric type also had a statistically significant effect on estimation error: $F = 17.17$, $p = 7.12 \times 10^{-8}$, $\eta p^2 = 0.081$. This confirms that estimation errors differed among fabrics F1, F2, and F3. At the same time, the effect size was also limited.

The largest effect size was obtained for the interaction between photograph type and fabric type: $F = 22.46$, $p = 3.41 \times 10^{-33}$, $\eta p^2 = 0.365$. This shows that the accuracy of estimation from a single photograph depended on the fabric type. Consequently, photographs P1–P6 are not fully universal sources of visual data for all fabrics.

To further determine whether a single photograph can influence DC values, the laboratory values adopted as references were compared with DC values generated from single photographs P1–P6. This comparison focused on whether one type of visual data could reliably serve as a basis for estimating fabric drapeability. Table 4.16 presents the DC values obtained from single photographs and the corresponding laboratory reference values.

Table 4.16 — Comparison of DC Values Obtained by GPT-5.1 Using a Single Photograph with Laboratory Reference Valu

Fabric	Drape coefficient DC						
	Real DC Value	Result of assessment based on a photograph					
		P1	P2	P3	P4	P5	P6
F1	0.42	0.5	0.48	0.59	0.53	0.34	0.45
F2	0.33	0.29	0.32	0.30	0.27	0.31	0.31
F3	0.45	0.42	0.41	0.41	0.43	0.40	0.39

As shown in Table 4.16, among the six photographs, photograph P6 provided the most accurate DC value for fabric F1. For fabric F2, DC values close to the real value were provided by photographs P2, P5, and P6. For fabric F3, all predicted DC values were lower than the laboratory reference value of 0.45, and photograph P4 gave the closest result, 0.43. These results show that DC estimation also depends on the photograph type.

The numerical DC values presented in Table 4.16 were further examined at the morphological level, since DC deviation may be manifested not only in the numerical result, but also in the shape of the draped virtual sample itself. For this purpose, the laboratory baseline variant was compared with virtual samples generated based on parameters obtained by AI using single photographs. Table 4.17 shows the laboratory baseline variant and the virtual samples with the maximum deviation from the laboratory result.

Table 4.17 — Visual Comparison of the Laboratory Sample and Virtual Samples Generated Based on AI Parameters

Fabric	Appearance of samples during measurement of the drape coefficient (DC)		Photo of fabric in prompt
	Laboratory session	AI-generated	
F1	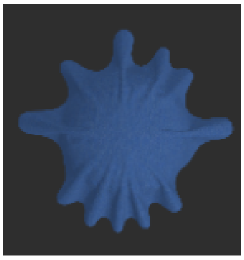	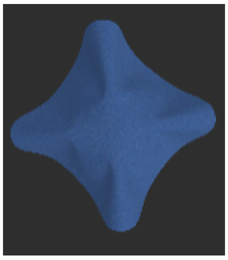	P3
F2			P3
F3	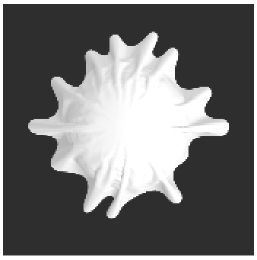	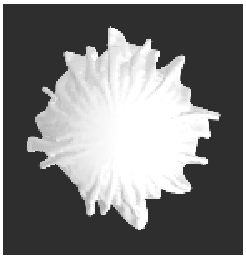	P6

As shown in Table 4.17, the numerical deviations presented in Table 4.16 were reflected in the morphology of the simulated draped sample. For fabric F1, the result obtained from P3 showed the largest structural deviation: the laboratory baseline variant had several radial folds and a relatively complex fold contour, whereas the result obtained from photograph P3 had a smoother four-fold contour with insufficient fold separation. This indicates that photograph P3 is insufficient for reproducing the complex draped surface of fabric F1. For fabric F2, the result obtained from photograph P3 did not completely lose the radial drape structure; however, the fold distribution became more concentrated and less uniform compared with the laboratory baseline variant. The deviation was manifested mainly in changes in the distance between folds and in fold density. For fabric F3, the result obtained from photograph P6 showed excessive fragmentation of the outer contour and denser local folds compared with the laboratory baseline variant, indicating that the fabric appearance in the suspended-state photograph did not correspond to its deformation behavior.

The results show that the instability of input data from a single photograph is not limited to numerical error, but also changes the morphology of the draped sample. A photograph with a single 2D or 3D view may reinforce one type of visual feature while simultaneously weakening another deformation capacity required for estimating the full set of physico-mechanical property indicators. Overall, the analysis of the influence of single photographs showed that one isolated image source cannot provide a sufficiently stable basis for estimating the complete parameter set.

Selection of the photographic-image group. After analyzing the results for single photographs, the further test was directed toward determining a rational combination of 2D and 3D photographic evidence. For fabrics F1–F3, single inputs P1–P6, the 2D baseline configuration P1 + P2, and four hybrid configurations were compared; in the hybrid configurations, one 3D view was added to P1 + P2: P1 + P2 + P3, P1 + P2 + P4, P1 + P2 + P5, and P1 + P2 + P6. For each configuration, MAPE was calculated for the complete parameter set ①–㉔. Figure 4.5 shows the error distribution for single, 2D-baseline, and hybrid photographic configurations for fabrics F1–F3

.

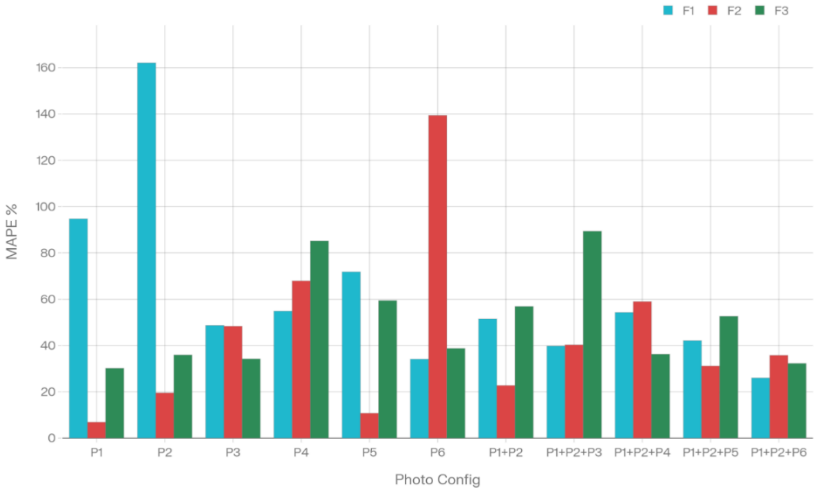

Figure 4.5 — Influence of Photograph Integration on AI Measurement Accuracy

As shown in Figure 4.5, the effect of photograph integration differed for F1, F2, and F3. For fabric F1, the single photograph P6 produced an error across all parameters with MAPE = 34.1%, while the photograph configuration P1 + P2 + P6 reduced the error to 26%, indicating the importance of the image of the fabric in the suspended state. For fabric F3, the configuration P1 + P2 + P6 also provided the lowest MAPE value, 32.29%. These results show that photograph P6 improves estimation accuracy because it provides useful information about the distance between folds and edge curvature.

However, the same photograph configuration was not effective for fabric F2. The baseline photograph configuration P1 + P2 produced a MAPE value of 22.71%, and adding photograph P6 with additional 3D effects did not reduce the error. Therefore, two cases were identified: the P1 + P2 + P6 combination improves measurement accuracy for fabrics F1 and F3, while no such positive effect was observed for fabric F2.

To compare the measurement difficulty of different parameters, parameter errors were grouped by category. Figure 4.6 shows the mean MAPE for different parameter groups aggregated across fabrics F1–F3. Here, ③–⑦ denote tensile parameters at small elongations in the warp direction, ⑧–⑫ denote tensile parameters at small elongations in the weft direction, ⑬–⑰ denote tensile parameters at small elongations in the bias direction, ① denotes thickness, and ② denotes GSM.

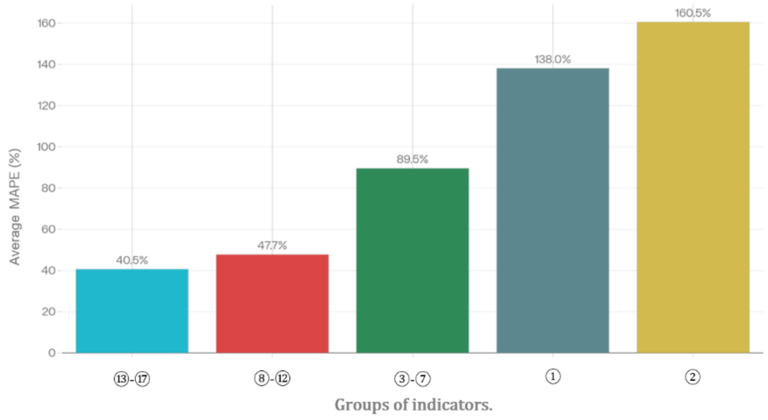

Figure 4.6 — Ranking of Textile Material Property Parameter Groups by Mean MAPE for Fabrics F1–F3

As shown in Figure 4.6, different parameter groups formed a clear hierarchy of measurement accuracy. The group of bias-direction tensile parameters ⑬–⑰ reached the lowest mean MAPE, equal to 40.5%, followed by the group of weft-direction tensile parameters ⑧–⑫, with a value of 47.7%. The group of warp-direction tensile parameters ③–⑦ showed a noticeably higher mean MAPE, indicating higher variability in the warp direction. The two basic physical property parameters had the highest errors: thickness ① reached 138%, and GSM ② reached 160.5%.

These results show that, under the aggregation scheme used in Figure 4.6, the groups of tensile parameters at small elongations in the bias and weft directions produced lower mean errors than thickness and GSM. This does not mean that all tensile parameters were stable; the group of warp-direction tensile parameters still showed a high MAPE, which is consistent with the earlier observation regarding the sensitivity of tensile results in the small-elongation region to the protocol and photograph configuration. By contrast, thickness and GSM did not have stable direct visual supports and therefore showed substantially higher mean errors. This result demonstrates that the measurability of different parameter categories is not the same. Accordingly, AI-based parameter acquisition should be interpreted separately for low-stress mechanical parameters and basic physical properties.

To determine the influence of 2D and 3D photographs on errors, photographs P1 + P2 were used as the 2D baseline configuration against which 3D photographs and the hybrid variant consisting of 2D + 3D photographs were compared. This comparison was used to determine the effective boundary of 3D photograph application for different fabrics. Table 4.18 contains the MAPE values for the baseline 2D photograph configuration, 3D-only photographs, and 2D + 3D photograph configurations.

Table 4.18 — MAPE Values for 3D and 2D + 3D Photograph Configurations Compared with the 2D Baseline Configuration

Fabric	MAPE for Baseline Configuration P1 + P2, %	Best 3D photo			Best 2D + 3D Photograph Configuration		
		Photograph	MAPE	Relative Change, %	Photograph	MAPE	Relative Change, %
F1	51,55	P6	34,10	−33,9	P1+P2+P6	26	−49,6
F2	22,71	P5	10,80	−52,4	P1+P2+P5	31,12	+37,0
F3	56,90	P3	34,23	−39,8	P1+P2+P6	32,29	−43,3

As shown in Table 4.18, the contribution of 3D photographs differed noticeably among the three fabrics. For fabric F1, the best 3D photograph was P6, corresponding to a relative improvement of 33.9% compared with the baseline configuration P1 + P2. When P6 was combined with P1 + P2, MAPE further decreased to 26%.

For fabric F2, the best 3D photograph was P5. However, the best hybrid configuration, P1 + P2 + P5, increased MAPE to 31.12%, corresponding to a deterioration of 37.0% relative to the baseline configuration. This result shows that a 3D photograph that is effective when used alone does not necessarily remain effective after being combined with 2D photographs.

The key distinction in Table 4.18 is that the best 3D photographs when used alone do not always retain their effectiveness after being combined with flat photographs, and the hybrid configuration should be evaluated based on the achieved result rather than only on the number of photographs.

To further verify the influence of hybrid photographic configurations, the DC parameter was examined separately. The laboratory DC value was compared with the results obtained using the 2D baseline configuration P1 + P2 and four hybrid configurations in which one 3D view was added to P1 + P2: P1 + P2 + P3, P1 + P2 + P4, P1 + P2 + P5, and P1 + P2 + P6. This comparison made it possible to determine whether the added 3D view brings the DC value closer to the laboratory reference or causes drift. Table 4.19 shows the DC values used to evaluate convergence and drift for the 2D-baseline and hybrid photographic configurations.

Table 4.19 — DC Convergence and Drift Between the 2D Baseline Configuration and Hybrid Inputs

Fabric	Value of the circular drape coefficient (DC)					
	Real DC Value	P1+P2	P1+P2+P3	P1+P2+P4	P1+P2+P5	P1+P2+P6
F1	0.42	0.50	0.29	0.35	0.33	0.34
F2	0.33	0.30	0.28	0.30	0.29	0.30
F3	0.45	0.58	0.44	0.41	0.64	0.43

As shown in Table 4.19, adding a third image to the baseline configuration P1 + P2 did not lead to a stable improvement in DC prediction. For F1, the baseline configuration P1 + P2 produced DC = 0.50, which was higher than the laboratory reference value of 0.42. After adding the third image, all four hybrid inputs produced lower DC values in the range from 0.29 to 0.35. Among them, the configuration P1 + P2 + P4 produced the closest value, 0.35; however, this result still underestimated the laboratory reference DC value. This shows that adding 3D deformation data corrected the overestimation caused by P1 + P2 and introduced an underestimation tendency for fabric F1.

For fabric F2, all combined photographic inputs produced relatively close DC values in the range from 0.28 to 0.30 compared with the laboratory reference value of 0.33. The configurations P1 + P2, P1 + P2 + P4, and P1 + P2 + P6 produced a value of 0.30, showing that adding one 3D view did not substantially change the DC output value for this fabric. For F3, the baseline configuration P1 + P2 overestimated DC to 0.58, whereas P1 + P2 + P3 and P1 + P2 + P6 reduced the values to 0.44 and 0.43, respectively; both values were closer to the laboratory reference value of 0.45. However, P1 + P2 + P5 increased DC to 0.64, showing that not all 3D evidence improved convergence.

At the DC level, the added 3D view did not provide a unified direction of convergence: DC convergence depends on the fabric type and the added deformation view.

To further determine whether there is a relationship between the numerical deviations of three-photograph hybrid inputs and the final drape morphology, the baseline simulation was compared with the hybrid simulation that produced the maximum deviation for each fabric. The purpose of this comparison was not only to verify the DC value, but also to evaluate whether incompatible integration of visual evidence distorts the outer contour, fold distribution, and local fold structure. Table 4.20 presents the hybrid cases with maximum deviation used to analyze the morphological consequences of incompatible evidence integration.

Table 4.20 — Visual Comparison of Morphological Deviations Caused by Hybrid Photographic Inputs with Maximum Deviation

Fabric	Laboratory Baseline Varian	Case with Maximum Deviation	Source of Deviation

F1	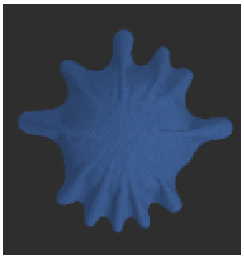	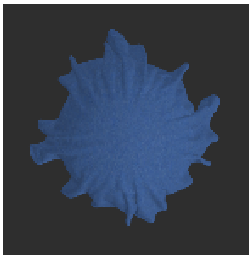	P1+P2+P3
F2		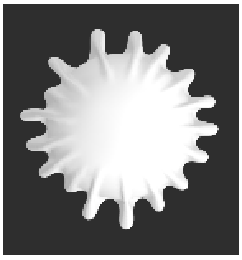	P1+P2+P3
F3	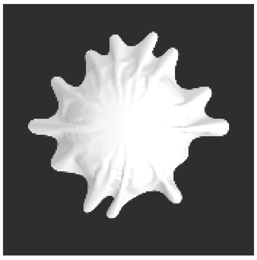	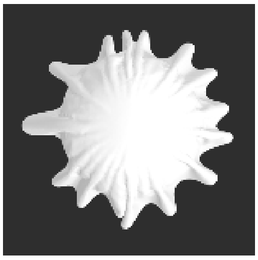	P1+P2+P5

As shown in Table 4.20, the numerical deviations identified in Table 4.19 were reflected in the morphology of the simulated drape. For F1, the case with the maximum deviation was obtained using the configuration P1 + P2 + P3. Compared with the laboratory baseline variant, the hybrid simulation showed a denser and more irregular outer contour, with increased fold subdivision and reduced smoothness of the radial contour. This indicates that adding P3 introduced a deformation feature that changed the original drape structure rather than stabilizing it.

For F2, the configuration P1 + P2 + P3 also led to the maximum deviation. The simulated drape retained the general radial form; however, the distance between folds became more open, and the local folds became less fine than in the laboratory baseline variant. This result shows that, for F2, the added photograph P3 changed the balance between contour expansion and local fold development, leading to visible morphological drift.

For F3, the largest deviation was caused by the configuration P1 + P2 + P5. Compared with the laboratory baseline variant, the hybrid simulation showed a more expanded silhouette with more pronounced protruding folds and a less compact central structure. This visual change is consistent with the overestimation of DC presented in Table 4.19, where the predicted DC value increased to 0.64 compared with the laboratory reference value of 0.45.

Overall, these comparisons show the morphological consequences of incompatible hybrid evidence. To further compare photograph configurations in terms of error and inter-fabric variability, a local photograph-selection metric was calculated for each configuration. This approach makes it possible to identify the preferred area of “lower selection error — lower variability” in a unified coordinate system and thereby evaluate the balance between accuracy and stability for both single photographs and multi-photograph combinations. Figure 4.7 shows the distribution of accuracy and stability for different evidence configurations based on the local evidence-factor selection metric.

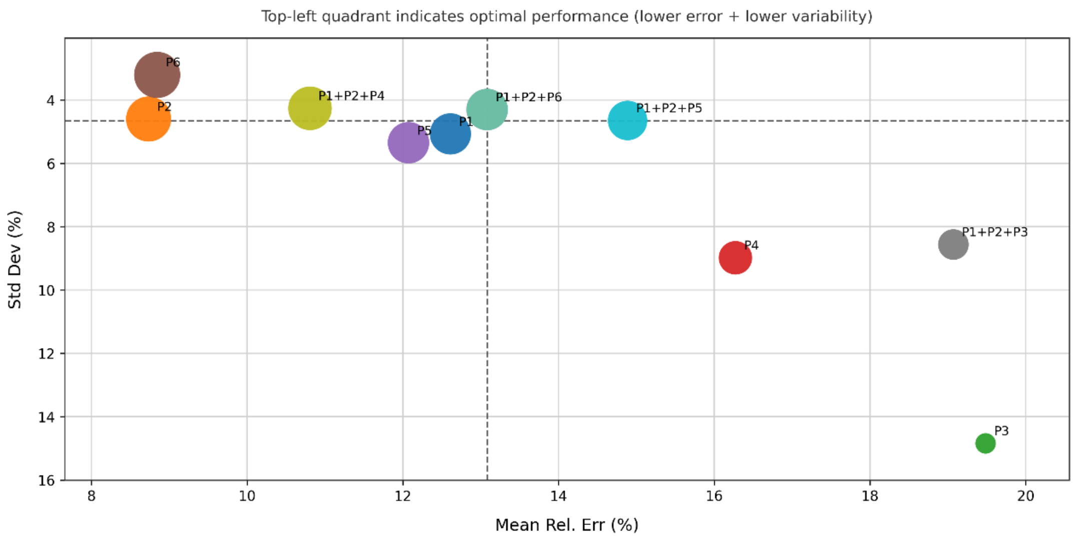

Figure 4.7 — Distribution of Accuracy and Stability for Different Evidence Configurations

As shown in Figure 4.7, the upper-left quadrant corresponds to the most desirable result area, indicating lower local selection error together with lower variability between fabrics. Among the tested configurations, P6 and P2 were located at relatively low levels of local selection error, approximately around 9%, with SD values of approximately 3.2% and 4.5%, respectively. The configuration P1 + P2 + P4 also remained in the low-variability area, with a local selection error of approximately 10.8% and an SD of approximately 4.0%. By contrast, P3 and P1 + P2 + P3 were located in the high-error area, with local selection errors close to 19%–20%; in particular, P3 also showed the largest SD value, approximately 14.9%, indicating weak inter-fabric stability within this additional metric.

The overall distribution shows that the effectiveness of photographic evidence did not improve monotonically with an increase in the number of input images. Some three-photograph configurations, such as P1 + P2 + P6, showed relatively good control of variability, although their local selection error was higher than that of P2 and P6. By contrast, the combination P1 + P2 + P3 showed high local selection error and high variability. Therefore, Figure 4.7 was not used as the sole basis for protocol selection; it was interpreted jointly with the full MAPE value across all parameters, DC convergence, and morphological comparisons.

Additional F1-specific analysis of photographs. To further separate the influence of the number of photographs from the influence of their type, an additional F1-specific analysis was conducted. This analysis used the local photograph-selection metric shown in Figure 4.8. One comparison summarized the error depending on the number of input photographs, whereas the other ranked the six single photographic inputs under the same F1-specific selection condition. Figure 4.8 shows the F1-specific comparison of the effect of photograph number and the ranking of single photographs

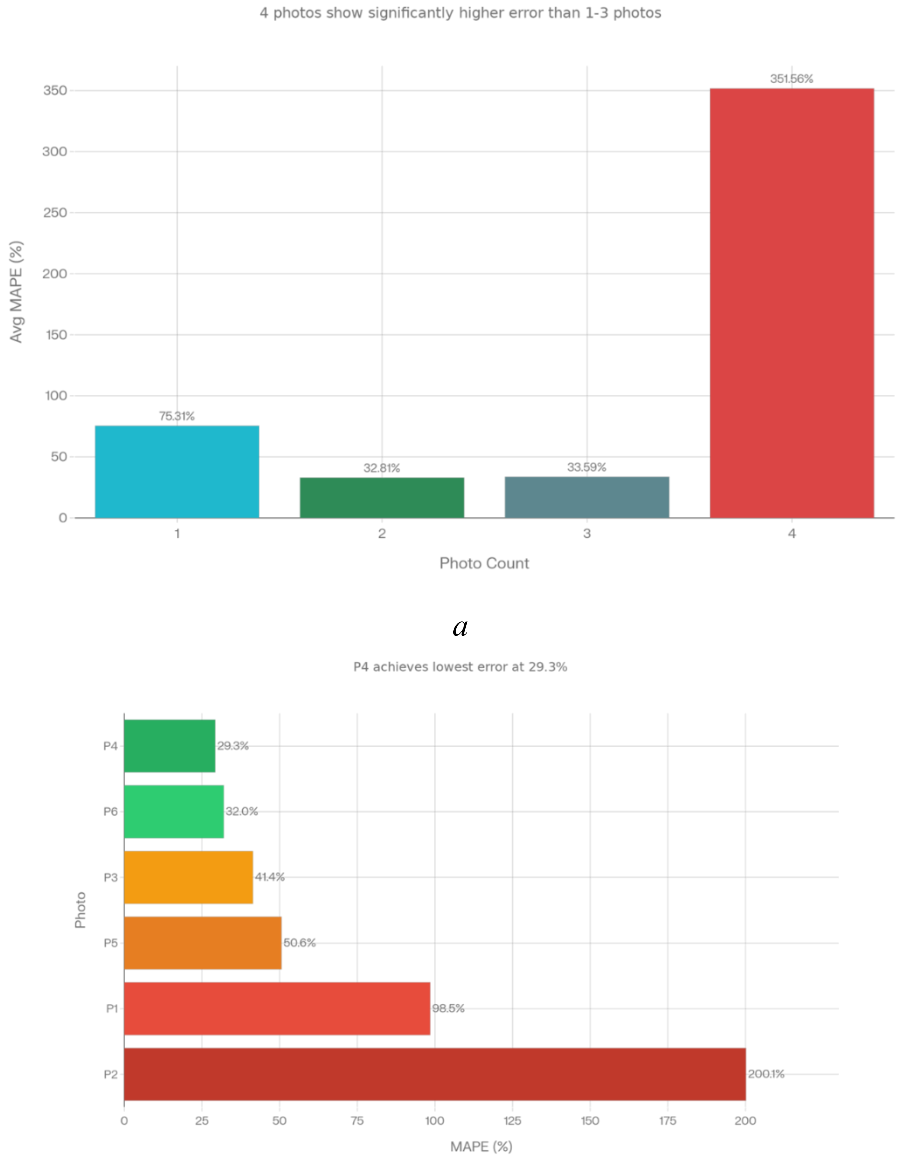

a

b

Figure 4.8 — Influence of the Number of Photographs and the Type of Single Photograph on Local Selection Error for F1: *a* — mean local selection error with different numbers of photographs; *b* — ranking of single input data P1–P6 by local selection error

As shown in Figure 4.8,a, the number of input photographs does not have a monotonic relationship with error reduction. When only one photograph was used, the mean local selection error was 76.3%. Using two photographs noticeably reduced the mean local selection error to 32.3%, while using three photographs produced a close result of 33.3%. However, when the number of photographs increased to four, the mean local selection error rose sharply to approximately 352.0%. This result shows that adding more photographs did not necessarily improve measurement accuracy. On the contrary, excessive or incompatible visual evidence could cause a substantial increase in error.

As shown in Figure 4.8,b, the six single photographic inputs also differed noticeably in effectiveness for F1. This ranking shows that not all sources of single photographic evidence contributed equally to the output of correct parameters. Taken together, Figure 4.8,a and Figure 4.8,b show that error control is determined not only by the number of photographs, but mainly by their type and compatibility.

4.3.4 Formation of the Final Set of Parameters Measured Using Artificial Intelligence

After the standard prompt protocol, the AI model, and the rules for using photographic evidence had been fixed, the AI measurement results were organized according to the parameter coding system defined in Chapter 2. This organization made it possible to compare AI measurements and traditional instrumental measurements in the subsequent modeling stage.

The output values ①–㉔ were combined into a single parameter table. The table includes parameters directly assigned in the Style3D material editor and auxiliary parameters used for error evaluation and physical-consistency verification. Table 4.21 presents the integrated coded parameter vector obtained using the final single-model AI measurement configuration.

Table 4.21 — Set of AI Material Parameters for Generating and Evaluating the Fabric Digital Twin

Parameter Code	F1	F2	F3
①	0.41	0.20	0.18
②	175	110	90
③	0.20	0.127	0.40
④	0.42	0.41	1.00
⑤	0.70	0.81	1.80
⑥	1.08	1.32	2.80
⑦	1.52	1.95	4.24
⑧	0.029	0.013	0.043
⑨	0.058	0.038	0.077
⑩	0.082	0.060	0.119
⑪	0.108	0.073	0.162
⑫	0.132	0.084	0.213
⑬	0.005	0.005	0.011
⑭	0.008	0.011	0.018

⑮	0.009	0.016	0.027
⑯	0.011	0.022	0.036
⑰	0.011	0.027	0.050
⑱	25.00	9.00	23.50
⑲	28.75	19.08	29.85
⑳	21.00	7.00	16.75
㉑	32.55	18.34	24.96
㉒	23.00	8.40	20.00
㉓	30.36	17.89	26.80
㉔	0.69	0.36	0.43
Overall MAPE, %	26.00	35.78	32.29

As shown in Table 4.21, AI produced the smallest error for fabric F1 and the largest error for fabric F2. For all three fabrics, the tensile forces in the warp, weft, and bias directions increased from an elongation of 1 mm to 5 mm, indicating that the output values conformed to the basic physical behavior of tensile deformation in the low-load region. The warp-direction tensile parameters for F2 were generally lower than the corresponding laboratory reference values, whereas those for F3 were generally higher. This comparison shows that directional tensile behavior in the small-elongation region remained a sensitive parameter group in the AI measurement route.

Overall, the route for obtaining parameters using AI was formed through three sequential stages: prompt calibration, AI model selection, and photographic protocol selection. Prompt 5 was selected as the standard protocol because it provided the lowest overall MAPE and a more stable output-value structure. Under the same protocol and identical image-input conditions, GPT-5.1 achieved the lowest overall error and was therefore selected as the main model. Selection of the photographic protocol further fixed the use of 2D photographs P1 + P2, the P4 rotation condition of 360°, and the P6-Warp rule for suspending the sample on the column. The single-model parameter set presented in Table 4.21 was obtained using P1 + P2 + P6-Warp as the final combination of visual evidence. The obtained AI parameter set formed the second material-input route, corresponding to the route of traditional instrumental measurements. Therefore, the validity of this AI-derived material-input route should be evaluated not only by parameter-level error, but also by the drape morphology formed under unified simulation conditions in Style3D.

4.4. Construction of the Fabric Digital Twin Using AI Parameters

4.4.1 Workflow for Constructing the Fabric Digital Twin

The workflow for constructing the fabric digital twin (DT) is based on the relationship between physical reference parameters, photographic evidence, the prompt protocol, AI parameters, and material assignment in Style3D. Figure 4.9 shows the complete workflow for converting photographs and AI parameter outputs into a fabric digital twin.

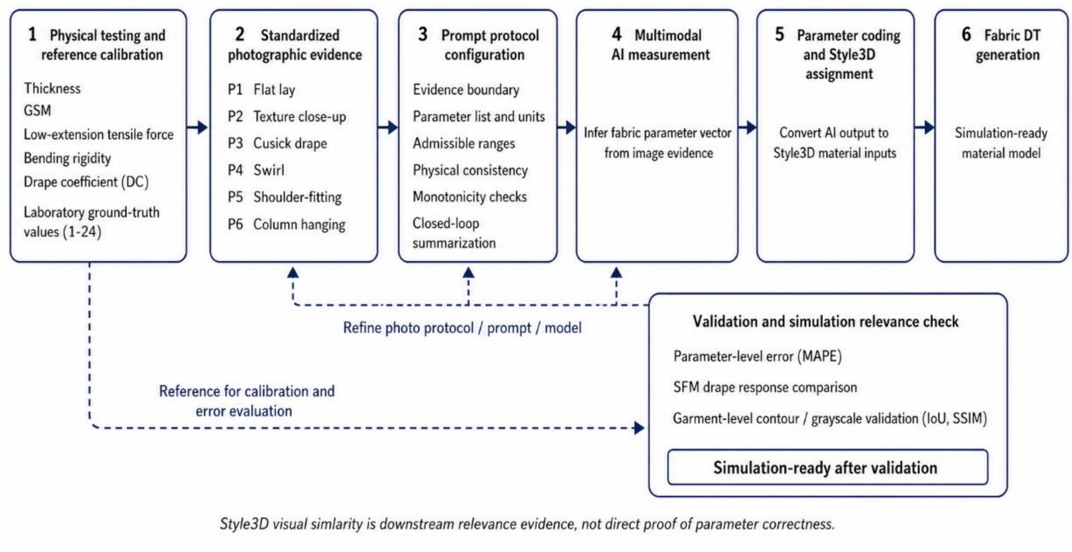

Style3D visual simlarity is downstream relevance evidence, not direct proof of parameter correctness.

Figure 4.9 — Workflow for Constructing the Fabric Digital Twin (DT) Based on AI Measurements

As shown in Figure 4.9, physical testing, photographic evidence, the prompt protocol, AI parameter output, and material assignment in Style3D form a continuous methodological chain. Physical testing provides the reference parameter set ①–㉔ for calibration and error evaluation. The photographic-evidence system provides controlled visual information for AI parameter output. The prompt protocol constrains the AI model through evidence boundaries, admissible parameter ranges, units of measurement, physical-consistency requirements, and closed-loop consolidation. The consolidated AI results are then coded according to Table 4.2 and transferred to Style3D for construction of the fabric digital twin. Parameters measured by AI are considered suitable for subsequent modeling only after parameter-level error evaluation, drape comparison using the new SFM method, and contour or grayscale-response verification at the garment level. Visual similarity in Style3D is considered evidence of adequacy.

4.4.2 Parameter Assignment in the Style3D Material Editor

Codes ①, ②, ③–⑰, ⑲, ㉑, and ㉓ were used to generate the fabric digital twin in Style3D. Figure 4.10 shows the Style3D interface used to input parameters obtained using AI.


测量物理属性

面料类型 梭织　模拟模型 非线...

测量重量和厚度

宽度/高度（毫米） 220.00 x 30.00 (...

厚度（毫米） 0.33

克重 (GSM) 136.36

重量（克） 0.90

测试弯曲强度

	经向	纬向	斜向
伸出长度（毫米）	52.80	32.60	37.60

测量拉伸强度

经向		纬向		斜向	
最大长度(%) 0.00		最大长度(%) 0.00			
长度（毫米）	拉力（kg...	长度（毫米）	拉力（kg...	长度（毫米）	拉力（kg...
1.000	0.148	1.000	0.030	1.000	0.010
2.000	0.344	2.000	0.058	2.000	0.011
3.000	0.555	3.000	0.084	3.000	0.016
4.000	0.798	4.000	0.111	4.000	0.019
5.000	1.123	5.000	0.138	5.000	0.022

Figure 4.10 — Style3D Interface for Parameter Input

As shown in Figure 4.10, Style3D uses thickness ①, GSM ②, tensile forces at small elongations of 1–5 mm in the warp direction ③–⑦, in the weft direction ⑧–⑫, in the bias direction ⑬–⑰, and bending parameters in three directions ⑲, ㉑, and ㉓. The contact-distance parameters ⑱, ⑳, and ㉒, as well as DC, are not directly assigned in this interface. After the assignable parameters are entered, the fabric digital twin is created automatically and can be used for subsequent simulations of SS, LS, BD, and PLD fabric samples and garments.

4.4.3 Comparison of Fabric Digital Twins

Using the unified parametric structure defined in Chapter 2 and identical modeling settings in Style3D, fabric digital twins (DTs) were constructed for fabrics F1, F2, and F3 using two methods of parameter acquisition. The first method, designated as Lab in Figure 4.11, used the parameter set measured using traditional laboratory instruments. The second method used the final single-model parameter set measured by AI, presented in Table 4.21. Figure 4.11 shows the fabric DTs formed based on the laboratory and AI methods.

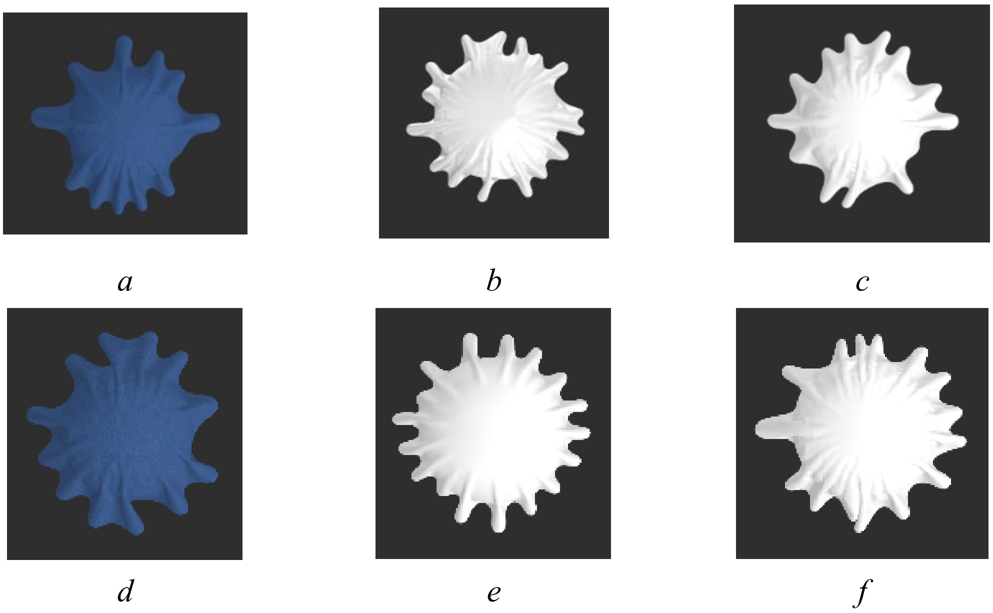

Figure 4.11 — Fabric Digital Twins Generated in Style3D Using Two Parameter-Acquisition Methods: *a* — F1-Lab; *b* — F2-Lab; *c* — F3-Lab; *d* — F1-AI; *e* — F2-AI; *f* — F3-AI

As shown in Figure 4.11, the three fabrics formed distinguishable drape states under both parameter-acquisition routes. The results based on laboratory parameters in Figure 4.11,a–c show clear differences in outer contour, fold formation, and radial fold distribution among F1, F2, and F3. The results based on AI parameters in Figure 4.11,d–f also preserved these fabric-level differences, indicating that the parameter set measured by AI did not reduce the three fabrics to visually similar forms.

For fabric F1 (Figure 4.11,a and Figure 4.11,d), both methods formed a compact radial drape contour with several folds. However, the AI-based result showed a slightly more simplified contour and less fine fold subdivision than the result based on laboratory parameters. This difference is consistent with the comparison between the AI-measured parameter set in Table 4.21 and the laboratory reference value in Table 4.6: the AI-measured DC value for F1 was 0.69, which is higher than the laboratory reference value of 0.42. This deviation did not prevent the formation of a recognizable DT of fabric F1, but it shows that the AI method changed the local manifestation of folds in this fabric.

For fabric F2 (Figure 4.11,b and Figure 4.11,e), the results obtained based on laboratory parameters and on AI parameters produced a relatively expanded and soft drape morphology. The AI-based result preserved the radial tendency of drape, but showed a more rounded and more regular outer contour, indicating a reduction in some fine fold variations. This observation corresponds to the higher overall MAPE for F2 in Table 4.21, which reached 35.78%, although the AI-measured DC value of 0.36 remained close to the laboratory reference value of 0.33 in Table 4.6. Therefore, the main deviation for F2 was reflected not only in DC, but also in the combined influence of tensile parameters and bending-related parameters on local morphology.

For fabric F3 (Figure 4.11,c and Figure 4.11,f), both methods formed a radially folded drape state with a clearly expressed wavy outer boundary. The AI-based result preserved the main fold structure and the direction of radial folds, although the local edge contour became slightly denser and more fragmented. This result is consistent with the comparison between Table 4.21 and Table 4.6, where the AI-measured DC value for F3 was 0.43 and the laboratory reference value was 0.45. The comparison shows that the AI route preserved the dominant drape response of F3 more effectively than in the case of F1.

Overall, Figure 4.11 shows that both parameter-acquisition methods are capable of forming recognizable and comparable fabric DTs. The AI-parameter method preserved the main differences among F1, F2, and F3; however, local deviations occurred in fold separation, contour regularity, and fold density. Therefore, AI-measured parameters should not be evaluated only by their numerical proximity to laboratory reference values. Their applicability also depends on whether the resulting fabric DTs preserve the main drape morphology under identical modeling conditions. Fabric-level comparison provides the material basis for subsequent garment-level validation, where the influence of these parametric deviations can be further investigated through silhouette and shape consistency.

4.5. Garment-Level Validation

*Relevance of the selected photographic protocol for garment-level simulation***.** To evaluate whether the selected photographic protocol can support garment-level simulation, fabric F1 was used as an example fabric to generate a skirt digital twin (DT) in Style3D. The Lab method used the parameter set measured by traditional instruments, whereas the AI method used the parameter set measured using AI based on the selected photographic protocol P1 + P2 + P6-Warp. These two methods are designated as Lab and AI in Figure 4.12. Both simulations were performed using the same patterns, avatar, settings, and material. Figure 4.12 shows the skirt simulations formed using the Lab and AI methods.

a *b*

Figure 4.12 — Skirts Generated in Style3D Using Two Parameter-Acquisition Methods: *a* — F1-Lab; *b* — F1-AI

As shown in Figure 4.12, both simulations formed similar drape states in Style3D. The skirt constructed based on AI parameters preserved the main A-line silhouette, hemline expansion, and overall vertical fall of the form observed in the simulation constructed based on laboratory parameters. Minor visual differences were observed in the side contour and lower part. However, the overall garment state remained visually comparable for the two parameter-acquisition methods.

The contours of the F1-Lab and F1-AI skirts were overlaid in standardized front, side, and bottom views. The red contour represents the AI-based result, and the black contour represents the laboratory reference. Figure 4.13 shows the overlaid skirt contours used for garment-shape comparison.

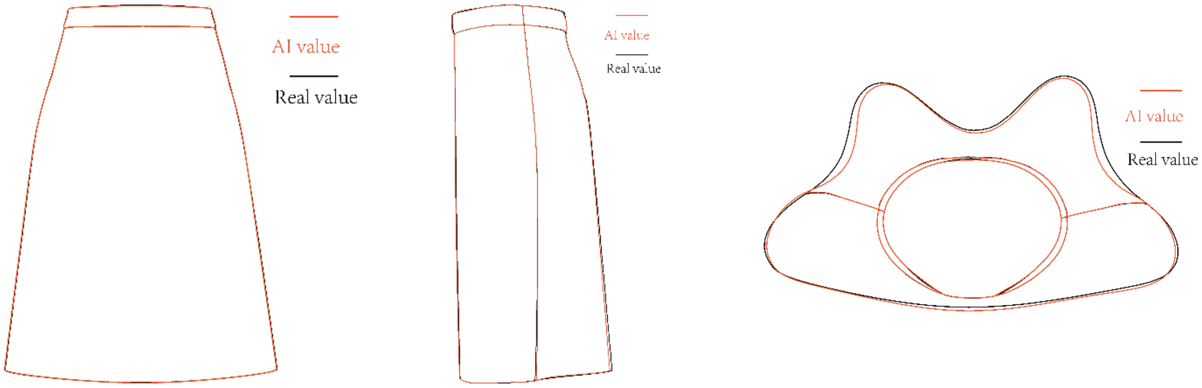

a *b* *c*

Figure 4.13 — Overlaid Contours of the F1-AI and F1-Lab Skirts: *a* — front view; *b* — side view; *c* — bottom view

As shown in Figure 4.13, the AI-based silhouette showed high geometric consistency with the laboratory reference in the front, side, and bottom views. In Figure 4.13,a, the contours in the frontal view almost coincided. In Figure 4.13,b, comparison of the side contours showed a small deviation along the lower contour, indicating that the influence of local stiffness was retained. In Figure 4.13,c, the contour in the bottom view retained a similar hem width and overall opening shape, although local contour differences appeared in areas with high curvature. These results show that the selected AI photographic protocol made it possible to reproduce the main drapeability response of fabric F1 in the skirt.

To quantitatively evaluate the geometric consistency between the F1-AI and F1-Lab skirt simulations, IoU, area difference, and statistical indicators of boundary deviation were calculated from the extracted silhouettes. The boundary-deviation indicators included the mean value, 95th percentile, and maximum deviation, which were used to evaluate overall overlap and local contour differences. Table 4.22 shows the quantitative geometric consistency between the F1-AI and F1-Lab skirt silhouettes.

Table 4.22 — Consistency of F1-AI and F1-Lab Skirt Silhouettes

View / Region	IoU	Area Difference, AI Compared with Lab, %	Boundary deviation, px		
			Mean	95%	Maximum
Front view	0.9963	-0.010	4.40	11.98	16.00
Side view	0.9872	-0.410	11.22	21.18	28.00
Bottom view (outer contour)	0.9654	-2.030	22.89	80.39	91.68
Waist contour (inner contour)	0.9210	+3.36	19.34	35.75	48.14

As shown in Table 4.22, the F1-AI skirt silhouette demonstrated high geometric consistency with the F1-Lab reference. The front view achieved the greatest overlap, with IoU = 0.9963 and an area difference of only −0.010%, indicating that frontal expansion and hem width were almost unchanged under the influence of AI-measured parameters. The side view also retained high consistency, with IoU = 0.9872 and an area difference of −0.410%, although the mean boundary deviation increased to 11.22 px. The largest deviation was observed in the outer contour in the bottom view, where IoU decreased to 0.9654 and the 95th percentile of boundary deviation reached 80.39 px. This indicates that the main residual error was concentrated in the hem contour. The waist contour had the lowest IoU value, equal to 0.9210, and a positive area difference of +3.36%, indicating that shape formation in the waist area, controlled by darts, remained more sensitive to parameter differences than the overall skirt contour.

Next, sleeveless dresses were generated from the three fabrics F1–F3. Figure 4.14 shows the ROI areas in the support-surface region.

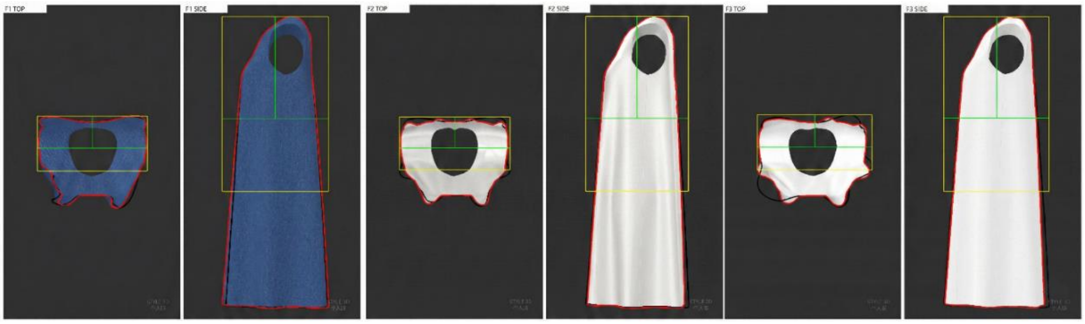

a *b* *c* *d* *e* *f*

Figure 4.14 — ROI Areas for Dress Analysis: *a, b* — F1; *c, d* — F2; *e, f* — F3

As shown in Figure 4.14, the ROI in the top view records the downward expansion of the dress, while the ROI in the side view records changes in the side contour. Thus, this ROI setting evaluates horizontal expansion and side-profile stability. The ROI in the support-surface region of the figure was subdivided into left and right parts to determine silhouette symmetry. For each fabric and each view, IoU, area difference, mean contour deviation, 95th percentile deviation, and maximum deviation were calculated. Table 4.23 shows the ROI consistency indicators for dresses generated based on AI parameters and Lab parameters.

Table 4.23 — ROI Consistency Indicators in the Support-Surface Region for Dresses Based on AI Parameters and Lab Parameters

Fabric	View	ROI	IoU	Area Difference, AI Compared with Lab, %	Отклонение контуров, px		
					Mean	95%	Maximum
F1	Top	Left	0,9630	−3,07	0,9	6,68	13,69
		Right	0,9558	−1,96	1,0	6,14	11,87
		Combined	0,9594	−2,51	0,9	6,68	13,69
	Side	Left	0,9824	+1,66	0,60	2,87	13,82
		Right	0,9838	+0,74	0,28	0,95	13,28
		Combined	0,9831	+1,19	0,50	1,91	13,82
F2	Top	Left	0,8685	−10,13	3,57	21,01	25,78
		Right	0,8373	−10,85	4,52	25,72	30,56
		Combined	0,8526	−10,49	4,23	22,92	30,56
	Side	Left	0,9923	+0,04	0,14	0,95	1,91
		Right	0,9875	−0,15	0,22	0,95	2,87
		Combined	0,9897	−0,06	0,23	0,95	2,87
F3	Top	Left	0,9428	−3,32	1,33	5,73	6,68
		Right	0,8008	−12,80	5,43	29,48	35,34

		Combined	0,8710	−8,05	3,46	21,95	35,34
	Side	Left	0,9960	−0,16	0,06	0,95	0,95
		Right	0,9863	−1,02	0,28	1,91	4,78
		Combined	0,9911	−0,62	0,23	0,95	4,78

As shown in Table 4.23, the ROIs in the side view showed consistently high agreement between the two dresses. The combined IoU values for the side view were 0.9831 for F1, 0.9897 for F2, and 0.9911 for F3, while the mean boundary deviations for all three fabrics were below 0.50 px. This indicates that the dress-generation method based on AI parameters preserved the vertical side contour. The ROIs in the top view were more sensitive than those in the side view.

The consistency between Tables 4.22 and 4.23 shows that the more pronounced discrepancy in the top view reflects higher sensitivity of drapeability to lateral expansion. Consequently, the selected AI photographic protocol reproduced the dress profile in the side view with high accuracy, while the top view revealed residual fabric-dependent deviations, especially for F2 and F3. This result confirms the appropriateness of using top-view ROI analysis for stricter verification of garment-level relevance.

*Optimization of Measurement Accuracy Using Hybrid Routing***.** It has previously been shown that different multimodal AI models offer distinct advantages regarding specific groups of parameters. Therefore, the feasibility of employing a hybrid routing strategy—utilizing multiple models to enhance the accuracy of the estimated parameters—was evaluated. In this strategy, Gemini 3 Pro was selected for thickness ①, Qwen3-Max for GSM ②, GPT-5.1 for tensile parameters at low elongations ③–⑰, and Grok-4.1 for bending-related parameters ⑱–㉓ as well as the drape coefficient ㉔. The parameters from Table 4.21 served as the baseline for comparison. Table 4.24 presents the hybrid multi-model parameter set and the corresponding MAPE values for fabrics F1–F3, based on the same set of photographs (P1+P2+P6-Warp).

Table 4.24 — Parameter Values Obtained by Different AI Models Using P1 + P2 + P6-Warp

Model	Parameter Code	Parameter value for the fabric		
		F 1	F 2	F 3
Gemini 3 Pro	①	0,42	0,14	0,18
Qwen3-Max	②	140	97,5	97
GPT-5,1	③	0,2	0,237	0,4
	④	0,42	0,635	1
	⑤	0,7	1,495	1,8
	⑥	1,08	2,485	2,8
	⑦	1,52	3,63	4,24

	⑧	0,036	0,024	0,06
	⑨	0,067	0,046	0,11
	⑩	0,099	0,079	0,17
	⑪	0,132	0,115	0,23
	⑫	0,166	0,157	0,3
	⑬	0,007	0,01	0,02
	⑭	0,009	0,02	0,04
	⑮	0,011	0,03	0,05
	⑯	0,012	0,04	0,07
	⑰	0,015	0,05	0,09
Grok-4,1	⑱	33,5	17	33
	⑲	38,5	36,4	42
	⑳	24,5	13	26
	㉑	38	34,6	39
	㉒	28	17	30
	㉓	37	36,2	40
	㉔	0,58	0,33	0,42
MAPE, %		22,93	9,81	24,6

As shown in Table 4.24, the hybrid routing strategy using several AI models reduced the overall MAPE value for all three fabrics compared with the single-model AI parameter set presented in Table 4.21. For fabric F1, MAPE decreased from 26% to 22.93%; for fabric F2, from 35.78% to 9.81%; and for fabric F3, from 32.29% to 24.60%. These results show that the greatest effect of hybrid routing was observed for fabric F2.

The improvement was mainly associated with assigning AI models to parameter groups. This assignment of AI models to parameter groups reduced dependence on a single multimodal model and made it possible to treat model selection as part of the measurement protocol. The hybrid routing strategy should be interpreted as an accuracy-enhancement mode rather than as the standard protocol, because it increases procedural complexity and requires preliminary information obtained at the model-selection stage. Therefore, the single-model route remains suitable for standard construction of fabric digital twins, while the hybrid multi-model route provides a higher-accuracy option in cases where additional computational and operational complexity is acceptable.

The results in Table 4.24 were visualized to clearly show the scale of error reduction achieved using hybrid routing. Figure 4.15 shows a comparison of MAPE between the single-model baseline variant and the hybrid routing configuration.

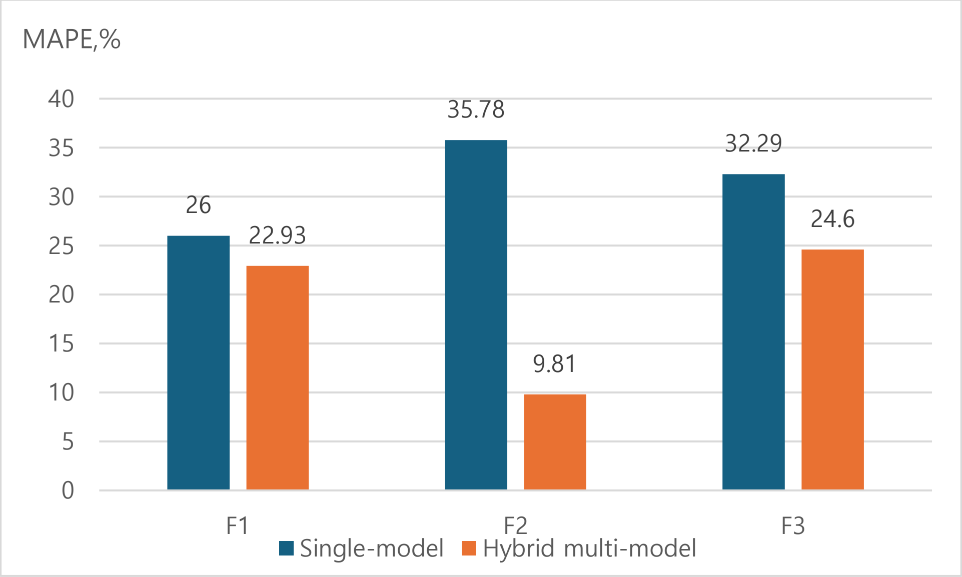

Figure 4.15 — Comparison of MAPE for the Single-Model Baseline Variant and Multi-Model Hybrid Routing for Fabrics F1–F3

As shown in Figure 4.15, hybrid routing reduced MAPE for all three fabrics; however, the degree of reduction was not the same. This comparison showed that hybrid routing was most effective for fabric F2, which previously had the largest error under the single-model baseline variant. This result confirms the possibility of using hybrid routing as an additional strategy for improving accuracy.

The hybrid parameter set for fabric F1 was imported into Style3D to generate a dress DT, and the obtained result was compared with the dress DT generated based on the F1-Lab parameter set. Figure 4.16 shows the frontal views of the dresses.

Figure 4.16 — Comparison of Dress Digital Twins Generated Based on the F1 Hybrid

Parameter Set and the F1-Lab Set: *a* — F1-hybrid; *b* — F1-Lab; *c* — overlay of the F1-hybrid and F1-Lab contours

As shown in Figure 4.16, the dress digital twin generated based on the F1-hybrid parameter set was very close to the F1-Lab reference: it had a similar neckline position, shoulder width, side contour, and hemline expansion. This indicates that the parameter improvement achieved through hybrid routing was not limited only to the numerical reduction of MAPE, but also improved dress modeling.

The contour overlay in Figure 4.16,c further shows that the central part and the outer contour coincided well. The visible deviation was mainly concentrated along the lower side contour of the dress. Consequently, the hybrid routing strategy can be interpreted as an additional route for improving accuracy in generating a garment digital twin. Its main value lies in reducing parameter-level error while reproducing dress morphology under identical modeling conditions.

The obtained experimental results are summarized in Figure 4.17 as the architecture of a protocol-driven integrated operational scheme.

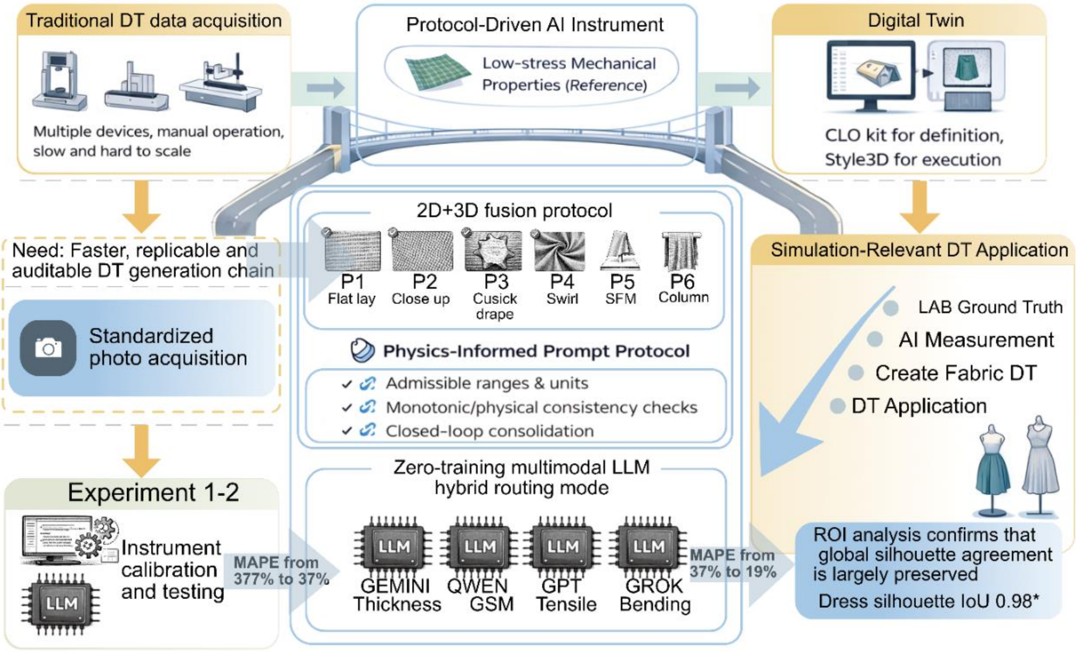

Figure 4.17 — Structure of the Protocol-Driven AI-Based Measurement Scheme

As shown in Figure 4.17, this structure functions as a protocol-driven AI tool for measuring fabric property indicators. **The workflow forms a strict metrological chain that proceeds sequentially from input evidentiary images, through protocol constraints, to obtaining a parameter vector, and concludes with verification of modelling relevance.** This scheme supports efficient generation of fabric digital twins by reducing repeated physical testing, while laboratory reference values remain necessary for calibration, error evaluation, and validation.

Conclusions to Chapter 4

1. A protocol-driven scheme for obtaining fabric parameters using AI was formed using a standardized set of fabric photographs showing the flat view, texture, circular drapeability, spiral folded surface, drapeability on an anthropomorphic stand, and suspended-state appearance. The output parameters were organized into a coded system covering thickness, GSM, tensile forces at small elongations, bending-related parameters, and drape coefficient. This system made it possible to link fabric visual features, laboratory reference values, and parameters assigned in the material editor of the Style3D three-dimensional garment simulation program into a unified measurement structure.

2. A standard AI-based measurement process was developed through sequential calibration of the prompt protocol, AI model selection, and configuration of fabric photographic images. Under the fixed prompt protocol, GPT-5.1 showed the best performance across parameter groups. The final photographic configuration included both 2D and 3D images.

3. It was shown that fabric digital twins in Style3D can be generated based on the results of laboratory contact testing and on non-contact, non-instrumental results obtained through AI estimation. The MAPE discrepancy between the two types of fabric digital twins ranged from 26% to 35.78%. Comparison of the appearance of the digital twins showed their similarity, including the general drape form, the character of the outer contour, and fold distribution.

4. Garment-level validation confirmed the suitability of the AI-based results for constructing and preliminarily validating digital twins of fabrics and garments.

CHAPTER 5. DRESS SHAPE PREDICTION

The drapeability parameters obtained using the new SFM method link the fabric digital twin with the dress digital twin and form the basis for dress shape prediction and pattern correction. In this chapter, this relationship is examined using the examples of the basic dress (BD) and the pleated dress (PLD).

5.1. Measured Objects and Parameter System

Dress shape prediction and pattern correction require the construction of a continuous parametric chain from the fabric sample to the garment. The short sample (SS), long sample (LS), basic dress (BD), and pleated dress (PLD), as the research objects in this chapter, correspond to different structural scales and perform different analytical functions. The SS sample characterizes the basic drape response of the fabric under shoulder-support conditions. The LS sample characterizes the intermediate drape response during the transition from a local sample to a sample whose dimensions are closer to those of a garment. The BD has a basic form, whereas the PLD has a complex pleated surface and provides data for analyzing shape formation and drapeability.

SS, LS, and BD are not objects with the same geometric form. They are objects made from the same fabric. SS is used to calculate the basic drapeability indicator DC_{SFM}. LS is obtained by increasing the length and width based on the SS sample and reflects the transition of the drape response from the sample scale to a scale closer to that of a garment. BD is the object used to extract garment-level parameters, and its parameters P_{d1}–P_{d4} reflect the combined influence of fabric, length, and width. The relationships between the drape coefficients DC_{SFM} for the SS and LS samples and the BD dress-shape parameters characterize the possibility of transferring the drape response of samples to the garment level.

Figure 5.1 shows the object relationships and the main measurement positions of SS, LS, and BD used to compare sample-level DC_{SFM} with BD shape parameters.

a *b* *c*

Figure 5.1 — Research Objects Used to Develop the Dress Shape Prediction Algorithm: a — five variants of the SS sample; b — five variants of the LS sample; c — BD1–BD5 measurement levels for the P_{d1}–P_{d4} parameters of the BD dress

As shown in Figure 5.1, SS1–SS5, LS1–LS5, and BD1–BD5 have five corresponding structural levels. The cross-sections of BD1–BD5 make it possible to observe changes in the expansion of the basic dress during the transition between levels. The parameters P_{d1}, P_{d2}, P_{d3}, and P_{d4} describe changes in BD shape through vertical length, frontal projected width, side inclination angle, and garment-level drape response, respectively. The following designations are adopted in this study:

- P_{d1} denotes the vertical length of the BD dress from the shoulder support point to the hemline and characterizes the longitudinal elongation of the dress under the action of gravity;
- P_{d2} denotes the frontal projected width of BD and characterizes the transverse expansion of the hemline and the overall silhouette;
- P_{d3} denotes the side inclination angle formed by the line from the underarm point to the hem edge and characterizes the lateral spread and change in the inclined contour of the dress;
- P_{d4} denotes the garment-level drape coefficient of BD and is a dimensionless parameter characterizing the overall drape response of the basic dress. Unlike P_{d1}, P_{d2}, and P_{d3}, P_{d4} is not a separate linear geometric quantity, but is calculated based on BD morphology as a garment-level drapeability indicator.

Table 5.1 shows the correspondence between measurement objects, parameter sources, and analytical functions used for dress shape prediction and pattern correction.

Table 5.1 — Parameter System for Dress Shape Prediction and Pattern Correction

Analytical	Measurement	Level or	Parameter	Acquisition	Analytical

Task	Object	Material		Method	Function
Prediction of the shape of the basic dress BD	SS	F1–F3, SS1–SS5	SS DC_{SFM}	Measurement and calculation using the SFM method	Input variable for predicting P_{d1}–P_{d4}
	LS	F1–F3, LS1–LS5	LS DC_{SFM}	Measurement and calculation using the SFM method	Intermediate parameter of the drape response between SS and BD
	BD	F1–F3, BD1–BD5	P_{d1}, P_{d2}, P_{d3}, P_{d4}	Geometric measurement in Rhinoceros and calculation of BD morphology	Output variables of garment-level shape
Validation of the shape prediction for the basic dress BD	VSS и VD	Validation samples F1–F3	VSSDC_{SFM}, VDP_{d1}–P_{d4}	Measurement using the SFM method and geometric measurement	Verification of errors in the Pd prediction equations
Pattern correction for the pleated dress PLD	PLD	F1–F3, PLDP1–PLDP5	Δ, $A_{overall}$, A_{ROI1}, A_{ROI2}	Pattern calculation and grayscale analysis in ImageJ	Construction of the relationship among pleat magnitude, fabric drape response, and grayscale response
Validation of pattern correction for the pleated dress PLD	Target physical dress B and validation dress V	Target fabric F4 and validation fabric F5	$A_{overall}$, A_{ROI1}, A_{ROI2}, SSIM	Grayscale analysis in ImageJ and image-similarity analysis	Verification of the consistency of the PLD grayscale response after correction

As shown in Table 5.1, the parameters are grouped according to the levels of the measurement objects. This structure forms the parametric chain “sample drape response — basic dress shape parameters — pleated dress pattern correction — validation of garment grayscale response”.

To fix the initial data matrix used to compare DC_{SFM} for the SS sample with BD shape parameters, Table 5.2 presents the values of DC_{SFM} and P_{d1}–P_{d4} for the three fabrics at five BD levels.

Table 5.2 — Matched Data Matrix of SS DC_{SFM} and BD Shape Parameters P_{d1}–P_{d4}

Fabric	BD Level	DC_{SFM} Value for SS Sample	Pd parameter values			
			P_{d1}	P_{d2}	P_{d3}	P_{d4}
F1	1	0.07	45.61	42.50	11.270	0.659
	2	0.15	65.95	49.21	10.570	0.568
	3	0.23	85.83	45.37	8.693	0.539
	4	0.38	105.94	48.94	6.790	0.435
	5	0.61	115.93	48.67	5.032	0.394
F2	1	0.10	45.93	35.94	5.932	0.590
	2	0.19	66.04	40.68	5.881	0.520
	3	0.28	86.36	41.73	4.754	0.430
	4	0.47	106.74	42.48	3.890	0.370
	5	0.67	116.83	43.04	3.607	0.350
F3	1	0.12	45.48	42.00	11.626	0.620
	2	0.20	65.87	49.77	10.710	0.580
	3	0.27	85.78	54.90	9.651	0.540
	4	0.46	105.89	56.22	8.841	0.450
	5	0.64	116.02	57.52	7.762	0.430

As shown in Table 5.2, the matrix records the correspondence between DC_{SFM} at the SS sample level and the BD dress shape parameters at the garment level. P_{d1} increased with the increase in BD level, reflecting the growth of the vertical dress length. P_{d2}, P_{d3}, and P_{d4} simultaneously depend on fabric drapeability, transverse expansion, and changes in the side contour; therefore, the relationship between DC_{SFM} and different Pd parameters requires separate correlation evaluation.

DC_{SFM} for the long sample LS characterizes the intermediate-scale drape response. This indicator is used to verify whether the directional change in drape response is preserved during the transition from the short sample to the longer sample. Table 5.3 shows the DC_{SFM} values for the LS sample, the mean value, and CV for fabrics F1–F3 at five levels, LS1–LS5.

Table 5.3 — Change in DC_{SFM} for the LS Sample at Five Levels

Fabric	LSDC_{SFM} Values						CV
	LS1	LS2	LS3	LS4	LS5	Mean	
F1	0.039	0.044	0.058	0.073	0.099	0.063	0.389
F2	0.132	0.131	0.148	0.161	0.171	0.149	0.116
F3	0.045	0.051	0.074	0.096	0.129	0.079	0.412

As shown in Table 5.3, LS DC_{SFM} generally increased with the increase in LS level. The mean LS DC_{SFM} value for fabric F2 was 0.149, which was higher than the values of 0.063 for F1 and 0.079 for F3. This indicates a higher drape response of F2 for the long sample. The CV values for F1 and F3 were 0.389 and 0.412, respectively, which were higher than the value of 0.116 for F2. Therefore, LS DC_{SFM} for F1 and F3 was more sensitive to changes in length and width levels, whereas the level response of F2 was more stable.

The data matrix for predicting the shape of the basic dress BD includes three fabrics and five levels. The sample for correlation analysis comprises 15 observations. The correlations among SS DC_{SFM}, LS DC_{SFM}, and P_{d4} characterize the continuity of the drape response among SS, LS, and BD. The presence of correlations between SS DC_{SFM} and the parameters P_{d1}, P_{d2}, P_{d3}, and P_{d4} characterizes the possibility of applying SS DC_{SFM} as an input parameter for predicting the shape of the basic dress.

Regression equations were constructed separately for each fabric. SS DC_{SFM} served as the input variable, while P_{d1}–P_{d4} served as the output variables. The mean value of the input variable ($\bar{x}$) in the regression equations corresponds to the mean measured value of SS DC_{SFM} for a specific fabric and a specific level. Each fabric-specific regression model is based on five paired levels of the given fabric and characterizes the ability of SS DC_{SFM} to predict BD shape parameters.

PLD pattern correction is based on grayscale image parameters that characterize the response of pleat form. PLDP1–PLDP5 denote five levels of pleat magnitude. The pleat positions at these levels remain unchanged, while the pleat magnitude increases sequentially. The pleat-formation coefficient Δ, defined by Equation (2.1) in Chapter 2, serves as the control parameter for pleat magnitude at the pattern level. After background removal, boundary cleaning, selection of the analysis region, and conversion of the frontal PLD image into an 8-bit grayscale image in ImageJ, threshold segmentation was performed. The grayscale threshold (T) defines the boundary for selecting the bright area in pixels: grayscale values equal to or greater than T are defined as the bright area.

In ImageJ, the result “percentage area” (%Area) denotes the area of selected pixels within a defined analysis region, measured as a percentage. This indicator is the original software term used in ImageJ. For mathematical description and subsequent modeling, the proportion of the bright-area pixels (A) within the total selected region was calculated using the following formula:

$$A_r = \frac{N_{b,r}}{N_r} \times 100\% \tag{5.1}$$

where Ar is the proportion of the bright area in region r, %; Nb,r is the number of bright-area pixels in region r for which the grayscale value is greater than or equal to threshold T; Nr is the total number of pixels in region r; and r is the index of the analysis region. When r = overall, Ar corresponds to $A_{overall}$; when r = ROI-1, it corresponds to A_{ROI1}; and when r = ROI-2, it corresponds to A_{ROI2}.

For different analysis regions, three indicators were selected: $A_{overall}$, A_{ROI1}, and A_{ROI2}. $A_{overall}$ denotes the proportion of the bright area in the frontal dress image and characterizes the pleated zone in grayscale. A_{ROI1} denotes the proportion of the bright area in the region of interest ROI-1, corresponding to the first upper zone of concentrated dense short pleats along the seam. A_{ROI2} denotes the proportion of the bright area in the region of interest ROI-2, corresponding to the second zone of diagonal pleat propagation, and characterizes changes in the bright area caused by diagonal pleat propagation, local sagging, and lateral deformation. $A_{overall}$ was used to construct the general prediction model for the pleat coefficient Δ, while A_{ROI1} and A_{ROI2} were used to evaluate the consistency of the local grayscale response.

The target dress B and the validation dress V were used to verify the pattern-correction result. Dress B defines the target grayscale pleat-formation response, whereas dress V represents the form obtained from the validation fabric after pattern correction. Comparison of $A_{overall}$, A_{ROI1}, and A_{ROI2} for dresses B and V makes it possible to evaluate whether the corrected pattern achieves the desired pleat-formation effect in the validation dress.

The structural similarity index (SSIM) was used to compare the image structure of dresses B and V in local regions. Therefore, the grayscale image parameters in the PLD analysis are not color-measurement parameters, but morphological indicators formed by pleat ridges, fold lines, illuminated surfaces, and shadow distribution.

Thus, the developed parameter system linked three analytical levels. At the first level, DC_{SFM} parameters of the short SS and long LS samples and the Pd parameters of the BD dress were used to identify relationships between sample drapeability and the shape of the basic dress. At the second level, the bright-area proportions $A_{overall}$, A_{ROI1}, and A_{ROI2} characterized the grayscale pleated surface of the PLD dress as the pleat magnitude changed. At the third level, sample drapeability DC_{SFM}, $A_{overall,B}$ of the target dress B, and the predicted value of the pleat coefficient Δ were used to correct the original PLD pattern and obtain the desired effect in the validation dress V.

5.2. Prediction of Basic Dress Shape-Formation Parameters

5.2.1. Relationship Between Specimen Drapeability and Basic Dress Shape Parameters

The transverse profiles of the basic dress were used to study the influence of dress level and fabric type on horizontal shape expansion [173]. Figure 5.2 shows the transverse profiles of BD1–BD5 when fabrics F1–F3 were used.

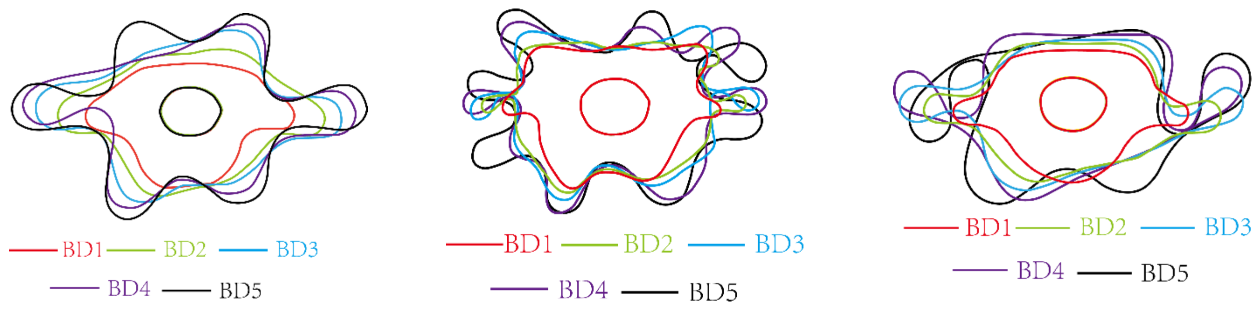

a *b* *c*

Figure 5.2 — Transverse Profiles of the Basic Dress at Levels BD1–BD5 Using Different Fabrics: *a* — F1; *b* — F2; *c* — F3

As shown in Figure 5.2, the transverse profiles of the dress made from all fabrics expanded as the sections approached the hemline; however, the character of expansion differed among the materials. Fabric F1 showed more noticeable width fluctuations between levels, fabric F2 demonstrated more compact transverse expansion, and fabric F3 showed more pronounced lateral expansion at the hem. Therefore, as dress length increases, frontal and lateral expansion also occur.

The relationship between DC_{SFM} for the SS and LS samples, on the one hand, and P_{d4}, on the other hand, characterizes the change in drapeability from the short sample to the long sample and to the basic dress level. Table 5.4 shows the correlation coefficients among SS DC_{SFM}, LS DC_{SFM}, and P_{d4}.

Table 5.4 — Correlation Coefficients Between DC_{SFM} and P_{d4}

Indicator	SS DC_{SFM}	LS DC_{SFM}	P_{d4}
SS DC_{SFM}	1		
LS DC_{SFM}	0.946**	1	
P_{d4}	0.880**	0.939**	1

Note: n = 15; ** denotes $p < 0.01$.

As shown in Table 5.4, SS DC_{SFM} has a significant positive correlation with LS DC_{SFM}, and LS DC_{SFM} has a significant positive correlation with P_{d4}. The correlation between SS DC_{SFM} and P_{d4} is also significant and positive. These results show that the drapeability of the short sample SS is closely related to the drapeability of the long sample LS and the drapeability of the BD dress. Consequently, this finding provides a basis for predicting dress shape using laboratory test results.

The applicability of the input variable SS DC_{SFM} for predicting all P_{d1}–P_{d4} dress-shape parameters was evaluated by correlation analysis. Table 5.5 shows the correlation coefficients between SS DC_{SFM} and P_{d1}–P_{d4}.

Table 5.5 — Correlation Coefficients Between the Short Sample SS DC_{SFM} Indicator and Basic Dress BD Parameters

Indicator	SS DC_{SFM}	P_{d1}	P_{d2}	P_{d3}	P_{d4}
SS DC_{SFM}	1				
P_{d1}	-0.834**	1			
P_{d2}	-0.563*	0.779*	1		
P_{d3}	0.818**	-0.992**	-0.799**	1	
P_{d4}	0.880**	-0.946**	-0.697**	0.942**	1

Note: n = 15; * denotes $p < 0.05$, and ** denotes $p < 0.01$.

As shown in Table 5.5, SS DC_{SFM} has statistically significant relationships with all four BD shape parameters. The strongest relationship is observed with P_{d4}, indicating the ability of the short sample to reflect changes in drapeability at any dress level. SS DC_{SFM} also had significant negative relationships with P_{d1} and P_{d2} and a positive relationship with P_{d3}. This shows that changes in BD shape are determined not only by the draping ability of the fabric, but also by dress level, frontal width, lateral spread, and changes in the transverse profile. Consequently, SS DC_{SFM} better explains P_{d1}, P_{d3}, and P_{d4}, whereas P_{d2} has a more complex dependence on dress width and fabric response.

5.2.2 Prediction Model and Validation of Basic Dress Shape-Formation Parameters

Regression equations were constructed separately for each fabric. SS DC_{SFM} served as the input variable, while P_{d1}–P_{d4} served as output variables. The mean value of the input variable ($\bar{x}$) in the regression equations corresponds to the mean measured value of SS DC_{SFM} for a specific fabric and a specific level, rather than to the overall mean value obtained by combining the five levels of one fabric. Fabric-specific regression equations were constructed for fabrics F1, F2, and F3. The equations for predicting the shape parameters of the basic dress BD are presented below:

$\overline{P_{d1}}_{F1} = -342\,\bar{x}_1 + 292$	$R^2 = 0.980$	(5.2)
$\overline{P_{d2}}_{F1} = -27\,\bar{x}_1 + 65$	$R^2 = 0.821$	(5.3)
$\overline{P_{d3}}_{F1} = 34\,\bar{x}_1 - 18$	$R^2 = 0.986$	(5.4)
$\overline{P_{d4}}_{F1} = 1.16\,\bar{x}_1 - 0.2$	$R^2 = 0.999$	(5.5)
$\overline{P_{d1}}_{F2} = -204\,\bar{x}_2 + 179$	$R^2 = 0.979$	(5.6)
$\overline{P_{d2}}_{F2} = -17\,\bar{x}_2 + 50$	$R^2 = 0.773$	(5.7)
$\overline{P_{d3}}_{F2} = 12\,\bar{x}_2 - 0.7$	$R^2 = 0.916$	(5.8)
$\overline{P_{d4}}_{F2} = 0.6\,\bar{x}_2 + 0.2$	$R^2 = 0.906$	(5.9)
$\overline{P_{d1}}_{F3} = -293\,\bar{x}_3 + 251$	$R^2 = 0.926$	(5.10)
$\overline{P_{d2}}_{F3} = -54\,\bar{x}_3 + 83$	$R^2 = 0.685$	(5.11)
$\overline{P_{d3}}_{F3} = 21\,\bar{x}_3 - 2$	$R^2 = 0.989$	(5.12)

$\overline{P_{d4}}_{F3} = 1.2\,\overline{x}_3 - 0.1$	$R^2 = 0.823$	(5.13)

Verification of Equations (5.2)–(5.13) was carried out as follows. The mean DC_{SFM} values for the virtual short sample VSS were substituted into the equations, and the obtained values were compared with the P_{d1}–P_{d4} values for the virtual basic dress VD. Figure 5.3 shows histograms for the theoretical and actual values.

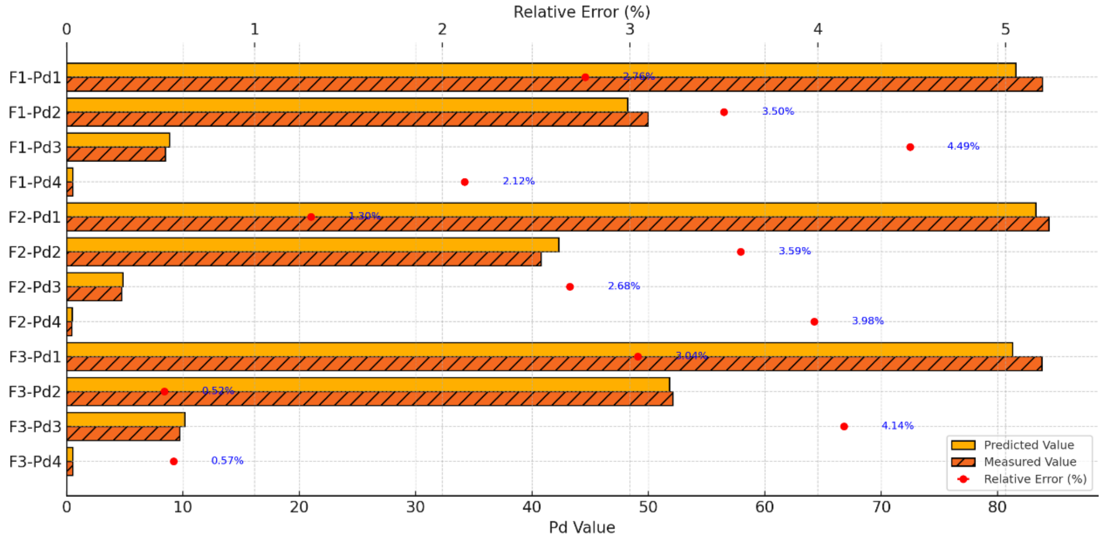

Figure 5.3 — Comparison of Prediction Errors for the Shape Parameters of the Virtual Basic Dress VD

As shown in Figure 5.3, the predicted and measured values of P_{d1}–P_{d4} for fabrics F1–F3 were close, and the relative errors were below 5%. The largest error was observed for P_{d3} in fabric F1 and was 4.49%. Such a low error confirms the adequacy of the obtained equations.

Thus, the drape coefficient of the short sample, SS DC_{SFM}, can be used as an input indicator for predicting the shape parameters of the basic dress BD. Consequently, the fabric-specific regression equations based on SS DC_{SFM} are suitable for predicting BD shape-formation parameters and can serve as a basis for further pattern correction [171].

5.3. Study of Dress Drapeability

5.3.1. Selection of the Bright Area for Pleat Analysis

Pleat formation on the dress surface in grayscale was used to quantitatively describe the visible morphological changes that occur after applying structural pattern-modelling techniques [175]. In accordance with the parameter system established in Section 5.1, **the indicator *A* characterizes the proportion of pixels selected after threshold segmentation within a defined analysis region**. This indicator does not directly describe the fabric color, but reflects the intensity of the visual response in relation to the area occupied by pleats.

In the images of the pleated dress PLD, the bright and dark areas carry different visual information about the pleats. The bright areas are mainly associated with pleat ridges, fold lines, and illuminated regions. The dark areas primarily correspond to pleat valleys and local overlaps, where shadow accumulation occurs. Since fabrics F1–F3 differ in color, texture, and light transmittance, the dark areas may additionally depend on the background of the black mannequin on which the dresses were photographed. Therefore, the dark and bright areas within the general pleat-location region were compared in order to select the main object for extracting indicator *A*. Figure 5.4 shows the dark and bright candidate areas formed on dresses made from fabrics F1–F3 under identical analysis conditions.

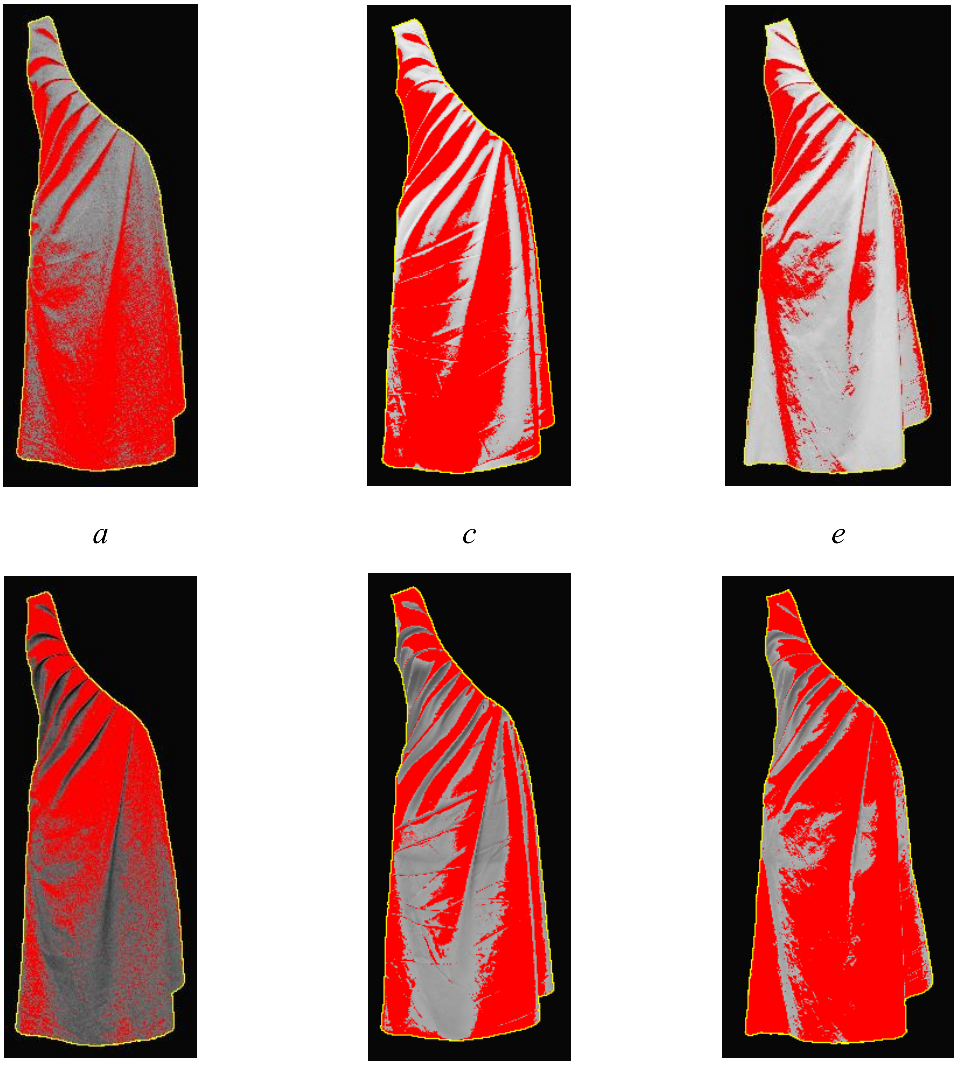

a *c* *e*

b *d* *f*

Figure 5.4 — Candidate Areas for the Study: *a* — dark F1; *b* — bright F1; *c* — dark F2; *d* — bright F2; *e* — dark F3; *f* — bright F3. Red denotes pixels selected as the candidate pleat-response area after threshold segmentation.

As shown in Figure 5.4, the dark candidate areas are mainly distributed in the zones of pleat valleys, shadows, and local overlap; their boundaries depend on shadow depth, fabric light transmittance, and the background of the black mannequin. In light or locally thinner regions, low grayscale values may include background influence unrelated to the pleat structure. By contrast, the bright candidate areas are located primarily along pleat ridges and fold lines and form a more continuous high grayscale response in all three fabrics. This shows that the bright area corresponds more directly to the visible form created by the pleats on the fabric surface.

The stability of the dark and bright candidate areas was evaluated using A, CV, the mean normalized grayscale value, and the mean within-group grayscale CV. Table 5.6 shows the quantitative indicators used to select the more stable pleat-response area, dark or bright.

Table 5.6 — Comparison of the Stability of Candidate Response Areas

Candidate Area	A, %, for fabrics			Inter-Fabric CV for A	Mean Normalized Grayscale Value	Mean Within-Group Grayscale CV
	F1	F2	F3			
Dark	7,48	14,61	10,03	0,337	0,114	1,080
Bright	21,76	15,14	19,03	0,179	0,874	0,127

As shown in Table 5.6, the inter-fabric CV for A in the dark candidate area was 0.337, which is higher than the value of 0.179 for the bright candidate area, indicating a stronger dependence of the dark-area proportion on the drapeability of the fabrics. The mean within-group grayscale CV of the dark area was 1.080, which was substantially higher than the value of 0.127 for the bright area. Therefore, the grayscale distribution within the dark area was less stable. The bright candidate area had a higher mean normalized grayscale value, equal to 0.874, and lower internal grayscale fluctuations. This result is consistent with the visual observation in Figure 5.4 and served as the basis for selecting the ***bright area*** as the main object for pleat analysis in the pleated dress PLD. Therefore, the A indicators extracted from bright areas were used to analyse the pleat response. $A_{overall}$ was used for the general region where pleats were located, while A_{ROI1} and A_{ROI2} were used for the local regions. This selection of local regions eliminates the influence of background shadows and fabric light transmittance and makes it possible to link the bright-area indicator with the visible morphology of the pleats.

5.3.2 Change in Bright-Area Proportion with Increasing Pleat Magnitude

The value of indicator A depends on the selected grayscale threshold T. Fabrics F1–F4, where fabric F4 was used to make the pleated dress, differ in color depth, surface reflectance, texture brightness, and shadow distribution; therefore, establishing a single fixed threshold for them may lead to unjustified excessive expansion or narrowing of the bright area. Threshold scanning makes it possible to determine the effective extraction range of the bright response, while the Otsu threshold [165] was used as an objective reference value.

Threshold-scanning curves were used to select fabric-specific thresholds that preserve the comparability of *A* among fabrics with different visual brightness. Figure 5.5 shows dress images that sequentially illustrate the change in *A* with increasing grayscale threshold *T* using fabric F1 as an example, as well as the dependence of *A* on *T* for fabrics F1–F4.

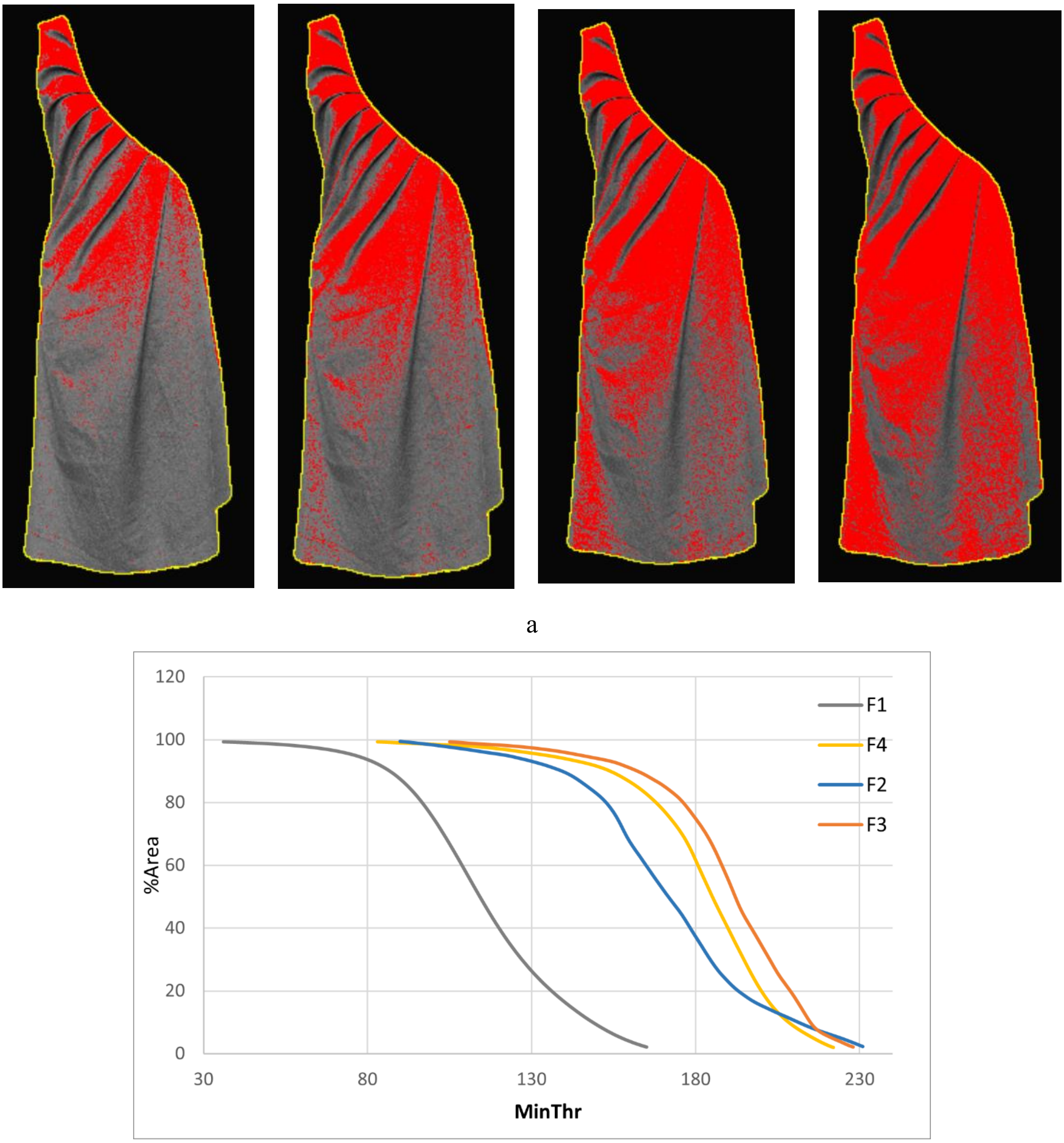

а

б

Figure 5.5 — Change in the Appearance of the Dress Made from Fabric F1 with Increasing Grayscale Threshold (*a*) and Curves of the Decrease in Bright-Area Proportion *A* with Changes in the MinThr *T* Threshold (*b*)

As shown in Figure 5.5, for all fabrics, area *A* decreases as threshold *T* increases; however, the effective response ranges differ noticeably among the fabrics. The curve for dark fabric F1 is located in the lower MinThr threshold range, showing that a lower threshold is required for the dark fabric in order to preserve the bright areas formed by pleat ridges and fold lines. The curves for fabrics F2, F3, and F4 are located in a higher threshold range, indicating that the bright response of light-colored fabrics is distributed at higher grayscale levels. Based on the response ranges of the curves for fabrics F1, F2, F3, and F4, the threshold values were determined as 112, 174, 191, and 180, respectively. The fabric-specific thresholds reduced the influence of differences in fabric color and reflection on bright-area extraction; therefore, the *A* values obtained for different fabrics became more suitable for pleat analysis.

The pleat-formation coefficient Δ for dresses PLDP1–PLDP5 increased from 0.48 to 1.24 (Table 2.4), which corresponded to a gradual increase in pleat magnitude at fixed pleat positions. Since the pleat positions in dresses PLDP1–PLDP5 remained unchanged, the change in Δ was used to analyze the influence of increased pleating on the grayscale response. Figure 5.6 shows the trends in $A_{overall}$, A_{ROI1}, and A_{ROI2} as Δ increased.

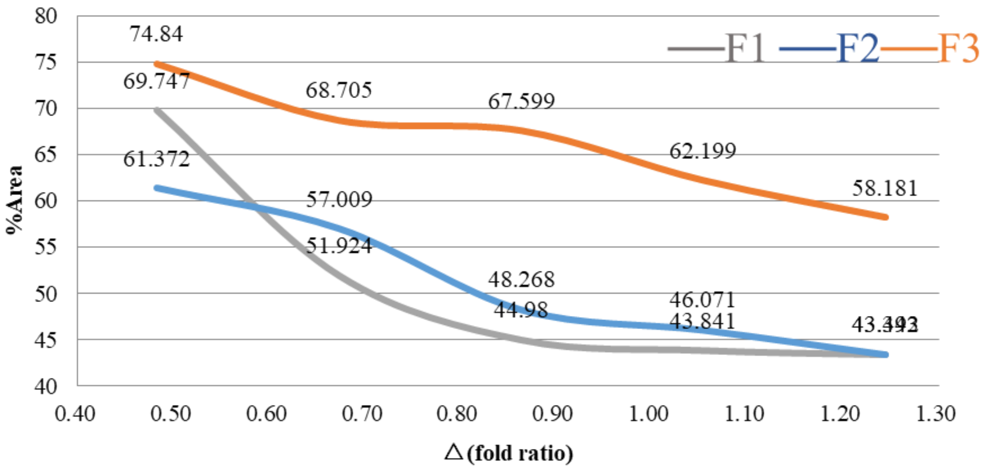

a

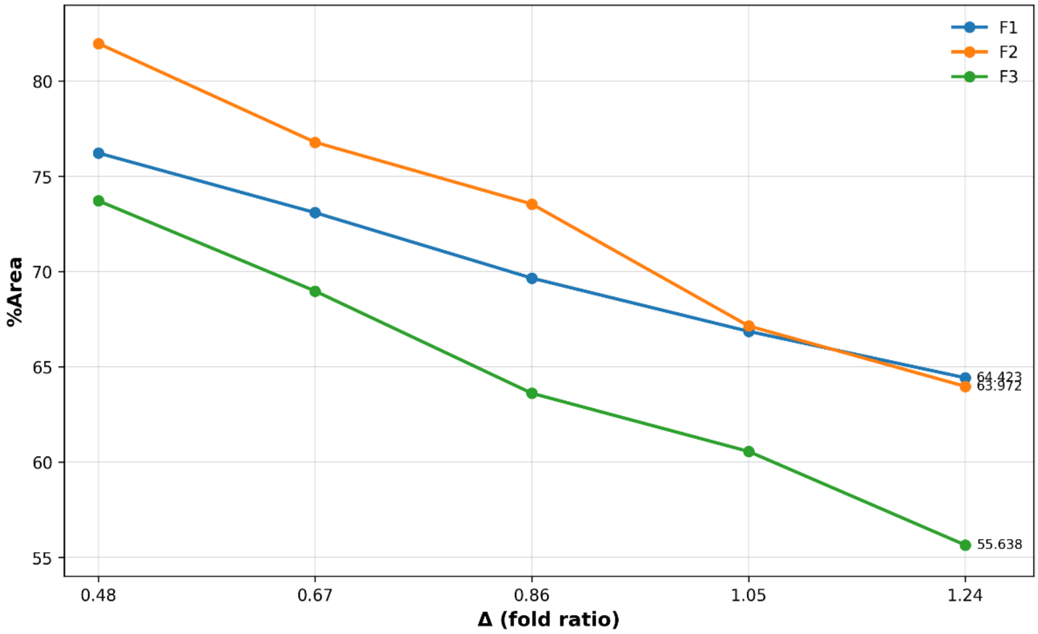

b

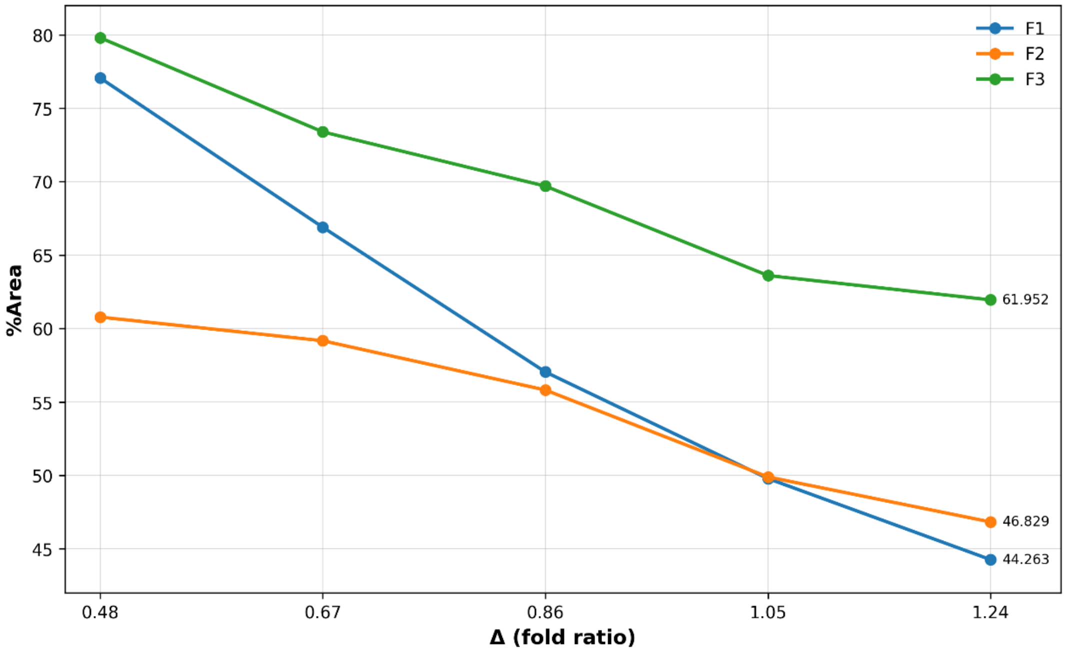

c

Figure 5.6 — Change in Bright-Area Proportion A with Increasing Δ: *a* — $A_{overall}$; *b* — A_{ROI1}; *c* — A_{ROI2}

As shown in Figure 5.6, as Δ increased from 0.48 to 1.24, the values of $A_{overall}$, A_{ROI1}, and A_{ROI2} generally decreased. This change shows that as pleat depth increases, the pleat ridges, fold lines, and illuminated surfaces contract, while the original bright regions are replaced by a denser pleated structure. $A_{overall}$ reflects the overall reduction of the bright area in the main pleat zone; A_{ROI1} reflects the local level response in the upper zone of pleat concentration; and A_{ROI2} reflects the sensitivity of the diagonal pleat-propagation region to local deformation and inter-fabric differences.

In the general pleat region, the strongest reduction in the bright area was observed for fabric F2: $A_{overall}$ decreased from 69.747% to 43.443%, that is, by 26.304 percentage points. For fabric F1, it decreased from 61.372% to 43.392%, corresponding to a reduction of 17.980 percentage points. For F3, it decreased from 74.840% to 58.181%, that is, by 16.659 percentage points. These data show that $A_{overall}$ reflects the total reduction of the bright area in the main pleat zone.

A_{ROI1} showed similar magnitudes for F2 and F3, indicating a relatively stable level response in the upper zone of pleat concentration as pleating increased. For A_{ROI2}, the differences between fabrics were more pronounced: the reduction reached 32.799 percentage points for F1, 13.950 percentage points for F2, and 17.846 percentage points for F3. Consequently, the diagonal pleat-propagation region was more sensitive to local deformation, fabric drapeability differences, and the ability to preserve the bright area.

The results for $A_{overall}$, A_{ROI1}, and A_{ROI2} jointly show that the bright-area proportion can reflect changes in pleat form on the PLD dress at both the general and local levels.

5.4. Pattern Correction of the Pleated Dress Based on Grayscale Response and Fabric Drape Coefficient

The complete data matrix, based on 15 observations formed by fabrics F1–F3 at five levels PLDP1–PLDP5, is presented in Appendix B. Fabrics F4 and F5 were not used in the matrix, but were applied only for validation pattern correction and subsequent verification. In the model for predicting the pleat-formation coefficient Δ, fabric DC_{SFM} and $A_{overall}$ were used as input variables. The equation is as follows:

$$\Delta = 1.4934 + 1.2866DC_{SFM} - 0.0230A_{overall} \tag{5.14}$$

where Δ is the predicted pleat-formation coefficient; DC_{SFM} is the fabric drape coefficient measured using the SFM method; and $A_{overall}$ is the proportion of the bright area in the overall pleat region, %.

In Equation (5.14), the coefficient of $A_{overall}$ is negative, meaning that the predicted value of Δ increases as the proportion of the overall bright area decreases. This corresponds to the trend identified in Section 5.3.2, where the bright-area proportion A decreased as pleat magnitude increased. The coefficient of DC_{SFM} is positive, indicating an increase in the predicted value of Δ as fabric DC_{SFM} increases.

Local models were developed to verify whether the relationship between grayscale response and coefficient Δ was preserved in different structural pleat zones. A_{ROI1} denotes the proportion of the bright area in ROI-1, and A_{ROI2} denotes the proportion of the bright area in ROI-2. Table 5.7 shows the regression coefficients, approximation indicators, and error level for the two local Δ prediction models.

Table 5.7 — Regression Results of Local Δ Prediction Models

Zone	Intercept	Coefficient for DC	Coefficient for *A*	R^2	Adj. R^2	RMSE
ROI-1	4,5908	−1,4505	−0,0436	0,918	0,904	0,086
ROI-2	1,6988	1,6867	−0,0275	0,796	0,763	0,136

Note: RMSE is the root mean square error; the coefficient for A in the ROI-1 model corresponds to A_{ROI1}, and in the ROI-2 model to A_{ROI2}; for both models, $p < 0.001$.

The local model for ROI-1 is described by the equation:

$$\Delta = 4.5908 - 1.4505DC_{SFM} - 0.0436A_{ROI1} \tag{5.15}$$

rwhere A_{ROI1} is the proportion of the bright area in ROI-1, %;

The local model for ROI-2 is as follows:

$$\Delta = 1.6988 + 1.6867DC_{SFM} - 0.0275A_{ROI2} \tag{5.16}$$

where A_{ROI2} is the proportion of the bright area in ROI-2, %.

In Equations (5.15) and (5.16), the coefficients of A_{ROI1} and A_{ROI2} are negative, meaning that the predicted value of Δ increases as the local bright-area proportion decreases. The absolute value of the coefficient for A in ROI-1 is greater than that in ROI-2, indicating higher sensitivity of Δ to changes in the bright area in the upper pleat-concentration zone. The different signs of the coefficients for DC_{SFM} in the two local models indicate that fabric drapeability plays different roles in different local structural zones.

The obtained equations were used to construct patterns according to the following algorithm.

1. The target dress B was made from light-colored fabric F4 to determine all indicators in the three zones that change under the influence of pleat coefficient Δ.
2. The drape coefficient DC_{SFM} was calculated for fabric F4.
3. In the image of the target dress B, $A_{overall,B}$ was measured as 54.76%.
4. Fabric F5, with a drape coefficient $DC_{SFM} = 0.46$, was selected for the validation dress V.
5. The initial data for structural pattern modelling of the validation dress V were calculated using $A_{overall,B}$ of the target dress B and the drape coefficient DC_{SFM} of fabric F5. After substituting these two values into Equation (5.14), the pleat-formation coefficient Δ required for pattern modification, namely conical spreading, was obtained:

$$\Delta = 1.4934 + 1.2866 \times 0.46 - 0.0230 \times 54.76 = 0.826 \approx 0.83$$

6. The required value $\Delta = 0.83$ was closer to PLDP3. This shows that, in order to approximate the overall bright-area response of the target dress B made from fabric F4, the validation dress

pattern V for fabric F5 should use a pleat-magnitude level close to the third level. Since the predicted value does not completely coincide with the existing PLD levels, the pleat magnitudes P_1–P_{10} were calculated by interpolation between adjacent levels.

Since the pleat coordinates P_1–P_{10} in the PLD pattern are constant, only the pleat magnitude at each fixed position was changed during structural pattern modelling. For the predicted Δ located between adjacent levels, the pleat magnitude at the i-th position was calculated using Equation (5.17):

$$P_i(\Delta) = P_{i,k} + \frac{\Delta - \Delta_k}{\Delta_{k+1} - \Delta_k}(P_{i,k+1} - P_{i,k}) \tag{5.17}$$

where $P_i(\Delta)$ is the pleat magnitude at the i-th position for the predicted Δ; $P_{i,k}$ and $P_{i,k+1}$ are the pleat magnitudes at the i-th position at two adjacent PLD levels; Δ_k and Δ_{k+1} are the pleat-formation coefficients for the two adjacent PLD levels; and $i = 1, 2, \ldots, 10$.

The corrected values P_1–P_{10} were obtained by linear interpolation between PLDP2 and PLDP3. From PLDP2 to PLDP3, the pleat magnitude at each position increases by 1 cm; therefore, the interpolated values are generally close to PLDP3, but slightly lower than PLDP3. Table 5.8 presents the pattern-correction results for the validation dress V made from fabric F5.

Table 5.8 — Pleat Parameters for the Validation Dress Pattern V Made from Fabric F5

Validation Fabric	Δ	Adjusted Fold Value, cm									
		P_1	P_2	P_3	P_4	P_5	P_6	P_7	P_8	P_9	P_{10}
F5	0.83	3.5	4.0	4.4	3.5	3.1	3.5	5.3	7.2	6.1	3.1

The corrected values P_1–P_{10} range from 3.1 to 7.2 cm. Larger pleat magnitudes were concentrated in P_7–P_9: P_8 was 7.2 cm, P_9 was 6.1 cm, and P_7 was 5.3 cm. This shows that the diagonal pleat-propagation zone remains the region with greater pattern opening. The values P_1–P_6 were comparatively smaller and mainly supported the local fold lines and pleat-ridge structure in the upper pleat-concentration zone.

7. The pattern was corrected while preserving the original main PLD contour, fixed pleat positions, and pleat-opening direction, changing only the magnitude of each fixed pleat based on the predicted Δ, as shown in Figure 2.3.

Thus, the overall grayscale response of the target dress F4 and the drape coefficient of fabric F5 were converted into pattern parameters directly used to produce the validation dress V from fabric F5.

5.5. Validation of the result of adjusting the pattern for a pleated dress

The target dress B and the validation dress V were used to verify morphological correspondence after pattern correction.

Validation was conducted at three levels. The first level was based on silhouette comparison. The second level was based on comparison of equivalent thresholds and characterized the closeness of the bright-area response in the overall pleat region, ROI-1, and ROI-2. The third level was based on the structural similarity index measure (SSIM) and characterized the local grayscale image structure in ROI-1 and ROI-2. Figure 5.7 shows the target dress B, the validation dress V, and the silhouette-overlay result after centroid alignment, used to identify the common overlap region and local boundary-deviation zones.

a *b* *c*

Figure 5.7 — Silhouette Comparison of the Target Dress B and Validation Dress V: *a* — target dress B; *b* — validation dress V; *c* — silhouette-overlay result after centroid alignment

As shown in Figure 5.7, the main contour regions of dresses B and V have a large overlap area. Differences are mainly concentrated in the upper shoulder region, along the right outer contour, along the hemline, and near the local boundary of pleat opening. This distribution indicates silhouette closeness; however, the free hem, edge sagging, and local pleat opening still cause boundary deviations. The non-overlapping areas are mainly located along the outer contour and local free boundaries rather than in the main dress region.

The degree of overlap of the binary silhouettes, area difference, and boundary deviation were used to quantitatively evaluate silhouette consistency. Table 5.9 shows the consistency indicators of the frontal silhouettes.

Table 5.9 — Consistency Indicators of Frontal Silhouettes

View	IoU	Dice	Area Difference, %	Boundary Deviation, px		
				Mean	95th	Maximum

					Percentile	
Frontal	0.9336	0.9657	+0.656	10.064	36.024	97.739

As shown in Table 5.9, the IoU between B and V in the frontal view was 0.9336, and the Dice value was 0.9657, indicating a high degree of area overlap. The frontal projected area of the validation dress is close to that of the target dress. The mean boundary deviation was 10.064 px, indicating a small spatial shift for most boundary points. The 95th percentile boundary deviation was 36.024 px, meaning that most boundary deviations remained within a relatively low range. The maximum boundary deviation was 97.739 px and corresponded to the local non-overlapping regions in the shoulder zone, right outer contour, and hemline shown in Figure 5.7. The silhouette analysis results show that the validation dress V made from fabric F5 is close to the target dress B made from fabric F4 at the level of the main overall shape, while residual differences are mainly expressed as local edge shifts.

Silhouette consistency reflects only the closeness of the overall outer contour and does not show how close the bright-area response in the pleats is. Therefore, comparison of the equivalent grayscale response was additionally used to evaluate whether dresses B and V formed similar bright-area responses in the overall pleat region, ROI-1, and ROI-2. The complete threshold-comparison data are provided in Appendix B. Table 5.10 shows the differences in equivalent response in the three regions.

Table 5.10 — Validation Results of Equivalent Grayscale Response

Analysis Region	Difference in Response, p.p.			
	Range	Mean	Minimum	Maximum
Overall	0,021–0,619	0,232	0,021	0,619
ROI-1	0,015–0,314	0,192	0,015	0,314
ROI-2	0,086–0,643	0,417	0,086	0,643

As shown in Table 5.10, an interpretable relationship of equivalent grayscale response was obtained in all three regions, although the level of consistency differed by region. The mean response difference in the overall pleat region was 0.232 percentage points, showing the similarity between dresses V and B in the main pleat zone. The bright-area response in the upper pleat-concentration zone ROI-1 was the most stable. The mean response difference in ROI-2 was 0.417 percentage points, which was higher than the values for the overall pleat region and ROI-1. Consequently, the diagonal pleat-propagation zone is more sensitive to fabric sagging, lateral opening, and the local boundary of fold lines. The equivalent-response results show that the predicted pleat magnitudes P_1–P_{10} allow dress V to approximate the overall bright-area response and the upper local response of dress B.

Figure 5.8 shows grayscale image fragments of dresses B and V in ROI-1 and ROI-2.

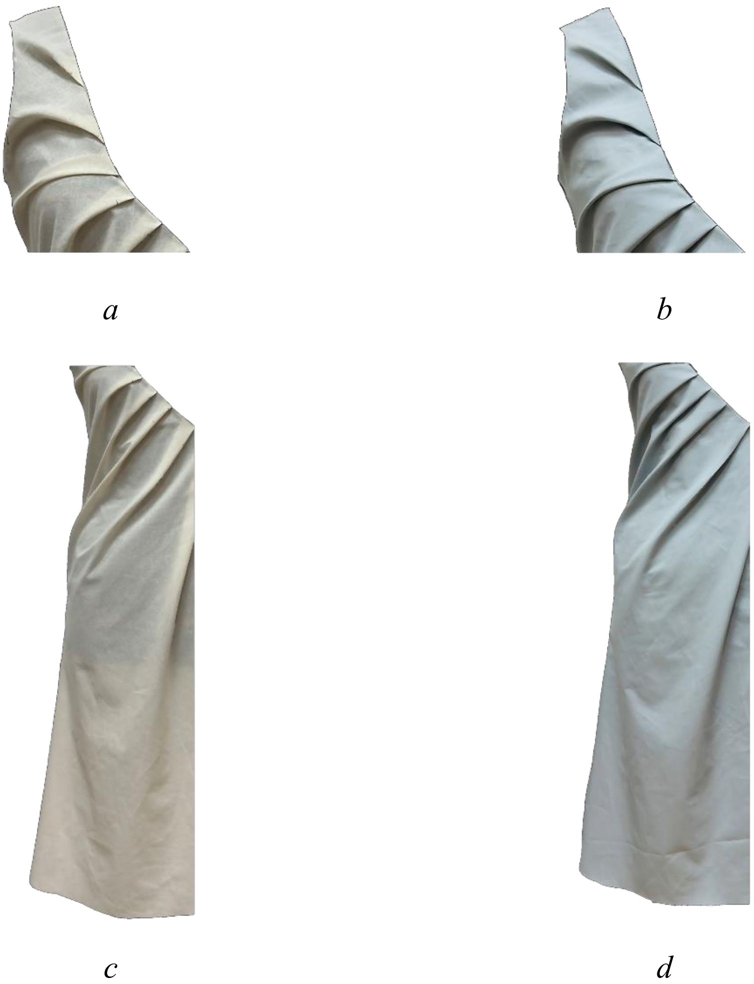

Figure 5.8 — Comparison of Local Structure: *a* — ROI-1 for dress B; *b* — ROI-1 for dress V; *c* — ROI-2 for dress B; *d* — ROI-2 for dress V

As shown in Figure 5.8, dresses B and V in ROI-1 have similar pleat direction, fold-line boundaries, and the character of transition between bright and dark regions. Both images show a similar pleated form concentrated from the shoulder region toward the bust area, and the main pleat ridges and local boundaries of the bright zones correspond well. In ROI-2, dresses B and V preserve a similar diagonal propagation direction; however, the local fold-line boundaries, grayscale gradient, and fine wrinkle texture differ more strongly.

Local structural similarity was further quantitatively evaluated using SSIM and its brightness, contrast, and structure components. Table 5.11 shows the SSIM decomposition results for dresses B and V in ROI-1 and ROI-2.

Table 5.11 — Local Structural Similarity Verification Results

Region	Brightness	Contrast	Structural	SSIM
ROI-1	0,9591	0,9062	0,8382	0,7690
ROI-2	0,9210	0,8674	0,7232	0,6096

As shown in Table 5.11, the SSIM in ROI-1 was 0.7690, which is higher than the value of 0.6096 in ROI-2. This shows that the local grayscale image structure of the upper pleat-concentration zone was more similar. Dresses B and V in ROI-1 were close not only in the overall grayscale level, but also in the amplitude of local light–dark transitions and the organization of the pleated structure. In ROI-2, the differences were mainly associated with local pleat texture, the position of fold lines, and the organization of the grayscale image structure.

Thus, silhouette overlap, equivalent grayscale response, and local SSIM jointly show that the validation dress V made from fabric F5 is close to the target dress B made from fabric F4 in terms of silhouette, bright-area response in the main region, and local structure in the upper ROI-1 pleat zone. The differences are mainly concentrated in ROI-2 and along local outer boundaries, showing the higher sensitivity of the diagonal pleat-propagation zone, free lower edge, and side boundaries to fabric differences. The predicted pleat magnitudes obtained based on the new drape coefficient DC_{SFM} confirm the applicability of the calculated pattern-correction scheme.

Conclusions to Chapter 5

1. A system of unified parameters was developed for laboratory samples, namely SS and LS, and two types of dresses, namely BD and PLD, making it possible to link the new drape coefficient with dress shape parameters and the structural pattern-modeling scheme. The drape coefficient DC_{SFM}, measured on the developed anthropomorphic stand for the short sample SS, characterizes basic drapeability, while the parameters P_{d1}–P_{d4} describe the dress shape. The bright-area indicators $A_{overall}$, A_{ROI1}, and A_{ROI2} characterize the grayscale response of pleats. This parametric chain provides a transition from fabric measurement to prediction of the draped dress form.
2. Fabric-specific regression equations based on the new drape coefficient DC_{SFM} make it possible to predict dress shape parameters with an error below 5%. This confirms the applicability of the new drape coefficient DC_{SFM} as a key input parameter and demonstrates the possibility of using it at the dress level.
3. For analyzing dress drapeability, the bright area was selected as the main object of grayscale response. Compared with the dark candidate area, it showed a lower inter-fabric coefficient of variation, a higher mean normalized grayscale value, and a lower within-group coefficient of variation for grayscale values. Threshold scanning made it possible to determine fabric-specific thresholds for the studied fabrics: 112, 174, 191, and 180, respectively.
4. The pattern-correction model was developed based on the new drape coefficient DC_{SFM} and the bright-area indicator $A_{overall}$, which was selected as a universal indicator ensuring equivalent perception of the draped pleated surface.
5. Validation of the corrected pattern showed the closeness of the validation dress V, constructed using the modified pattern, to the target dress B, constructed using the original pattern, at the levels of silhouette, bright-area response, and local structure of the upper pleat zone. The

algorithm for correcting the original pattern when replacing one fabric with another made it possible to preserve the silhouette and local pleat structure.

6. The research results confirmed that the new drape coefficient DC_{SFM} can be used as an indicator of fabric drapeability, a calculated parameter for predicting dress shape, and a controlling factor for parameterizing structural pattern-modeling techniques. The relationship among DC_{SFM}, dress shape parameters, and grayscale pleat parameters forms a new basis for constructing digital twins of garments.

RESEARCH RESULTS

RESULTS OF THE COMPLETED RESEARCH

1. A new anthropomorphic method for evaluating fabric drapeability was developed, reproducing the shape-formation conditions of shoulder garments and making it possible to predict the parameters of the three-dimensional silhouette form and the pleated surface of women's dresses. The method demonstrated a high differentiating capacity for measuring fabric drapeability compared with existing methods.

2. The geometric parameters of the two-component sample and the degree of their influence on the value of the anthropomorphic drape coefficient were determined through variation of the joining seam type (33.2%), cutting direction (27.8%), width (21.5%), and configuration of the joined edges (17.5%). Virtual–physical validation of the new method showed the absence of statistically significant differences between virtual and physical measurements ($p > 0.05$, correlation coefficient $r = 0.96$) and the possibility of parallel application in physical and virtual environments.

3. A method for quantitative analysis of the pleated surface of dresses using computer vision in grayscale was developed, quantitatively linking the expression of pleat relief with fabric drapeability ($r = -0.78$).

4. A method for correcting the patterns of model constructions of women's dresses was developed, for the first time combining the grayscale response indicator of the pleated surface, the anthropomorphic fabric drape coefficient, and the pleat coefficient, thereby ensuring visual similarity of pleated surfaces made from different fabrics. The developed method implements a parametric algorithm for structural pattern modeling of dress patterns: "anthropomorphic drape coefficient → visual morphology of the pleated surface → quantitative pleat indicator → pattern parameter of the model construction".

5. A methodology was developed for simulation modeling of the physico-mechanical property indicators of fabrics, including extensibility, bending, thickness, surface density, and drapeability, for fabric digital twins using neural networks as a non-contact, non-instrumental measurement tool.

6. An algorithm was developed for generating fabric digital twins based on the use of non-contact, non-instrumental measurement results obtained after analyzing photographic images containing information about the appearance of the pleated fabric surface formed under the influence of different types of deformation, including gravity, drapeability, and twisting, as well as after performing the measurement-protocol and validation procedures. It was shown that the difference between digital twins of fabrics and women's dresses generated in three-dimensional simulation programs using laboratory contact testing results and non-contact, non-instrumental results ranges from 26% to 35.8% according to MAPE, while preserving similarity in three-dimensional form, drapeability, outer contour, and fold distribution.

7. An end-to-end process for obtaining digital twins of women's dresses with a pleated

surface was formed. This process can be fully implemented in the digital environment using computer programs and includes the use of a new quantitative and visual database, measurement of physico-mechanical property indicators of fabrics by instrumental and non-instrumental methods, assessment of surface pleating, generation of adequate digital twins of fabrics and dresses, and predictive-corrective pattern modelling.

RECOMMENDATIONS AND PROSPECTS FOR FURTHER DEVELOPMENT OF THE TOPIC

1. The results of the work are recommended for implementation in the educational process for bachelor’s and master’s students studying within the enlarged group 29 in the field of “Technology of Light Industry Products”, as well as at garment enterprises for the digitalization of product development.
2. A promising direction is the expansion of the database of studied materials, including knitted fabrics and highly elastic fabrics.
3. The development of virtual design technology can be implemented in dynamic 4D twins of the “body–garment” system, taking into account changes in material properties and garment shape during movement.

REFERENCES

1. Peirce F. T. The handle of cloth as a measurable quantity // Journal of the Textile Institute. – 1930. – Vol. 21, no. 9. – P. T377–T416.
2. Booth J. E. Principles of Textile Testing. – 3rd ed. – London : Butterworths, 1969.
3. Abbott G. M. The measurement of stiffness in fabrics // Journal of the Textile Institute. – 1951. – Vol. 42. – P. T213–T224.
4. Chu C. C., Cummings C. L., Teixeira N. A. Mechanics of elastic performance of textile materials Part V: A study of the factors affecting the drape of fabrics—the development of a drape meter // Textile Research Journal. – 1950. – Vol. 20, no. 8. – P. 539–548.
5. Cusick G. E. A study of fabric drape : dissertation. – Manchester : University of Manchester, 1962.
6. Cusick G. E. The dependence of fabric drape on bending and shear stiffness // Journal of the Textile Institute. – 1965. – Vol. 56, no. 11. – P. T596–T606.
7. Cusick G. E. The measurement of fabric drape // Journal of the Textile Institute. – 1968. – Vol. 59, no. 6. – P. 253–260.
8. British Standards Institution. BS 5058: 1973 Method for the assessment of drape of fabrics. – London : BSI, 1973.
9. British Standards Institution. BS EN ISO 9073-9: 1998 Textiles—Test methods for nonwovens—Part 9: Determination of drape coefficient. – London : BSI, 1998.
10. International Organization for Standardization. ISO 9073-9: 2008 Textiles—Test methods for nonwovens—Part 9: Determination of drapability including drape coefficient. – Geneva : ISO, 2008.
11. Hearle J. W. S., Amirbayat J. Analysis of drape by means of dimensionless groups // Textile Research Journal. – 1986. – Vol. 56, no. 11. – P. 727–733.
12. Kawabata S. The Standardization and Analysis of Hand Evaluation. – Osaka : The Textile Machinery Society of Japan, 1980.
13. Kawabata S., Niwa M. Fabric performance in clothing and clothing manufacture // Journal of the Textile Institute. – 1989. – Vol. 80, no. 1. – P. 19–50.
14. Morooka H., Niwa M. Relation between drape coefficient and mechanical properties of fabrics // Journal of the Textile Machinery Society of Japan. – 1976. – Vol. 22, no. 3. – P. 67–73.
15. Niwa M., Seto F. Relationship between drapeability and mechanical properties of fabrics // Journal of Textile Machinery Society of Japan. – 1986. – Vol. 39, no. 11. – P. 161–168.
16. Gaucher C., King M. W., Johnston R. D. The relationship between fabric mechanical properties and drape in knitted fabrics // Textile Research Journal. – 1983. – Vol. 53, no. 5. – P. 294–300.
17. Collier B. J., Paulins V. A., Collier J. R. Effects of interfacing type on shear and drape behavior of apparel fabrics // Clothing and Textiles Research Journal. – 1989. – Vol. 7, no. 3. – P. 51–56.

18. Vangheluwe L., Kiekens P. Time dependence of the drape coefficient of fabrics // International Journal of Clothing Science and Technology. – 1993. – Vol. 5, no. 5. – P. 5–8.
19. Robson D., Long C. C. Drape analysis using imaging techniques // Clothing and Textiles Research Journal. – 2000. – Vol. 18, no. 1. – P. 1–8.
20. Jeong Y. J. A study of fabric-drape behaviour with image analysis Part I: Measurement, characterisation, and instability // Journal of the Textile Institute. – 1998. – Vol. 89, no. 1. – P. 59–69.
21. Yang M., Qin L., Matsudaira M. Measurement of drape coefficients of fabrics and description of those hanging shapes, Part 6: Evaluation of dynamic drape behavior of fabrics in swinging motion // Journal of the Textile Machinery Society of Japan. – 2001. – Vol. 54, no. 3. – P. T57–T64.
22. Tamás P., Geršak J., Halász M. Sylvie 3D drape tester—new system for measuring fabric drape // Tekstil. – 2006. – Vol. 55, no. 10. – P. 497–502.
23. Kenkare N. S. Three-Dimensional Modelling of Garment Drape : dissertation. – Raleigh : North Carolina State University, 2007.
24. Breen D. E., House D. H., Wozny M. J. Predicting the drape of woven cloth using interacting particles // Computer Graphics. – 1994. – Vol. 28. – P. 365–372.
25. Volino P., Thalmann N. M. Virtual Clothing: Theory and Practice. – Berlin : Springer, 2000.
26. Buyukaslan E., Kalaoglu F., Jevsnik S. Drape simulation and subjective assessment of virtual drape // IOP Conference Series: Materials Science and Engineering. – 2017. – Vol. 254. – Article 162005.
27. Magnenat-Thalmann N. [et al.]. From measured fabric to the simulation of cloth // 2007 10th IEEE International Conference on Computer-Aided Design and Computer Graphics. – IEEE, 2007. – P. 449–452.
28. Sanchez H. Hem finishes and digital drape evaluation : dissertation. – Ithaca : Cornell University, 2022.
29. Kenkare N., Lamar T. A. M., Pandurangan P., Eischen J. Enhancing accuracy of drape simulation. Part I: Investigation of drape variability via 3D scanning // The Journal of the Textile Institute. – 2008. – Vol. 99, no. 3. – P. 211–218.
30. Jevsnik S., [et al.]. The study of fabric drape behaviour in the virtual environment // International Istanbul Textile Congress. Istanbul, 2013.
31. Fozzard G. J. W., Rawling A. J. Simulation of dressing and drape for garment CAD // Proceedings of the 6th International Forum on CAD. – 1991. – P. 157–162.
32. Hardaker C. H. M., Fozzard G. J. W. Towards the virtual garment: three-dimensional computer environments for garment design // International Journal of Clothing Science and Technology. – 1998. – Vol. 10, no. 2. – P. 114–127.

33. Spanlang B., Vassilev T., Walters J., [et al.]. A virtual clothing system for retail and design // Research Journal of Textile and Apparel. – 2005. – Vol. 9, no. 1. – P. 74–87.
34. Sayem A. S. M., Kennon R., Clarke N. 3D CAD systems for the clothing industry // International Journal of Fashion Design, Technology and Education. – 2010. – Vol. 3, no. 2. – P. 45–53.
35. Lee S. Y., Kang I. A. A comparative study of the shapes of 3D virtual skirts and actually made skirts // Journal of the Korean Society of Costume. – 2009. – Vol. 59, no. 8. – P. 26–36.
36. Kim H. A., Ryu H. S., Lee J. H., [et al.]. A study on the comparing visual images between the actual garment and the 3D garment simulation of flare skirts // Science of Emotion and Sensibility. – 2011. – Vol. 14, no. 3. – P. 385–394.
37. Lee J., Kim H. A., Nam Y. J., [et al.]. Drape Evaluation of 3D Garment Simulations for Flared Skirts // The Korean Fashion and Textile Research Journal. – 2014. – Vol. 16, no. 1. – P. 128–136.
38. Buyukaslan E., Jevsnik S., Kalaoglu F. Drape of virtual garments on body models: impact of mechanical properties of the fabrics // Proceedings of the 6th International Conference on 3D Body Scanning Technologies. – Lugano, 2015. – P. 127–133.
39. Buyukaslan E., Jevsnik S., Kalaoglu F. Comparative analysis of drape characteristics of actually and virtually draped fabrics // International Journal of Clothing Science and Technology. – 2018. – Vol. 30, no. 3. – P. 286–301.
40. Shim E., Koo D. S., An J. S., [et al.]. Comparison of the silhouette of virtual clothes by fabric characteristics of nylon fabric for the utilization of virtual clothes // ACS Omega. – 2022. – Vol. 7, no. 50. – P. 47156–47164.
41. Bell S., Upchurch P., Snavely N., Bala K. Material recognition in the wild with the Materials in Context Database // Proceedings of the IEEE Conference on Computer Vision and Pattern Recognition. – 2015. – P. 3479–3487.
42. Schwartz G., Nishino K. Automatically discovering local visual material attributes // Proceedings of the IEEE Conference on Computer Vision and Pattern Recognition. – 2015. – P. 3565–3573.
43. Li J., Wang W., Deng N., Xin B. A novel digital method for weave pattern recognition based on photometric differential analysis // Measurement. – 2020. – Vol. 152. – Article 107336.
44. Hussain M. A. I., Khan B., Wang Z. J., [et al.]. Woven fabric pattern recognition and classification based on deep convolutional neural networks // Electronics. – 2020. – Vol. 9, no. 6. – P. 1048.
45. Meng S., Pan R., Gao W., Zhou J., Wang J., He W. A multi-task and multi-scale convolutional neural network for automatic recognition of woven fabric pattern // Journal of Intelligent Manufacturing. – 2021. – Vol. 32, no. 4. – P. 1147–1161.

46. Wu H., Chen X., Zhang C., Zhou B., Zhao Q. Modelling yarn-level geometry from a single micro-image // Frontiers of Information Technology & Electronic Engineering. – 2019. – Vol. 20. – P. 1165–1174.
47. Wang X., Georganas N. D., Petriu E. M. Fabric texture analysis using computer vision techniques // IEEE Transactions on Instrumentation and Measurement. – 2011. – Vol. 60, no. 1. – P. 44–56.
48. Bouman K. L., Xiao B., Battaglia P., Freeman W. T. Estimating the material properties of fabric from video // Proceedings of the IEEE International Conference on Computer Vision. – 2013. – P. 1984–1991.
49. Mamun A. A., Nabi M. M., Islam F., Bappy M. M., Uddin M. A., Hossain M. S., Talukder A. Streamline video-based automatic fabric pattern recognition using Bayesian-optimized convolutional neural network // The Journal of The Textile Institute. – 2024. – Vol. 115. – P. 1878–1891.
50. Mahanta L. B., Mahanta D. R., Rahman T., Chakraborty C. Handloomed fabrics recognition with deep learning // Scientific Reports. – 2024. – Vol. 14. – P. 7974.
51. Chaka K. T., Shiferaw A. A., Sharew S. T. Inspection of cotton woven fabrics produced by Ethiopian textile factories through a real-time vision-based system // Journal of Natural Fibers. – 2023. – Vol. 20. – Article 2286615.
52. Das A. Deep learning to authenticate traditional handloom textile // Information. – 2024. – Vol. 15, no. 8. – P. 465.
53. Dominguez-Elvira H., Nicás A., Cirio G., Rodríguez A., Garcés E. Practical methods to estimate fabric mechanics from metadata // Computer Graphics Forum. – 2024. – Vol. 43, no. 2. – Article e15029.
54. Tu Y. F., Kwan M. Y., Yick K. L. A systematic review of AI-driven prediction of fabric properties and handfeel // Materials. – 2024. – Vol. 17, no. 20. – P. 5009.
55. Güder O., Işık Ş, Anagun Y. Fabric defects identification for textile industry with a deep learning approach // Journal of the Textile Institute. – 2025. – Vol. 116, no. 8. – P. 1493–1502.
56. Li J., Li D., Savarese S., Hoi S. BLIP-2: Bootstrapping language-image pre-training with frozen image encoders and large language models // Proceedings of the 40th International Conference on Machine Learning. – 2023.
57. Liu H., Li C., Wu Q., Lee Y. J. Visual instruction tuning // Advances in Neural Information Processing Systems. – 2023. – Vol. 36.
58. Dai W., Li J., [et al.]. InstructBLIP: Towards general-purpose vision-language models with instruction tuning // Advances in Neural Information Processing Systems. – 2023. – Vol. 36.
59. OpenAI. GPT-4V(ision) system card : report. – 2023.
60. Wu W., Zhang T., [et al.]. GPT4Vis: What Can GPT-4 Do for Zero-shot Visual Recognition? // arXiv preprint arXiv:2311.15732. – 2024.

61. Lei G., Gkoumas K., [et al.]. Materials science in the era of large language models: a perspective // Digital Discovery, 2024, 3:. – DOI: 10.1039/D4DD00074A.
62. Yu S., Ran N., Liu J. Large-language models: The game-changers for materials science research // Artificial Intelligence Chemistry. – 2024. – Vol. 2, no. 2. – Article 100076.
63. Korolev V., Protsenko P. Accurate, interpretable predictions of materials properties within transformer language models // Patterns. – 2023. – Vol. 4, no. 10. – Article 100803.
64. Rubungo A. N., Arnold C., Rand B. P., Dieng A. B. LLM-Prop: Predicting physical and electronic properties of crystalline solids from their text descriptions // arXiv preprint arXiv:2310.14029. – 2023.
65. Choudhary K. AtomGPT: Atomistic Generative Pre-trained Transformer for Forward and Inverse Materials Design // The Journal of Physical Chemistry Letters. – 2024. – Vol. 15, no. 27. – P. 6909–6917.
66. Welty C., Paritosh P., Aroyo L. Metrology for AI: From benchmarks to instruments // arXiv preprint arXiv:1911.01875. – 2019.
67. National Institute of Standards and Technology. Artificial Intelligence Measurement and Evaluation at the National Institute of Standards and Technology : report. – NIST Draft, 2021.
68. Hatakeyama-Sato K., [et al.]. Perspective on utilizing foundation models for laboratory automation in materials research // Materials Research Communications. – 2025.
69. Stach E., Blaiszik B., Foster I., [et al.]. Autonomous experimentation systems for materials development: a community perspective // Matter. – 2021. – Vol. 4, no. 9. – P. 2702–2726.
70. Litzinger J., Neumann J., Peters D., Thiel F. Streamlining conformity assessment of software applying large language models // Measurement: Sensors. – 2024. – Vol. 38. – Article 101792.
71. Schmelter S., Fortmeier I., Heißelmann D. Metrology for Virtual Measuring Instruments Illustrated by Three Applications // Metrology. – 2025. – Vol. 5, no. 3. – P. 54.
72. Barbosa C. R. H., Sousa M. C., Almeida M. F. L., Calili R. F. Smart Manufacturing and Digitalization of Metrology: A Systematic Literature Review and a Research Agenda // Sensors. – 2022. – Vol. 22, no. 16. – P. 6114.
73. Xiong X. C., Zhu Y., Li J., Duan Y., Fang X. A digital framework for metrological information // Measurement: Sensors. – 2021. – Vol. 18. – Article 100122.
74. JCGM. Evaluation of Measurement Data—Guide to the Expression of Uncertainty of Measurement (JCGM 100:2008). – Paris : BIPM, 2008.
75. JCGM. International Vocabulary of Metrology—Basic and General Concepts and Associated Terms (JCGM 200:2012). – Paris : BIPM, 2012.
76. Taylor B. N., Kuyatt C. E. Guidelines for Evaluating and Expressing the Uncertainty of NIST Measurement Results : report. – NIST Technical Note 1297, 1994.
77. Possolo A. Simple Guide for Evaluating and Expressing the Uncertainty of NIST Measurement Results : report. – NIST Technical Note 1900, 2015.

78. Puig R. B., Gallegos J. G., Mohino Herranz I., Pérez Sanz F. J., Vicente Mussons T. Digital transformation: Ensuring metrological traceability // Measurement: Sensors. – 2025. – Vol. 38, suppl. – Article 101801.
79. Bilson S., Cox M., Pustogvar A., Thompson A. A metrological framework for uncertainty evaluation in machine learning classification models // Metrologia. – 2025. – Vol. 62, no. 6. – Article ae1bae.
80. Adel T., Bilson S., Levene M., Thompson A. Trustworthy artificial intelligence in the context of metrology // arXiv preprint arXiv:2406.10117. – 2024.
81. Fung Y. W., Lim K. H., Phang J. T. S. Review on three-dimensional clothing modelling and digital human reconstruction for virtual try-on applications // Multimedia Tools and Applications. – 2026. – Vol. 85. – P. 359. – DOI: 10.1007/s11042-026-21423-2.
82. Jung G., Kang M., Kim S. Development and evaluation of accurate 3D human models using scan data: a comparison with SMPL and CLO models // Fashion and Textiles. – 2025. – Vol. 12. – P. 17. – DOI: 10.1186/s40691-025-00427-w.
83. He J., Cao Y., Guo T., Liang W., Huang J., Liu Q., Yang H., Liu S., He R. From physically-based to learning-based in cloth simulation: evolution and future—a scoping review // The Visual Computer. – 2025. – Vol. 41. – P. 12711–12742. – DOI: 10.1007/s00371-025-04182-3.
84. Kim J. H., Lee J. S. Investigating parameters affecting the real and virtual drapability of silk fabrics for traditional Hanbok // Fashion and Textiles. – 2024. – Vol. 11. – P. 21. – DOI: 10.1186/s40691-024-00388-6.
85. Wang H., O’Brien J. F., Ramamoorthi R. Data-driven elastic models for cloth: modelling and measurement // ACM Transactions on Graphics. – 2011. – Vol. 30, no. 4. – P. 71.
86. Miguel E., Bradley D., Thomaszewski B., Bickel B., Matusik W., Otaduy M. A. Data-driven estimation of cloth simulation models // Computer Graphics Forum. – 2012. – Vol. 31, no. 2pt2. – P. 519–528.
87. Nealen A., Müller M., Keiser R., Boxerman E., Carlson M. Physically based deformable models in computer graphics // Computer Graphics Forum. – 2006. – Vol. 25, no. 4. – P. 809–836.
88. Bridson R., Marino S., Fedkiw R. Simulation of clothing with folds and wrinkles // Proceedings of the 2003 ACM SIGGRAPH/Eurographics Symposium on Computer Animation. – 2003. – P. 28–36.
89. Liu Y. M., Jang H. K. A study on the functional characteristics of apparel 3D CAD system // Advanced Materials Research. – 2013. – Vol. 627. – P. 501–505.
90. Choi K. H. 3D dynamic fashion design development using digital technology and its potential in online platforms // Fashion and Textiles. – 2022. – Vol. 9. – P. 9.

91. Wetherell S. V., Nicholson T. R., James A. M. Utilising 3D fashion design software to enable remanufacturing in sportswear // International Journal of Fashion Design, Technology and Education. – 2024. – Vol. 17, no. 2. – P. 249–259.
92. Lim H., Istook C. L. Drape simulation of three-dimensional virtual garment enabling fabric properties // Fibers and Polymers. – 2011. – Vol. 12, no. 8. – P. 1077–1082.
93. Power J. Fabric objective measurements for commercial 3D virtual garment simulation // International Journal of Clothing Science and Technology. – 2013. – Vol. 25, no. 6. – P. 423–439.
94. Luible C., Magnenat-Thalmann N. Suitability of standard fabric characterisation experiments for the use in virtual simulations // Proceedings of World Textile Conference AUTEX 2007. – Tampere, 2007.
95. Kuijpers S., Luible-Bär C., Gong R. H. The Measurement of Fabric Properties for Virtual Simulation—A Critical Review : report. – IEEE Standards Association, 2020. – P. 1–43.
96. Jung U., Istook C. L. Comparison of objective measurement methods of fabric tensile properties for 3D virtual garment software // ITAA Proceedings. – 2020. – DOI: 10.31274/itaa.12158.
97. Dai X., Hong Y. Fabric mechanical parameters for 3D cloth simulation in apparel CAD: A systematic review // Computer-Aided Design. – 2024. – Vol. 167. – Article 103638.
98. Duong P. D., Phuong L. T. T., Phan D. N., Thang V. T. Correlation between material properties and actual-simulated drape of textile products // Results in Engineering. – 2024. – Vol. 22. – Article 102077.
99. Wang R., Fang F., Chen Q. A Sustainable Framework for Realism Evaluation and Optimization of Virtual Fabric Drape Effect // Sustainability. – 2025. – Vol. 17, no. 12. – P. 5550. – DOI: 10.3390/su17125550.
100. Mahnić Naglić M., Petrak S., Tomljenović A. Analysis of woven fabric mechanical properties in the context of sustainable clothing development process // Polymers. – 2025. – Vol. 17, no. 15. – P. 2013.
101. Grieves M., Vickers J. Digital twin: Mitigating unpredictable, undesirable emergent behavior in complex systems // Transdisciplinary Perspectives on Complex Systems / ed. by F. J. Kahlen, S. Flumerfelt, A. Alves. – Cham : Springer, 2017. – P. 85–113.
102. Kritzinger W., Karner M., Traar G., Henjes J., Sihn W. Digital twin in manufacturing: A categorical literature review and classification // IFAC-PapersOnLine. – 2018. – Vol. 51, no. 11. – P. 1016–1022.
103. Tao F., Cheng J., Qi Q., Zhang M., Zhang H., Sui F. Digital twin-driven product design, manufacturing and service with big data // The International Journal of Advanced Manufacturing Technology. – 2018. – Vol. 94. – P. 3563–3576.

104. Riedelsheimer T., Dorfhuber L., Stark R. User centered development of a Digital Twin concept with focus on sustainability in the clothing industry // Procedia CIRP. – 2020. – Vol. 90. – P. 660–665.
105. Alam M. D., Kabir G., Mirmohammadsadeghi S. A digital twin framework development for apparel manufacturing industry // Decision Analytics Journal. – 2023. – Vol. 7. – Article 100252.
106. Papachristou E., Kalaitzi D., Pissas V. A methodological framework for the integration of 3D virtual prototyping into the design development of laser-cut garments // Journal of Engineered Fibers and Fabrics. – 2023. – Vol. 18. – DOI: 10.1177/15589250231194621.
107. Doungtap S., Petchhan J., Phanichraksaphong V., Wang J. H. Towards digital twins of 3D reconstructed apparel models with an end-to-end mobile visualization // Applied Sciences. – 2023. – Vol. 13, no. 15. – P. 8571.
108. Angelova R. A. Digital twins for a sustainable textile industry: A critical analysis of unexplored applications and future directions // Textiles. – 2025. – Vol. 5, no. 4. – P. 49.
109. Yoon K., Lim S. C. Real-to-sim high-resolution cloth modelling: Physical parameter optimization using particle-based simulation with robot manipulation data // Journal of Computational Design and Engineering. – 2025. – Vol. 12, no. 8. – P. 29–44. – DOI: 10.1093/jcde/qwaf065.
110. Kenkare N., May-Plumlee T. Evaluation of drape characteristics in fabrics // International Journal of Clothing Science and Technology. – 2005. – Vol. 17, no. 2. – P. 109–123.
111. Sayem A. S. M. Objective analysis of the drape behaviour of virtual shirt, part 2: technical parameters and findings // International Journal of Fashion Design, Technology and Education. – 2017. – Vol. 10, no. 2. – P. 180–189. – DOI: 10.1080/17543266.2016.122381.
112. Pandurangan P., Eischen J., Kenkare N., Lamar T. A. M. Enhancing accuracy of drape simulation. Part II: Optimized drape simulation using industry-specific software // The Journal of the Textile Institute. – 2008. – Vol. 99, no. 3. – P. 219–226.
113. Mahnić Naglić M., Petrak S., Tomljenović A. Analysis of woven fabric mechanical properties in the context of sustainable clothing development process // Polymers. – 2025. – Vol. 17, no. 15. – P. 2013.
114. Papachristou E., Kalaitzi D., Pissas V. A methodological framework for the integration of 3D virtual prototyping into the design development of laser-cut garments // Journal of Engineered Fibers and Fabrics. – 2023. – Vol. 18. – Article 15589250231194621. – DOI: 10.1177/15589250231194621.
115. Doungtap S., Petchhan J., Phanichraksaphong V., Wang J. H. Towards digital twins of 3D reconstructed apparel models with an end-to-end mobile visualization // Applied Sciences. – 2023. – Vol. 13, no. 15. – P. 8571. – DOI: 10.3390/app13158571.

116. Song H. K., Ashdown S. P. Investigation of the validity of 3-D virtual fitting for pants // Clothing and Textiles Research Journal. – 2015. – Vol. 33, no. 4. – P. 314–330.
117. Angelova R. A. Digital twins for a sustainable textile industry: A critical analysis of unexplored applications and future directions // Textiles. – 2025. – Vol. 5, no. 4. – P. 49.
118. Lagė A., Ancutienė K., Pukienė R., Lapkovska E., Dāboliņa I. Comparative study of real and virtual garments appearance and distance ease // Materials Science. – 2020. – Vol. 26, no. 2. – P. 233–239.
119. Kim H. A., Lim H. S. Measurement of drape appearance similarity between real and digital stretch fabric // Fashion & Textile Research Journal. – 2021. – Vol. 23, no. 5. – P. 645–654.
120. Brubacher K., Tyler D., Apeagyei P., Venkatraman P., Brownridge A. M. Evaluation of the Accuracy and Practicability of Predicting Compression Garment Pressure Using Virtual Fit Technology // Clothing and Textiles Research Journal. – 2023. – Vol. 41, no. 2. – P. 107–124.
121. Hu J., Chung S., Lo M. T. Effect of seams on fabric drape // International Journal of Clothing Science and Technology. – 1997. – Vol. 9, no. 3. – P. 220–227. – DOI: 10.1108/09556229710168351.
122. Orzada B. T., Moore M. A., Collier B. J. Grain alignment: effects on fabric and garment drape // International Journal of Clothing Science and Technology. – 1997. – Vol. 9, no. 4. – P. 272–284. – DOI: 10.1108/09556229710175515.
123. Chen B., Govindaraj M. A physically based model of fabric drape using flexible shell theory // Textile Research Journal. – 1995. – Vol. 65, no. 6. – P. 324–330. – DOI: 10.1177/004051759506500603.
124. Chen B., Govindaraj M. A parametric study of fabric drape // Textile Research Journal. – 1996. – Vol. 66, no. 1. – P. 17–24. – DOI: 10.1177/004051759606600103.
125. Park C. K., Kim S., Yu W. R. Quantitative fabric drape evaluation system using image processing technology (Part 1): Measurement system and geometric model // Journal of Testing and Evaluation. – 2004. – Vol. 32, no. 2. – P. 131–137. – DOI: 10.1520/JTE11755.
126. Kown E. S., Yoon S. Y., Sul I. H., Kim S., Park C. K. A quantitative fabric drape evaluation system using image-processing technology, Part 2: Effect of fabric properties on drape parameters // Journal of Testing and Evaluation. – 2010. – Vol. 38, no. 3. – P. 263–270. – DOI: 10.1520/JTE102361.
127. Sun M. N. A new tester and method for measuring fabric stiffness and drape // Textile Research Journal. – 2008. – Vol. 78, no. 9. – P. 761–770. – DOI: 10.1177/0040517507084284.
128. Issa M., Elgholmy S., Sheta A., Fors M. N. A new method for measuring the static and dynamic fabric/garment drape using 3D printed mannequins // The Journal of The Textile Institute. – 2021. – Vol. 112, no. 1. – P. 1–13. – DOI: 10.1080/00405000.2020.1748803.

129. Hussain A., Zhong Y., Naveed T., Yu Z., Xi Z., Ge W. A new approach to evaluate fabric hand based on three-dimensional drape model // Autex Research Journal. – 2020. – Vol. 20, no. 2. – P. 155–167. – DOI: 10.2478/aut-2019-0011.
130. Demir M., Balci Kilic G. A research for the effectiveness of stitch type and stitch direction on dynamic drape behaviors // International Journal of Clothing Science and Technology. – 2023. – Vol. 35, no. 6. – P. 971–985. – DOI: 10.1108/IJCST-04-2023-0053.
131. ASTM International. ASTM D1388-18: Standard test method for stiffness of fabrics. – West Conshohocken, PA : ASTM International, 2018.
132. ASTM International. ASTM D1777: Standard test method for thickness of textile materials. – West Conshohocken, PA: ASTM International.
133. ASTM International. ASTM D5034: Standard test method for breaking strength and elongation of textile fabrics (grab test). – West Conshohocken, PA: ASTM International.
134. ASTM International. ASTM D4032-08(2016): Standard test method for stiffness of fabric by the circular bend procedure. – West Conshohocken, PA : ASTM International, 2016.
135. CLO Virtual Fashion. How accurate are virtual fabrics? [Электронный ресурс]. – CLOHelpCenter. – UpdatedMay 16, 2023. – URL: https://support.clo3d.com/hc/en-us/articles/115013660747-How-accurate-are-virtual-fabrics (дата обращения: 29.05.2026). – Текст : электронный.
136. CLOVirtualFashion. Emulator [Электронный ресурс]. – CLOHelpCenter. – UpdatedMay 29, 2024. – URL: https://support.clo3d.com/hc/en-us/articles/115015983027-Emulator (дата обращения: 29.05.2026). – Текст : электронный.
137. CLOVirtualFashion. FabricKitManual [Электронный ресурс]. – CLOHelpCenter. – UpdatedMay 29, 2024. – URL: https://support.clo3d.com/hc/en-us/articles/360041074334-Fabric-Kit-Manual (дата обращения: 29.05.2026). – Текст : электронный.
138. CLO Virtual Fashion. How are fabrics simulated in CLO? [Электронный ресурс]. – CLOHelpCenter. – UpdatedAugust 12, 2021. – URL: https://support.clo3d.com/hc/en-us/articles/115013821448-How-are-fabrics-simulated-in-CLO (дата обращения: 29.05.2026). – Текст : электронный.
139. CLO Virtual Fashion. Does CLO come with a fabric database? [Электронный ресурс]. – CLOHelpCenter. – UpdatedOctober 13, 2025. – URL: https://support.clo3d.com/hc/en-us/articles/115013821388-Does-CLO-come-with-a-fabric-database (дата обращения: 29.05.2026). – Текст : электронный.
140. Style3D. 3Dfabricscanning&real-timesimulation [Электронный ресурс]. – Style3Dofficialwebsite. – URL: https://www.style3d.com/products/fabric (дата обращения: 29.05.2026). – Текст : электронный.

141. Yang Y. C., Zhang W. Y., Cong S. Investigating the development of digital patterns for customized apparel // International Journal of Clothing Science and Technology. – 2007. – Vol. 19, no. 3/4. – P. 167–177. – DOI: 10.1108/09556220710741632.
142. Bye E., LaBat K., McKinney E., Kim D. E. Optimized pattern grading // International Journal of Clothing Science and Technology. – 2008. – Vol. 20, no. 2. – P. 79–92. – DOI: 10.1108/09556220810850469.
143. Hernández N., Mattila H., Berglin L. A systematic model for improving theoretical garment fit // Journal of Fashion Marketing and Management. – 2018. – Vol. 22, no. 4. – P. 527–539. – DOI: 10.1108/JFMM-10-2017-0112.
144. Kim S. Simulation of bespoke garments using parametrically designed patterns // International Journal of Clothing Science and Technology. – 2012. – Vol. 24, no. 5. – P. 350–362. – DOI: 10.1108/09556221211259000.
145. Kim S. H., Kim S., Park C. K. Development of similarity evaluation method between virtual and actual clothing // International Journal of Clothing Science and Technology. – 2017. – Vol. 29, no. 5. – P. 743–750. – DOI: 10.1108/IJCST-01-2017-0001.
146. Zulkifli S. Z. B., Kim K., Takatera M. Similarities and differences between virtual and actual pants // International Journal of Clothing Science and Technology. – 2021. – Vol. 33, no. 2. – P. 199–217.
147. Gong D. X., Hinds B. K., McCartney J. Progress towards effective garment CAD // International Journal of Clothing Science and Technology. – 2001. – Vol. 13, no. 1. – P. 12–23. – DOI: 10.1108/09556220110384833.
148. Yan J., Kuzmichev V. E. A virtual e-bespoke men's shirt based on new body measurements and method of pattern drafting // Textile Research Journal. – 2020. – Vol. 90, no. 19-20. – DOI: 10.1177/0040517520913347.
149. McKinney E., Gill S., Dorie A., Roth S. Body-to-pattern relationships in women’s trouser drafting methods: Implications for apparel mass customization // Clothing and Textiles Research Journal. – 2017. – Vol. 35, no. 1. – P. 16–32. – DOI: 10.1177/0887302X16664406.
150. Jin P., Fan J., Zheng R., Chen Q., Liu L., Jiang R., Zhang H. Design and research of automatic garment-pattern-generation system based on parameterized design // Sustainability. – 2023. – Vol. 15, no. 2. – P. 1268. – DOI: 10.3390/su15021268.
151. Lee M.-J., Sohn H.-S., Kim J.-J. A Study on Representation of 3D Virtual Fabric Simulation with Drape Image Analysis II - Focus on the Comparison between Real Clothing and 3D Virtual Clothing - // Journal of Fashion Business. – 2011. – Vol. 15, no. 3. – P. 97–111. – DOI: 10.12940/jfb.2011.15.3.097.
152. Seçkin M., Seçkin AÇ., Demircioglu P., Bogrekci I. FabricNET: A Microscopic Image Dataset of Woven Fabrics for Predicting Texture and Weaving Parameters through Machine Learning // Sustainability. – 2023. – Vol. 15, no. 21. – Article 15197. – DOI: 10.3390/su152115197.

153. Lee S., Han Y., Yun C. Development of a fabric classification system using drapability and tactile characteristics // Fashion and Textiles. – 2024. – Vol. 11. – Article 2. – DOI: 10.1186/s40691-023-00368-2.
154. Yun E., Yun C. Development of a test method for the dynamic drapability of fabrics using reciprocating motion // Fashion and Textiles. – 2023. – Vol. 10. – Article 35. – DOI: 10.1186/s40691-023-00355-7.
155. Kim H. S., Choi H. E., Park C. K. [et al.]. Standardization of the size and shape of virtual human body for apparel products // Fashion and Textiles. – 2019. – Vol. 6. – Article 33. – DOI: 10.1186/s40691-019-0187-z.
156. Wang R., Fang F., Chen Q. A Sustainable Framework for Realism Evaluation and Optimization of Virtual Fabric Drape Effect // Sustainability. – 2025. – Vol. 17, no. 12. – P. 5550.
157. Chen J., Guo Z., Li T., [et al.]. Construction of Pattern Optimization Model Driven by Fabric Parameters in 3D Garment Development Using Artificial Neural Networks // Technologies. – 2025. – Vol. 13, no. 11. – P. 487.
158. Winn L. J., Schwarz E. R. Technical Evaluation of Textile Finishing Treatments // Textile Research Journal. – 1939. – Vol. 10, no. 1. – P. 5–16.
159. Sanad R., Cassidy T., Cheung V. Fabric and Garment Drape Measurement - Part 1 // Journal of Fiber Bioengineering and Informatics. – 2012. – Vol. 5, no. 4. – P. 341–358. – DOI: 10.3993/jfbi12201201.
160. Sanad R., Cassidy T., Cheung V., Evans E. Fabric and garment drape measurement - Part 2 // Journal of Fiber Bioengineering and Informatics. – 2013. – Vol. 6, no. 1. – P. 1–22. – DOI: 10.3993/jfbi03201301.
161. Kuzmichev V., Yan J. The application of digital twins in the field of fashion // Digital twins: basics and applications. – Cham : Springer International Publishing, 2022. – P. 45–57.
162. ASTM International. ASTM D5034-21. Standard Test Method for Breaking Strength and Elongation of Textile Fabrics (Grab Test). – West Conshohocken, PA : ASTM International, 2021. – DOI: 10.1520/D5034-21.
163. ASTM International. ASTM D1388-23. Standard Test Method for Stiffness of Fabrics. – West Conshohocken, PA : ASTM International, 2023. – DOI: 10.1520/D1388-23.
164. International Organization for Standardization. ISO 9073-9:2008. Textiles — Test methods for nonwovens — Part 9: Determination of drapability including drape coefficient. – Geneva : ISO, 2008.
165. Otsu N. A threshold selection method from gray-level histograms // IEEE Transactions on Systems, Man, and Cybernetics. – 1979. – Vol. 9, no. 1. – P. 62–66. – DOI: 10.1109/TSMC.1979.4310076.

166. Wang Z., Bovik A. C., Sheikh H. R., Simoncelli E. P. Image quality assessment: from error visibility to structural similarity // IEEE Transactions on Image Processing. – 2004. – Vol. 13, no. 4. – P. 600–612. – DOI: 10.1109/TIP.2003.819861.
167. Taha A. A., Hanbury A. Metrics for evaluating 3D medical image segmentation: analysis, selection, and tool // BMC Medical Imaging. – 2015. – Vol. 15. – P. 29. – DOI: 10.1186/s12880-015-0068-x.
168. Nai Y. H., Teo B. W., Tan N. L., O'Doherty S., Stephenson M. C., Thian Y. L., Chiong E., Reilhac A. Comparison of metrics for the evaluation of medical segmentations using prostate MRI dataset // Computers in Biology and Medicine. – 2021. – Vol. 134. – Article 104497. – DOI: 10.1016/j.compbiomed.2021.104497.
169. General Administration of Quality Supervision, Inspection and Quarantine of the People's Republic of China; Standardization Administration of China. GB/T 1335.2-2008. Standard sizing systems for garments — Women. – Beijing : Standards Press of China, 2008.
170. Чэнь, Ч. Совершенствование испытания тканей для одежды в виртуальной среде/ Ч. Чэнь, Ч. В.Е. Кузьмичев // Известия вузов. Технология текстильной промышленности. 2024, 5(413). С. 83-95. DOI 10.47367/0021-3497_2024_5_83.– 0,81п.л./0,6 п.л.
171. Chen Chengyu, Kuzmichev Victor. Digital Twin of Textile Fabric in Draping Test 2025 IEEE Smart World Congress (SWC).18-22 Aug 2025, Calgary, Canada. 2025. C.1591-1598. - DOI 10.1109/SWC65939.2025.00250. – 0,5п.л./0,4 п.л.
172. ЧэньЧэнюй, Кузьмичев В.Е. Совершенствование тестирования текстильных материалов в виртуальной среде //Молодые ученые – развитию Национальной технологической инициативы (ПОИСК – 2024): сб. материалов национальной (с международным участием)молодёжной научно-технической конференции. – Иваново: ИВГПУ, 2024, с.770-775. – 0,38 п.л./0,3 п.л.
173. Чэнь Чэнюй, Кузьмичев В.Е. Прогнозирование параметров формы женского платья с использованиемнового коэффициента драпируемости // Молодые ученые – развитию Национальной технологической инициативы (ПОИСК – 2025): сб. материалов Национальной (с международным участием) молодёжной научно-технической конференции. – Иваново: ИВГПУ, 2025. – С.501-505. – 0,31 п.л./0,25 п.л.
174. Chen Chengyu, KuzmichevVictor. Virtual simulation of Apparel Draping: IFFTI Annual Proceedings, London, 2025, Vol. 4, March 2025, pp.1406-1424 https://iffti.org/downloads/iffti-publication/annual-proceedings/lcf-2025/1406-1424%20394,%20Virtual%20Simulation%20of%20Apparel%20Draping.pdf – 1.1 п.л./ 0.7 п.л.
175. Чэнь, Ч. Количественное управление формообразованием платьев: подход на базе машинного зрения и антропоморфного коэффициента драпируемости / Ч. Чэнь, В.Е. Кузьмичев // Известия вузов. Технология текстильной промышленности. 2026, 3(423). С.230-245. - 1 п.л./0,8 п.л.

LIST OF ABBREVIATIONS

3D - Three-dimensional; three-dimensional modeling or three-dimensional technology
AI / ИИ - Artificial intelligence
ANOVA - Analysis of variance
APE - Absolute percentage error
$A_{overall}$ - Percentage of the bright area in the overall pleat region
A_{ROI1} - Percentage of the bright area in ROI-1
A_{ROI2} - Percentage of the bright area in ROI-2
ASTM - American Society for Testing and Materials; ASTM standards system
B - Basic element of the prompt protocol; in the validation section, also the target dress B
BD - Basic dress
BD1–BD5 - Five dimensional-structural levels of the basic dress
CAD - Computer-aided design
C1–C3 - Additional virtual fabrics from the Style3D library
CLO3D - Software environment for three-dimensional garment simulation
CV - Coefficient of variation
DC - Drape coefficient obtained by the traditional disk method
DC_{SFM} - Drape coefficient measured using the SFM method
DT - Digital twin
E01–E15 - Elements of the prompt protocol
F1–F5 - Codes of real fabrics used in the study
FAST - Fabric Assurance by Simple Testing; fabric property testing system
G - Fabric surface density
GSM - Grams per square metre; surface density, g/m²
GPT - Generative Pre-trained Transformer; multimodal model by OpenAI
IoU - Intersection over union
KES - Kawabata Evaluation System; system for evaluating fabric mechanical properties
Lab - Laboratory reference values or parameter set obtained by laboratory measurements
LS - Long sample
LS1–LS5 - Five levels of the long sample
LSDC_{SFM} - DCSFM obtained for the long sample LS
MAE - Mean absolute error

MAPE - Mean absolute percentage error
T - Minimum grayscale threshold T
OBJ - OBJ file format for three-dimensional geometry
P1–P6 - Six types of photographic evidence for AI measurements
P_1–P_{10} - Fixed pleat positions in the PLD pattern
P_{d1}–P_{d4} - Shape parameters of the basic dress BD
PLD - Pleated / draped dress
PLDP1–PLDP5 - Five levels of the pleated dress PLD pattern
RE - Relative error
RMSE - Root mean square error
ROI - Region of interest
ROI-1 - Local region of the upper pleat-concentration zone
ROI-2 - Local region of diagonal pleat propagation
SD - Standard deviation
SFM - Shoulder Fitting Method
SNP - Side neck point
SP - Shoulder point
SPSS - IBM SPSS Statistics; statistical processing software
SS - Short sample
SS1–SS5 - Five levels of the short sample
SSDC_{SFM} - DCSFM obtained for the short sample SS
SSIM - Structural similarity index measure
Tf - Fabric thickness
V - Validation object; in the prompt section, also a variable element of the protocol
VD - Validation basic dress
VF1–VF5 - Virtual fabrics from the Style3D library
VSS - Validation short sample
Δ - Pleat coefficient
$\Delta 1$ - Normalized expansion parameter in the front–back direction
$\Delta 2$ - Normalized parameter of mean-width change
α - Total inclination angle of the front and back parts of the SS sample
Dd - Maximum front–back distance of the sample after draping
Wm - Effective width of the SFM drapemeter
$W0$ - Mean sample width before draping
Wd - Mean sample width after draping
L_{sh} - Shoulder seam length

L_{SS} - Length of the short sample SS

W_{SS} - Width of the short sample SS

L_{LS} - Length of the long sample LS

W_{LS} - Width of the long sample LS

s_1–s_3 - Types of shoulder seams

o_1–o_3 - Sample cutting directions

h_1–h_3 - Variants of lower-edge finishing

R1–R5 - Radius parameters of the cross-section of the shoulder support surface

X1–X5 - Coded factors in the model of influence on DCSFM

①–㉔ - Codes of fabric physico-mechanical parameters

LIST OF TABLES

LIST OF FIGURES

of PLD: a — pleats near the seam connecting the upper and lower parts of the dress as ROI-1; b — pleats in the diagonal propagation zone toward the hem and side as ROI-2; c — overall pleated region of the target PLD combining ROI-1 and ROI-2; d — original image of the target PLD before cropping; e — PLD dress made from fabric F1; f — PLD dress made from fabric F2; g — PLD dress made from fabric F3

2.5 - Dimensions of physical specimens prepared for GSM, thickness, tensile, and bending tests

2.6 - Devices and measurement principles used in the tests: a — GSM measurement; b — thickness measurement; c — tensile test; d — bending test; e — circular drapeability test

3.1 - Virtual geometric supports used for preliminary comparison of drapeability: a — spherical support in CLO3D; b — cylindrical support in Style3D; c — conical support in Style3D

3.2 - Extraction and parametric definition of the virtual shoulder-support surface: a — virtual figures of different size gradations and the selected shoulder region; b — definition of geometric parameters of the support surface

3.3 - New virtual shoulder support generated in Style3D: a — front view; b — left view; c — back view; d — right view

3.4 - Physical prototype of the drapemeter and auxiliary measuring device: a — front view; b — side view; c — auxiliary laser reference device

3.5 - Geometric forms and local structural variables of specimens: a — SS; b — LS; c — s_1 plain seam; d — s_2 lapped seam with enclosed edges; e — s_3 flat-felled seam; f — h_1 lower edge without hemming; g — h_2 lower edge with folded edge; h — h_3 lower edge with hem seam

3.6 - Fixed placement position and stabilized draped state of SS: a — initial placement of SS in the fixed position; b — stabilized draped state of SS

3.7 - Testing process using the SFM method and traditional methods based on projected area in Style3D and Rhino 7: a — simulation of the SS specimen on the SFM support; b — simulation of the circular specimen on the spherical support; c — projected contour of the SS specimen; d — projected contour of the circular specimen

3.8 - Specimen placement for the SFM drape test: a — SS placement in the virtual test; b — LS placement in the virtual test; c — physical SS specimen placement

3.9 - Measurement scheme of parameters for calculating DCSFM: a — measurement of flat SS width before draping; b — measurement of SS width

APPENDIX A

Prompt Structure 5

E01: *You are a textile testing expert.*

E02: *Based only on the visual information in the uploaded fabric photos, give your best rough estimates for the following fabric parameters.*

These are not lab measurements; only approximate ranges inferred from the image.

Remember: all values are visual guesses, not real test results. Do not claim any standard or instrument was actually used.

E04: *The DC value must be a range between 0–1 (dimensionless).*

Thickness unit column: mm.

Forces at 1–5 mm extension unit column: kgf

E05: *If the image does not give enough information, use a very wide range and set confidence to low.*

Confidence level must be one of low, medium, high.

E06: *Keep the same structure for 4 table and column headers as in the first test:*

Table 1. General properties

Table 2. Tensile behavior (forces at 1–5 mm extension)

Table 3. Bending behavior in a cantilever test from 25 mm

Table 4. Drape coefficient

E07: *Answer only with Markdown tables, no extra text before or after the tables.*

Table 1 General properties

Parameter	*Estimated value (range)*	*Unit*	*Confidence*	*Reasoning (visual cues)*
Material (fiber +structure)				
Thickness				
GSM				

Table 2Tensile behavior (forces at 1–5 mm extension)

Direction	*forces at 1–5 mm extension*					*Unit*	*Confidence*	*Reasoning (visual cues)*
	1	*2*	*3*	*4*	*5*			
Warp								
Weft								
Bias								

Table 3 Bending behavior in a cantilever test from 25 mm

Direction	*Contact distance (range)*	*Horizontal travel (range)*	*Unit*	*Confidence*	*Reasoning (visual cues)*
Warp					
Weft					
Bias					

Table 4 Drape coefficient

Parameter	*Estimated value (range)*	*Unit*	*Confidence*	*Reasoning (visual cues)*
DC				

E08: *Answer only with Markdown tables, no extra text before or after the tables*

E09: *All numeric values must be ranges in the form min–max, not single exact numbers.*

All forces must be ranges, e.g. 0.01–0.05.

E10: *Reasoning (visual cues)*

In the reasoning, briefly explain which folds, curl, or stiffness cues you used to estimate each direction.

Explain briefly which aspects of the shape (number and depth of folds, silhouette, fullness, etc.) led to your estimate.

APPENDIX B

Measurement results for the light region within the overall folded surface at five PLD pattern levels

Fabric	PLDP level	Folding coefficient Δ	Share of the light area, %Area, %
F1	1	0.48	61.372
F1	2	0.67	51.924
F1	3	0.86	44.980
F1	4	1.05	43.841
F1	5	1.24	43.392
F2	1	0.48	69.747
F2	2	0.67	57.009
F2	3	0.86	48.268
F2	4	1.05	46.071
F2	5	1.24	43.443
F3	1	0.48	74.840
F3	2	0.67	68.705
F3	3	0.86	67.599
F3	4	1.05	62.199
F3	5	1.24	58.181